Heterogeneous catalysis using low cost and waste derived reagents for sustainable chemistry applications

PERERA-SOLIS, DIEGO,DE,JESUS

Heterogeneous catalysis using low cost and waste derived reagents for sustainable chemistry applications

Diego D. Perera-Solis

A thesis submitted for the degree of Doctor of Philosophy

Department of Chemistry

2021

Declaration

The work described in this thesis was carried out in the Department of Chemistry, at Durham University between October 2017 and May 2021. All of this work is my own unless specifically stated otherwise. No part of this work has previously been submitted for a degree at this or any other institution.

Statement of Copyright

Acknowledgments

First of all, I would like to say thank you to my supervisor, the professor Chris Greenwell, for his support during my time at Durham University, words are not enough to thank him for his guidance, ideas and enthusiasm. He was always there for me, no matter how busy he was and as a foreign student, I really appreciate that effort.

Secondly, I would like to thank my other supervisor, Andy Whiting who showed me how a chemistry "magician" really looks like. Although knowing I am not a chemist, he was very patient with me and guided me through concepts I did not understand at that moment. He made me get a true love for organic chemistry, at least at a "notebook" level, because my skills in the lab are not that good.

For all the latter I will always be forever grateful with both, Andy and Chris, without them, my personal and professional growth would not have been possible.

I also want to say thanks to my wife Alexandra Traslaviña, whom I met while being at Durham. You changed my life for the best and I have the rest of my life to keep being grateful with you for that. I love you.

Special mention to my mother who was very supportive during the whole process of being far from home, and my sister who showed me the true meaning of taking risks and not looking back. You two are always in my mind and heart.

Moreover, I would like to say thanks to my labmates, which made me feel like home while being working in the lab although I am pretty sure I got them tired because of my lack of laboratory knowledge. Thanks for always being there Melinda, Eric, Alba and Eva.

I would also like to say thank you to my friends in Mexico, who were always there for me when I needed them, Daniel Corral and Miguel Rodriguez. Your friendship is one of my most valuable treasures. To my friends in Durham, David Palacios, Balder Nieto, Yazmin Santos and Hector Escamilla, some of the most caring persons I have ever met. Thanks for being there for me all the time, for the videogame nights, or for the mates at the Musgrave.

Thus, I would like to thank my sponsor, the Consejo Nacional de Ciencia y Tecnologia (CONACyT) in Mexico for providing the funding for this research to be carried out.

Last but not least, to all the people in the department, specially to Dr. Aileen Consgrave, Lennox Launch, Gary Oswalt and Emily Unsworth. Without your assistance, most of my work would not have been possible. To the rest of my family and close people, each one of you can be sure have been part of this work, if I keep you in my life, its because you mean a lot.

Publications

- Perera-Solis, D.D., et al., *Heterogeneous ketonic decarboxylation of dodecanoic acid: studying reaction parameters.* RSC Advances, 2021. **11**(56): p. 35575-35584.
- Perera-Solis, D.D., et al., *Adding Value to Waste Minerals in a Circular Economy Framework: Ochre-Derived Layered Double Hydroxide Catalysts in Fatty Acid Ketonisation.* Minerals, 2019. **9**(11): p. 681.
- Smith, B., et al., *Ketone Formation via Decarboxylation Reactions of Fatty Acids Using Solid Hydroxide/Oxide Catalysts.* Inorganics, 2018. **6**(4): p. 121.

Table of contents

List of Tables

List of Figures

List of abbreviations

BET	Braunner-Emmett-Teller
BJH	Barrett-Joyner-Halenda
BSTFA	N,O-Bis(trimethylsilyl)trifluoroacetamide
EDS	Energy-dispersive spectroscopy
FTIR	Fourier transform infra-red
FWHM	Full width at half maximum
GC	Gas chromatography
ICP-OES	Inductively coupled plasma optical emission spectroscopy
ICP-MS	Inductively coupled plasma mass spectrometry
LDH	Layered-double hydroxide
MS	Mass-spectrometry
PXRD	Powder x-ray diffraction
SEM	Scanning-electron microscopy
SD	Standard deviation
TEM	Transmission-electron microscopy
TGA	Thermogravimetric analysis
TLC	Thin layer chromatography
UV-vis	Ultraviolet-visible

Abstract

Concepts related to sustainability and the circular economy are more important today than ever, with focus on reducing primary extraction of resources, geopolitics and the high energy demand for primary resource exploitation and shipping [1-4]. In this thesis, sustainability and circular economy concepts are explored through the study of the ketonic decarboxylation of fatty acids and the use and characterisation of low-cost catalysts.

In Chapter 1, a review of the emergence of the need for circular economy principles, and how this couples with energy demand and climate change is given, along with an overview of the role of biomass and catalysis within a circular economy framework. A detailed breakdown of what the circular economy is and how biomass could play a crucial role to produce bio-derived added value products in the future is shown. Moreover, the chapter goes further in exploring the different products that can be obtained from biomass, such as ketones derived from fatty acids through the ketonic decarboxylation reaction. Thus, the introduction explores in detail the different mechanisms that could potentially happen during the latter ketonic decarboxylation reaction and the catalyst used to activate such reaction. A wide variety of the catalysts mentioned in the literature and the different reaction conditions in which the catalysts related to the ketonic decarboxylation reaction were used is also covered. The final part of the review explores a particular family of catalytic materials named the layered double hydroxides (LDHs), which can potentially be developed out of waste materials to deliver the diverse range of applications the latter LDHs can be applied for.

Chapter 2 explains in detail all the analytic methods used in this thesis, from the methods employed to synthesise and characterise the catalysts, the reactants through to the methods employed to quantify the latter obtained reaction products. Among the techniques used and detailed in Chapter 2 are powder X-ray diffraction, Fourier-transform infra-red spectroscopy, thermogravimetric analysis, inductively coupled plasma optical emission spectroscopy, gas chromatography, mass-spectrometry, surface area analysis and scanning electron microscopy.

In Chapter 3, MgO was used to catalyse the ketonic decarboxylation of dodecanoic acid to form 12-tricosanone at moderate temperatures (250 °C , 280 °C and 300 °C) with low catalyst loads of 1% (w/w), 3% (w/w) and 5% (w/w) with respect to the dodecanoic acid, with a reaction time of 1 hour under batch conditions. Three different particle sizes for the MgO were tested (50 nm, 100 nm and 44 μm) and the ketone yield was found to increase with increasing reaction temperature, reaching approximately 75% yield for all the samples tested. The temperature was found to be the main control on reaction yield, rather than surface area or particle size, which we show is related to recrystallization of the catalysts during the reaction such that all particle sizes show similar crystalline domain sizes.

Chapter 4 continues to explore the use of MgO as an accessible and highly basic catalyst to catalyse a more complex reaction mixture, the cross-ketonisation reaction of different carboxylic acids (i.e. having different carbon chain lengths, unsaturated acids, lacking α-hydrogens). This allows the study of the effect of catalyst-substrate and substrate-substrate interactions in a given solvent system. The reactions were carried out at 300 ˚C for 1 hour, using a 5% (w/w) of MgO with respect to the carboxylic acid mixtures. The carboxylic acids lacking α-hydrogens did not react to form ketones, whereas the saturated carboxylic acids favoured the formation of symmetrical and asymmetrical ketone products, in clean post-reaction mixtures. When carboxylic acids containing unsaturated C-C bonds were used, a Diels-Alder reaction seemed to be outperforming the ketonic decarboxylation reaction, favouring the formation of a variety of different products which were not fully identified.

Starting to explore the concept of circular economy, in Chapter 5, Mg/Fe layered double hydroxide (LDH) materials, were successfully synthesised via the co-precipitation method from a dissolved acid mine drainage precipitate waste mineral assemblage, known as "ochre", which is normally put to landfill. The prepared LDH materials were tested as a heterogeneous base catalyst to promote the production of the ketone, 12-tricosanone, from lauric acid, a component of plant oils, through a ketonic decarboxylation reaction, giving a circular economy route to catalysts for sustainable ketone production. The highest yield of the ketone observed was 80%. In order to examine other sustainable uses, an energy application was also considered in Chapter 6, where a Mg-Fe layered double hydroxide material (LDH) of ratio 4 was synthesized from the acid mine drainage waste "ochre", which otherwise would end as landfill. The prepared ochre LDH was fully characterised and compared against an LDH made of synthetic salts as an active

photocatalyst for the hydrogen evolution reaction, producing up to 1272 μmol.h^{-1}.g^{-1} of hydrogen.

Chapter 7 concludes ideas explored in Chapter 5 and Chapter 6, where a LDH catalyst was prepared from ochre, by preparing a material wholly out of waste. Using a waste material obtained from water treatment plants (i.e. struvite, a Mg mineral) and the Fe containing mining waste ochre, LDHs of Mg/Fe ratio 2 and ratio 4 were synthesised. Although the materials were not further tested as catalysts or adsorbents, obtaining a material made wholly of waste was successful and the latter material was fully characterised.

Finally, Chapter 8 summarises the key findings from this study. Among some of the achievements, it was concluded that the crystallite size might be playing a major role in the ketonic decarboxylation reaction of dodecanoic acid in conjunction with the temperature parameter, with the surface area and the active site availability having less impact on the product yield. Moreover, it was also observed that the presence of unsaturation within the carbon chain of carboxylic acids might influence the Diels-Alder reaction to outperform ketonic decarboxylation reactions, however, as the literature is not fully clear on that process, more experimental work was needed to give stronger conclusions. Finally, exploring the concept of circular economy yielded the production of different LDH materials, partially and wholly made of waste, producing the first ochre-struvite derived LDH material, which can potentially be used in a wide variety of applications. The partial waste LDH was successfully used for catalytic applications such as the production of ketones from carboxylic acids and the production of hydrogen trough the hydrogen evolution reaction. Moreover, thefuture work section discusses ways in which the gaps from this work could be addressed through future work from other members of the group.

1. Introduction

1.1. Context

During the 1980s, the concept of sustainable development was defined. This definition stated that the needs of the current generation should be met without compromising the needs of future generations [5]. Today, this definition remains as valid as it was 40 years ago. However, and more importantly, the population worldwide has become three times bigger than it was in 1950 (2.5 billion people to 7.8 billion in 2020) and it is expected to keep growing up to 9.7 billion by 2050, according to an estimation made by Yale University and the United Nations [6,7]. Undoubtedly, this rise in population will bring, as well, increases in consumption of goods and energy resources from all around the World. If we take into account that the impacts to the environment to fulfil today's population demands in terms of energy and commodities can be already observed by way of global warming, air pollution and resources depletion, it is no secret that efforts are being undertaken by several nations to try to mitigate these negative effects by changing energy policies and working towards the production of cleaner energy rather than using oil and coal, aiming for a cleaner future [8,9]. Shylesh *et al.,* [3] pointed out that the impact to the environment caused by the use of oil and coal, such as the emission of greenhouse gases, can be reduced when fuels are generated from renewable sources. Tied to the search for a more sustainable industry sector, and society in general, exists the concept of the circular economy, which has gained a lot of popularity in recent years, being an active part of many countries and major private companies' agendas [1]. Based on several contributions throughout the years towards the circular economy concept, Geissdoerfer *et al.,* [1] provided the following definition: "a regenerative system in which resource input and waste, emission, and energy leakage are minimised by slowing, closing, and narrowing material and energy loops. This can be achieved through long-lasting design, maintenance, repair, reuse, remanufacturing, refurbishing, and recycling." However, sustainability and circular economy should not be used as equal concepts, rather they share similarities and have differences, where they share different relationships in terms of conditional, beneficial and trade-off directions [1,2]. Addressing some of the energy problems society faces today, while trying to work out the principles of circular economy and sustainable development, is not an easy task. According to Manayil *et al.,* [10] despite fossil fuel reserves still being added to, the exploitation of 65 to 80 % of these would lead to a break with the United Nations framework

convention on climate change (UNFCC) in which it is aimed to keep the rise in temperature in this century to below 2 °C. The emission of greenhouse gases (GHG) is another key environmental problem, directly related GHG include, notably, CO_2, NO_x and CH_4. GHG emissions are mainly produced when fossil fuel is combusted in order to produce energy within an internal combustion engine. The reduction of the latter GHG are of significative importance, due to the fact that the GHG not only accumulate in the atmosphere but also contribute to also trap heat in the atmosphere, contributing hugely to what is called global warming [11]. Despite significant efforts to mitigate the effects of GHG using renewable electrical energy sources, there are still many transportation vehicles (e.g. ships, aircrafts and trucks) that use, and will continue using, high energy-density hydrocarbon fuels [3,12,13]. Nevertheless, the increase in pollution and the negative effects on the environment are not only due to the use of oil and coal, but also the waste generated by human activities plays a role as critical as the one related to fossil fuels. Without a proper solid waste management system, the shortage of landfills and the higher prices paid to dispose waste, as well as the negative effects to the ecosystems (e.g., water contamination, spreading of diseases, erosion of lands, etc) will keep increasing [14,15]. Tackling the pollution problems through circular economy and sustainable development approaches could be achieved to some extend by swapping gradually towards the use of clean energy sources such as wind, solar, biomass, among others, to produce and offer environmentally friendly services and goods.

The use of biomass to transit towards a biomass-based economy could successfully, in the coming future, produce the fuels and commodities that otherwise would be produced following the conventional fossil fuel approaches [3,16]. Producing under green chemistry principles, giving use to what otherwise could be considered waste to produce added-value products such as catalysts or adsorbents for different applications using a circular economy framework could also be another potential pathway to keep mitigating the negative effect of any inefficient solid waste management and disposal.

1.2. The circular economy framework

Waste materials could receive different uses rather than just being disposed of. This trend, although not new, has been increasing in recent years as more and more countries worldwide try to reduce their carbon footprint or fulfil environmental agreements with other nations, pursuing the goal of a sustainable society development in the coming years [1,9,14]. The latter fits very well with the concept of the circular economy described by Geissdoerfer *et al.,* [1]. In his review, Geissdoerfer *et al.,* encapsulates the essence of 114 statements made by different authors. In their description, Geissdoerfer *et al.,* [1] define the circular economy as: "an economic system in which resource input and waste, emission, and energy leakages are minimised by cycling, extending, intensifying, and dematerialising material and energy loops. This can be achieved through digitalisation, sharing solutions, long-lasting product design, maintenance, repair, reuse, remanufacturing, refurbishing, and recycling". According to the latter statement, it is clear that a circular economy approach for industrial purposes is more advantageous than any other approach when moving towards sustainable societies. However, nowadays societies are dealing with significant tasks when trying to tackle problematic pollution. Among some of the latter societies having complex pollution and emission problems is Mexico. Mexico is one of several countries where the pollution levels and emission could be high enough to be detrimental for the inhabitants [17]. The country growing at a fast pace during the last 20 years has lead to an unprecedent production of waste streams [18]. In this work, the effect of the reaction parameters and the effect to the catalyst in the ketonic decarboxylation reaction were explored (i.e., the formation of ketones from the coupling of two carboxylic acids, such as fatty acids). Thus, products from waste streams (i.e., struvite and ochre) were used to prepare a catalytic material. The former and the latter were decided to be explored as in Mexico, mine tailings, waste cooking oil streas and wastewater treatment plant streams are pollutant streams from industrial processes [19,20], which can be potentially included within a circular economy model. Although not specifically related to Mexico, but to show the importance of using a circular economy framework within the different production processes, some other examples are presented in the following lines. he waste coming from the food industry can vary depending on the specific business segment and geographic position, as the supply chain for the latter is massive [21,22]. According to Redcorn *et al.,* [23] up to 1.3 x 10^9 tons of food is lost annually worldwide. However, most of the waste streams are organic in nature, which confers them with an excellent opportunity to be exploited, possibly recovering valuable compounds from

them [21,24]. For instance, phenols from fruit processing, as well as protein from cheese production and hemicellulose from fiber product production are some examples among others where waste steams could be potentially revalorized taking advantage of such "waste materials" [25]. Nevertheless, although the circular economy is a concept that needs to be further considered among the societies today, to work towards a more sustainable future, there are several barriers that prevent circular economy to be implement in many economies today, such as lacking economic viability of circular economy models, no compromise to engage in circular economy projects and the lack of proven, mature and cost-effective technologies nowadays to favour the implementation of the latter circular economy, in Mexico and the world in general [26].

1.3. The role of the biomass and biofuels in a circular economy framework

Biomass involves all organic matter on the planet with the exception of fossil fuels. It is mainly composed of carbon (C), hydrogen (H), oxygen (O), nitrogen (N) and sulphur (S), the latter in relatively small quantities, as well as trace elements, and can be found in different forms. It can be found in high volumes and almost in every place around the globe. It is considered to be renewable, CO_2 neutral, clean and the most abundant source of carbon. Included in biomass resources are forestry, organic wastes originated from people's daily activities as well as agricultural wastes. Thus, biomass is a promising alternative to obtain chemicals and fuels and has been seen as a competitive option to obtain bioresources, generating high expectations, as reported in the literature [16,27-30]. Fitting into the definition of the circular economy explained in Section 1.2, the use of biomass as a raw material for energy and commodities production is not a new one, moreover when referring to the production of so-called biofuels. Triglycerides, lignocellulose and starchy feedstocks are all suitable feedstocks from which to produce biofuels [4,26,28]. Depending on these sources, biofuels can be organized into four different generations. The first generation (bioethanol, biodiesel and vegetable oils) comes from feedstocks based on traditional arable crops for human consumption such as rice, wheat, sugarcane, oil palm, soybean, etc. Pyrolysis of lignocellulose biomass (e.g. wood chips, bagasse, pine, oak, etc) produces bio-oil that can be considered as a second-generation biofuel because the feedstock for its generation comes from non-food based crops [4,27,28,31]. Algae (aquatic feedstock) lead to third generation biofuels. Their rate of production is high and theoretically use considerable

less land area than the other two generations in order to get a significant amount of fuel [31-34]. According to Azizi *et al,* [31] genetically modified microorganisms (e.g., fungi, cyanobacteria and microalgae) are the feedstock for fourth generation biofuels and direct conversion of CO_2 to fuels can potentially be achieved.

1.3.1 Biofuels drawbacks

Despite first generation biofuels being a mature and proven technology, concerns exist over the sustainability of their production, competing with the land normally used to produce food, competitive cost against actual fossil fuels and limited reduction in greenhouse gases emissions [35,36]. In addition, high viscosity and cloud point as well as low energy content and high acid number make biodiesel unsuitable to use as a fuel for all environments and engines [25,37]. First generation biofuels also include vegetable oils (e.g. soybean, palm and waste cooking oil), as they can be used as a fuel directly within a combustion engine instead of using them to produce biodiesel, however, high viscosity remains a major problem in conjunction with low cetane number generating deposits within the combustion chamber, delays in the ignition, clogging, poor atomization of fuel spray, etc [37-39]. Modifications to engines, preheating methods and blending with fossil fuels are some of the proposed solutions to overcome the latter drawbacks, making the use of vegetable oils unsuitable with the existing infrastructure [38-41]. On the other hand, second generation biofuels avoid the controversy of the first-generation fuels as they are made of non-food-based crops. However, an important drawback is that the actual infrastructure and the scope of this technology remains limited at large scale [42,43]. Thermochemical processing, such as pyrolysis or gasification of biomass, leads to promising products for the generation of fuels and chemicals. Bio-oil is the liquid fraction of the pyrolysis of biomass. The major drawback is that it is a highly oxygenated, unstable and corrosive product [44,45]. In order for it to be used as a biofuel, this complex mixture of organic compounds needs to be upgraded, for example through hydro-deoxygenation and hydro-denitrogenation [35,44-46]. Although third generation biofuels can yield a significant amount of high quality fuel for less landmass than the other two, the actual infrastructure for its production needs to be improved in order to make the process feasible and sustainable at scale [33,47,48].

1.4 Biomass-derived products

As mentioned in Section 1.3, biomass can be converted into biofuels, and depending on their source, these fuels can be classified into different generations. However, biomass could also be used to generate other added value products using diverse strategies [49]. Shylesh, *et al.,* [3] discussed different routes that can lead to conversion of biomass into diverse products using pyrolysis, plant and algal oils as well as C_5 and C_6 sugars coming from hemicellulose and cellulose from lignocellulosic biomass. They identify two different "biomass-derived synthons" as intermediate products coming from the sugars and oils from biomass. The first ones are ketones and alcohols derived from glucose and xylose. The second ones are carboxylic acids derived from pyrolysis oils and fatty acids [3]. The latter mentioned biomass-derived synthons are presented in Figure 1-1.

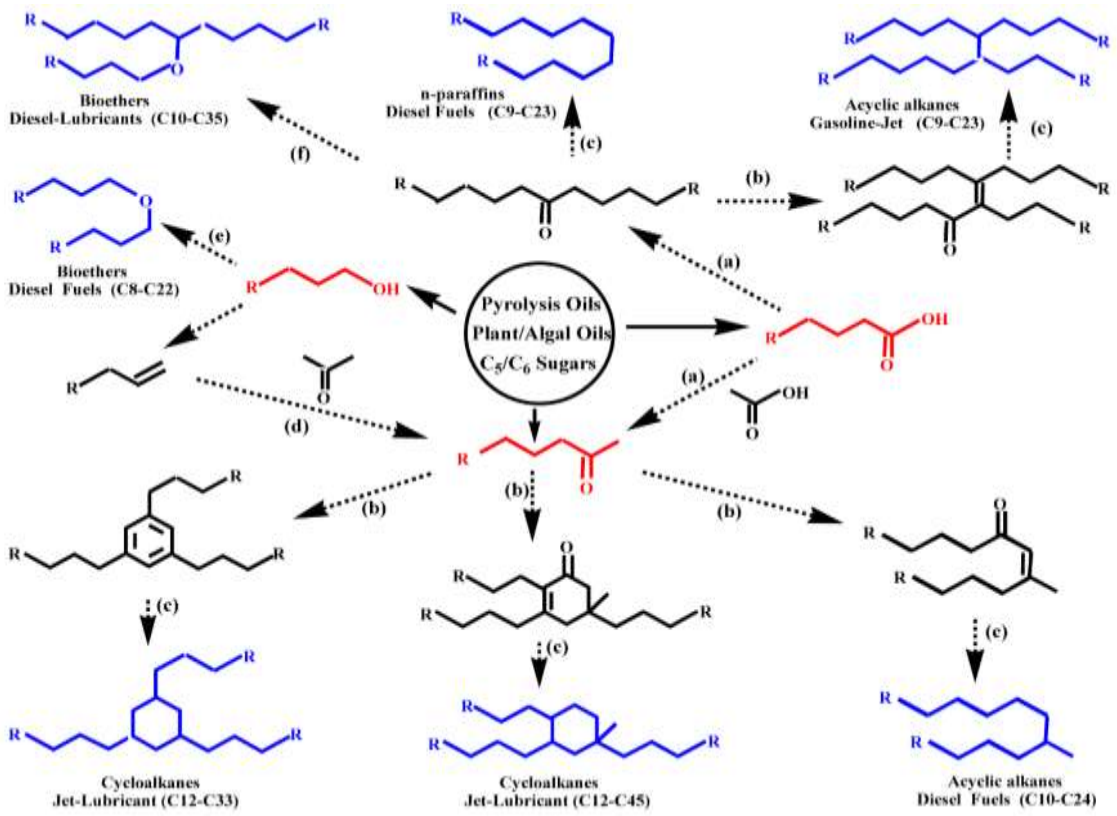

Figure 1-1. Biomass synthons to produce fuels and chemical products. The solid arrows represent biomass-derived compounds (coming from treatment of sugars and oils) while the dotted arrows represent the

transformation of the latter into different value-added products following (a) self-cross ketonisation, (b) condensation, (c) hydro-deoxygenation, (d) alkylation, (e) direct etherification and (f) reductive etherification reactions. Reprinted with permission from from Shylesh, *et al.,* [3]. Copyright 2021 American Chemical Society.

According to Figure 1-1, diesel-like products, gasolines and lubricants can be obtained once the three main raw materials (carboxylic acids, ketones and alcohols) undergo different transformation routes. Thus, it can also be seen in Figure 1-1 that hydrodeoxygenation is involved in most of the transformation routes as a final conversion step, favouring the deoxygenation of the synthons. However, hydro-deoxygenation has important disadvantages when being considered as an upgrading process, nevertheless, that will be covered in the following pages. A clear observation from Figure 1-1, is that, theoretically using biomass as the starting point and producing a diverse range of different synthons, the synthons can be further processed into something else, and so on until obtaining the desired final product, which is what was further explored in subsequent chapters (i.e., Chapter 3 and Chapter 4, where fatty acids were used as reactants when analysing the ketonic decarboxylation reaction). For instance, carboxylic acids can be further reduced to ketones and alcohols, which are the other two building blocks to produce other molecules, they are also presented in Figure 1-1**.** Thus, the carboxylic acids can be obtained from plant oils and animal fats (e.g. soybean, jatropha, rapeseed, sunflower oil, etc.) in the form of triglycerides [50]. Carboxylic acids also have a large carbon number, similar to the length of the carbon chains from fossil fuels and this has made researchers focus their attention on trying to produce bio-derived fuels using them [51]. Common fatty acids structures in vegetable oils are presented in Table 1-1 [52]. The effect of the unsaturations within the fatty acid's chain was further explored in Chapter 4, in an attempt to understand how the presence of such unsaturations could potentially affect the reaction mechanisms of the ketonic decarboxylation. Table 1-1 is a summary of the most common fatty acids that exist in vegetable oils, divided by the degree of saturation.

Table 1-1. Common fatty acid presented in vegetable oils. Adapted from from Issariyakul, *et al.,* [52].

System name	Common name	Symbol	Formula	Double bond position[a]
Saturated				
Decanoic	Capric	C10:0	$C_{10}H_{20}O_2$	-
Dodecanoic	Lauric	C12:0	$C_{12}H_{24}O_2$	-
Tetradecanoic	Mystiric	C14:0	$C_{14}H_{28}O_2$	-
Hexadecanoic	Palmitic	C16:0	$C_{16}H_{32}O_2$	-
Octadecanoic	Stearic	C18:0	$C_{18}H_{36}O_2$	-
Eicosanoic	Arachidic	C20:0	$C_{20}H_{40}O_2$	-
Docosanoic	Behenic	C22:0	$C_{22}H_{44}O_2$	-
Tetracosanoic	Lignoceric	C24:0	$C_{24}H_{48}O_2$	-
Unsaturated				
Hexadecenoic	Palmitoleic	C16:1	$C_{16}H_{30}O_2$	9c
Octadecenoic	Petroselinic	C18:1	$C_{18}H_{34}O_2$	6c
Octadecenoic	Oleic	C18:1	$C_{18}H_{34}O_2$	9c
Octadecenoic	Elaidic	C18:1	$C_{18}H_{34}O_2$	9t
Octadecenoic	Vaccenic	C18:1	$C_{18}H_{34}O_2$	11c
Eicosenoic		C20:1	$C_{20}H_{38}O_2$	5c

Eicosenoic	Gadoleic	C20:1	$C_{20}H_{38}O_2$	9c
Eicosenoic	Gondoic	C20:1	$C_{20}H_{38}O_2$	11c
Eicosenoic	Euric	C20:1	$C_{20}H_{38}O_2$	13c
Polyunsaturated				
Hexadecadienoic		C16:2	$C_{16}H_{28}O_2$	
Octadecadienoic	Linoleic	C18:2	$C_{18}H_{32}O_2$	9c12c
Octadecatrienoic	Linoleic-α	C18:3	$C_{18}H_{30}O_2$	9c12c15c
Octadecatrienoic	Linoleic-ϒ	C18:3	$C_{18}H_{30}O_2$	6c9c15c
Octadecatrienoic	Eleostearic	C18:3	$C_{18}H_{30}O_2$	9c11t13t
Octadecatrienoic	Calendic	C18:3	$C_{18}H_{30}O_2$	8t10t12c

[a] c = *cis*-form; t = *trans*-form

The most common vegetable oils (edible and non-edible) with their respective fatty acid composition are presented in Table 1-2 [52-54].

Table 1-2. Fatty acids composition in common plant's oils [52-54]. Each oil is composed from different fatty acids with different carbon chains, such as C12, C14, etc.

Fatty acids (% of total fatty acids)												
Oil type	C12:0	C14:0	C16:0	C16:1	C18:0	C18:1	C18:2	C18:3	C20:0	C22:0	C22:1	Reference
Soybean	0.0	0.0	10.1	0.0	4.3	22.3	53.7	8.1	0.0	0.0	0.0	[53]
Sunflower	0.0	0.0	5.2	0.1	3.7	33.7	56.5	0.0	0.0	0.0	0.0	[53]
Palm	0.0	0.0	44.8	0.0	4.6	38.9	9.5	0.4	0.0	0.0	0.0	[53]
Jatropha	0.0	0.0	18.5	0.0	2.3	49	29.7	0.0	0.0	0.0	0.0	[54]
Canola	0.0	0.0	3.1	0.2	1.3	56.6	22.4	14	0.4	0.2	0.1	[52]
Coconut	50.9	21.1	9.5	0.0	4.9	8.4	0.6	0.0	0.0	0.0	0.0	[52]

It can be seen from Table 1-2 that every oil (e.g., soybean, sunflower, etc) have different fatty acid composition, which derives in a mixture of carboxylic acids with different carbon chain lengths. As further explored in Chapter 4, the effect of the carbon chain as well as the unsaturation degree of the fatty acids seemed to be impacting the ketonic decarboxylation reaction, unfavouring a clean reaction product. Another important message

to take from Table 1-2 is that when further processing the bio-derived synthons, the oxygen content of the molecules is reduced. For instance, carboxylic acids are reduced to ketones, alcohols to alkenes, ketones to alkanes, and so on. The latter reduction of the molecules is due to the fact that current infrastructure for chemical commodities and fuel production mostly use non-oxygenated compounds, which are petroleum derived products [35,44], therefore bio-derived products need to fulfil the latter infrastructure requirements. Therefore, if the bio-derived synthons are planned to be used without modifying the current oil infrastructure, these bio-derived synthons are required to be upgraded, in most cases, reduced (i.e., deoxygenated) into other compounds.

1.5 The deoxygenation of biomass-derived products

Biomass derived synthons, which are further used as building blocks for the production of fuels and chemical commodities have seen exponential research growth over the past decade [55,56]. As observed in Figure 1-1, some studies suggest the production of a first set of synthons, such as glucose or oils, which can be obtained from biomass sources [3,57] and use the latter synthons to further undergo into chemical transformation to more complex molecules. A great example in terms of a well-known technology that represents the latter statement is the production of the first-generation biofuels. As explained in Section 1.3.1, biodiesel is produced through transesterification of triglycerides coming from vegetable oils, animal fats or waste cooking oil. The result is a mixture of esters with properties which are similar to a diesel fuel [58]. Bioethanol, on the other hand, is produced on large scale using sugarcane and starch grains, raising the problem of using food for fuel production [59]. Although blends of biodiesel and bioethanol with petroleum-derived fuel are used globally, both of them are not fully compatible with the petroleum infrastructure existing today, as the oxygen content present within these biofuels leads to poor storage stability, poor cold flow properties and reduced energy density [60,61]. Another example where upgrading to the bio-derived product is needed, specifically mentioned in Section 1.3.1, is the liquid product from biomass pyrolysis (i.e. bio-oil). The most important drawback of bio-oil to be accounted as an efficient petroleum substitute, is the highly oxygenated composition of the oil, which leads the latter to have undesirable and poor ignition properties, which makes the bio-oil unsuitable even for preliminary combustion applications, inside boilers or kilns [62,63]. Therefore, alternatives to completely remove the

oxygen from the produced biofuels or at least reduce their oxygen content is crucial if the aim is to incorporate such biofuels into the actual petroleum infrastructure while seeking to achieve the highest energy potential possible [64,65]. Through catalytic deoxygenation, the aforementioned goal could be attained. The latter reaction encapsulates three main chemical transformations, which are: 1) hydro-deoxygenation (HDO); 2) decarboxylation (the reaction of interest within this word); and 3) decarbonylation. All three are of use to reduce the oxygen content within a molecule. Depending on the conditions and the required properties of the final products, HDO, decarboxylation or decarbonylation can be used to improve the properties of oxygenated fuels to the point where they can be considered oxygen-free [60]. When the deoxygenation reactions are used with oils, typically the oxygen is eliminated from the carboxylic acid structures and leaves in the form of H_2O, CO_2 and CO. Temperature, type of catalyst, reaction atmosphere, reactant types and pressure, all play an important role in the total conversion of the fatty acids into petrol-like fuels [61]. HDO transforms fatty acids and oils into diesel-like fuels removing oxygen to form water and n-paraffins [66]. There are some large companies, such as Neste Oil and UOP-Eni (with the NExBTL and the Ecofining processes, respectively) that have implemented HDO into a large-scale scheme [67]. Despite the advantages of achieving a full conversion of the biomass raw materials to produce hydrocarbons compatible with the current fossil fuel infrastructure (*e.g.*, green diesel), hydrodeoxygenation operates at a range of temperature, typically between 325-360 °C and uses high pressure hydrogen (between 50 to 80 bar of pressure), making the process expensive to engineer and energy demanding. In addition, special care needs to be taken with the facilities where hydrogen is used, due to the explosive nature of the molecule [66-68]. Green diesel composition and properties are close to conventional diesel, and unlike biodiesel, it is a hydrocarbon mixture rather than an oxygenated compound with some desirable diesel properties [69]. A comparison between different diesel types is presented in Table 1-3.

Table 1-3 Properties comparative between diesel, biodiesel and green diesel. Adapted from Baldiraghi, *et al.,* [69].

As observed in Table 1-3, green diesel is almost identical to diesel fuel, with a high cetane number, low sulphur content and a good heating value among other desirable properties, making it adequate to use with conventional fuel infrastructure in engines and refineries, avoiding the need to adapt the existing technology to make it compatible with the fuel. Both, the biodiesel and the green diesel can be obtained using waste raw materials such as waste cooking oil, as the former and the latter are products of chemical reactions with carboxylic acids (e.g., fatty acids) through the transesterification reaction (biodiesel) and the hydrogenation reaction (green diesel) [4,68,70]. The other two deoxygenation reactions are decarbonylation and decarboxylation. Decarbonylation is a reaction in which oxygen is also eliminated from fatty acids and oils molecules. The carbonyl group present in carboxylic acids leaves in form of CO [71]. The decarboxylation of fatty acids and their esters is a well-studied process in which oxygen leaves in the form of CO_2. Although this process is less expensive than HDO, selectivity to certain products can be low and enlargement of the carbon chain length cannot be attained [25,67,68,72-74].

	Ultra-low sulphur diesel (ULSD)	**Biodiesel (FAME)**	**Green diesel**
Oxygen content (%)	0	11	0
Specific gravity	0.84	0.88	0.78
Sulfur content (ppm)	<10	<1	<1
Heating value (MJ kg^{-1})	43	38	44
Cloud point (˚C)	0	-5 to 15	-20 to 20
Distillation range (˚C)	200-360	340-370	200-320
Polyaromatics (wt%)	11	0	0
NOx emission (wt%)	Baseline	+10%	-10%
Cetane number	51	Between 50 and 65	Between 70 and 90
Stability	Baseline	Poor	Baseline

The two latter deoxygenation reactions are illustrated in Figure 1-2 [75].

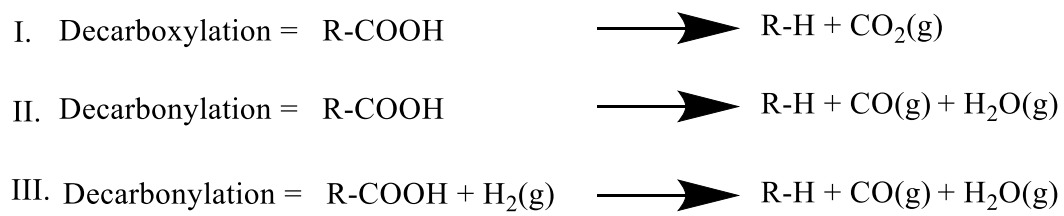

Figure 1-2. Production of linear hydrocarbons from fatty acids. Adapted from Murzin *et al.,* [75].

Romero *et al.,* [76] worked with deoxygenation reactions, specifically with the decarboxylation and decarbonylation of *Jatropha curcas* and waste cooking oil, using Mg-Al mixed oxides and calcium oxide as catalysts (without hydrogen involved in the reaction) to evaluate the grade of conversion of these compounds into diesel-like fuels. In their study, Romero *et al.,* used approximately 180 g of each oil with 3% wt. of catalyst in batch and semi-batch schemes at 400 °C for 6 hours, each reaction. The researchers concluded that batch experiments led to a higher yield of liquid products, over 80% of them. On the other hand, the semi-batch experiments gave less liquid yield and higher gas phase products. Liquid products were composed of high hydrocarbon composition, concluding that the oils could be potential raw material to produce diesel-like fuels. The results are presented in Figure 1-3.

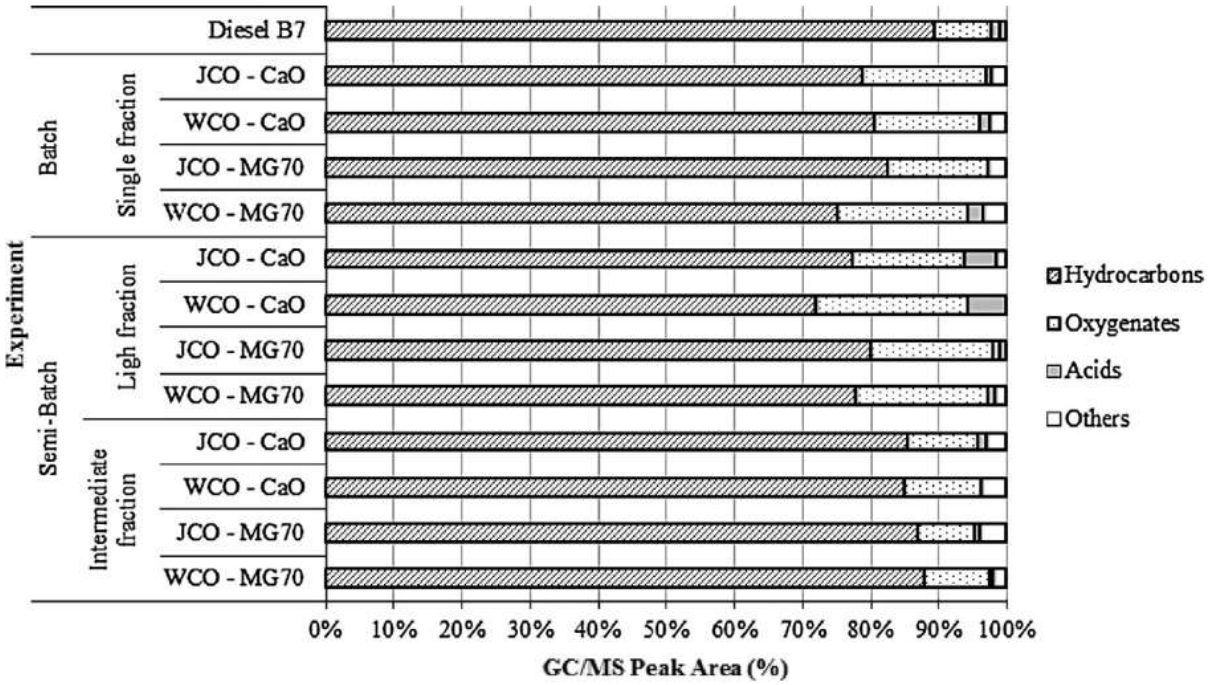

Figure 1-3. GC/MS analysis of the products obtained from the different deoxygenation reactions. JCO refers to *Jatropha curcas* and WCO refers to waste cooking oil. CaO (i.e., Calcium oxide) and MG70 (i.e., hydrotalcite) were used as catalyst. Taken with permission from Romero, *et al.,* [76].

In a different study, Fu *et al.,* [77] conducted hydrothermal decarboxylation reactions using palmitic and oleic acids with activated carbon as catalyst (no metals involved). Some of the catalyst samples were treated with either H_2 or N_2 to remove impurities that could be present over the surface of the activated carbon. The control experiment in which SiO_2 was used instead of the activated carbon showed no pentadecane formation after 3 hours at 370 °C. The subsequent results of the hydrothermal decarboxylation with the different carbon catalysts are shown in Table 1-4. All reactions were performed at 370 °C over 3 hours using different catalyst loadings (5 to 100 mg). Thus, the reactions were performed varying the temperature from 330, 350, 370 up to 385 °C over 3 hours and using a catalyst load of 15 mg.

Table 1-4. Conversion and selectivity of the decarboxylation reactions of palmitic and oleic acid, where AC-1N is the activated carbon pre-treated with nitrogen, AC-1H is the one pre-treated with hydrogen, AC-1 is activated carbon made via a phosphoric acid washing and AC-2 was made of peat and was activated using steam. Adapted from Fu, *et al.,* [77].

[a] 17-hour batch without catalyst

Catalyst	Reactant (acid)	Decarboxylation product	Conversion (%)	Molar yield (%)	Selectivity (%)
None[a]	Palmitic	pentadecane	-	0.7 ± 0.2	-
AC-1N	Palmitic	Pentadecane	20 ± 4	10 ± 2	52 ± 5
AC-1H	Palmitic	Pentadecane	21 ± 2	10 ± 2	48 ± 6
AC-1	Palmitic	Pentadecane	24 ± 3	9 ± 2	38 ± 6
AC-2	Palmitic	Pentadecane	33 ± 13	19 ± 6	58 ± 4
AC-1	Oleic	Heptadecane	80 ± 4	6 ± 1	7 ± 1

According to the results in Table 1-4, pretreatment did not play a significant role in the conversion and selectivity towards the desired product as the results were similar. However, the source of the activated carbon affected the activity of the catalyst as observed between AC-1 and AC-2. Fu *et al.,* concluded that neither hydrogen nor noble-metal catalysts are required and that the activated carbon can transform fatty acids (saturated and unsaturated ones) to petrol-like fuels. In addition, the lack of unsaturated compounds as products is a clear indicator that hydrogenation occurred during the decarboxylation reactions, with the hydrogen donors coming from either water or fatty acids molecules [77]. Also, by using activated carbon as catalysts, Hossain *et al.,* [78] examined the effects of the decarboxylation of oleic acid without using either hydrogen pressure or hydrogen-donor solvent. The reaction temperature was set to 400 °C using 5 g of catalyst, and H_2O to feed ratio of 4:1, with a stirring speed of 800 rpm and for a reaction time of 2 hours. The products from the experiment are presented in Table 1-5.

Table 1-5. Product distribution of the hydrothermal decarboxylation. Adapted from Hossain *et al.,* [78].

Compound	Selectivity (% composition)
Octane (C_8H_{18})	0

Nonane (C_9H_{20})	0
Decane ($C_{10}H_{22}$)	0
Undecane ($C_{11}H_{24}$)	0
Dodecane ($C_{12}H_{26}$)	2.2
Tridecane ($C_{13}H_{28}$)	5.1
Tetradecane ($C_{14}H_{38}$)	2.8
Pentadecane ($C_{15}H_{32}$)	4.4
Hexadecane ($C_{16}H_{34}$)	4.0
n-Heptadecane ($C_{17}H_{36}$)	81
Heptadecene ($C_{17}H_{34}$)	0.6
Octadecane ($C_{18}H_{38}$)	0
Nonadecane ($C_{19}H_{40}$)	0
Icosane ($C_{20}H_{42}$)	0
Oleic acid	0

The production of *n*-heptadecane in greater quantity than heptadecene indicates that hydrogen is generated *in situ* during the decarboxylation process as no source of hydrogen was added to the reactor. A possible explanation is that the CO produced by decarbonylation (which is occurring at the same moment during decarboxylation) reacts with water in the water-gas shift reaction to produce hydrogen. In addition, at elevated temperatures, oleic acid can undergo thermal cracking, which will generate hydrogen too [78]. The proposed reaction mechanism can be observed in Figure 1-4.

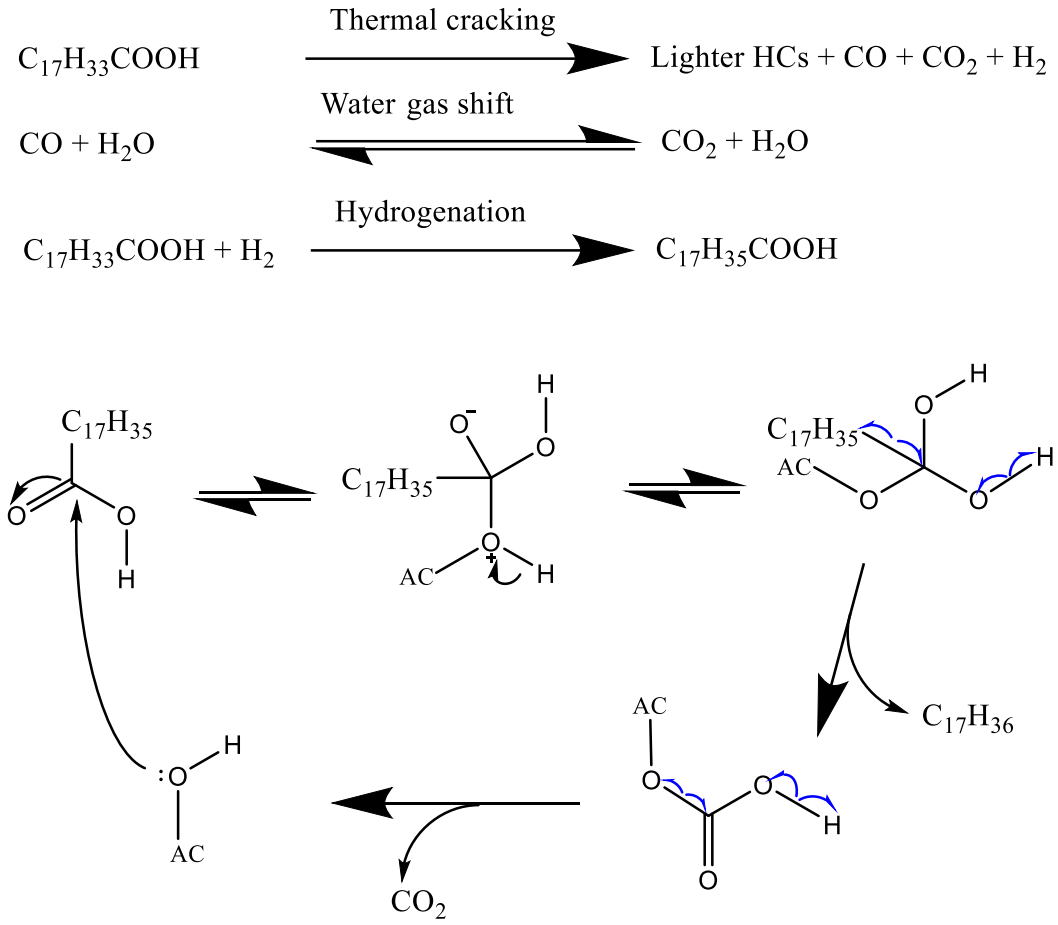

Figure 1-4. Hydrothermal decarboxylation mechanism, adapted from Hossain *et al.,*[78]

Zhang *et al.,* [79] worked with supported Cu-Ni bimetallic catalysts to carry out the decarboxylation of oleic acid. The authors used methanol as a hydrogen donor to examine the production of hydrogen *in situ* during the reaction and what effect the catalyst has in hydrogen generation. They used 50 mg of oleic acid with 15 mg of catalyst and an unspecified amount of water and methanol, with reaction temperature of 330 °C In addition, they concluded that for decarboxylation reactions using Cu-Ni catalysts, $CuNi_2Al$ favours the hydrogen generation *in situ* whereas a NiAl catalyst favours the decarboxylation of unsaturated fatty acids. Moreover, they also concluded that the presence of the Cu-Ni alloy inhibited the possibility of the carbon bonds to crack into forming smaller molecules,

favouring a higher selectivity towards heptadecane. Their results are presented in Figure 1-5 and Figure 1-6, respectively.

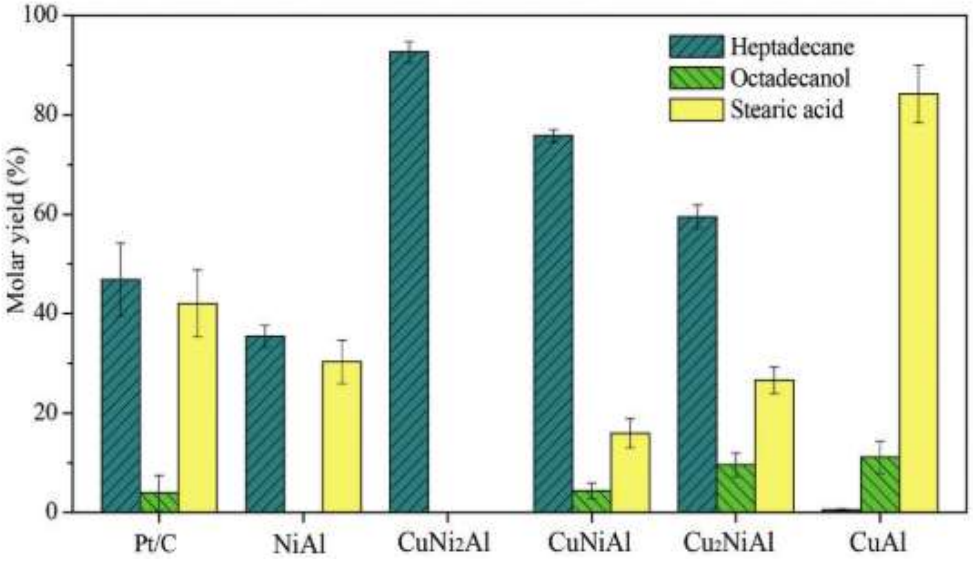

Figure 1-5. Yield in moles of the products from the decarboxylation reaction of oleic acid using different catalyst. Taken with permission from Zhang *et al.,* [79].

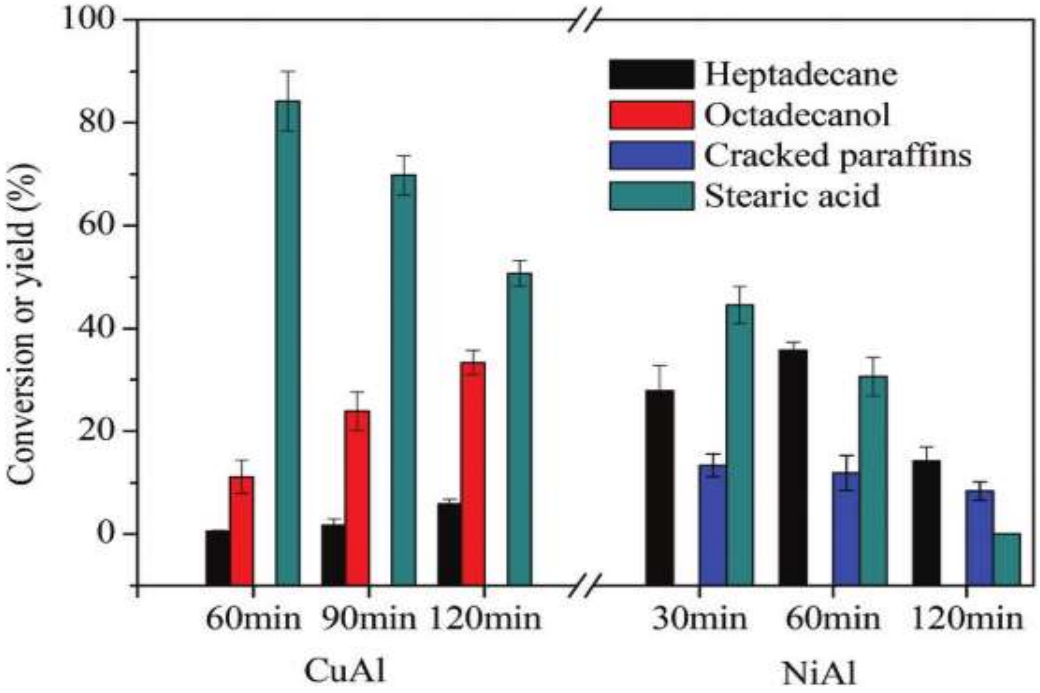

Figure 1-6. Yield of products over the CuAl and NiAl catalyst with the reaction times used. Taken with permission from Zhang *et al.,* [79].

Dominguez-Barroso *et al.,* [80] investigated the production of diesel oil-like fuels using sunflower oil as the raw material using subcritical water conditions and Pt-Ni/Al_2O_3 and Pd/C catalysts. The parameters were varying according to the experiment using a water to oil ratio of 1 or 2, a 0.5 to 1 % w/w of catalyst respect to the feed, a reaction time from 2 to 4 hours and using different temperatures from 200 to 300 °C. The pressure was generated by the reaction within the vessel reaching from 2 up to 10 MPa. Prior to the reaction, the catalysts were activated in a H_2 atmosphere at 700 °C for 2 hours. The main products obtained by Dominguez-Barroso were a mixture of hydrocarbon with diesel-like properties, in a wide range of yields (from 20% up to 45% yield).

From the paragraphs above, it can be seen that the deoxygenation of molecules with and without the presence of hydrogen through the use of a diverse set of different catalysts is achievable, to greater or lesser extents. However, most of the latter mentioned reactions where hydrocarbons were planned to be obtained from fatty acids, used catalysts with a wide variety of metals, which are mainly composed of acidic lewis sites, non exploring the use of solid base catalyst and the outcome of the deoxygenation reaction when basic lewis sites are involved. Some deoxygenation of molecules, specifically through decarboxylation also occurs through a specific mechanism named ketonic decarboxylation, in which it has been found that the basic lewis sites play an important role. The ketonic decarboxylation reaction will be further explored in detail as the latter mechanism is highly important to produce ketones, which as discussed in Section 1.2 and Section 1.3, can be considered a highly valuable biomass-derived synthon

1.5.1 Ketonic decarboxylation

Another deoxygenation pathway that has been extensively investigated is the ketonisation reaction (also known as ketonic decarboxylation) [81-83]. This reaction can be classified within the decarboxylation reactions mentioned in Section 1.5 and, as observed in Figure 1-1, a ketone, CO_2 and water are formed from the coupling of carboxylic acids (which could be referred to as primary bio-derived synthons, Shylesh *et al.,* [3]) and proceeds as follows:

$$R_1\,COOH + R_2COOH \rightarrow R_1COR_2 + CO_2 + H_2O \qquad 1.1$$

Thus, the carbon chain length of the compounds can be increased by removing carboxylic groups and generating a stable product with an increase in density, melting point, flash point, boiling point and viscosity for subsequent hydrogenation or aldol condensations to yield liquid alkanes [29,64,81,84,85], or used as ketones in their own right. Despite being studied through the years, there is no agreement within the field regarding a single mechanism by which the reaction proceeds. However, there are two different pathways that have been proposed for the ketonisation reaction; these are a surface-based process and a bulk reaction pathway [64,81]. The latter was derived according to the behaviour of acetic acid with metal oxides with different lattice energies, when trying to convert the acetic acid into acetone [86,87]. Oxides present high catalytic activity for the ketonisation reaction, which is mainly attributed to the crystal structure, bond strength between metal and oxygen of the catalyst and finally, the reaction is influenced by the presence of Lewis acid and base sites in the catalyst [87]. According to the literature, low lattice energy or strong basicity oxides lead to the formation of a bulk carboxylate that then undergoes decomposition into acetone, water and carbon dioxide, whereas high lattice energy oxides lead to a reaction on the catalyst surface [29,81,83,88].

1.5.1.1 Ketonisation through the surface carboxylate mechanism

According to Pham *et al.,* [81], high lattice energy oxides (e.g. TiO_2, CeO_2, ZrO_2 and MnO_2) drive the acetic acid molecules to react over the catalyst's surface to form acetone though the ketonic decarboxylation reaction. However, Pestman *et al.,* [89] reformulated the idea from results obtained from their experiments, stating that oxides with high metal-oxygen bond strength proceed *via* surface ketonisation, since no salt was observed to be formed when the strength of the bond of the oxides was high. According to Kumar *et al.,* [64], ketonic decarboxylation occurs through the surface of the catalyst used for the reaction, but following any of the three identified possible surface routes, which are based on either a ketene intermediate mechanism, a concerted mechanism or a β-ketoacid mechanism. Thus, several authors agreed with the importance of the α-hydrogen within the mechanism of the ketonisation reaction [81,82,89-92]. This hydrogen is the one bonded to the carbon in the α-position in the molecule. Pestman *et al.,* [89] demonstrated that as the amount of α-hydrogen decreased in the experiment (i.e., four different acids were used were the number of the α-hydrogens varied from 3 to 0), less ketone was formed. Pham *et al.,* [81] stated that

it is common to observe a strong relation between the number of α-hydrogens on the carboxylic acids and the reaction activity in all surface ketonisation studies. Corma *et al.* and Pulido *et al.,* [82,90] showed that a β-ketoacid mechanism involving α-hydrogens was kinetically favoured over other possible mechanisms. Pacchioni [91] highlighted the importance of the abstraction of the α-hydrogens, in concordance with other researchers, to form the correct intermediates for the ketonisation to occur. Finally, according to the work of Neunhoeffer and Paschke [92], a carboxylic acid without α-hydrogens does not undergo the ketonisation reaction.

The β-ketoacid mechanism

As mentioned before, according to Pham *et al.,* [81] the activity of the ketonisation reaction depends on the number of the α-hydrogens present in the molecule. Neunhoeffer and Paschke [92] proposed a mechanism taking into consideration the α-hydrogen effect. This can be observed in Figure 1-7.

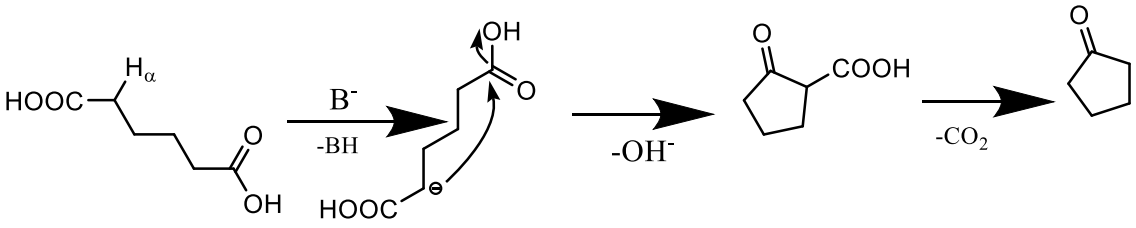

Figure 1-7. Mechanism in which the β-ketoacid is formed. The β refers to the position of the specific carbon, within the carbon chain-lengh, which is the second carbon to the right of the carbonyl group. Adapted from the proposed mechanism by Neunhoeffer and Paschke [92].

According to Figure 1-7, the reaction to transform adipic acid to cyclopentanone proceeds with the formation of a β-ketoacid intermediate. The catalyst basic surface abstracts an α-hydrogen to form a nucleophile that attacks a different carbonyl group to form a ketone. A β-keto acid intermediate is obtained through the coupling an enolate (or equivalent) and another carboxylate (or equivalent, such as an acylium ion), which can then undergo further decomposition to form a ketone and CO_2 following a concerted decarboxylation pathway. The β-keto acid mechanism has been studied by some authors and despite being widely supported, no β-keto acid has ever been detected in the reaction, perhaps due to its rapid

decomposition [81]. Looking further into the ketonic decarboxylation mechanism involving β-keto acid formation, Nagashima *et al.,* [93] conducted a cross-ketonisation reaction using propanoic acid and branched carboxylic acids over a CeO_2-based catalyst. The authors reached the conclusion that the less α-hydrogens involved in the reaction, the less the ketonisation proceeded. According to these authors, the route for the cross-ketonisation of the propanoic acid to happen was through the β-keto acid mechanism, as the carboxylates were formed at the surface for a subsequent α-hydrogen abstraction to produce a β-keto acid intermediate that underwent decarboxylation to form a ketone. In a different study, Pham *et al.,* [88] prepared and tested a $Ru/TiO_2/C$ (activated carbon) catalyst to study the ketonisation of acetic acid in the liquid phase, in which incorporating Ru helped to increase the activity of the catalyst by more than 50%. Their research is in concordance with other authors in pointing out the existence of α-hydrogens as a requirement for the ketonisation to proceed. Thus, the authors proposed an explanation for the ketonisation mechanism in which two carboxylates, one of them previously enolised, react to form a C-C bond for the subsequent formation of a β-keto acid intermediate that then undergoes decarboxylation to form the ketone. Moreover, Pulido *et al.,* [82] worked with different oxide catalysts in order to transform decanoic acid into 10-nonadecanone through ketonisation. Monocyclic zirconium oxide was chosen as the most appropriate catalyst leading to good conversion and selectivity towards the ketone. They concluded that the latter could not only be used with decanoic acid, but with other carboxylic acids with a wide range of molecular weights. To have a better understanding of the mechanism behind the ketonisation, these authors conducted a computational chemistry density functional theory (DFT) study of the decarboxylation of two molecules of acetic acid. The results showed that the β-keto acid mechanism is kinetically more favoured that the any other possible route. The mechanism proposed is shown in Figure 1-8.

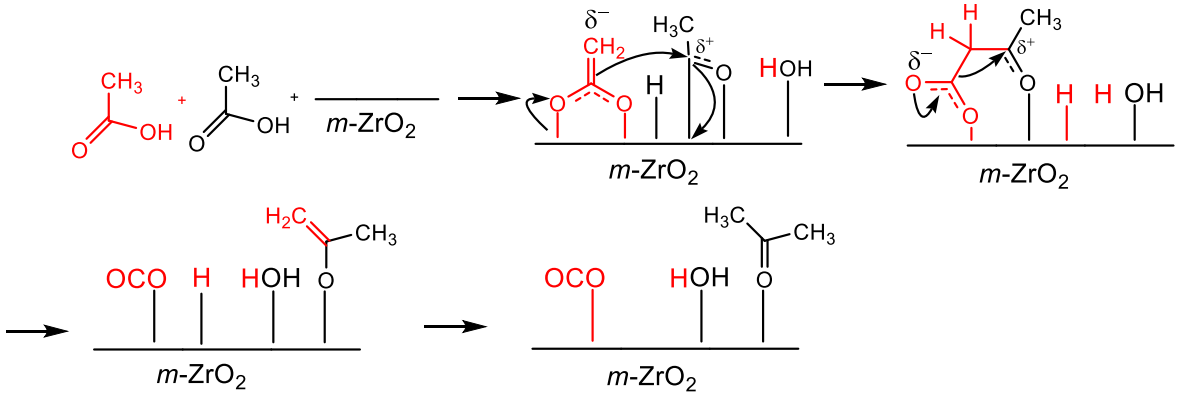

Figure 1-8. β-Keto acid mechanism for the conversion of acetic acid over monocyclic zirconium oxide. Adapted from Pulido *et al.* [82].

The concerted mechanism of ketonisation

This is another proposed pathway for the ketonic decarboxylation to occur, which mainly differs from the β-keto acid mechanism due to the fact that C-C bond formation as well as CO_2 formation occurs at the same step (i.e., in a concerted step) [64,82]. Figure 1-9 shows the concerted route for acetic acid over a zirconium oxide catalyst. Recent research has proven that this route is not as strongly favoured as the β-ketoacid one [82,90], however it works to explain the ketonisation reaction in molecules lacking α-hydrogens [82].

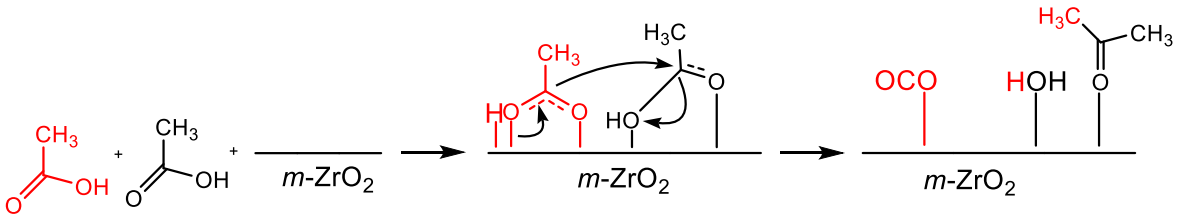

Figure 1-9. Mechanism for the concerted route of the ketonic decarboxylation. Adapted from Pulido *et al.,* [82].

1.5.1.2 The Effect of the different catalysts on ketonisation

According to the literature, the ketonisation reaction is likely occurs through a surface carboxylate mechanism, as seen in Section 1.5.1.1. For the latter to happen, it is imperative that a carboxylate species can be formed over the surface of, for instance, an oxide catalyst and that the oxide can favour adsorbate-adsorbate interactions though coordination at unsaturated cation sites that can lead to intermediates for further production of a ketone, as discussed by Pham *et al.,* [81]. The intermediates would likely be produced through the β-keto acid mechanism, also described in Section 1.5.1.1. The metal oxides are one type of catalyst that have shown high activity for the ketonisation reaction, in which acetic acid has been the most tested carboxylic acid. Possibly, the basicity of the sites, the strength of metal-oxygen bonds and the lattice energy are the main variables to take into account when considering ketonisation on metal oxide surfaces [64]. Some widely studied metal oxides include CeO_2, MnO_2, ZrO_2 and in less quantity MgO and TiO_2. Presented below, Table 1-6 is a condensed report of the information found in the literature regarding the catalysts used for the ketonisation reactions. A deeper review for each of the main catalysts for ketonisation mentioned in Table 1-6 is presented in the following sections.

Table 1-6. Condensed table with a wide variety of catalysts used in the literature to promote the ketonic decarboxylation reaction, with the optimal reaction temperature and the obtained conversion of the desired product.

Type of catalyst	**Desired reaction product**	**Conversion (%)**	**Reaction phase**	**Optimal performance temperature (°C)**	**Reference**
CeO_2	Acetone	97	Vapour	400	[76]
CeO_2-Mn_2O_3	3-Pentanone	73.9	Vapour	350	[93]
CeO_2	Acetone	51.3	Vapour	350	[87]
CeO_2/SiO_2 (Supported over silica)	Acetone	97.3	Vapour	450	[94]
CeO_2	Acetone	Traces	Liquid	150	[83]
CeO_2	10-Nonadecanone	95	Vapour	425	[82]
MgO	12-tricosanone	96.4	Vapour	400	[95]
MgO	Acetone	100	Vapour	300	[86]
Rutile TiO_2	C_2-C_4 Ketones	9-11	Vapour	530-560	[96]
Monoclinic ZrO_2	C_2-C_4 Ketones	9-11	Vapour	530-560	[96]
CeO_2-ZrO_2	5-Nonanone	93.2	Vapour	355	[97]
Monoclinic ZrO_2	10-Nonadecanone	100	Vapour	400	[82]
ZrO_2	5-nonanone (intermediate)	100	Vapour	400	[90]
ZrO_2	5-Nonanone	82	Vapour	355	[16]
TiO_2	5-Nonanone	80	Vapour	355	[16]

CeO_2 catalyst

Cerium oxide has several characteristics that make it a suitable oxide for ketonisation at high temperatures. These are its stability at elevated temperatures as well as its high lattice energy and its strong metal-oxygen bond strength [64]. Glinski *et al.,* [98] carried out experiments with twenty different oxide catalysts at a temperature range between 250 to 450 °C. Using 10% wt. of metal oxide supported on silica, they determined that at 400 °C the CeO_2, La_2O_3, CdO and the MnO_2 catalysts presented higher activity in comparison with the rest of catalysts for the ketonisation of acetic acid, with a quantitative conversion observed, with the CeO_2 and the MnO_2 being the most active ones. The results from the latter research are shown in Table 1-7.

Table 1-7. Yield of acetone at different temperatures using a 10 wt.% of metal oxides supported on silica catalysts. Adapted from Glinski *et al,* [98].

Active phase	**Yield of acetone (%)**						
	300 °C	**325 °C**	**350 °C**	**375 °C**	**400 °C**	**425 °C**	**450 °C**
Pure silica support	2	2	3	4	5	20	32
B_2O_3	2	2	2	2	3	6	7
MoO_3	2	2	1	4	5	5	5
WO_3	2	4	6	6	5	5	6
P_2O_5	1	1	6	10	12	9	5
V_2O_5	3	4	4	9	21	29	24
Bi_2O_3	10	6	5	11	18	28	44
NiO[b]	7	9	10	31	B	b	B
Al_2O_3	0	0	4	15	37	45	52
CuO[c]	5	5	6	29	39	43	50
ZnO	6	9	10	19	33	54	67
PbO	6	10	15	36	76	79	75
Cr_2O_3	1	8	52	48	39	46	54
Fe_2O_3	13	32	39	66	59	60	52
CoO	13	15	48	50	63	64	68
MgO	7	20	39	53	59	68	74
Nd_2O_3	3	3	6	22	61	70	-
La_2O_3	3	12	14	50	87	-	-
MnO_2	18	22	34	72	96	-	-
CdO	6	27	73	76	94	-	-
CeO_2	9	24	31	96	97	-	-

Table 1-7 includes MgO, a highly basic catalyst used in this work (see Chapter 3 and Chapter 4). Nevertheless, the ketone yield (i.e., acetone) produced in Glinski *et al.,* work when using MgO showed a relatively small yield percentage, which is contrary to the results obtained in this study at a temperature of 300 °C, which were superior (up to 80% yield of ketone) meaning other factors apart from temperature are involved in the ketone production through the ketonic decarboxylation reaction. In another study, Nagashima *et al.,* [93] used CeO_2-based composite oxides to perform the ketonisation of propanoic acid at 350 °C and with 10 mol% of a second metal added, achieving significant results when Mn was put together with the CeO_2. The resultant compound (CeO_2-Mn_2O_3) delivered the highest percentages of conversion and selectivity with 73.9% and 97.4%, respectively, among other metals used including Mg, Al, Cr, Fe, Co, Ni, Cu and Zr. The authors found out that not only the Mn, but also the Mg and Cu, showed higher conversion of the carboxylic acid when combined with CeO_2 in comparison with the CeO_2 without any metal added. Moreover, Yamada *et al.,* [87] showed that CeO_2, as well as other rare metal oxides such as La_2O_3, Pr_6O_{11} and Nd_2O_3, had high catalytic activity for the conversion of acetic acid to acetone at 350 °C. The conversion and selectivity values for CeO_2 were 51.3% and 99.9%, respectively. Working with bio-derived products, Deng *et al.,* [94] undertook research that was focused on upgrading bio-oil produced from fast pyrolysis using weak solid bases to reduce its high acidity and oxygen content and synthetize ketones that can further be converted to diesel-like fuel with aldol condensation and hydrotreatment. In their experiments, CeO_2 catalyst supported over silica (CeO_2/SiO_2) showed excellent performance as it was still converting 97.3% of acetic acid after a run of 96 hours at 450 °C.

Snell and Shanks [83] also worked with bio-oil and a ceria catalyst in order to understand how the reaction of acetic acid with this oxide catalyst proceeded at lower temperatures. They found out that the reaction occurred in toluene at 230 °C but when the temperature was decreased, almost all acetic acid remained unreacted. On the other hand, when the temperature rose to 300 °C, full conversion of the acid was obtained. In a different study, Pulido *et al.,* [82] showed full conversion of decanoic acid to 10-nonadecanone with CeO_2 at 425 °C reaching a selectivity of 95%. As ceria is a catalyst that has shown an excellent performance to favour surface ketonisation of acetic acid, different temperature ranges have been investigated to understand its behaviour. According to Pulido *et al.,* no metal carboxylates were formed when the temperatures were under 150 °C. Within the

temperature range, between 150 °C to 300 °C, the acetic acid form cerium acetates and at temperatures higher than 300 °C, the metal carboxylates decompose into acetone [64].

MgO catalyst

Corma *et al.,* [95] used a fixed-bed reactor at 400 °C to promote the formation of 12-tricosanone using dodecanoic acid as starting material. Corma *et al.,* however does not disclose the characteristic of the MgO used during the study. After several runs at different catalyst to feed ratios, high conversion of the dodecanoic acid up to 96.4% and high selectivities towards the desired ketone product (98%) were achieved. No mechanism was proposed in this study, however, they concluded that MgO could easily work as a reliable catalyst for the ketone production at high yields. Mekhemer *et al.,* [86] studied the formation of acetone using MgO as the catalyst for the ketonic decarboxylation, trying to bring insights regarding whether the reaction proceeds over the surface of the catalyst or through a possible bulk mechanism, as the one mentioned in Section 1.5.1.2., although the latter seemed to be unlikely as it is believed that high-lattice energy oxides will tend to avoid the formation of bulk carboxylate structures [89]. The authors carried out the reactions at 300 °C as they mentioned temperature above 400 °C could bring secondary reactions into play, such as cracking and pyrolysis, affecting the maximum yield of expected ketone product. *In situ* IR studies were performed during the reactions, in conjunction with the reaction products, leading Mekhemer *et al.,* [86] to conclude that despite the MgO being a high-lattice energy oxide, the magnesia powder did promote the formation of bulk carboxylates that were activated at around 225 °C to decompose into acetone, water and carbon dioxide followed by an activation of the adsorbed carboxylate species over the surface at around 300 °C. Acetone is further adsorbed and oxidised into acetate and carbonate species. The work performed by Mekhemer *et al.,* was important during the development of Chapter 3 and Chapter 4 in this work, as in Chapter 3 and Chapter 4, the formation of bulk carboxylate species (as Mekhemer *et al.,* suggested) was discarded through the analysis of the obtained FTIR peaks, which lead us to think rather than forming the bulk carboxylate species, the reaction proceeded merely through a surface reaction mechanism, as mentioned in Section 1.5.1.1.

ZrO_2 and TiO_2 catalysts

In work presented by Wang and Iglesia [96], a comparison between the aldol condensation reaction and ketonisation of carboxylic acids in the gaseous phase was studied, pointing out that ketonisation requires enolate-like species in the form of 1-hydroxy enolates for a subsequent reaction with another acid to occur, and further decompose *via* CO_2 and H_2O elimination. They considered the latter enolates as important intermediates species for the reaction over the catalysts TiO_2 (anatase and rutile) and ZrO_2 (monoclinic and tetragonal) at 230 – 260 °C with a selectivity of >95%. They also reported the behaviour of the carboxylates depending on which TiO_2 oxide they were using. Monodentate carboxylates can saturate acid-base pairs of the anatase form of TiO_2 while bidentate carboxylates will do the same over the rutile TiO_2 structure. According to their research, some side products were present at the end of the reaction. Acid anhydrides and α,β-unsaturated alkanones can be formed due to intermolecular dehydration of the reactants, or from a further aldol condensation of the alkanone products first formed, respectively. The work of Wang and Iglesia resulted interesting when performing the ketonic decarboxylation reactions in Chapter 3 and Chapter 4, as when analysed through FTIR, carboxylate species were observed to be adsorbed over the surface of the MgO, which lead us to think that the surface mechanism (see Section 1.5.1.1) could be happening promoted through the presence of the called enolate specie, further reacting with another adsorbed carboxylate specie over the surface of MgO.

Shutilov *et al.,* [97] also worked with ZrO_2 and CeO_2-ZrO_2 catalysts to convert pentanoic acid into its corresponding ketone (5-nonanone). In their study, Shutilov *et al.,* used different zirconium catalysts. ZrO_2 was made by calcination in air at 450 °C (Zr-450) and a different one following the same calcination route but with a subsequent calcination in H_2 at 355 °C (Zr-450-H). According to their results, at 355 °C, both zirconium oxide catalysts achieved a conversion of 85.5% and a selectivity of 78.4% for Zr-450 and 75.9% for Zr-450-H. However, maximum conversion under the same conditions was obtained by CeO_2-ZrO_2 catalyst, with values of conversion and selectivity of 93.2% and 78.7%, respectively. Pulido *et al.,* [82] tested the performance of alumina, silica, ceria, zirconia and mixed zirconium cerium oxides to decarboxylate decanoic acid into 10-nonadecanone at different temperatures and getting full conversion of the carboxylic acid at 400 °C with ZrO_2 and

$CeZrO_4$ with a selectivity in between 90 to 95%. As the m-ZrO_2 (monocyclic zirconium oxide) exhibited full conversion at 400 °C and a selectivity of 95% without showing significantly lower activity below that temperature when compared to the $CeZrO_4$ and CeO_2, they concluded that m-ZrO_2 is a suitable catalyst to perform ketonisation of carboxylic acids. Corma *et al.,* [90] conducted experiments using zirconium oxide as a metal oxide support catalyst for the ketonisation of decanoic acid and valeric acid (i.e., pentanoic acid, a carboxylic acid with the formula $C_5H_{10}O_2$), separately, at 400 °C. In the case of the decanoic acid, using 2.5 g of the catalyst for the reaction favoured full conversion of the latter acid and a selectivity superior to 95% without changes for 24 hours. Even though they processed 100 g of substrate per gram of catalyst, the results did not change. On the other hand, 1 g of catalyst was used for the reaction of the valeric acid, a substrate that was chosen for being a biomass-derived compound. The conversion reached 85% and dropped to 70% when more than 90 g of valeric acid was used per gram of catalyst. To reactivate (after four catalytic cycles), the catalyst was calcined at 500 °C for two hours with an air flow of 50 mL/minute. The authors concluded that ZrO_2 is a suitable catalyst to perform ketonisation reactions. Wu *et al.,* [84] investigated the ketonisation of acetic acid over ZrO_2 in an aqueous-phase at 340 °C for 12 hours. However, they included different amounts of carbon within the catalyst to study their behaviour and how ketonisation was affected by its use. Their results are summarised in Table 1-8, where ZrO_2-HT600C, ZrO_2-HY600C, ZrO_2-UiO600C and ZrO_2-CA600C are the catalyst made by hydrothermal precipitation, hydrolysis of organic zirconium, carbonization of Zr-based MOF materials and the Sol-Gel with citric acid methods, respectively. Only ZrO_2-UiO600C and ZrO_2-CA600C were carbonized during their preparation method and further characterization showed poorly crystallized t-ZrO_2 existence for them.

Table 1-8. Ketonisation of acetic acid in aqueous phase with zirconia catalysts with different amounts of carbon within them. Adapted from Wu *et al.,* [84].

Catalysts	Acid conversion (%)	Production (mmol/gcat)	Production (mmol/gZrO2)
ZrO_2-HT600C	13.27	13.32	13.54
ZrO_2-HY600C	18.24	14.99	15.51
ZrO_2-UiO600C	25.30	23.72	34.13
ZrO_2-CA600C	38.56	38.09	62.09

As observed in Table 1-8, ZrO_2-UiO600C and ZrO_2-CA600C presented higher conversion, acetone yield and also possessed higher carbon content than the other two. They concluded that the presence of carbon helped poorly crystallised t-ZrO_2 enhancing its surface properties, leading to the results presented before. Tosoni and Pacchioni [99] worked with a zirconium catalyst in its tetragonal phase (t-ZrO_2) trying to find a reaction route for the ketonisation of acetic acid. They highlighted that the reactivity of the catalyst was determined by Lewis basicity of the surface cations, their under-coordination and the presence of reduced centers, and that the catalyst possess excellent thermal and mechanical properties. They conducted a DFT study, concluding that a hydrogen pre-treatment that can result in surface reduction to help to stabilise key intermediates and make the reaction proceed more readily was beneficial. According to Pham *et al.,* [88] who worked with two different catalysts for the ketonisation of acetic acid in the liquid phase, TiO_2/C and Ru/TiO_2/C, in which C is activated carbon, it was expected that activation could enhance the dispersion of TiO_2. The reaction parameters were 180 °C, lower in comparison with most studies as they usually work with higher temperatures (<300 °C), and a varying pressure of 400-800 psi. The authors concluded that pre-reduction of the catalyst is an important step to improve ketonisation activity no matter whether the reaction is in the gas phase or liquid phases, as the conversion with non-reduced catalyst was compared with the pre-reduced one and the latter showed a better conversion percentage (10%, in comparison with 1.5% exhibited by the non-reduced catalyst). The Ru/TiO_2/C catalyst obtained a conversion of 54.2%, which was higher than the 15.9% obtained by the TiO_2/C catalyst, showing that the addition of Ru enhanced the activity of the catalyst, making it suitable for a ketonisation reaction in the liquid phase at low temperatures. Simakova and Murzin [16] tested Al_2O_3, TiO_2, ZrO_2 and CeO_2 at 355 °C in a ketonisation reaction to couple carboxylic acids. Among the tested catalyst, ZrO_2 and TiO_2 showed the highest conversion (82 and 80 %, respectively). Thus, binary systems were tested in order to discover a catalyst showing a better activity

than the single ones. When adding ceria in a 10% to the zirconia-based catalyst, the conversion raised up to 92 – 93%, however, the selectivity was not affected by the amount of ceria in the system.

Zeolites as heterogeneous catalysts to promote ketonic decarboxylation

Ketones from acetic acid have been reported since 1980 over acidic zeolites, however, the mechanism details, the role of the water and the condition for high selectivity remains uncertain. When performing the ketonisation over a zeolite catalyst, reactions like aldol condensation or aromatisation may appear, leading to difficulties to track the mechanism. In addition, the catalyst can be deactivated by secondary reaction of products, such as acetone, when working with acetic acid [100]. Stefanidis *et al.,* [101] highlighted that the use of acid zeolitic catalysts with strong BrØnsted sites leads to the formation of CO, H2O and aromatic compounds with a low concentration of oxygen. The findings in the work of Stefanidis *et al.,* seems to agree with has been discussed throught the use of oxides to promote ketonic decarboxylation, which is that the presence of basic sites (e.g., BrØnsted basic sites and Lewis basic sites) favour the possible abstraction of a α-hydrogen which leads to the formation of an enolate species which further reacts with the other carboxylate species adsorbed over the surface of the basic catalyst, as pointed out in Section 1.5.1 and Section 1.5.1.1.

Other catalysts and the reaction atmosphere effect on the ketonic decarboxylation reaction

Finally, some recent studies have demonstrated the efficiency of layered-double hydroxide (LDH) materials to act as catalysts to promote ketonic decarboxylation, mostly due to their basic properties [102]. Layered-double hydroxides are a hydrotalcite-like materials with several applications, of which one is serving as heterogeneous catalysts. An hydrotalcite is part of a class of clays called anionic clays with brucite-like layers (i.e., Mg(OH)2) containing interchangeable anions in the interlayer [103]. The structure of these types of materials (LDHs) consist of octahedrally coordinated layers of M^{2+} and M^{3+} cations with hydroxides, with anions in the interlayer balancing the positive charge [104]. In this thesis, apart from studying the effects of a low-cost catalyst as MgO, LDHs were also synthesised using different methodologies and raw materials, such as waste materials, therefore, before going into more detail of LDHs, the preparation of the catalysts using waste raw materials, appealing to green chemistry principles and the circular economy framework (Section 1.2), gains importance on being addressed.

1.6 Catalyst development from waste raw materials, improving process sustainability

The production and use of heterogeneous catalysts are highly important areas for the chemical industry. Heterogeneous catalysts have been used over the past decades as an alternative to catalyse reactions while avoiding some of the inconveniences from using conventional homogeneous catalysts for chemical reactions, such as corrosion of the machinery, difficulties to recycle the resultant streams, catalyst separation, amongst others. [105,106]. Therefore, a heterogeneous catalyst can be described as a solid material which promotes the conversion of reactants into products while regenerating during the process and that can be easily separated from gas or liquid mixtures [107]. Moreover, the production of such heterogeneous catalysts from waste sources has increased in the last decade [108-110]. The latter sentence is relevant to this work, as in Chapter 5, Chapter 6 and Chapter 7, waste materials (i.e., the mining waste ochre and the phosphorous waste from watertreatment plants, struvite) were used to produce a catalytic material, therefore, the review of what has been done with waste and potential catalytic applications of the latter waste is important for this thesis. A well cited work proved the efficiency of using eggshells as a basic heterogeneous catalyst to promote the transesterification reaction to produce

biodiesel more than a decade ago [108]. In a similar manner, Maneerung *et al.,* [111] calcined chicken manure at 850 °C to obtain a highly active and low-cost CaO catalyst, which was subsequently used to produce biodiesel through transesterification of waste cooking oil. In another interesting work, also focused on biodiesel production with high yields, Mohamed *et al.,* applied a fast pyrolysis process to produce a highly stable sulphonated catalyst using rice straw (i.e., lignocellulosic biomass, that is plant dry matter) as the raw material [109]. Castro-León *et al.,*[112] explored the production of catalysts derived from waste sludge (such as the mining waste used during the development of Chapter 5 to Chapter 7) obtained from the mining and petroleum industries. Such catalysts proved to be efficient enough when compared against commercial catalysts for CO chemisorption and cracking of crude oil. Zhan *et al.,*[113] used the Bayan Obo tailings in China (the largest deposit of rare earth elements on earth) for catalytic purposes. With the presence of elements such as Fe, Ce, Ti, F, Si and O, the catalyst produced through calcination of the tailings proved to be efficient for the catalytic combustion of low-concentration methane. In a recent effort from the Greenwell group, the mining waste material Ochre (FeO(OH)) from Saltburn, England, was used to synthesise a layered-double hydroxide (LDH) which was employed as a basic heterogeneous catalyst for the production of a ketone (12-tricosanone) from dodecanoic acid through the ketonic decarboxylation reaction[114].

1.7 The abundant and non-toxic magnesium oxide (MgO) as a catalytic alternative for sustainable processes

MgO, periclase, can be found naturally in other minerals such as magnesite (i.e., magnesium carbonate) and dolomite, which is a mixture of calcium and magnesium carbonate. Through the mining of magnesium carbonate and subsequent thermal decomposition, MgO can obtained [101,115]. MgO has been widely studied in the literature because it is an oxide that exist in abundance in nature, also considered to be non-toxic (i.e., not harmful when manipulated) [101,116,117]. Due to these characteristics of MgO, the use of MgO in the literature covers a vast range of applications related to sustainability, such as being used as an adsorbent, as an insulator, as a heterogeneous catalyst, as a photocatalyst, among others [116,118]. The intrinsic characteristic of the MgO as a catalyst include a highly basic nature, having various Mg^{2+} and O^{2-} coordinated sites on the surface and a ionic high lattice bulk structure [86,119]. As already described in Section 1.5.1.2, MgO has been explored

as a catalyst to promote the ketonic decarboxylation reaction of carboxylic acids, however, as a heterogeneous catalyst, MgO has been widely used with different sustainability applications. Demirbas [120] used MgO as a catalyst for the production of biodiesel through the transesterification of vegetable oils such as rapeseed, soybean and sunflower oil, with methanol at supercritical conditions. Varying the catalyst loads from 1% wt. to 5% wt. while increasing the temperature (from 250 °C to 400 °C) of the reaction favoured the production of the derived methyl esters [120]. Hae Won *et al.,* [121] used MgO in conjunction with supports such as carbon, Al_2O_3 and ZrO_2 to examinate the effect of the latter MgO in suppressing the production of coke that would inhibit the catalyst activity towards transforming lignin biomass into pyrolysis derived oil (i.e., bio-oil). The MgO supported over carbon proved to be efficient in producing a high yield of aromatic hydrocarbons when lignin was put to react in pyrolytic conditions. In an interesting study, Zheng et al., [122] produced highly photocatalytic MgO particles with a flower-like morphology. The MgO samples were obtained after calcination of the reaction product of precipitating Mg^{2+} and CO_3^{2-} at a temperature of 70 ˚C. The product which size was in the microns, proved to be efficient to degrade organic dyes under, such as Congo red, thymol blue, bromothymol blue and a mix of all the latter dyes plus the presence of methylene blue. All the latter dyes were degraded at UV light irradiation and using 10 mg of the catalyst per 100 mg/L of dye solution. Moreover, for the same conditions, the MgO particles also degraded more than other photocatalyst such as ZnO and Degussa P25 TiO2.

1.8 The Layered-double hydroxides (LDH) materials

The layered-double hydroxides (LDHs) are a family of synthetic and naturally occuring layered minerals, often referred to as hydrotalcite-like materials, after the most commonly encountered natural mineral form. The most widely used forms have the chemical formula $[M^{2+}_{1-x}M^{3+}_{x}OH_2]^{x+}[A^{n-}]_{x/n}\,y.H_2O$, where M^{2+} and M^{3+} represent a divalent and trivalent cation respectively, with A representing the anion which will lay in the interlayer [123,124]. These materials are made of layers consisting of positively charged metal hydroxides, which has the charge balanced with the anions that exist in the interlayer region [102]. LDHs have attracted a lot of research attention due to their versatility as a material when it comes to the synthesis (relatively easy synthesis protocols), recyclability and tuneability in terms of cations on the layer and anions in the interlayer [125]. It is the tuneability factor of the LDHs

that make their applications span a vast range. They can be found in the literature being used for different applications, not necessarily related one another, however the catalytic uses of LDH have been increasing over the years. In a comprehensive review, Xu and Wei [126] explored the uses of the LDHs as solid-base catalysts. Xu and Wei mention that LDH can be "activated" by firstly calcining the sample and subsequently hydrating the latter calcined LDH, which causes the material to regenerate, through the so-called "memory effect", which according to Xu and Wei, the re-hydrated LDH will perform better than the original LDH material. Such LDHs, as mentioned before, can be used for base-catalysed reactions such as aldol condensations, Claisen-Schmidt condensation, among others, which are important chemical reactions to produce value-added chemical commodities. For instance, Bing *et al.,* [127] prepared Ca-Al LDHs which were re-hydrated after the calcination and used the later re-hydrated LDH to promote the aldol condensation of isobutyraldehide with formaldehyde to produce hydroxypivaldehyde with a yield of ~ 65%. Feng *et al.*, [128] summarised the potential uses of LDHs as supports for catalytic applications, such as the catalytic oxidation and hydrogenation reactions, more in concrete the partial hydrogenation of acetylene, methanation, selective oxidation of biomass, among others that are representative reactions in different chemistry fields, such as the petrochemical and fine chemical industries but also related to the new sustainability and green energy fields. In terms of the partial hydrogenation of acetylene and methanation, one of the main conclusions is that the capabilities of the LDH to introduce active cations onto the interlayers, which then after calcination and reduction should improve the catalytic properties of the material. Due to the basic properties of the LDH and the basic sites act in conjunction with the metallic sites, potentially selective oxidation reactions of biomass occur towards the production of added-value bio-derived products. Focusing into the use of LDH in the sustainability area, Gupta *et al.,* [129] used an LDH-supported gold nanoparticle catalyst to promote the production of 2,5-furandicarboxylic acid (i.e., FDCA) up to a yield of ~99%, from the reaction of the latter catalyst with 5-hydroxymethylfurfural, which is considered to be among the 12 most important bio-derived products. The catalyst had a reusability of up to three times without significatively losing the activity [129]. Smith *et al.* [102], used LDH compounds as heterogeneous basic catalyst to promote the ketonic decarboxylation reactions of carboxylic acids at high temperature. Smith *et al.,* obtained a conversion of stearic acid into the corresponding symmetric ketone (i.e., stearone) towards the use of Mg-Al LDHs of different R-values (i.e, $[Mg^{2+}]/[M^{3+}]$) ranging the latter R-values

from 1 to 6 and obtaining ketones yields up to 90% at reaction temperatures of 250 ˚C. To aid to visualise what an LDH is, Figure 1-10 is a schematic representation of the LDH structure.

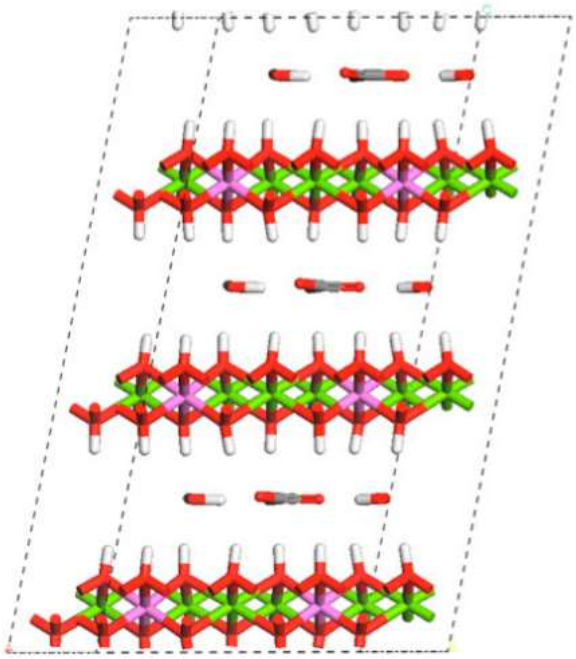

Figure 1-10. Schematic structure of the LDH material. The interlayer anion as well as the layers are represented. Taken with permission from Smith *et al.,* [102].

As observed in Figure 1-10, the LDH are composed of brucite-like layers (i.e., $Mg(OH)_2$). In the brucite, the Mg^{2+} is 6-fold coordinated to OH^- (i.e., octahedral coordination) where the Mg^{2+} shares edges which subsequently forms infinite sheets that exists being stacked on the top of one another [103]. In the LDH layers, similar to the brucite, some of the M^{2+} (i.e., divalent cations, which are 6-fold coordinated to OH^-) are replaced by M^{3+} (i.e., trivalent cations) which results in positively charged layers that are balance by the presence of an anion in the interlayer (the interlayer also contains water) [103,130]. Due to the latter characteristics of the LDHs and as a summary of the advantages that the latter LDHs represent for the area of heterogeneous catalysis, LDHs have high cation tuneability in the layers and the anion present in the interlayer is highly exchangeable. Moreover, LDHs also can be calcined to form mixed metal oxides which make them suitable to immobilise active catalytic species on the surface. Finally the basicity of the LDHs can also be tuned [128].

1.8.1 Layered-double hydroxide synthesis through co-precipitation

The synthesis of LDH materials can be performed following different approaches. According to Smith *et al.,* [102] the most used synthesis approach is the co-precipitation method, as the latter would lead to the formation of a crystalline material with a high surface area, due to the low supersaturation conditions. On a typical co-precipitation procedure, a solution of a desired M^{2+}/M^{3+} ratio to form the LDH would be precipitated into a solution containing an excess of the anion (supersaturation conditions) that will reside in the interlayer. The pH of the solution during the whole co-precipitation procedure is an important parameter to consider, as varying or keeping the latter constant, would highly influence the characteristics of the obtained product [102,124]. According to Crepaldi *et al.*, [124] and He *et al.,* [123] keeping the pH constant during the co-precipitation synthesis of the LDH materials lead to a highly crystalline and phase pure material when compared to the ones obtained through a synthesis where pH was varied. The pH is usually controlled by adding a highly basic solution into the reaction such as NaOH or KOH. The conditions of constant pH favour the precipitation of the divalent and trivalent cations into an LDH material under low super-saturation conditions. When the pH of the solution is constantly varied throughout the whole LDH preparation, it is said the reaction was carried under high super-saturation conditions. Contrary to the low super-saturation conditions in which higher crystallinity is obtained, when working under high super-saturation conditions, rapid nucleation is favoured over crystal growth, which then results in more crystals but with a less crystalline condition [123]. He *et al.,* [123] mention that, in order to precipitate the cations to form the brucite-like layers, it is necessary to carry out the reaction in high super-saturation conditions, obtained by having control over the pH of the solution, tuning the pH to a higher number than the one expected for the most soluble hydroxide to precipitate. The pH values of some common hydroxides formed with divalent or trivalent cations are presented in Table 1-9.

Table 1-9. The pH at which hydroxides made of trivalent and divalent cations would precipitate. Adapted from He *et al,* [123].

Cation	pH at 10^{-2} M	pH at 10^{-4} M	pH at which hydroxide re-dissolves
Al^{3+}	3.9	8.0	9.0 – 12.0
Cr^{3+}	5.0	9.5	12.5
Cu^{2+}	5.0	6.5	
Zn^{2+}	6.5	8.0	14
Ni^{2+}	7.0	8.5	
Fe^{2+}	7.5	9.0	
Co^{2+}	7.5	9.0	
Mn^{2+}	8.5	10.0	

As observed in Table 1-9, the pH conditions over 7, and *circa* 10 ~ 11 favour the precipitation of divalent and trivalent cations, as hydroxide species, such as the ones used in this study (Fe^{3+} and Mg^{2+}), during the development of Chapter 5, Chapter 6 and Chapter 7. Once the co-precipitation product is formed, an ageing of the resulting mixture at room temperature or higher is required for the product to crystallise even further [104,123]. Finally, the mixture should be passed through a filter and washing to remove any presence of impurity. The steps of the co-precipitation method found in the literature seem to be considered advantageous in terms of synthetic procedures when compared to others such as sol-gel or hydrothermal, as most of the literature agrees the methodology is easy to follow and reliable [102,123,124], however, it is far from being the right approach as a scaled-up process for the production of LDH materials. The latter statement arises from the fact that some of the major drawbacks from the latter lies mostly in the excess of the anion solution needed to be incorporated in the interlayer to avoid competing carbonate, the necessity for inert atmosphere to prevent carbonate inclusion as well as the highly basic supernatants generated when the product is washed [123,124].

1.8.2 Other methodologies to synthesize LDH materials

The co-hydration is another LDH synthesis procedure which overcomes the disadvantages of the co-precipitation methodology. The co-hydration synthesis (i.e., the mixing of oxides with water) of LDHs has been explored by Greenwell *et al.,* [131]. Rather than using inorganic interlayer anions, in this study organic anions were used in the interlayer. The co-hydration synthesis could be considered cleaner and more sustainable than the co-precipitation method, since the oxides containing the M^{2+} and the M^{3+} cations are mixed with water (at a slurry of 1% wt. with respect the amount of metal oxides) and the organic acids (e.g., malonic acid, succinic acid, glutaric acid and adipic acid) are incorporated later at a slight molar excess with respect of the M^{3+} cation. In their study, Greenwell *et al.,* obtained a phase pure organo-LDH after the stirring, filtering, and drying of the resulting reaction product. Following the methodology of Greenwell *et al.,* [131], Smith *et al.,* [102] prepared Mg-Al LDH materials through the co-hydration approach and tested them as effective catalysts to promote the ketonic decarboxylation of stearic acid. When compared against Mg-Al LDH prepared through co-precipitation, the difference in reactivity of both, co-hydrated and co-precipitated LDHs, was not big enough to establish that one route could lead to the formation of a material with better reactivity to act as a heterogenous catalyst. In a slightly different approach but following the same principles, Madej and Tyrala [132] used a co-hydration approach with nano particles of MgO and Al_2O_3. Both samples mixed with water at a weight ratio of dry mix to water of 3 to 1 which produced Mg-Al CO_3 LDHs. The crystallinity and phase purity of each sample varied with the time left for them to age at 50 °C and humidity conditions of 95%, resulting in the sample left for 49 days as the one with best crystallinity and phase purity.

LDH can also be prepared through ion exchange methodologies. According to He *et al.,* [123], when the layer cations or the interlayer anions are unstable under basic conditions or the co-precipitation of the solutions is not viable, ion-exchange offers an alternative synthesis process. For the ion-exchange to be suitable, the affinity of the incoming anion, the exchange medium, the pH value and the chemical composition of the layers needs to be considered. For instance, Bish *et al.,* [133] deintercalated carbonate anion from the interlayer and intercalated chloride anion when takovite (i.e. nickel hydroaluminate) was treated with HCl, with the samples left to age over one month period at 200 °C. In a recent

study, Bhojaraj *et al.,* [134] through butanol mediation at 120 °C, accomplished the removal of carbonate anions from Mg-Al and Ni-Al LDHs to successfully incorporate monovalent anions such as bromide, iodide, nitrate and chloride. Moreover, Bhojaraj *et al.,* also mentioned that the monovalent anions could also be incorporated into the interlayer through mechanochemical conditions (solid-solid reactions with no presence of solvent under standard conditions), that although more environmentally friendly, has the drawback of making the LDH material lose the morphology. Mechanochemical anion exchange was also explored by Intasa-ard *et al.,* [135] with a vast list of formed M^{2+} (i.e. magnesium, copper and calcium) and M^{3+}(i.e. aluminium, iron and tin) LDHs. Most of the materials produced were made with no solvent and with or without mechanical actions such as grinding, milling or stirring involved. Nevertheless, according to Intasa-ard *et al.,* the process is limited as there was no control over the morphology and particle size of the formed material. However, the solvent-free synthesis environment, as well as the selective intercalation of anions, make the process efficient and feasible. Hydrothermal synthesis of LDHs has also been explored in the literature. According to He *et al.,* [123], there are organic species which will not be intercalated into the interlayer by co-precipitation or anion exchange, due to a lack of affinity of such species with LDHs. Hydrothermal synthesis seems to be an alternative solution to the latter, as insoluble hydroxides could be used to provide the cations to form the LDH, with no other anion competing against the organic molecules to go into the interlayer of the material[123]. Greenwell *et al.,* [136] prepared ordered-organo-layered double hydroxides of Mg-Al terephthalate with a Mg to Al ratios of 2, 3, 4 and 5. The intercalation of the terephthalate anion into the interlayer obtained by Greenwell *et al.,* was in a range of 76 to 80% with a highly ordered arrangement.

Xu *et al.,* [137] formed a Mg-Al LDH using a hydrothermal process. The pH seemed to affect the formation of the material, as working at pH 7 reduced the presence of hydroxide impurities such as $Mg(OH)_2$ when compared to the formed material at more alkaline pHs, which agrees with Greenwell *et al.,* [136]. Finally, another interesting LDH synthesis is the so-called "rehydration through memory effect". The latter is a procedure in which after controlled thermal decomposition (calcination) of the LDH, they can be rehydrated in aqueous solutions to incorporate anions into the interlayer, which are dissolved in solution. During the calcination process the LDH loses the interlayer and adsorbed water, as well as the anion in the interlayer and will also dehydroxylate, forming mixed metal oxides

[102,123,138]. However, once rehydrated, the anion incorporated does not need to be the one that the LDH was originally made from, which gives the material greater versatility to produce different inorganic and organic anion variations of LDHs [123]. Invoking the latter, the LDH memory effect has been extensively studied due to the applicability of such synthesis in adsorption studies. Santos *et al.,* [139] prepared Zn-Al CO_3 LDHs through the co-precipitation method at room temperature. The materials were used to remove the pollutant Acid Blue 113 (AB) dye through adsorption mechanism. The adsorption capabilities of the Zn-Al CO_3 LDHs were compared against adsorption capabilities of the resulting mixed metal oxides from calcining the former at 450 °C. Through the removal of the AB dye, reconstruction of the lamellar LDH structure was obtained, incorporating the dye into the new formed LDH material rather than the carbonate anion, which was the initial interlayer anion when the Zn-Al CO_3 LDHs were first synthesized through co-precipitation. Moreover, and according to Santos *et al.,* the resulting synergy between the intercalation of dye into the interlayer of the LDHs and the removal capacity of the mixed metal oxides outperformed the adsorption capacities of the Zn-Al CO_3 LDHs by up to six times. Appealing to the same principle, Teixeira *et al.,* [140] prepared photoluminescent LDHs (Zn-Al-Eu NO_3) which were subsequently calcined at two different temperatures (350 °C and 600 °C). Apparently, according to the Teixeria *et al.,* study, a better memory effect was found to occur in the samples calcined at lower temperature, with rehydration happening faster, incorporating 1,3,5-benzenetricarboxilate (BTC) into the interlayer. The lower calcination temperature better effect on the reformation of LDH seems to be in agreement with the literature[123,139], as when higher calcination temperatures are reached, more stable spinel, which then have a negative effect on the rehydration of the LDHs. Although in this study, LDH were prepared from using the co-precipitation method (Section 1.8.1), it is important to understand the drawbacks of such methodology, in producing highly basic supernatants which cannot be disposed without further chemical treatment to make them pH neutral.

1.8.3 Synthesis of LDH from waste materials

Appealing to the circular economy framework (Section 1.2), production of LDHs using waste materials as the cation donors has also been explored. In a recent study, performed by Kwok *et al.,* [141] an LDH using struvite (i.e. a magnesium orthophosphate mineral) which is encountered in water treatment plants as a precipitate due to the insolubility of the latter in water. The struvite chemical formula is $MgNH_4PO_4(6H_2O)$. Kwok *et al.,* used the magnesium and phosphate content in the struvite to produce Mg-Al CO_3 – PO_4 LDH through a *in situ* solid-solid growth method. In a recent study, Ping *et al.,* [142] managed to extract MgO from waste serpentine tailings in China, which is believed to have over a thousand millions tonnes of waste of the latter serpentine tailings. The serpentine is a layered crystal structure, and the main composition of the latter serpentine is ~38% of MgO and 40% of SiO_2. The extracted MgO was used to produce a partially waste-derived Mg-Al LDH through a co-precipitation approach. The latter Mg-Al LDH was used as an adsorbent of Pb and P, with an efficiency of 99% and 85%, respectively. The work of Ping *et al.,* is similar to the work performed during the development of Chapter 5 to Chapter 7 as the LDH obtained by Ping *et al.,* was also prepared using mining waste, such as the ochre waste used in this work. Moreover and working with red mud (i.e., mining waste mostly composed of goethite and hematite, also similar to the ochre waste used in this work), Li *et al.,* [143] used a mechanochemical approach that took advantage of the high amount of iron oxides-hydroxides presents in the latter red muds to prepare a Fe_2O_3/Zn-Al LDH. The mechanochemical approach consisted of a dry-wet milling operation, using a mixture of $Zn(NO_3)_2{\cdot}6H_2O$ to red mud of 2:1 which resulted in a crystalline LDH material.

1.9 Summary and conclusions

The world is changing and moving towards more sustainable approaches to the current manufacture and production chain infrastructures. From the simple task of transportation to the complexity of producing chemical commodities and fuels, nowadays and more than ever, green chemistry is taking an important role. Moreover, the circular economy approach gains in importance as more research concludes that in the future, producing goods under a circular economy framework could bring more advantages than disadvantages to the next generations. Using waste to generate added-value products encompasses the definition of what the circular economy is. Several authors [108-110,144] have studied the production of added-value products such as biofuels or heterogeneous catalysts using waste as the source of the raw materials, with a wide variety of results. A particular type of material that becomes relevant when dealing with circular economy and sustainability issues, is the layered-double hydroxide (LDH). The LDHs are a brucite-like material with plate-like sheets stacked upon one another with a wide variety of synthesis methodologies as well as different applications. Mostly used as heterogeneous catalysts or adsorbents, LDH materials can also be prepared using waste. LDH synthesis using ochre or struvite as raw materials have proved the capabilities of the latter waste materials as the foundation to produce heterogeneous catalysts to promote different chemical reactions as well as acting as efficient adsorbents [114,141], while providing value to materials that otherwise would be considered waste and either disposed properly or end up contaminating the environment. On the other hand, biomass, an accessible raw material for the production of bio-derived products, is already producing an impact on the environment to generate bio-derived products that can help combat pollution and greenhouse gas emissions nowadays. Nowadays, much of the technology to produce bio-derived products from biomass is being commercialised or is already at pilot/demonstration plant scale [145]. However, fully commercially available first-generation biofuels such as biodiesel and a few of those coming from second generation have some drawbacks, one of the most important being the high amount of oxygen content they have. The latter affects their energy density and make them have undesirable characteristics in cold weather scenarios [146]. Deoxygenation processes of biofuels are mandatory when a diesel-fuel like compound is desired. Processes as hydrodeoxygenation and decarboxylation are two of the most studied ones. The first one, however, requires a vast amount of hydrogen in order to deoxygenate biomass raw materials as fatty acids and convert them into diesel-like compounds[68]. Thus,

a different pathway to remove oxygen out of biomass raw materials or bio-derived products is decarboxylation. In this process, the molecules lose oxygen in the form of CO_2. The latter can occur when a C-C coupling reaction happens, as with ketonic decarboxylation, in which long chain hydrocarbon chains are formed out of biomass derived molecules, which usually are not that long before coupling [147]. Ketonic decarboxylation (ketonisation) is a reaction that has been well-studied, however, no agreement regarding the mechanism has been reached since it was discovered [64,82,148]. Several studies have been conducted using different catalyst types, in order to finally find a reaction pathway and fully understand the behaviour of the ketonic decarboxylation. Although no agreement has been reached yet, several researchers conclude that the most logic pathway for the reaction to occur is the one involving the so called β-keto acid mechanism, a reaction that need high lattice energy oxides (e.g. TiO_2, CeO_2, ZrO_2 and MnO_2) and in which the molecules react over the catalyst surface [64,81,82,88,93]. Therefore, the use of low-cost or waste-derived materials to be further utilised in sustainable processes to transform biomass into valuable bio-derived added value products is a topic of research worthy of being explored due to the climate change circumstances our society is living under.

Aim of this study

In today's world, societies are moving faster towards a more sustainable and circular economy, as new green objectives and policies are being push forward in order to mitigate the adverse effects that the current production infrastructure is causing to the environment [1,2]. In alignment with the trend towards more sustainable production processes, this work focuses in exploring low-cost (in the context of using catalysts that does not require expensive metals) catalytic alternatives to transform potentially biomass derived feedstocks into added-value bio-derived products, thereby coupling a sustainable catalyst to a sustainable process. Going one step further, applying a circular economy framework of waste reuse, to recycle and minimise waste, waste streams derived materials could potentially deliver low-cost catalysts wholly made of waste [1-3].

The specific objectives of this thesis are: *Objective 1. To evaluate whether highly basic low-cost catalysts based on MgO can be used in biomass transformations using vegetable oil components*. The use of abundant and environmentally friendly catalyst for heterogeneous catalytic processes has been encouraged over the years, aiming to make the chemical conversion processes more sustainable [3,55,101]. MgO is a mineral derived low cost and non-toxic oxide that has been widely used for catalytic purposes, due to its highly basic nature [101,117]. MgO has been used for biomass transformation reactions in the past [86,120,149], however, in this study different particle size MgO powders will be evaluated to promote the ketonic decarboxylation of dodecanoic acid. The variability of the surface area in conjunction with varying the reaction parameters such as the catalyst loads, and reaction temperature will also be tested in order to identify key reaction conditions to tune to further favour the production of the desired ketone products. Often, the use of nanoparticles results in additional reactivity owing to the increase in grain boundaries. The role of the substrate interactions will also be studied through using binary mixtures of different carboxylic acids and studying the product distribution

Objective 2. Using a mining waste material for catalyst production. In the search of other low-cost catalytic alternatives for catalytic purposes within the sustainability framework and adhering to the concept of circular economy, the production of a catalytic material such as a layered double hydroxide (LDH) using a waste stream as one of the mineral precursors for the synthesis of the latter LDH will be performed. The mining waste ochre was selected as

the high amount of iron in the sample could work as the M^{III} donor during the LDH synthesis and ochre is a prevalent regional waste material [150]. The formed LDH material will be tested as a catalyst to promote the ketonic decarboxylation of dodecanoic acid into the respective ketone product, in comparison with the MgO work, and also in the search of giving more added-value to a waste-derived material, the production of hydrogen through the hydrogen evolution reaction. Hydrogen can potentially be subsequently used for the hydrogenation of biomass-derived products [102,151].

Objective 3. Using waste materials from mining and watertreatment plant waste streams for catalysts synthesis. If the ochre successfully acts as the donor of the M^{III} to form a ochre-derived LDH, due to the ochre's high content of iron, if used in the proper stoichiometric amount, another waste stream containing a M^{II} cation can be potentially act as a M^{II} donor and a wholly made of waste LDH material would form [150,152]. We will attempt to use ochre and struvite (struvite is obtained from concretions within the pipelines of a wastewater treatment plant) to act as cation donors for the production of an LDH material, which encloses the essence of the circular economy, the revalorisation of waste and the extended lifespan of the products.

2. Analytical methods and experimental

In the present study different materials were synthesised. Some of them (i.e., layered-double hydroxides (LDH)) were synthesized and evaluated as catalysts to promote deoxygenation reactions (e.g., ketonic decarboxylation), while some other LDHs were synthesized using waste materials as precursors in the search of giving a novel use to what otherwise would be considered a waste to dispose. Moreover, magnesium oxide of different particles sizes (i.e., MgO) were also used as catalysts to promote the ketonic decarboxylation reaction in an effort to use a low-cost, environmentally friendly and effective catalyst to further investigate the effect that the particle size, the temperature or the catalyst load could cause in the ketonic decarboxylation reaction. Therefore, characterisation of such materials had to be performed, for the as-synthesised LDHs as well as for the MgO powders that were supplied by the chemical manufacturers. Characterisation analysis of the all the reactants and precursors used in this study as well as the post-reaction products were performed using analytical techniques such as powder X-Ray diffraction (PXRD), Fourier-transform infra-red (FTIR) spectroscopy, nitrogen adsorption and desorption isotherms, scanning electron microscopy (SEM), inductively coupled plasma optical emission spectrometry (ICP-OES), inductively coupled plasma mass-spectrometry, gas chromatography (GC), mass spectrometry (MS), differential scanning calorimetry (DSC), ultraviolet-visible spectroscopy (UV-Vis), photoluminescence (PL) and thermogravimetric analysis (TGA). Thus, the experimental procedure to carry out the chemical reactions are also explained as well. All the latter techniques and experimental procedure are explained in detail, however, in each subsequent results chapter, a brief description of the instrumentation and the experimental procedures used is also presented.

2.1 Powder X-Ray Diffraction (PXRD)

Powder x-ray diffraction (PXRD) is a well-known analytical technique used for identification and characterization of crystalline structures. PXRD was employed during the whole of the work presented in this thesis, for instance, in Chapter 3 and Chapter 4, the MgO powders used to catalyse the ketonic decarboxylation reactions of fatty acids were characterise before and after being put to react. From Chapter 5 to Chapter 7, PXRD was used as an essential technique in order to determine whether the LDH was successfully formed or not, after the co-precipitation synthesis procedures. Moreover, the crystallinity of the LDHs and the possible different phases existing within the LDHs can also be addressed through the use of PXRD. X-rays belong to the electromagnetic radiation spectra with wavelengths within the 0.5 to 2.5 angstroms (Å) (0.05 to 0.25 nm) [153]. Collision and loss of kinetic energy of electrons between two electrodes at high voltage result in production of X-rays with different wavelengths [154]. Electrons around the nuclei of the atoms from the samples scatter the incident X-rays, resulting in constructive or destructive interference, giving peaks or flat lines when full in-phase or out of phase. The latter behaviour can be detected and measured by different approaches, with measuring the diffraction angle using a diffractometer being the most commonly applied one [154]. A diffractometer is an analytical instrument which can collect data as a function of angle to satisfy Braggs' law, which is an equation that was formulated as a relation between the diffraction angles, interplanar spacing and wavelength. Using the Miller indices (crystallographic indices that describe crystallographic planes) and based on mirror reflections, the appliance of the Braggs' law is shown in Figure 2-1 [155].

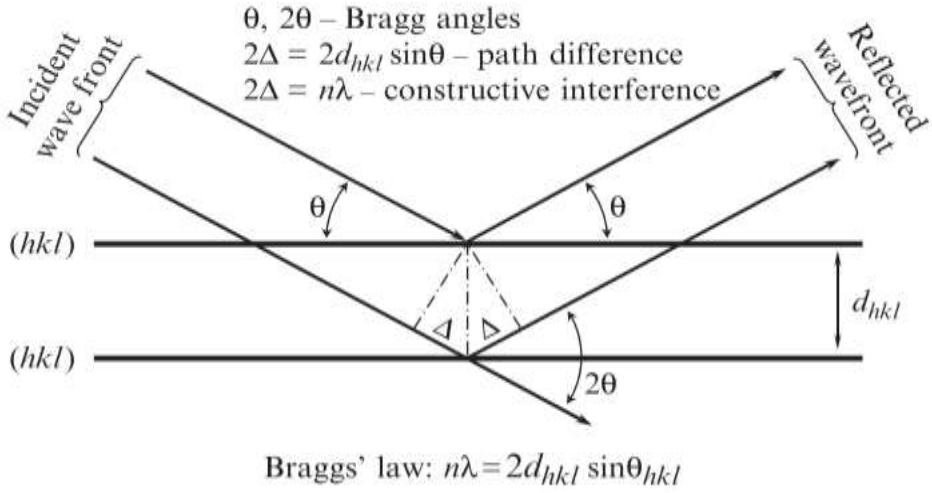

Figure 2-1. Illustration of the fundamental mechanism which derived into the Braggs' law. Taken with permission from Pecharsky, and Zavalij [155].

For the scattering of the x-rays to occur, a solid sample is needed. However, not all solids can be included in the crystalline material category. The less order exists in a solid, the more amorphous can be considered. Therefore, the more ordered the particle of a solid is, the more crystalline it can be considered [154,155]. Assuming that by nature a crystal will be an infinite repeated arrangement of three-dimensional molecules or atoms, such arrangements receive the name of unit cell, as observed in Figure 2-2.

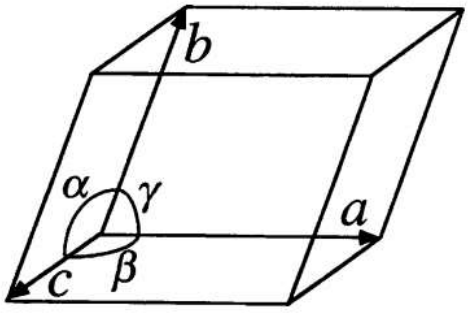

Figure 2-2. Three-dimensional representation of a unit cell, showing all the lattice parameters. Taken with permission from Pecharsky, and Zavalij [155].

The unit cell components are called the lattice parameters a, b, c, α, β and γ, which are the representation of vectors or lengths (a, b and c) and the interaxial angles (α, β and γ) of the unit cell, usually measured in angstroms (Å). Although in reality the crystallography planes are used as a spatial representation of mathematical equations emerging from the diffraction over a unit cell, they can be represented as observed in Figure 2-3. The latter crystallography planes can be fully described by the Miller indices (i.e., *h, k* and *l*) and are usually enclosed within a parenthesis (e.g., (*hkl*)). Therefore, when using the indices, the plane's lattice vectors a, b and c are respectively divided into *h, k* and *l* equal parts (Figure 2-3). The space in between planes correspond to the interplanar space or *d*-spacing . The value of the latter indices will be set to 0 whenever the plane is parallel to the corresponding axis [154,155], as seen in Figure 2-3.

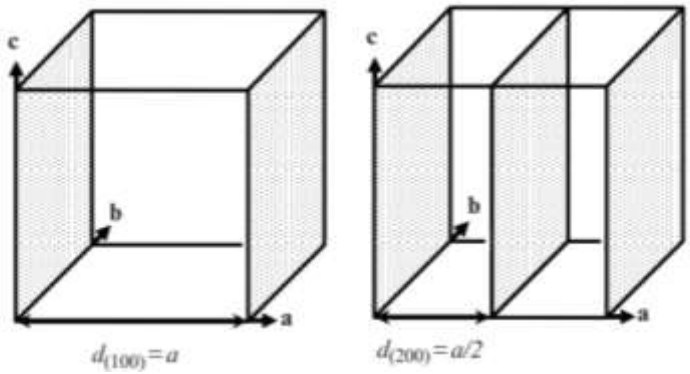

Figure 2-3. Representation of a unit cell with the plane parallel to c and b. The simple cubic structure showed in this figure was chosen due to the simplicity of such structure, where the planes can be observed easily. Taken with permission from Pecharsky, and Zavalij [155].

For this work, all the PXRD analysis of the as-synthesized LDHs (i.e., Chapter 5, Chapter 6 and Chapter 7) and the MgO powders (Chapter 3 and Chapter 4), were performed in a Bruker D8 Advanced XRD machine in the Chemistry department, at Durham University. The machine used a copper tube with radiation of 1.5418 Å wavelength. The 2θ angle range was set to be 10-90 degrees. All the samples, MgO and LDHs, characterised in this work, ran for a period of 60 minutes as total scan time. In a typical preparation of an XRD sample within this work (all the samples from Chapter 3 to Chaper 7 analysed through PXRD, followed the same preparation steps), a few mg (~20 mg of the sample) were ground and

placed over a PXRD slide through a 120-mesh sieve to uniformly disperse the sample over the whole surface of the slide. To fix the dispersed sample over the slide, a thin layer of vaseline was put over the surface of the latter slide, prior dispersion of the sample. Characteristic lattice parameters and diffraction patterns exist for LDH materials, consequently, when synthesized and analysed through PXRD, the lattice parameters of LDHs can be calculated with ease. The diffraction patterns obtained from PXRD for some of the materials used in this study are shown in Figure 2-4((Figure 2-4(a), goethite (red asterisk) and hematite (blue asterisk), respectively) and a LDH (Figure 2-4(b)).

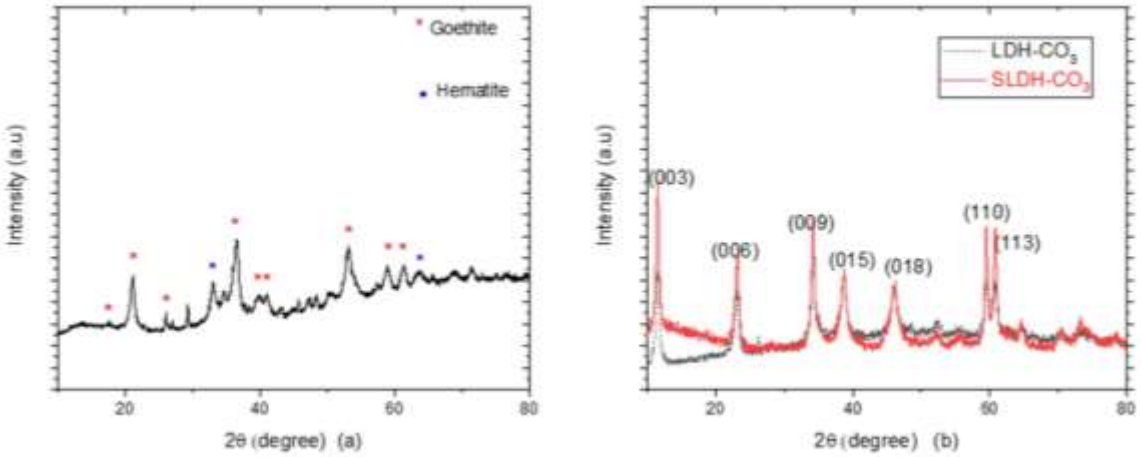

Figure 2-4. Powder X-ray diffraction patterns from different samples. a) The diffraction pattern of the Saltburn ochre. b) The diffraction pattern characteristic of LDH materials. Taken from Chapter 5.

In Figure 2-4(b), the diffraction peaks (003), (006) and (009) represent the characteristic LDH diffraction peaks. Due to LDHs being rhombohedral/hexagonal systems, different reflections are used to obtain the all the different unit cell parameters (e.g., Figure 2-3), where *a* is equal to *b*, in this particular case. Using the (110) reflection, *a* is calculated as $a = 2d_{(110)}$ and using the (003) reflection $c = 3d_{(003)}$. As observed, to obtain *a* and *c*, the *d*-spacing was needed to be calculated first. To calculate *d*, the following equation is used.

$$2d\sin\theta = \lambda \qquad \textbf{2.1}$$

Equation $2d\sin\theta = \lambda$ 2.1 is the most used form of the Bragg's law where *d* refers to the interplanar *d*-spacing, λ and θ the wavelength and angle of the incident x-rays, respectively.

2.2 Fourier-transform infra-red spectroscopy (FTIR)

The importance of the infra-red spectroscopy analysis relies on the capability of the technique to obtain data related to the functional groups that form different molecules [156]. According to the FTIR theory, the absorption of infra-red light within a molecule can be observed as a transition from one energy level to a different one in terms of the molecules' bond vibration represented by a vibrational spectrum (i.e., where the energy of the light wave is equal to the vibrational frequency , the latter light wave will be adsorbed) [157]. The most common way that the bonds vibrate in molecules are through stretching and bending, as observed in Figure 2-5.

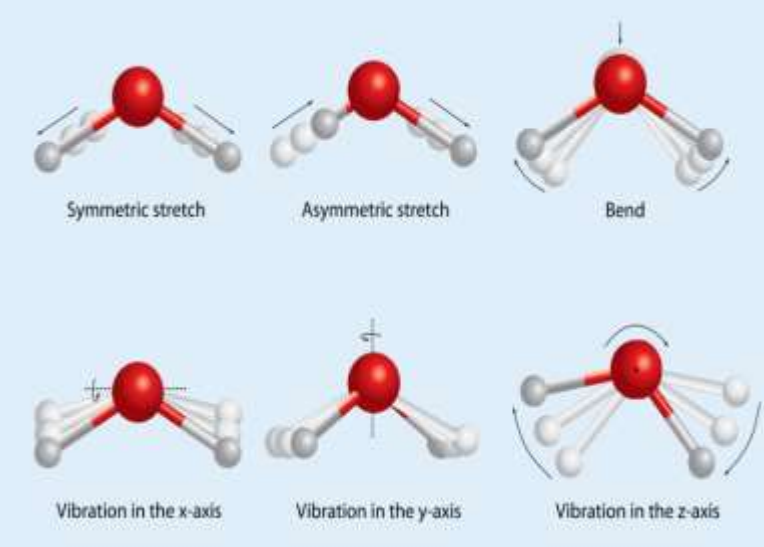

Figure 2-5. Different vibration and stretching of bonds in a water molecule. Taken with permission from Cristy *et al.,* [157].

Nevertheless, the latter vibration or stretching of the molecule bonds can be registered using an infra-red spectrometer, which gives readings of the energy needed for the bonds to move in terms of a wavenumber (cm^{-1}) once the infra-red light has been absorbed by the molecule [158]. In this study, the MgO powder used in Chapter 3 and Chapter 4, before and after being put to react, as well as the as-synthesized LDHs in Chapter 5, Chapter 6 and Chapter 7 were characterized through FTIR using a Perkin Elmer FTIR Spectrophotometer, in the Chemistry department at Durham University. In a typical characterisation through FTIR performed to all the samples from Chapter 3 to Chapter 7, a few mg of the sample (~5 mg) were carefully placed on the instrument. The wavelength

range was set from 4000 to 400 cm^{-1}. The force gauge set at a consistent 105 units on the ATR cell anvil. Finally, pressure was applied on the sample through the force gauge on the sample and the readings were observed on the screen of the computer. A FTIR spectra typical of an LDHs (specifically in this picture, a Mg-Fe CO_3 LDH) is presented in Figure 2-6.

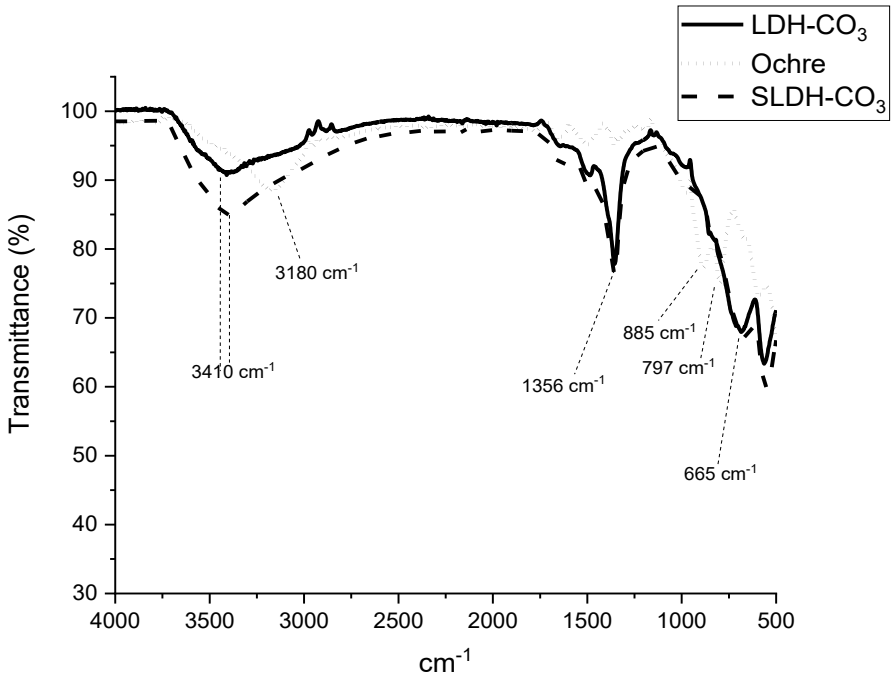

Figure 2-6. Fourier-transformed infrared spectra from a Mg-Fe CO_3 LDH spectra with characteristic adsorption peak related to the interlayer carbonate at 1356 cm^{-1}. Taken from Chapter 5.

As observed, the carbonate LDH exhibited a behaviour specifically attributed to the antisymmetric deformation of the carbonate anion, which is usually observed at 665 cm^{-1} and antisymmetric stretching vibration of the carbonate is observed at 1356 cm^{-1}[86,114]. The broad peak *ca* 3410 cm^{-1} can be assigned to the stretching vibrations of the OH groups in the brucite-like layers. Therefore, in the case of LDHs, for instance, the material will have a characteristic FTIR "blueprint" (i.e., expected peaks to be observed at certain wavenumbers due to the interlayer water, the OH bonds with the metals in the brucite-like layer, the anion in the interlayer) that can be used as an identifier, to ensure the synthesized material meet the desired characteristics that were aimed to be obtained.

2.3 Nitrogen adsorption and desorption isotherms

According to Rouquerol *et al.,* [159] adsorption occurs when a liquid or gas get in contact with a solid surface and can be described as: "The enrichment of material or increase in the density of the fluid in the vicinity of an interface". Adsorption and desorption of gases is powerful technique when it comes to the characterisation of the surface properties of fine powders, with nitrogen (at 77.4 K or -195.7 ˚C) being the most used gas for such task [160,161]. Adsorption occurs as a measure from a surface to reduce the surface tension, as molecules located at the solid's surface will feel a resultant force pointing towards the bulk of the solid, differing from zero, as shown in Figure 2-7. The adsorption mechanism can occur through chemisorption (i.e., adsorption due to covalent or ionic bonds) and physisorption, which is mainly attributed to the Van-der-Waals forces) [162]. Desorption, in the other hand is the inverse process in which the molecules leave the surface to return to the fluid phase [159].

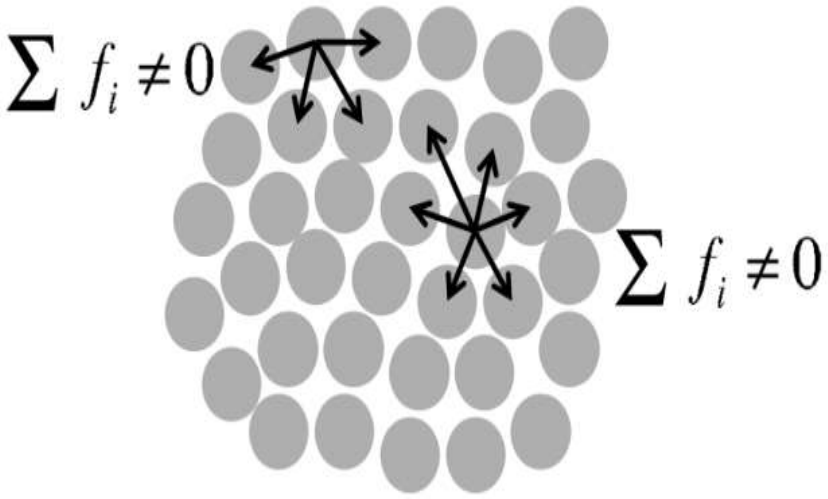

Figure 2-7. Resultant forces experienced by surface molecules at a solid. Molecules in the bulk will experience resultant forces equals to zero whereas molecules at the surface will feel a resultant force towards the bulk, leading to a surface tension. Taken with permission from Che and Vedrine [161].

Most of the heterogeneous catalysts developed nowadays belong to the porous materials category. Some of them would include zeolites, LDHs, metal oxides, among others. The pores of a material can be classified according to their size in micropores, mesopores and macropores, with a size of < 2 nm, between 2 nm and 50 nm and above 50 nm,

respectively [163,164]. The work of Freundlich, Langmuir and in more recent years the introduction of the BET method (Brunauer-Emmet-Teller) regarding the adsorption and desorption of nitrogen to analyse surfaces [165], have become a tool to characterise a material in terms of the latter mentioned pore size as well as the pore volume and the specific surface area [161] therefore, according to the pore characteristics of the material, different adsorption and desorption isotherms can be obtained [163]. The adsorption and desorption isotherms can be divided into six different types with sub categories (according to IUPAC), as observed in Figure 2-8 however, when solely used for catalysis, the isotherms classification can be reduced to four different ones, which are Type I, Type II, Type IV and Type VI [159,160,164], which correspond to the isotherms for microporous, macroporous, mesoporous and to ultra-microporous solids, respectively [166]. Type III and Type V isotherms are uncommon; however, Type III is considered to be a reversible isotherm with presence in systems such as nitrogen on polyethylene. Type V is related to the Type III as it is expected to happen when the adsorbent-adsorbate interactions are weak [162].

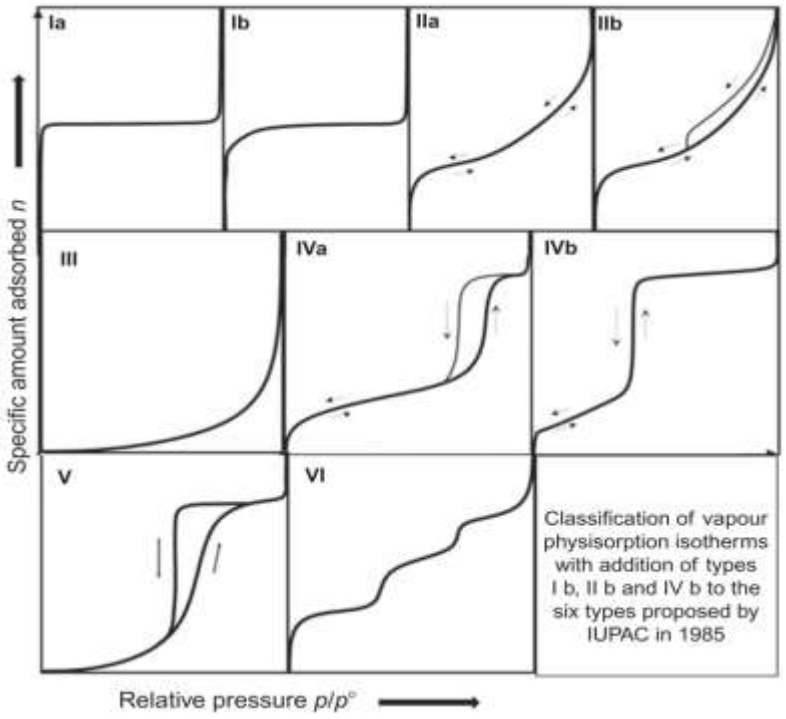

Figure 2-8. Different six types of adsorption Isotherms expected to be observed when performing nitrogen adsorption-desorption studies. Taken with permission from Sing [166].

In this study, MgO powders were characterised through BET in Chapter 3 and Chapter 4, as the study of the surface area of each sample was important during the development of the experimental analysis of such chapters. From Chapter 5 to Chapter 7, BET was also employed to characterise the as-synthesized LDHs, in terms of surface area and pore volume. Moreover, MgO powders and LDHs usually display Type IV isotherms, and they are classified among the category of mesoporous materials [8,102,114]. Thus, mesoporous materials, when analysed using nitrogen adsorption-desorption isotherms, often present what is called a hysteresis loop. As observed in Figure 2-8, on the Type IVa isotherm, hysteresis loop is the name given when the adsorption and desorption curves does not match one another [160,162,166]. In the studies carried out in this thesis, the nitrogen adsorption and desorption experiments were performed using a Micromeritics ASAP 2020, in the Chemistry department at Durham University. The system was set at -196 °C, with the samples being degassed at 80 °C. Thus, all the samples (The MgO or LDH samples, from Chapter 3 to Chapter 6) were dried prior analysis overnight at 70 ˚C. In a typical experiment, a few mg (~25 mg) of dried samples were placed inside the degassing glassware, to further proceed with the degassing under vacuum of 200 μm Hg for a period of 5 hours. Once completed, the samples were removed from the degassing port and placed into the analysis port with an isothermal jacket covering the glassware and using liquid N_2 to cool while running the adsorption and desorption experiments. As mentioned before, one of the main purposes of using a nitrogen adsorption-desorption technique to characterise a porous material is to measure the surface area of the latter material. For such task, it is important to carry the experimental work having some concepts in mind, such as the equation describing the BET method.

The BET equation can be described as follows:

$$\frac{\mathbf{p}}{\mathbf{n^a(p^0-p)}} = \frac{\mathbf{1}}{\mathbf{n_m^a(C)}} + \frac{\mathbf{(C-1)p}}{\mathbf{n_m^a(C)(p^0)}} \qquad 2.2$$

where n^a refers to the amount of gas adsorbed at the relative pressure p/p^0 and n_m^a is the monolayer capacity [162]. The monolayer refers to the surface layer of the material, where, according to Sing [162], when working with mesoporous materials, physisorption is expected to happen through monolayer and multi-layer adsorption. To obtain the BET surface area, a

linear relation needs to exist between $\frac{p}{n^a(p^0-p)}$ and $\frac{p}{(p^0)}$ to obtain the values of n_m^a and *C*, which will subsequently be used in the following equations.

$$\mathbf{A_s(BET)} = \mathbf{n_m^a \,.\, L \,.\, a_m} \qquad 2.3$$

$$\mathbf{a_s(BET)} = \frac{\mathbf{A_s(BET)}}{\mathbf{m}} \qquad 2.4$$

where A_s (BET) and a_s (BET) are related to the total surface area and the specific surface area, respectively, m refers to the mass of the material and L to the Avogadro number [160,162]. Nevertheless, due to certain considerations made when running the BET procedure (i.e., a constant a_m value for nitrogen at -196 ˚C, which is the molecular cross-sectional area, as well as assuming the monolayer of the adsorbent is filled first rather than the other layers, which is unlikely to always occur) the surface area determination has an estimated error value of 20 % [160,162].

2.4 Gas Chromatography (GC)

The gas chromatography (GC) is an analytical technique used to identify and quantify chemical compounds using a mobile phase (i.e., a carrier gas), which transports the analyte of interest and will move through the stationary phase that reside inside a column [167]. The Figure 2-9 is a schematic representation of how to represent a gas chromatography process.

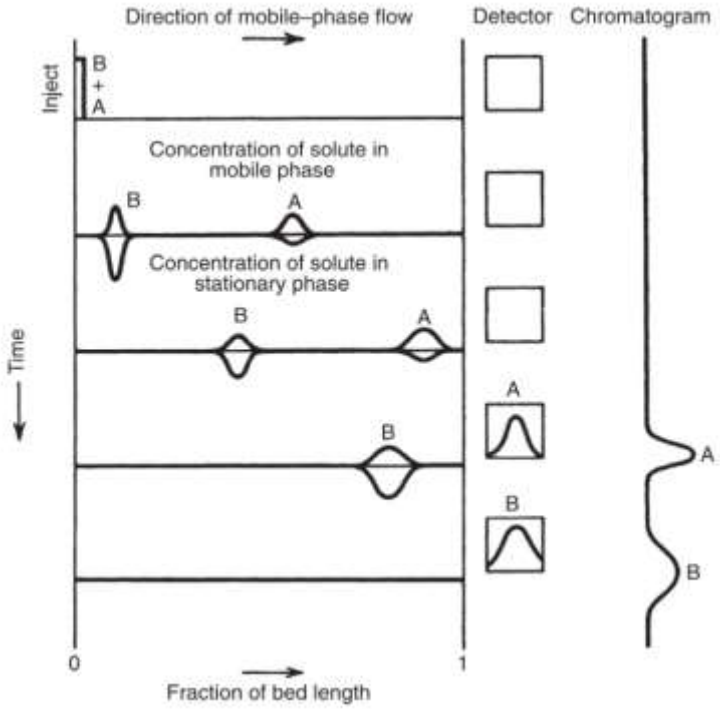

Figure 2-9. The schematic representation of a gas chromatography process from injection to elution of the analyte of interest. Taken with permission from Jennings [167].

As observed in Figure 2-9, once a sample containing 2 different analytes of interest (A, B) goes inside a column, they will be distributed based on their affinity with the stationary phase and their relative vapour pressures, being eluted at ideally, different times (i.e., retention time) to pass through a detector that will generate a signal that will be later interpreted as a chromatogram [168,169].

2.4.1 Columns and detectors

To further understand the gas chromatography analytical technique, it is important to introduce the concept of columns and detectors. columns are considered the most important part within the chromatography instrument, and depending on the characteristics of the adsorbent residing inside the operation modes, they can be differentiated from one another [170,171]. Table 2-1, which was extracted from Rahman *et al.,* [171] presents a good overview for the understanding of the columns classification.

Table 2-1. Column classification based on the manufacture characteristics. Adapted from Rahman *et al.,* [171]

Columns	
Packed columns	Capillary columns
Stationary phase is coated directly in the column	Stationary phase is coated with the inner wall of the column
Applicable for both GSC and GLC	Applicable only for GLC
Liquid phase is adsorbed onto the surface of the beads in a thin layer or onto the solid inert packing	Liquid stationary phase is immobilized on the capillary tubing walls

*GSC refers to the stationary phase being a solid adsorbent, i.e., gas-solid chromatography and when the solid phase it is a liquid in an inert support it is called GLC, i.e., gas-liquid chromatography.

According to the literature, packed columns were used during the early days of chromatography however, nowadays capillary columns are involved in up to 90 % of all the chromatographic analysis [168]. Packed columns are restricted in length up to 10 meters longs and most packed columns used nowadays go up to 4 meters long. The latter restriction is due to the mobile phase experiencing resistance to flow due to the packing within the column [169]. On the other hand, as capillary columns have the stationary phase located as a layer in the inner wall, resistance is unlikely to occur as in packed columns, therefore lengths of up to 50 meters are possible [169]. Differences between both columns can be further appreciated in Figure 2-10.

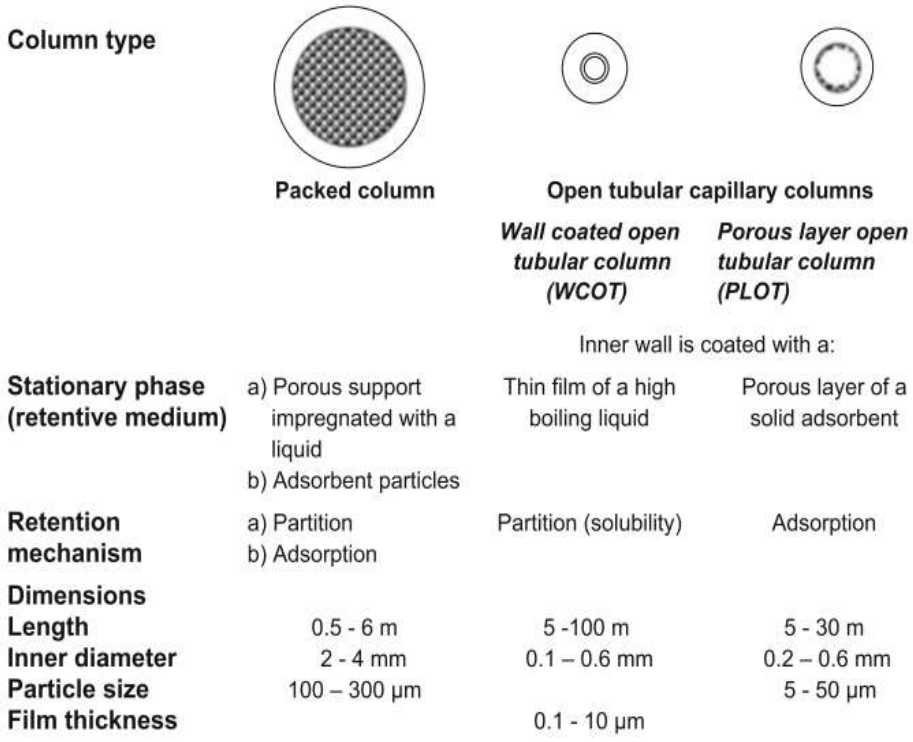

Figure 2-10. Graphic representation of the physical differences between a capillary and packed column. Taken with permission from Dettmer-Wilde and Engewald [169].

Among a wide range of detectors (over 60), the most used is the flame ionization detector (FID), which is the one used for this study to quantify the analytes of interest. In a FID detector, a high temperature flame produced by hydrogen burns the effluent from the column to its ionization state to form a current and deliver a signal that can be read by the detector [168]. When introduced in 1958, the detector capabilities in conjunction with the little to none maintenance needed, low detection limits (10^{-13} g/s) as well as its universality to be used with organic compounds made the latter FID detector very popular in laboratories around the world, something that is maintained until nowadays [169].

A schematic representation of the FID detector is shown in Figure 2-11.

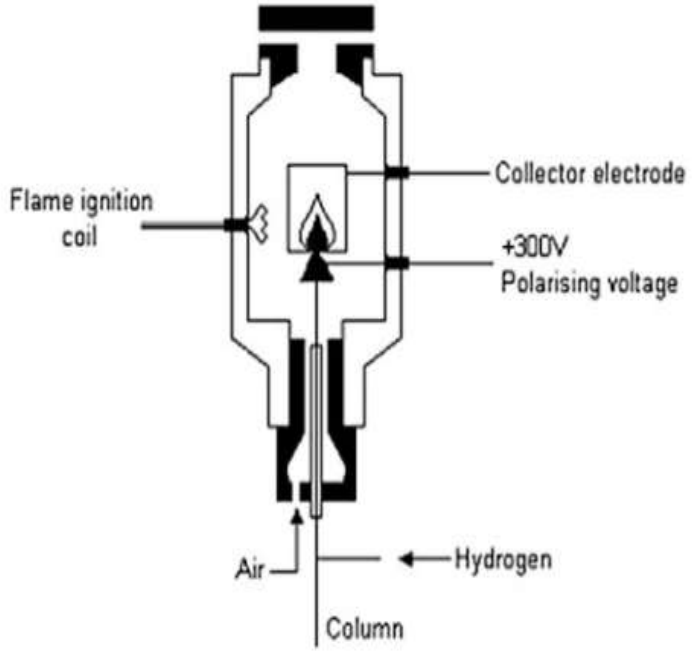

Figure 2-11. A representation of the flame ionization detector used in a gas chromatography system. Taken with permission from Dettmer-Wilde and Engewald [169].

Another powerful use of the chromatography technique occurs when the chromatograph is coupled with a mass spectrometer. Initially developed in 1955 to solve industrial difficulties, the gas chromatography mass spectrometry technique (GC-MS) is extremely powerful for compound identification [172]. When the GC-MS technique is used, the sample will receive the same treatment as explained in Section 2.4, for gas chromatography. However, when the vaporized sample leaves the chromatography column, the mass spectrometer ionizes the sample and proceeds to fragment it, which are further accelerated through the quadrupole or ion trap, where the separation of the ions occurs based on their m/z (mass/charge) ratios [173].

One important consideration when using lipids during GC analysis is that the lipids need to be derivatised (i.e., silylated) to improve the quality of the analysis, that is make

them more volatile so they can reach the detector. The silylation reaction was presented in Figure 2-12.

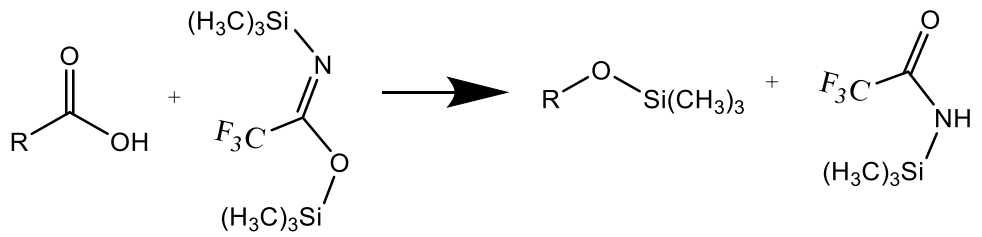

Figure 2-12 Sylylation mechanism of fatty acids using N,O-Bis(trimethylsilyl)trifluoroacetamide.

In this study, to have a proper quantification of the non-reacted fatty acid post-reaction, derivatisation was used. Though derivatisation, highly polar hydrogens from the analyte are converted to lower polarity, which therefore reduces the boiling point of the molecule and making it more volatile, which is essential to carry on a GC analysis [174,175]. In this work, from Chapter 3 to Chapter 5, several fatty acids were studied and derivatised accordingly. The un-reacted fatty acids as well as the ketonic decarboxylation products obtained were quantified and conversion and purification processes qualitatively analysed by applying the corresponding derivatisation and quantification procedures (through gas chromatography) explained in the following sections.

2.4.2 Derivatisation process using the crude post-reaction mixture of the ketonic decarboxylation reaction

The extracted crude product from the ketonic decarboxylation reaction was put into a 50 ml Falcon tube and centrifuged using a Beckman Coulter Avanti J-20XP centrifuge (1000 rpm, 30 min) to separate the solid catalyst. Prior to the GC analysis, the crude post-reaction mixture (2 ml) of the ketonic decarboxylation reaction of dodecanoic acid was derivatised using N,O-Bis(trimethylsilyl)trifluoroacetamide (BSTFA) in the presence of pyridine as catalyst [175]. The samples were left in continuous agitation for 2 hours and 1 ml was taken afterwards. Depending on the initial amount of fatty acid used for the ketonic decarboxylation reaction, the amount of BSTFA and pyridine was stoichiometrically

calculated based on the assumption that if no reaction occurs at all, all the initial fatty acid would remain in solution, therefore, depending on the amount of fatty acid initially used, BSTFA and pyridine would be added at 100 % excess.

2.4.3 Quantitative analysis of ketonic decarboxylation reaction products using GC-FID

After derivatisation, 1 ml of the sample with 0.5 ml of 0.1 M eicosane solution (in toluene) were put inside a chromatography glass vial and analysed using a Shimadzu GC-2010 instrument with a flame ionization detector (FID) with a HP-5 30M length column, of 0.25 mm internal diameter and 0.25-micron film thickness coating. Before injection, a calibration curve using the internal standard method was constructed to subsequently perform the quantitative analysis (Section 2.4.5).

2.4.4 Qualitative analysis of crude reaction products through GC-MS

The same extraction procedure from Section 2.4.2. After derivatisation, 1 ml of the sample was put inside a chromatography glass vial and analysed through a Xevo QToF mass spectrometer equipped with an Agilent 7890 GC. The library of chemical compounds within the database of the instrument and the use of standards from chemical suppliers were used to assess a qualitative analysis of the post-reaction crude product. Using the software Chemdraw®, the possible m/z ratios for all compounds were calculated and compared with the data obtained by the GC-MS analysis.

2.4.5 Calibration curve and the internal standard methodology for quantification of post-reaction products.

All the calibration curves and the dilution tables, as well as the linear regression plots are given in detail in Appendix A, however, a brief description on how to properly prepare a calibration curve was explained in the following lines. In a typical quantitative analysis of the analytes using the internal standard method for GC [176], a stock solution containing either a known amount of the analyte of interest was prepared, assuming no conversion of the substrate happened during the reaction (based on the initial amount (mol) of the substrate

used for the latter reaction) or a known amount of the product assuming full conversion and selectivity of the starting material into the desired product. The mother solution was diluted to into smaller concentrations using the following equation:

$$\mathbf{(V1)x\,(C1) = \ (V2)x\,(C2)} \qquad \mathbf{2.6}$$

Where V1 and C1 represents the initial volume and concentration of the mother solution, respectively and V2 and C2 represents the final volume and concentration, respectively. After a wide variety of different solutions with reduced concentrations of the analyte were prepared, a known concentration of an internal standard was added in the same quantity to all the different prepared solutions. It is important to consider than the internal standard retention time peak does not interfere with the peak of the analyte of interest expected to be observed in the chromatogram. The more points a calibration curve has, the better in terms of accuracy. According to the internal standard method, once the different peak areas of the analyte of interest and the standard are obtained [176], a linear regression plot is needed, where the X-axis will be the concentration of analyte to concentration of internal standard ratio (Ca/CIS, where Ca is concentration of analite and CIS is concentration of the internal standard) and the Y-axis will be the area of the analyte to area of the internal standard ratio (Aa/AIS, where Aa is area of the analite and AIS is area of the internal standard). In case some points of the latter calibration curve are out of the linear regression line, they could be removed to increase the R^2 of the analysis.

2.5 Column chromatography and Thin-Layer Chromatography (TLC)

The column chromatography is a purification technique used to separate individual chemical compounds from a mixture of compounds [177]. According to Chakravarti *et al.,* [178], from a simplified approach, a chromatographic column can be considered a continuous filtration device. A schematic representation is presented in Figure 2-13.

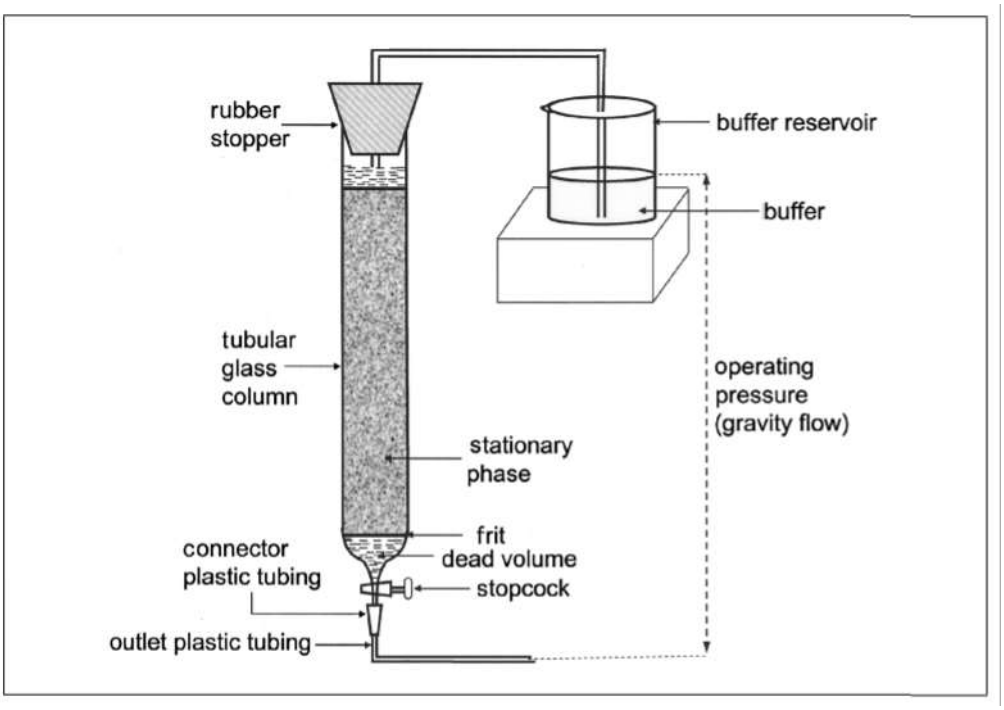

Figure 2-13. A schematic representation of a packed column to analyte purification through column chromatography. Taken with permission from Chakravarti *et al,* [178].

As observed in Figure 2-13, several things are part of the whole chromatographic column extraction process, such as the stationary phase, the glass column, and the dissolved analyte, among others. Different strategies can be used to separate a mixture of products through column chromatography. In this study, when column chromatography was needed to be performed, the glass column was first packed with cotton, which allowed the fluid to pass through and support the stationary phase. Over the cotton, a layer of sand was added (which allowed the retention of insoluble materials, in case they exist) and over the sand a layer of silica powder (stationary phase) was added up to two thirds of the column size, mixing the silica powder with the mobile phase intended to be used. The same principle explained in Section 2.4 for gas chromatography applies for the column chromatography, in terms of mobile and stationary phase. Once the silica powder was added, another layer of sand is added on top of the silica to help to retain impurities or insoluble materials, as well as to avoid disturbing the silica bed [177,179]. Once the latter addition of sand was performed, some flushes of the column using the mobile phase were done to ensure the

column was properly packed. Subsequently, the analyte was added into the column and the mobile phase was also added slowly increasing the polarity of the mobile phase. To define the ratio of solvents used for the mobile phase during the column chromatography separation, a first approach using the Thin-Layer Chromatography (TLC) technique was performed. On a typical TLC experiment used in this study, a small amount of the concentrated mixture (post-reaction mixture, Section 2.4.2) after evaporating all the solvents was taken using the capillary tubes designated for TLC analysis and deposit over a silica plate (Fischer). By trial and error (as the behaviour of the sample within the mobile phase can vary depending which concentration and polarity the mobile phase hase), increasing the polarity of a hexane to petroleum ether solution from the ratios 99:1 to 95:5, the TLC plates with the concentrated solution were put inside a glass container that contained the latter hexane/petroleum ether solution, and left inside until the mobile phase travelled upward the silica plate due to capillary effects. Once the mobile phase travelled up to 1 cm before the top of the silica plate, the plate was taken out and further analysed through UV light to observe the separation spots.

2.5.1 Rotary evaporation and addition of the sample onto the column

When needed, the rotary evaporator was used to fully remove any solvent present in the post-reaction mixtures in this study. Moreover, and during the development of Chapter 4, the rotary evaporation was performed to have a dry solid to be further dissolved in an appropriate solvent to be added into the column for the mixture separation through column chromatography. In a typical rotary evaporation procedure, a specific temperature and pressure are set on the instrument to favour the evaporation of a solvent. The temperature and pressure conditions to operate the rotary evaporator are set according to the manufacturer data sheet. The mixture with the solvent to be evaporated was poured into a round bottom flask and heated through a water bath until the desired temperature is reached. The solvent was then evaporated at reduced pression and further condensed. The rotation speed of the round bottom flask was set as desired by the user. Once the solvent was completely removed, the remaining dry solid was subsequently concentrated dissolving the solid using a few drops of another solvent to be further poured onto the column. The concentrated mixture was poured onto the column using a Pasteur pipette spreading the solution on the sides of the column to ensure a homogeneous distribution of the sample.

2.6 Thermogravimetric analysis (TGA), differential scanning calorimetry (DSC) and temperature-programmed desorption (TPD).

The International Confederation for Thermal Analysis and Calorimetry defines thermal analysis as "a group of techniques in which a property of a sample is monitored against time or temperature while the temperature of the sample, in a specified atmosphere, is programmed" [180]. According to the desired property of a material to be studied, different techniques for analysis exist in the area of the thermal analysis. Optical properties can be evaluated using thermoptometry whereas differential scanning calorimetry for power difference gives insight into enthalpic changes during adsorption/desorption, among others. The mass change of a sample during processes involving dehydration, oxidation and decomposition can be analysed through thermogravimetry (thermogravimetric analysis, TGA) [181]. TGA consist on an analysis based on the change of mass of a sample in function of the sample's temperature or time [182,183]. The sample is placed over a balance, with the temperature increasing at a constant rate, in an oxidizing or inert atmosphere, depending on the required data to obtain [182]. A thermogravimetric analyser (Thermobalance), the instrument to perform the latter mentioned analysis, contains four important parts (the electrobalance, the furnace an temperature sensors, the computer and the recorder), as shown in the schematic in Figure 2-14 [181].

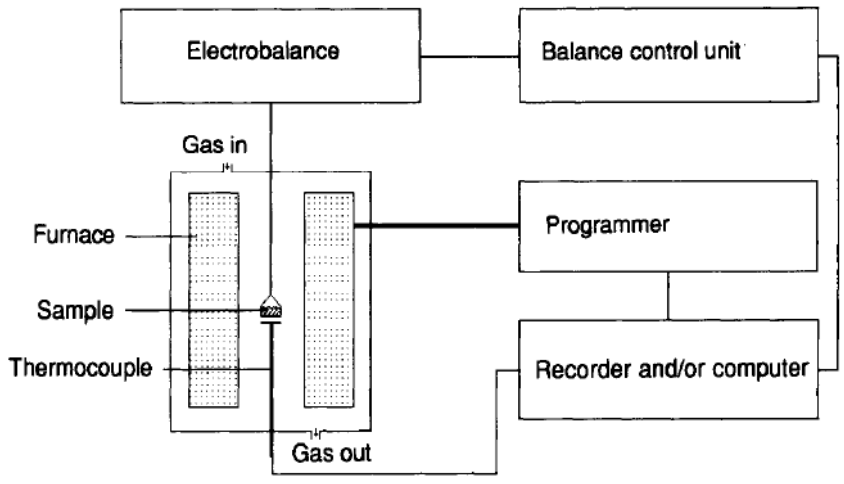

Figure 2-14. Schematic representation of the thermogravimetric analyser system. Taken with permission from Hainess [181].

The data obtained from the TGA experiments is plotted in a curve that can vary depending on the process the sample goes into (decomposition, dehydration, etc.), as observed in Figure 2-15 [180].

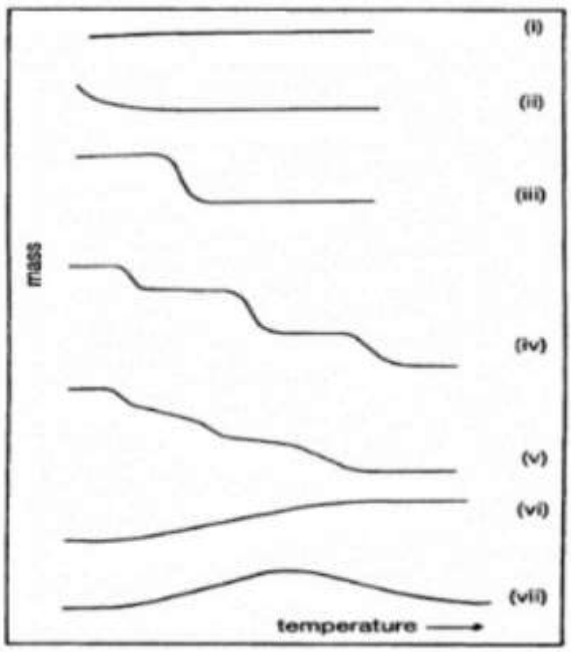

Figure 2-15. Different thermogravimetric curves related to the process experienced by the sample. Taken with permission from Brown [180]. The description of each different plot is explained below.

According to Brown [180] the seven types of plots observed in Figure 2-15 for any compound can be interpreted as follows:

- Type (i): The material is stable at the whole range of temperature examined.
- Type (ii): Often related to the drying or desorption of molecules over the surface of the material.
- Type (iii): Related to a single stage decomposition.
- Type (iv): A multistage decomposition with stable intermediates.
- Type (v): A multistage decomposition without stable intermediates.
- Type (vi): Rather than loosing mass due to any heating effect, it gains mass due to reactions with the atmosphere in which the sample is involved.
- Type (vii): Not often observed, relates to the oxidation of a metal followed by decomposition soon after.

In this work, TGA analysis was performed using a Perkin Elmer Thermogravimetric Analyzer 8000 under N_2 gas flow (30 ml.min-1) in the Chemistry department, at Durham University. The temperature was varied from room temperature to 1000 °C, increasing at 30 °C per minute. The TGA analysis were mostly used to characterize the as-prepared LDHs (Chapter 5 to Chapter 7), however, the MgO samples used in Chapter 3 and Chapter 4 were also analysed through TGA. In a typical TGA analysis, a few mg of the sample were placed over the balance within the instrument, and the temperature was put in a 10 °C/min ramp, until the desired final temperature was reached. The experiments were performed by the laboratory technician, Doug Carsten. For instance, usually for LDH materials, three decomposition steps occur, with the loss of adsorbed water when the temperature raises up to 120 ˚C. Secondly, the water in the interlayer is lost from 120 to 250 ˚C, which corresponds to the second decomposition step. Finally, an overlap occurs when temperature raises over 250 ˚C, with the loss of the interlayer anion, followed by the dehydroxylation of the layers from 400 to 700 ˚C, resulting in spinel formation above 750 ˚C [102,114,184]. Depending on the material composition, different mass losses curves are expected to be observed. The differential scanning calorimetry (DSC) analysis is one calorimetric technique usually applied to materials when insights of the latter material can be obtained when analysing the chemical reactions or transition phases of such materials in terms of temperature [185]. In other words, when analysing the sample while the temperature increases, a curve with peaks representing the enthalpy changes in terms of the rising temperature would be obtained [186]. Thus, these enthalpy changes observed as peaks on the curve could be assigned to different exothermic and endothermic processes that the sample undergoes when its temperature increased.

Specifically for Chapter 3, the DSC analysis were carried out by Professor Vladimir Zholobenko from Keele University. On a typical DSC analysis, the thermal decomposition of the samples would be studied once the sample has been weighted and put it over the instrument balance to be subsequently heated up to 850 °C, at a rate of 30 °C per minute. The DSC scans obtained from the analysis of the MgO samples are shown in Chapter 3, Figure 3-5. Moreover, also during the development of Chapter 3, temperature-programmed desorption (TPD) analysis was performed, trying to quantify the number of active sites in the as-received MgO samples. One of the most important uses of TPD experiments through the years, is the possibility to study more in depth the interaction of the surface of a material

with a gas (in this case, CO_2), to keep gaining insights into the mechanism of adsorption, desorption and the possible reactions occurring over the surface of such material [187]. The TPD and the DSC analysis were performed by Professor Vladimir Zholobenko from Keele University using a Rheometric Scientific STA 1500 instrument. On a typical TPD analysis, only performed during the development of Chapter 3, blank experiments were first run for all the as-received MgO samples using a heating ramp of 10 °C per minute from room temperature up to 800 °C in flowing nitrogen. After the blank experiments (which mainly removed all the adsorbed species over the surface of the CO_2), all the as-received samples were activated to 300 °C prior saturation at room temperature with CO_2 for 30 minutes. After saturation, another heating ramp of 10 °C was used to heat up the samples up to 800 °C for the desorption experiments. The TPD plots are shown in Chapter 3, Figure 3-5.

2.7 Inductively coupled plasma optical emission spectrometry (ICP-OES) and inductively coupled plasma mass spectrometry (ICP-MS)

The quantification and trace of the elements that exist within a sample are of relevance when performing analytical chemistry analysis. The most common techniques used for such tasks rely on atomic spectroscopy, which uses light that interacts with the atoms, to be adsorbed or emitted [188]. Atomic spectroscopy techniques involve decomposition at elevated temperatures due to the presence of thermal sources, which could be flames, furnaces and electronic discharges. Depending on the chosen technique, they can be further sub-divided into atomic adsorption, atomic emission, atomic fluorescence and atomic mass spectrometry [188]. A representation of such techniques is shown in Figure 2-16.

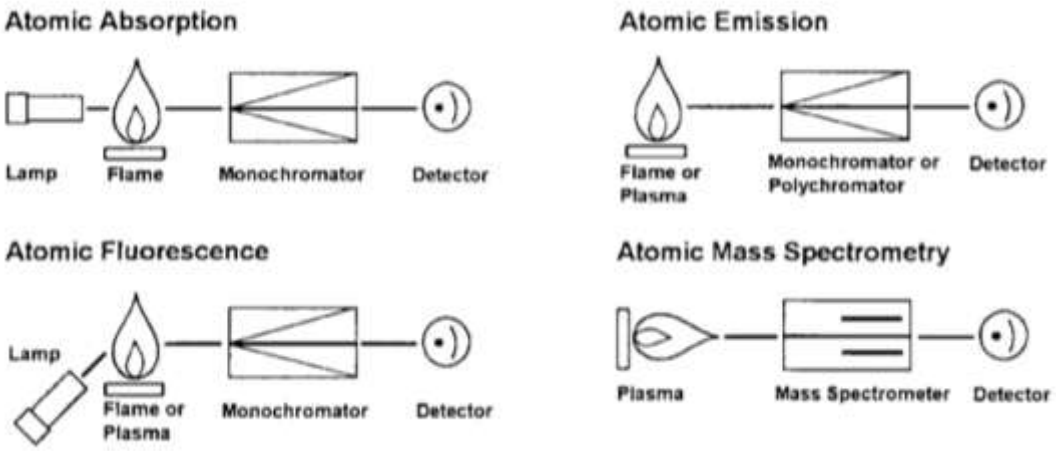

Figure 2-16. The four different atomic spectroscopy systems used for atom and ion detection. Taken with permission from Boss and Fredeen [188].

According to Boss and Fredeen [188], when working with a technique such as the atomic emission spectroscopy, ionization of the atoms from the sample occur due to the high temperatures used during the analysis, favouring the atoms moving from ground state energy levels towards an excitation state. As a consequence of the atom decay into lower energy states, energy is emitted in the form of light, which is further quantified and can be assigned to the concentration of a specific element in the sample. The latter summarizes the working principle of the ICP-OES technique. Although the same plasma torch is used for both, ICP-OES and ICP-MS, to ionize the gas, the analysis procedure between the two instrument differs from one another. Contrary to the ICP-OES, which quantifies characteristic wavelengths of the elements that are emitted when the atom decay from higher energy state to a lower one, the ICP-MS generates positive plasma ions from the atoms, which are further quantified in large amounts. Based on that principle, the ICP-MS can quantify up to four orders of magnitude more than the ICP-OES, making the technique suitable for precise low-ppt concentrations (i.e., ng/L concentrations). In the present study, ICP-OES and ICP-MS were used specifically to quantify the amount of the M^{II} and M^{III} cations within the as-synthesized LDHs and to semi-quantify the amount of other metals also present within the samples, respectively (Chapter 5 to Chapter 7). The experiments were performed using a Jobin Yvon Horiba Ultima 2 ICP-OES, fitted with a sequential monochromator and a radial torch (power

1050 W) with cyclonic spray chamber and concentric nebulizer. For semi-quantitative analysis of elements, the instrument scanned across the electromagnetic spectrum from 190 to 800 nm. The emission lines recorded are then processed with the 'Image' software which compares them with those in its library to identify and quantify the elements present in the sample. All the analysis were performed at the Department of Chemistry at Durham University with the aid of Dr. Emily Unsworth.

2.8 Scanning-Electron Microscopy (SEM)

SEM techniques are widely applied to characterise materials, to gain insights into the morphology and composition of the materials by enlarging them up to several orders of magnitude bigger (i.e., 200,000x) [189,190]. Through the scanning of an electron beam of high energy over the surface of the material, and due to the wavelength of the electrons, which are smaller in comparison to the wavelength of visible light (see Figure 2-17), significantly higher resolution imaging of the adsorbent can be detailed than when using an optical light microscope [189].

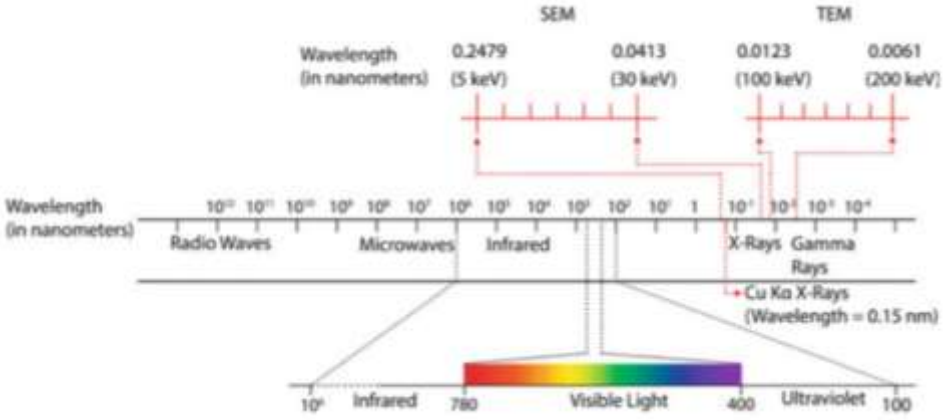

Figure 2-17. Wavelength of the different techniques used for microscopy. Taken with permission from Ul-Hamid [189].

SEM images are formed when the electrons, traveling in vacuum from the source through a column which contains electromagnetic lenses, are directed into a small probe which is located over the surface of the material under study [189]. The interaction of such contact is collected by the SEM detectors which then transform such interactions into observable images. SEM can be used for bulk samples, with a resolution of 1 nm and a useful magnification up to 200,000 x. With the aid of the Physics department at Durham University, SEM analysis of LDHs and MgO were performed by Mr. Leon Bowen, using a FEI Helios Nanolab 600 with a field-emission gun (FEG) source, 5kV and a Karl Zeiss Sigma 300 VP SEM, 10kV. In this study, SEM characterisation was mainly used to determine the morphology of the as-synthesized LDHs (Chapter 5 to Chapter 7), however, SEM was also used in Chapter 3 to further characterise the MgO. For instance, in terms of LDHs, the morphology of the material could vary; nevertheless, it is usual for LDHs to have either a platelet-like morphology or a *rose des sables* as observed in Figure 2-18 [102,191].

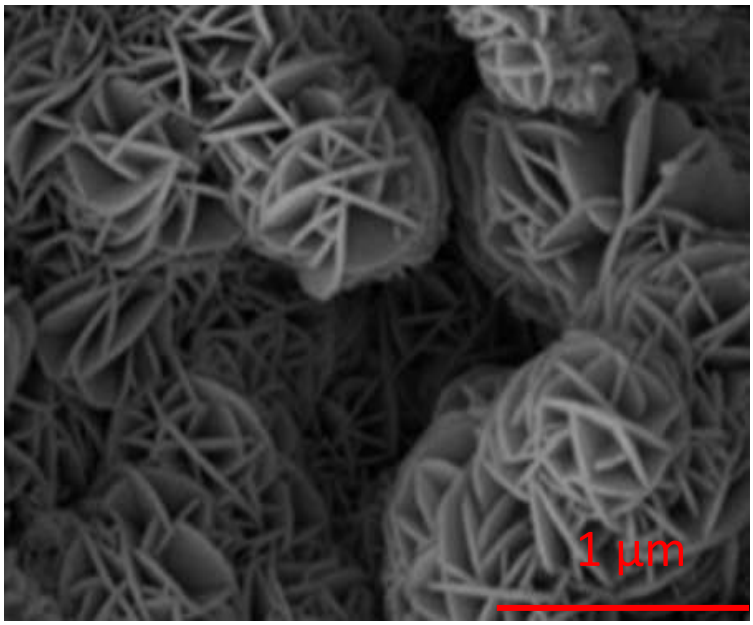

Figure 2-18. Expected scanning electron microscopy morphology obtained when analyzing layered-double hydroxide materials. Taken with permission from Smith, *et al.,* [102].

In a typical SEM experiment, all the samples were prepared dispersing a few mg (~10 to 20 mg) over the aluminium stubs and were further coated with a 20 nm (thickness) layer of carbon. The same prerparation procedure were followed along for MgO and LDH samples. A typical MgO SEM image looks as the one presented in Figure 2-19, showing the typical agglomerations of particles [192,193].

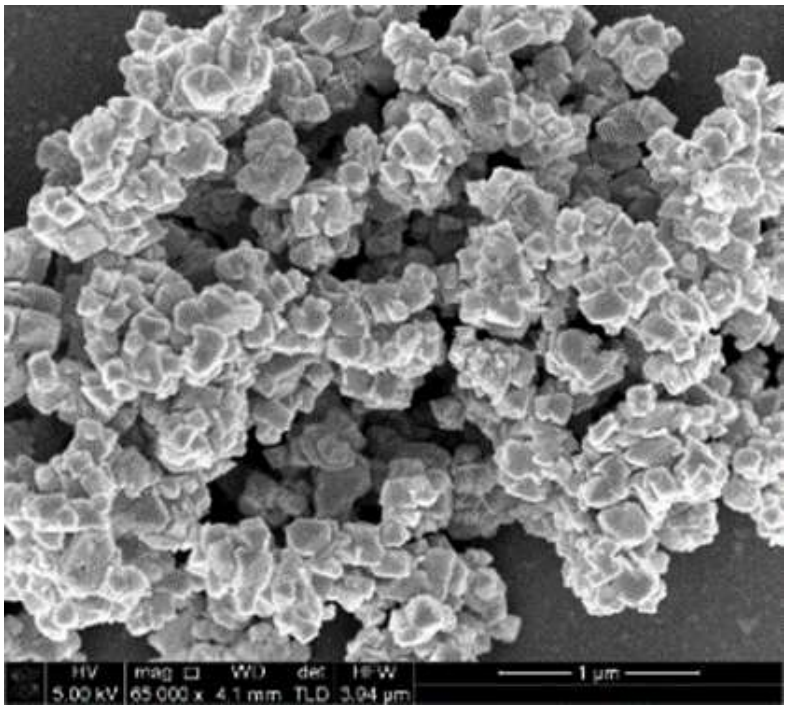

Figure 2-19. Scanning-electron microscopy image obtained from MgO particles. Agglomeration of the particles can be observed. Taken from experimental data in this work.

2.8.1 Transmission-Electron Microscopy (TEM)

Although sharing similarities with the SEM, the TEM technique provides more details of the inner structure from a material than what is usually obtained through SEM. The main difference between both techniques is that with SEM electrons are reflected from the sample whereas with TEM the transmitted electrons are the ones that create the image (i.e., the electrons that pass through the sample, allowing to obtain structural imaging and crystallography details of the sample [194,195]. An illustrated example of the TEM is shown in Figure 2-20.

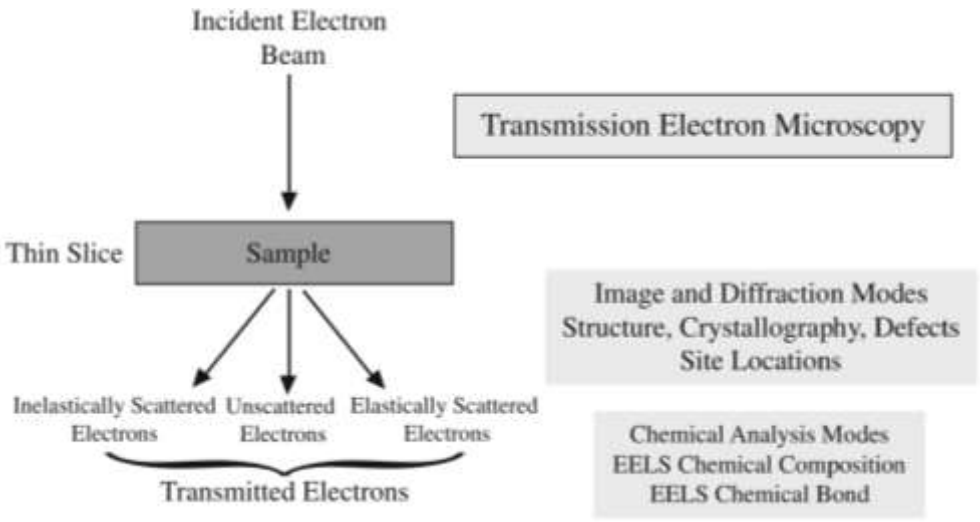

Figure 2-20. Diagram of the distribution of the signals resulting from a transmission-electron microscopy analysis. Taken with permission from Ayache *et al.,* [194].

Moreover, during TEM analysis, the sample needs to be thin (*ca* 200 nm) using a high voltage which can be in the range of the 80 to 200 keV[194,195]. In this study, the TEM experiments were performed using a bright field (BF) and high-angular annular dark field (HAADF-STEM) imaging technique in a FEI TITAN G2 80–300, microscope, which was operated at 300 kV, by Dr Ali Huerta-Flores, at Universidad Autonoma de Nuevo Leon, Mexico.

2.9 Spectroscopy in the ultraviolet and visible region (UV-Vis)

UV-Vis is a spectroscopy technique which allows the quantification of analytes of interest. Moreover, UV-Vis can also be used to perform optical characterisation of materials. The basic principle consists of the irradiation of electromagnetic rays, which will be further absorbed by an unknown sample dissolved within a cuvette. Then, the instrument (i.e., the UV-vis spectrophotometer) will measure (with the aid of the corresponding detector) and compare the intensity of the light before it passes through the cuvette containing the sample with the intensity of the light after it passed through the aforementioned cuvette [196,197]. A schematic representation is presented in Figure 2-21.

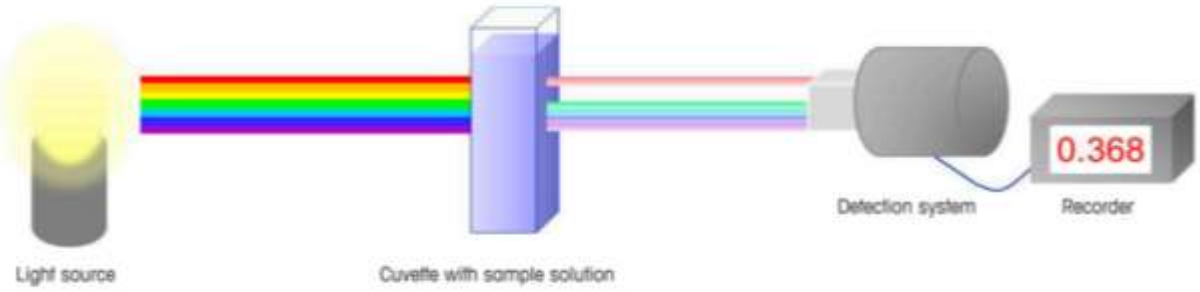

Figure 2-21. Functionality principle of the UV-vis spectroscopy analysis. Taken from De Caro and Claudia [196].

Based on the measurements from the light attenuation when passing through the cuvette, a relation between the latter attenuation of light, the particles within the cuvette and the path length of the cuvette. The name of such relationship is the Lambert-Beer law, which is the foundation of the light-absorption measurements [198] and corresponds to the following equation:

$$\boldsymbol{\varepsilon = \frac{A}{C*d}} \qquad 2.7$$

Where ε refers to the extinction coefficient, *d* to the path length of the cuvette, *c* the concentration of the analyte and *A* to the absorbance. Therefore, the absorbance can be

expressed as a function of the cuvette path length and the concentration of the analyte, as observed in Figure 2-22.

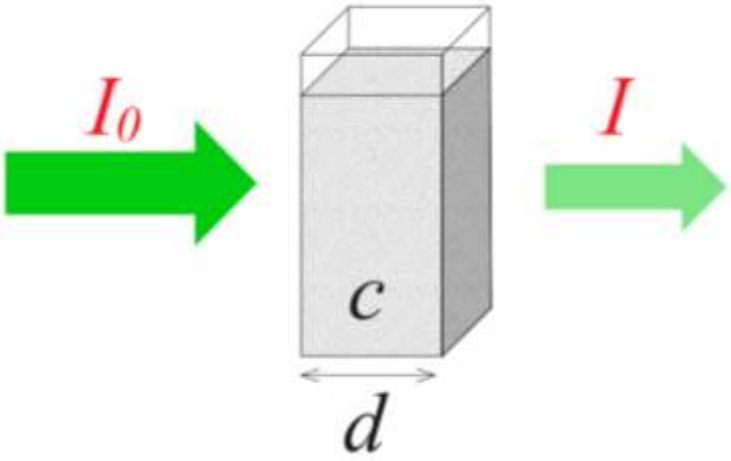

Figure 2-22. The relation between the light attenuation, the concentration of the analyte and the cuvette length. Taken from De Caro and Claudia [196].

The main parts of a spectrophotometer consist of a light source, a monochromator which is in charge of splitting the light into light's wavelengths and the usual range of the instrument to operate goes from 190 to 900 nm. The light passes through the sample and goes directly to the detector. Then, the instrument compares the intensity of the light that passed through the sample with the intensity of the light obtained with a blank. In most cases, the instrument has two lamps which serve as light sources. A deuterium lamp which emits in the ultraviolet wavelength and a tungsten lamp which emits in the visible range [197-199]. A conventional spectrophotometer configuration is shown in Figure 2-23.

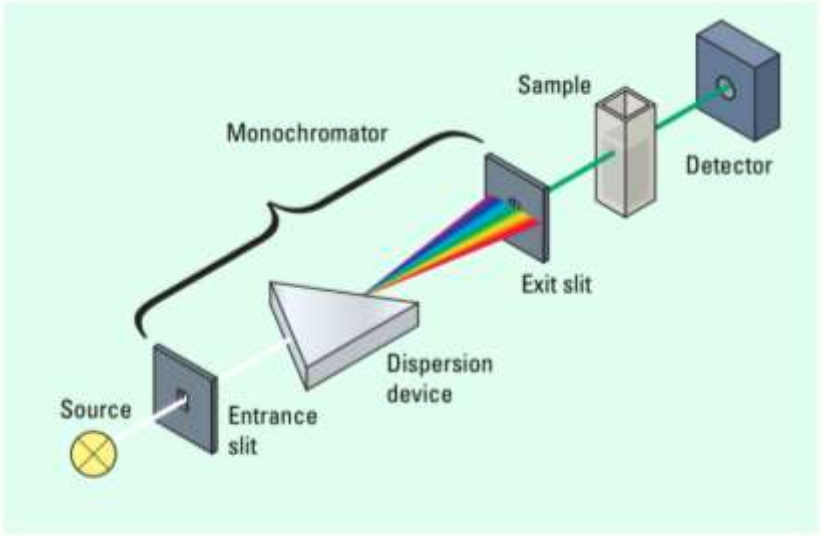

Figure 2-23. Schematic representation of a conventional spectrophotometer parts. Taken from De Caro and Claudia [196].

In this study, UV-Vis analysis was performed in Chapter 6, as the use of an LDH as photocatalyst was explored. The instrument used for such analysis was a UV-vis NIR spectrophotometer (Cary 5000), setting the wavelength range from 200 nm to 800 nm. The simples were optically characterised through UV-vis but also through photoluminescence. Considered a routine characterisation tool for materials, usually for semiconductors, photoluminescence is used to give insights regarding the bandgap of the material. Due to the intrinsic characteristic of LDH materials, semiconductor characterisation such as photoluminescence can be applied to them. In a simple photoluminescence experiment, light directed into a sample will be absorbed to excite the electrons, which will move from the one energy state to a different one. When returned to ground state, the electrons will release energy in the form of light which equals the energy difference between the ground state and the excited state [200,201]. In this work and also for Chapter 6, a fluorescence spectrophotometer (Cary Eclipse) was used. The latter spectrophotometer is integrated with a Xenon flash lamp. The width of excitation as well as the emission slit were both 5 nm. A photoluminescence plot is shown in Figure 2-24.

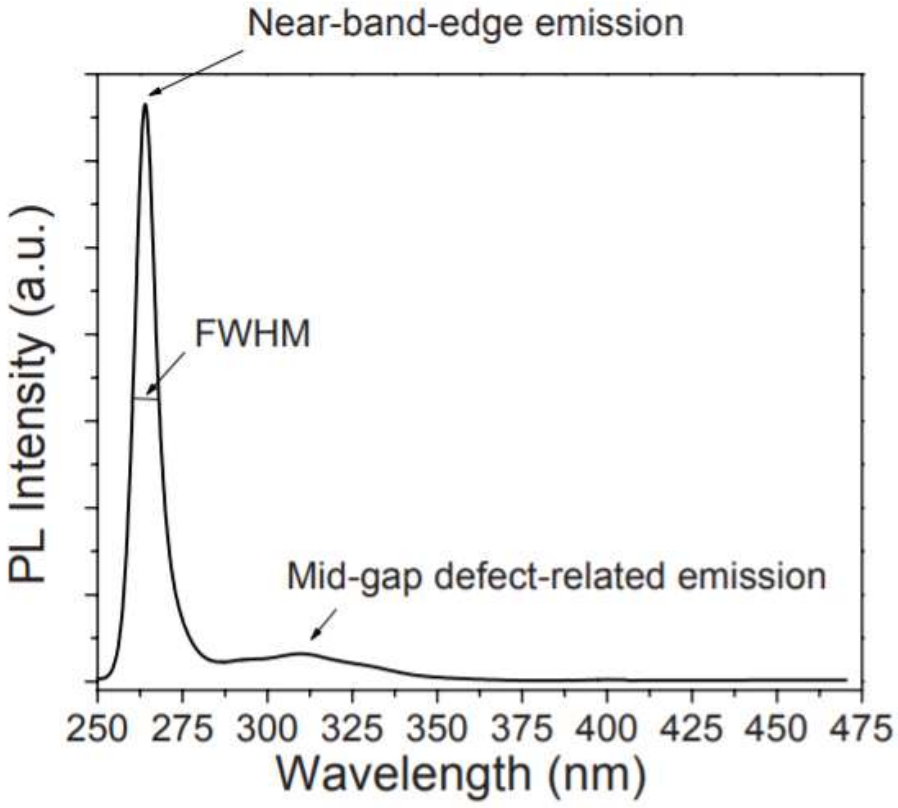

Figure 2-24. A photoluminescence plot from an AlGaN sample. A peak of relative high intensity can be observed mostly due to the band-edge emission. Taken from with permission of Razeghi [202].

2.10 Using the Parr Autoclave for the ketonic decarboxylation reactions

To perform the ketonic decarboxylation experiments in this study (Chapter 3 and Chapter 4) a Parr autoclave was employed. In a typical ketonic decarboxylation reaction performed in this study, the catalyst used (either LDHs or MgO) as well as the reactants used, and the solvent were put inside a Parr Autoclave (0.075 L). Once all the materials were inside the autoclave, it was sealed and further purged with N2 several times. The N2 pressure was up to 10 bars to 15 bars. Once the pressure was raised to the latter 15 bars, it was released so the manometer goes back to zero. Subsequently, the autoclave was heated up to a temperature range varying between 250 to 300 °C to yield a crude post-reaction mixture that also had to be analysed. The autoclave was left to react over the period of one hour and automatically stopped until the autoclave cooled down, naturally, for a period of 3 hours, until reaching room temperature. The crude-post reaction mixture could be extracted. The latter experimental procedure was executed within the control room in the High-Pressure lab in the chemistry department, at Durham University. Figure 2-25 shows the autoclave connected prior the starting the heating ramp. The Parr Autoclave was mainly used during the development of Chapter 3, Chapter 4 and Chapter 5. In a typical experiment performing the ketonic decarboxylation inside the Parr Autoclave, 2 mmol of the carboxylic acids that were decided to be used (i.e., dodecanoic acid, hexanoic acid, pivalic acid, etc) were weighted and the corresponding number of catalysts (i.e., MgO or LDH) with respect the carboxylic acid in %wt. (i.e., 1 %wt., 3 %wt., 5% wt. or 10% wt.) was also weighted. Both, carboxylic acid and catalyst were added into the Parr reactor, with a subsequent addition of solvent, and further sealed to put it to react at the desired temperatures. The detailed procedure of the ketonic decarboxylation reaction was further explained in Chapter 3, Chapter 4 and Chapter 5.

Figure 2-25. Parr autoclave set up prior reaction

2.11 Preparation of Layered-Double Hydroxides (LDH) materials through co-precipitation

The co-precipitation methodology was the synthesis technique used in this study to prepare the all the LDH materials presented in this work. As already explored in Chapter 1, Section 1.8, LDHs can be prepared using different techniques such as co-hydration, ion-exchange or co-precipitation. In a co-precipitation experiment a solution containing the dissolved precursors containing the M^{II} and the M^{III} in the desired stoichiometric ratio would be added dropwise into a solution containing an excess of the desired anion that wants to be incorporated in the interlayer of the material, at low-supersaturation conditions, keeping the pH constant (depending on the desired LDH to be synthesized, the constant pH can be set to different ranges) through the addition (dropwise as well) of a solution of NaOH. The temperature needs to be constant (~65˚C to 75˚C) and the stirring high and constant as well [103,203]. LDHs were prepared and used in Chapter 5, Chapter 6 and Chapter 7, with further details about the synthesis of each particular LDH described in the corresponding chapters.

3. Promoting ketonic decarboxylation of dodecanoic acid with magnesium oxide: The key role of temperature

3.1 Introduction

Among renewable energy sources and sustainable provision of chemical feedstocks, biomass plays an important role. To date, biomass contributes to the production of 2 million barrels a day of transportation fuels and to 14% of the world's primary energy demand [3,204]. Biomass is thus key to the search for a more sustainable infrastructure for the future that helps to reduce dependence on fossil fuel derivatives as well as meeting demands from society in terms of green energy. Although generally referring to organic matter coming from plants, biomass can be subdivided into wastes (e.g., agricultural production wastes, crop residues, urban organic wastes), forest products (e.g., wood, trees, shrubs, wood residues from forest cleanings) and energy crops (e.g. starch crops, sugar crops, oilseed crops). The most important drawback of using biomass as an energy source compared to fossil fuels is its low heating value, making it less suitable for direct application for primary energy production. However, due to its high ignition stability and sustainability, biomass can be easily processed using thermochemical approaches and converted into higher value fuels [204]. Different strategies are also being studied to transform biomass-derived oils and sugars into commodity chemicals [3]. One class of thermochemical transformation routes for biomass-derived oils are the deoxygenation reactions, in which oxygenated compounds (e.g., biodiesel, pyrolysis oils and fatty acids) are converted into higher energy density fuels. These reactions include decarboxylation, decarbonylation and hydro-deoxygenation, with the latter the most expensive in terms of energy requirements and the only one that involves hydrogen [64,65,205]. Ketonic decarboxylation (i.e. ketonisation) is a deoxygenation reaction widely studied over the last decades, although the reaction mechanism has yet to be fully determined. Increasing carbon chain length while removing oxygen in the form of carbon dioxide and water, the reaction proceeds as follows:

$$R_1\,COOH + R_2COOH \rightarrow R_1COR_2 + CO_2 + H_2O \quad 3.1$$

The reaction mechanism for ketonic decarboxylation has been studied extensively in recent years, as well as the behaviour of different catalysts and substrates under different conditions [16,81-83,95,98,148,206,207]. In a recent study, [102] ketonisation of stearic acid in the liquid phase was explored using solid mixed metal hydroxides/oxides catalyst with promising results. The catalysts used were layered double hydroxides (LDHs) and the respective mixed metal oxides (MMOs) obtained from LDHs after calcination. Yields of the ketonisation product from stearic acid (i.e., stearone) of up to 90% were obtained using the LDH at relatively moderate reaction temperatures (250 °C). The corresponding MMOs also exhibited a ketone yield of 80%. In this initial study the feed to catalyst ratio was high (20% wt.) and the effects of varying key parameters were not explored. In this study, a different catalyst has been used for the ketonisation reactions. In our earlier study, we used MgO as a control against the LDH and it was shown to also possess activity for the ketonisation reaction [19]. Due to its strong basic properties, magnesium oxide (MgO) is used here as the heterogeneous catalyst. Following the findings from our last study, moderate to high reaction temperatures are explored, as well as the impact of varying the catalyst to feed ratio. In addition, the effect of the particle size of the catalyst on the production of the ketones was explored using three different sizes, two in the range of the nano-size (100 nm and 50 nm) and a third one within the μm range. Through evaluating the effect of particle size, and hence surface area, whether the reaction was controlled by surface reactive site availability could be probed. The effect of particle size on intrinsic reactivity of the MgO is also studied through analysis of basic site strength and distribution.

3.2 Experimental

All chemicals and reagents were used as received from commercial sources, without any further purification: magnesium oxide 100 nm (Alfa Aesar, 99%), magnesium oxide -325 mesh (44 μm, Alfa Aesar, 98%), magnesium oxide 50 nm (Sigma-Aldrich, 99%), dodecanoic acid (TCI, 98%) and toluene (Fischer, analytical-grade 99%). All the characterisation techniques employed to characterise the MgO powders used in this section of the study have been explained in further details in Chapter 2, however, a brief description of the instruments and techniques employed are also provided below.

3.2.1 Catalyst characterization

The catalysts were characterised through Powder X-ray Diffraction (PXRD), Fourier Transform Infrared (FTIR) Spectroscopy, Thermogravimetric Analysis (TGA), N2 adsorption and desorption measurements, Scanning- Electron Microscopy (SEM) and Temperature Programmed desorption (TPD) as described in Chapter 2, for each of the characterization techniques employed in this chapter. The TPD plots were put in Figure 3-5. The rest of the figures were added into Section 3.3.1.

3.2.2 Ketonic decarboxylation reaction procedure

0.4004 g (2 mmol) of dodecanoic acid (TCI, 98%) were reacted at temperatures ranging from 250 to 300 °C with different catalyst loads of each of the different MgO samples. The amount of catalyst used was varied between 5, 3 and 1% wt., with respect to the feed of dodecanoic acid. The different samples were named using the letters UR as a prefix on the name to refer to the as-received un-reacted MgO powder. MgO 325 mesh (as-received, un-reacted MgO micron size: URMgO micro), MgO 100 nm (as-received, un-reacted MgO 100 nm size: URMgO 100 nm) and MgO 50 nm (as-received, un-reacted MgO 50 nm size: URMgO 50 nm). The carboxylic acid as well as the catalyst were put inside an autoclave (0.075 L Parr) using toluene (20 ml) as solvent (analytical grade, Fischer chemicals). Once sealed, the autoclave was purged with nitrogen four times to remove any trace of oxygen. Afterwards, the autoclave was heated up to the desired temperature and left to react for one hour. Once the reaction time was over, the vessel was left to cool down and, once at room temperature, the crude product mixture was extracted. Further details about the autoclave use, see Chapter 2, Section 2.10.

Analysis of crude product

The extracted crude product was put into a 50 ml Falcon tube and centrifuged using a Beckman Coulter Avanti J-20XP centrifuge (1000 rpm, 30 min) to separate the solid catalyst. Catalyst material, spun to the bottom of the tube, was recovered to be further analysed using PXRD and FTIR spectroscopy. Afterwards, the crude product was analysed using a Shimadzu GC- 2010 instrument with a flame ionisation detector (FID) with a HP-5 30M length column, of 0.25 mm internal diameter and 0.25-micron film thickness coating. Before injection, a calibration curve using the internal standard method for the expected ketone was employed to perform the quantitative analysis (Appendix A, Figure A-1).

Analysis of the MgO powders

For the spent catalyst (used for reaction at 300 °C), the letter S was used as a prefix before the name of the different spent MgO powders. MgO 325 mesh (spent MgO micron size: SMgO micro), MgO 100 nm (spent MgO 100 nm size: SMgO 100 nm) and MgO 50 nm (spent MgO 50 nm size: SMgO 50 nm). The spent catalyst from the 300 °C reactions, for all the different particle sizes, was recovered by centrifugation. The samples were filtered to recover the wet catalyst, which was subsequently dried at room temperature for 1 hour and put inside an oven at 70 °C for 12 hours. Following this, the samples were put under high vacuum for 4 hours to remove any trace of the toluene solvent. In order to determine the relative sorption of the dodecanoic acid on to the catalyst, the as-received MgO powders in all the different particle sizes, (named URMgO), were contacted with dodecanoic acid dissolved in toluene using the exact same conditions as when the dodecanoic acid, catalyst and toluene were put inside the autoclave. Concentration of the dissolved dodecanoic acid was 0.1 M. The reaction proceeded at room temperature and at a stirring speed of 500 rpm for 12 hours. After completion, the samples were separated following the same methodology as the one mentioned above for the SMgO. These room temperature samples were named with the letters RT as a prefix before the name of each MgO sample. MgO 325 mesh (44 μm; MgO micron size: RTMgO micro), MgO 100 nm (MgO 100 nm size: RTMgO 100 nm) and MgO 50 nm (MgO 50 nm size: RTMgO 50 nm). The SMgO samples, as along with the RTMgO and URMgO samples, were analysed by TGA, PXRD and FTIR. For further description of the instrumentation used, refer to Chapter 2.

3.2.3 Preparation and analysis of magnesium dodecanoate

As a potential reaction byproduct analytical standard, and surface species on the MgO, magnesium dodecanoate (Mg dodecanoate) was prepared following a methodology described elsewhere [208]. 10 g of dodecanoic acid (50 mmol) and 60 ml of water were heated and stirred inside a round-bottom flask in a bath at 80 °C until dodecanoic acid fully melted. Excess sodium hydroxide (NaOH, 100 mmol, 4 g) was added to the round bottom flask and leave it to react for 90 minutes. 10.1 g of $MgCl_2$ (50 mmol) was added to the sodium dodecanoate slurry and left to stir over 60 minutes. Once the reaction was completed, sample was collected and washed with plenty of water and ethanol and left to dry at 70 °C for 12 hours. Magnesium dodecanoate was characterised through FTIR and PXRD.

3.3 Results

3.3.1 Magnesium oxide characterisation

The PXRD patters for the URMgO, RTMgO and the SMgO samples are shown in Figure 3-1 respectively. Moreover, the peak width (FWHM) was calculated for all samples (Table 3-1) based on the strongest diffraction peak (200), *ca* 43.03 °.

Table 3-1. Full witdh at half maximum (FWHM) for all the MgO samples. Note that almost the same values of FWHM can be observed for the spent catalyst.

FWHM	Sample
0.257	URMgO micro
0.744	URMgO 100 nm
0.224	URMgO 50 nm
0.168	RTMgO micro
0.688	RTMgO 100 nm
0.215	RTMgO 50 nm
0.268	SMgO micro
0.265	SMgO 100 nm
0.239	STMgO 50 nm

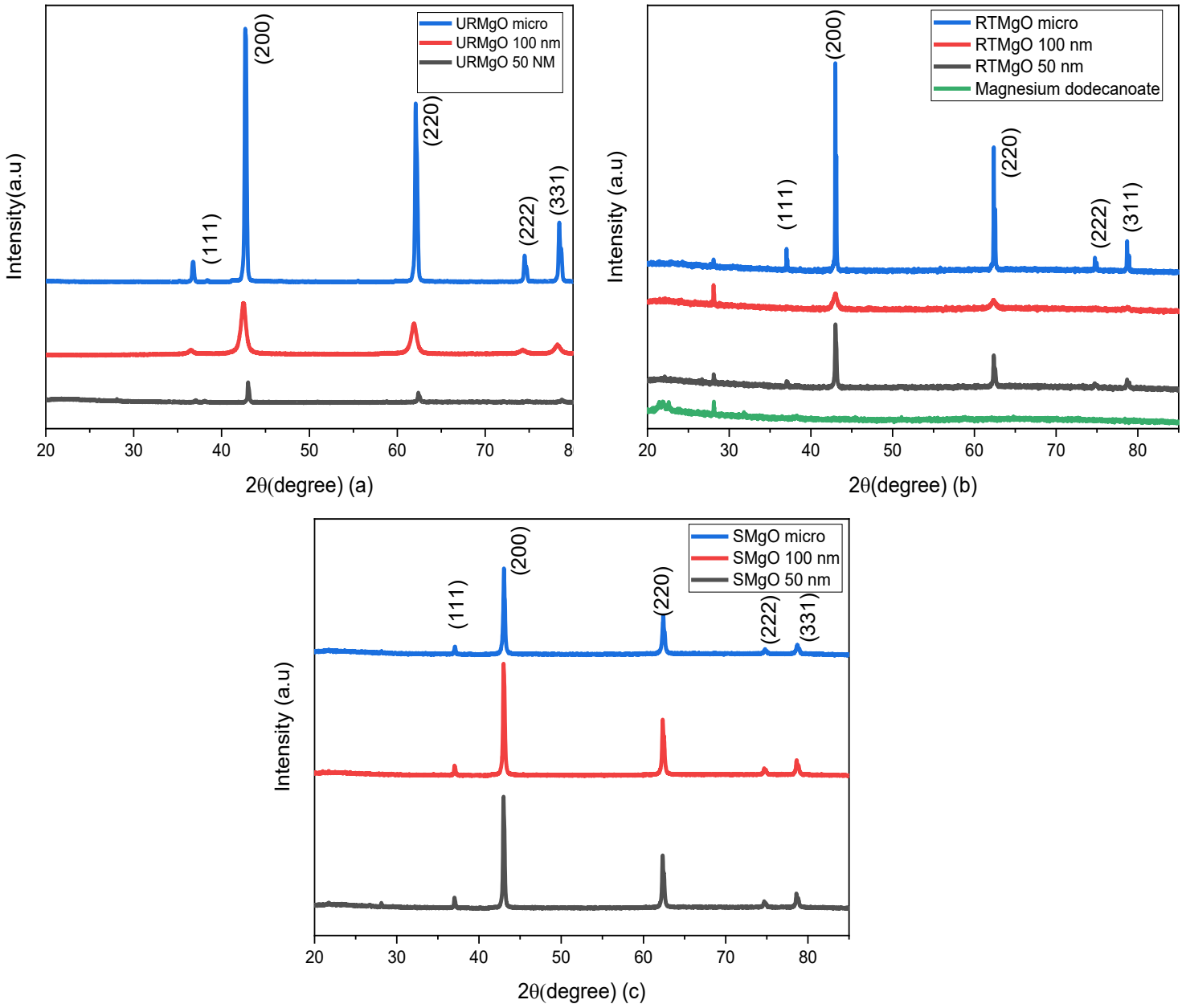

Figure 3-1. Powder X-ray Diffraction patterns of the different size MgO samples. Figure 3-1(a) refers to the as received MgO samples (URMgO). Figure 3-1(b) refers to the MgO samples exposed to the dissolved dodecanoic acid for 12 hours (RTMgO) and Figure 3-1(c) shows the diffraction patterns for the spent MgO.

Analysing Figure 3-1, typical sharp peaks referring to a cubic phase of MgO can be observed *ca* 43 °, 62 ° and 74°, for all the samples [209,210]. However, for the MgO samples contacted with dodecanoic acid (RTMgO), an extra peak, at *ca* 28 ° can be observed. The peak may arise owing to the formation of magnesium dodecanoate [210]. As a point of comparison, the plot corresponding to the diffraction of the Mg dodecanoate is given in Figure 3-1(b), which seem to support the latter statement, as the same peak *ca* 28 ° is observed for the Mg dodecanoate sample. As the PXRD patterns from the RTMgO samples and the SMgO ones are otherwise similar to the URMgO, complete change in the bulk structure can be discarded. Nevertheless, and as seen in Figure 3-1(c), the SMgO samples present almost the same intensity principle XRD reflections across the three different particle sizes, also observed in Table 3-1, where the FWHM for the latter samples are almost equal to one another. This is a possible indicative of recrystallisation of the MgO at the reaction temperature of 300 ° C, as the crystallite domain size increase is dependent of the FWHM, according to the Scherrer equation [211,212]. The FTIR spectra from URMgO, SMgO and RTMgO samples are shown in Figure 3-2.

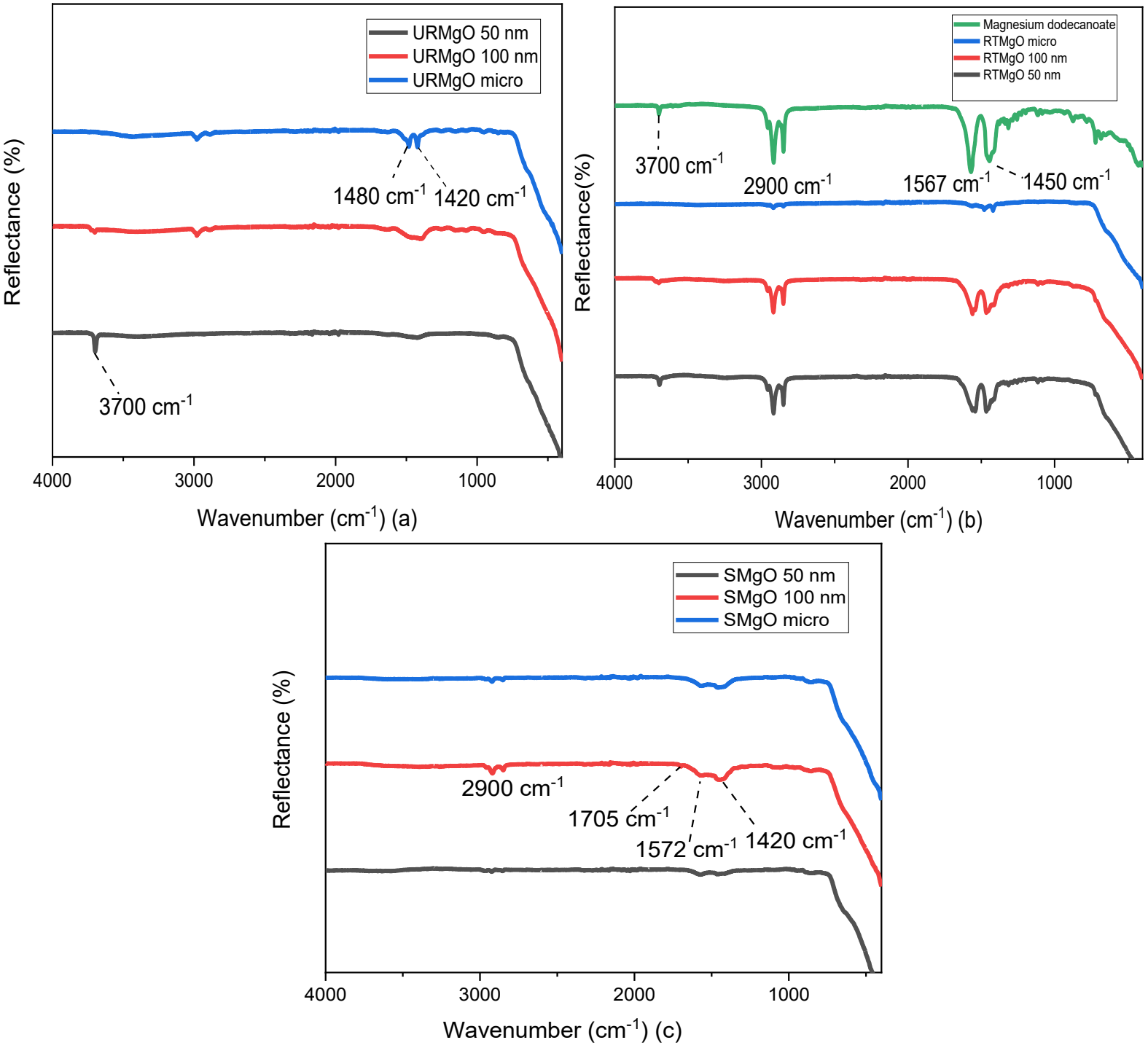

Figure 3-2. The Fourier Transformed Infra-red spectra of the URMgO, RTMgO and SMgO shown in Figures 3-2(a), 3-2(b) and 3-2(c), respectively. Figure 3-2(a) is the evaluation of the catalyst as received, whereas Figure 3-2(b) shows the catalyst after exposition with dodecanoic acid. Figure 3-2(c) is the analysis of the post reaction MgO.

The characteristic vibration of the Mg-O bond is exhibited with a broad shoulder from around 470 cm^{-1} [213] for all samples. For the URMgO samples (Figure 3-2(a)), some amount of adsorbed atmospheric water is present in the form of rehydrated $Mg(OH)_2$, with a clear peak at 3700 cm^{-1} for all three samples [214]. Thus, the presence of peaks related to adsorbed atmospheric CO_2 are observed around 1417 – 1420 cm^{-1} for the symmetric stretching of monodentate carbonate species, whereas other peaks can be encountered within the range of 1410 to 1480 cm^{-1}. Those are assigned to the symmetric stretching of the bicarbonate species [215]. In the case of the RTMgO samples, the spectra of the magnesium dodecanoate was added to the ones of the MgO, to be used as a point of comparison and to evaluate the formation of the carboxylate species over the surface of the material. As can be observed in Figure 3-2(b), specifically for the magnesium dodecanoate curve, the sharp peaks at 1567 and 1450 cm^{-1} could be assigned to the antisymmetric and symmetric stretching of the COO bonds [216]. These stretching bands were also observed on all three RTMgO samples, indicating that the carboxylate species adsorbed over the surface of the catalyst. Moreover, the presence of stretching of the C-H bonds can be observed, which are usually encountered at around 2900 cm^{-1} [217]. A small 3700 cm^{-1} peak can be observed for all the samples Figure 3-2(b), related to the presence of brucite (i.e., $Mg(OH_2)$) in the material, as the stretching vibration of the O-H is characteristic at 3700 cm^{-1}. The samples corresponding to the SMgO (Figure 3-2(c)) show small peaks at 1705 cm^{-1} and a broader one at 1572 cm^{-1}, associated to the stretching of the CO bonds [86,218,219]. Another set of small peaks from 1460 to 1420 cm^{-1} associated to the stretching of the C-H bonds, as well as the vibration of the C-O and C-C bonds, are present. No brucite was observed by FTIR in the SMgO samples, suggesting the temperature was sufficient to drive dehydroxylation. Several TGA analysis were performed for all the catalyst samples. The results are shown in Figure 3-3.

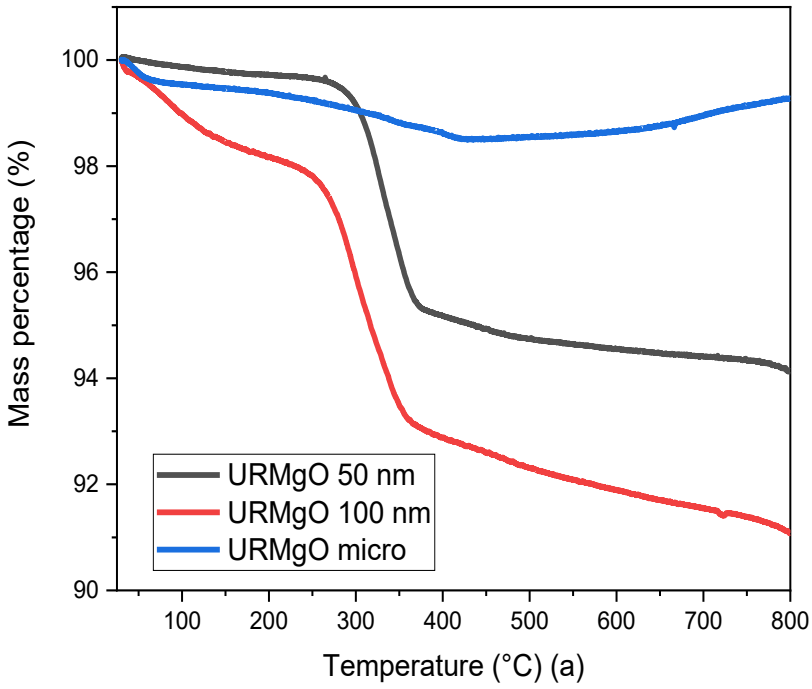

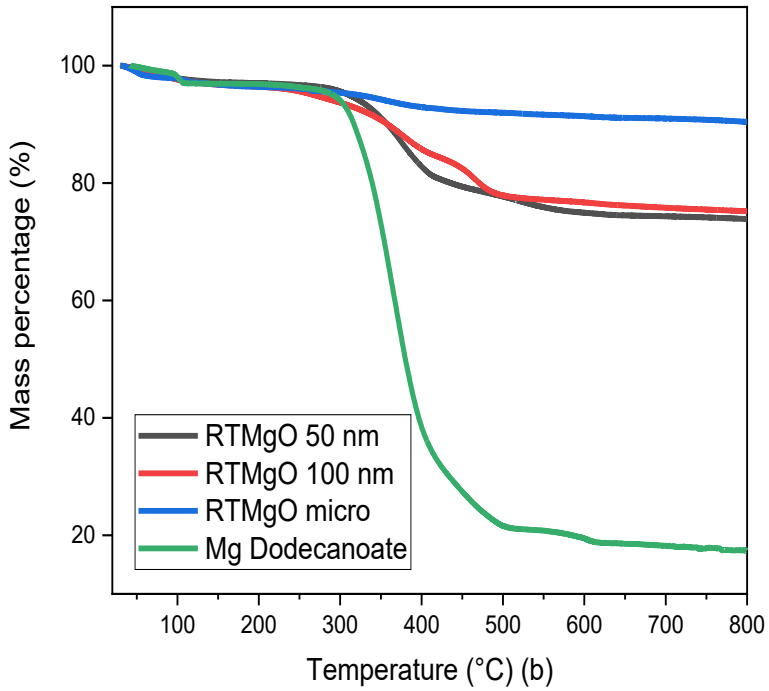

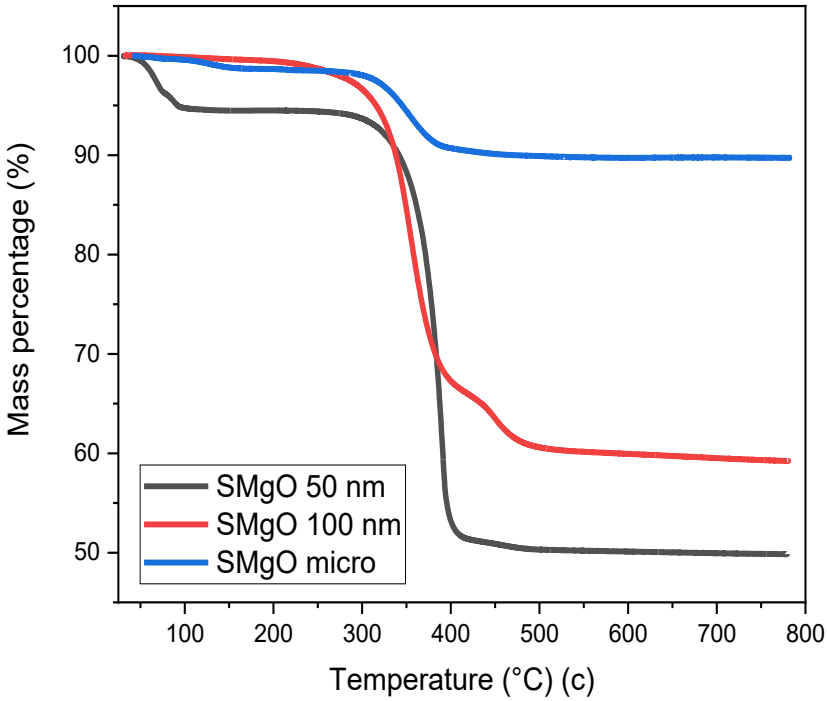

Figure 3-3. Thermogravimetric analysis graphs for all the MgO samples. Figure 3-3(a) is for URMgO, whereas Figure 3-3(b) and Figure 3(c) are for RTMgO and SMgO respectively.

Although URMgO samples showed almost no presence of adsorbed atmospheric water, the presence of rehydrated $Mg(OH)_2$ is clear, as well as the presence of some adsorbed atmospheric CO_2, with the latter confirmed by FTIR in Figure 3-2(a) and by TGA, as observed in Figure 3-3(a). A clear dehydroxylation (loss of the $Mg(OH)_2$) species is observed around 270 ℃ [114,132], followed by decarbonylation [114,220], causing a mass loss of up to 9 %. Figure 3-3(b) shows a clear two-step decomposition for the RTMgO samples. The first step could be attributed to dehydroxylation of the $Mg(OH)_2$ species, followed by decomposition of the carboxylate species 290 ℃ up to 400 ℃ [220,221]. The TGA curve of Mg dodecanoate shows a similar behavior to the rest of the RTMgO samples, supporting the idea that the reaction requires sorption of the acid as an initial step. For RTMgO 100 nm, a small shoulder around 450 ℃ is observed, which could be attributed to some $MgCO_3$ species formed due to the contact of the sample with environmental CO_2. Subsequent degradation could be attributed to the complete decarbonylation of the catalyst, losing the carbonate to fully convert again into a metal oxide [220,221]. Figure 3-3(c) shows a one-step decomposition for SMgO samples, which could be attributed to the presence of adsorbed post-reaction ketone as observed in Figure 3-2(c), being completely removed from the catalyst once 400 ℃ is reached. Thus, no, or negligible, presence of Mg(OH)2 was observed in the samples, as presented by Figure 3-2(c), which then implies no dehydroxylation occurs. The surface area and pore analysis results are presented for the all the URMgO samples in Table 3-2. Nitrogen adsorption/desorption isotherms as well as the pore size distribution plots are shown in Figure 3-4.

Table 3-2. Specific surface area and pore volume and pore radius obtained for the URMgO samples.

Sample	**Surface area (m^2g^{-1})**	**Pore volume (cm^3g^{-1})**	**Pore radius (nm)**
URMgO micro	3.5	0.003	8.7
URMgO 100 nm	60.4	0.11	3.6
URMgO 50 nm	46.2	0.05	5.3

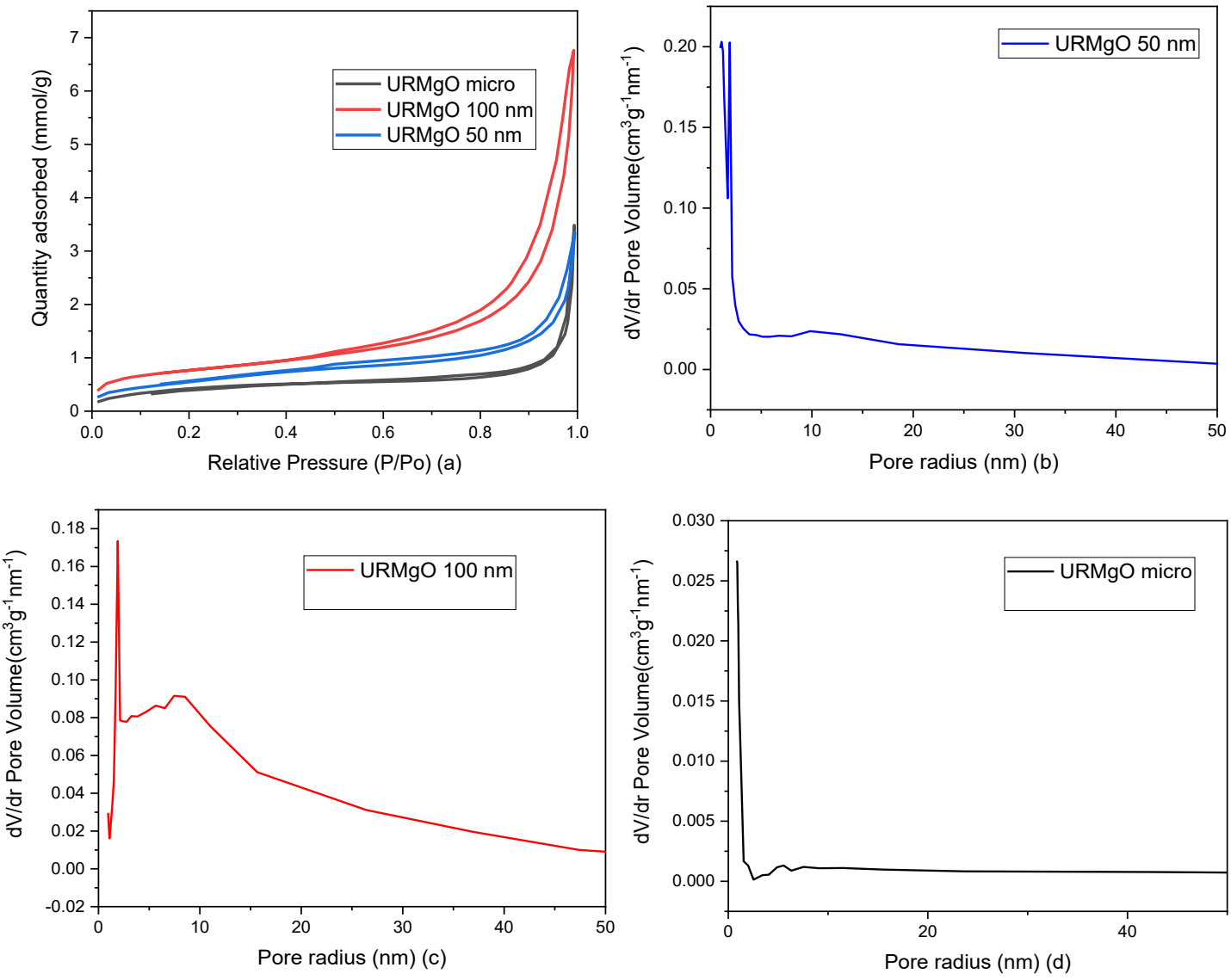

Figure 3-4. (a) Nitrogen adsorption/desorption isotherms for the URMgO samples and (b) pore size distribution of URMgO samples.

TPD analysis of the URMgO samples are shown in Figure 3-5. The behaviour of the material regarding the desorption of the CO_2 molecules did not favour the quantification of the active sites, as neither the derivative of the TGA could be calculated, nor the mass loss due to desorption. The SEM characterisation of the three URMgO samples is shown in Figure 3-6 URMgO 50 nm, URMgO 100 nm and URMgO micro corresponds to Figure 3-6(a), Figure 3-6(b) and Figure 3-6(c), respectively.

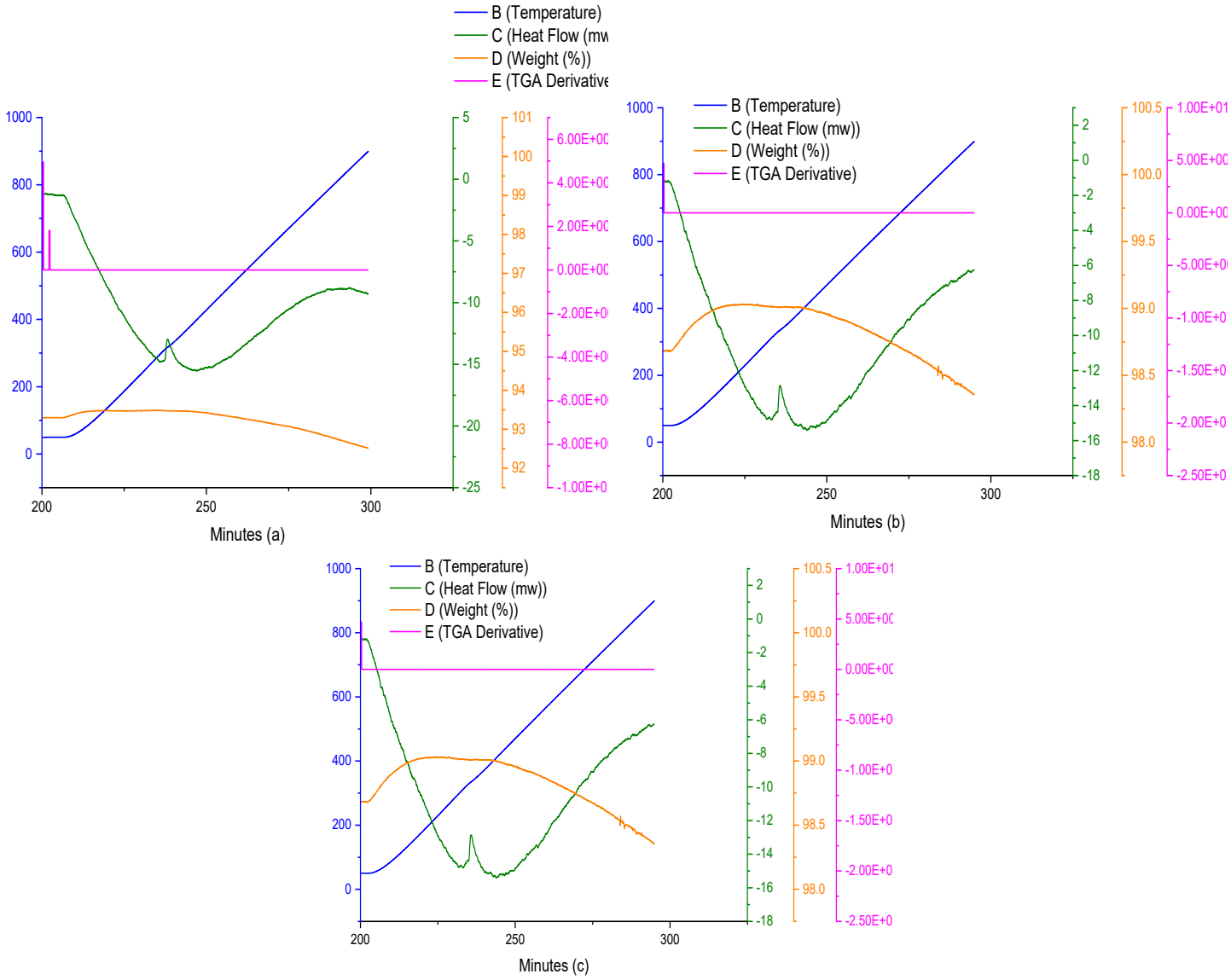

Figure 3-5. Temperature-programmed desorption curves from the URMgO samples. Figure 3-5(a) represents URMgO 50 nm, whereas URMgO 100 nm and URMgO micro are Figure 3-5(b) and Figure 3-5(c), respectively.

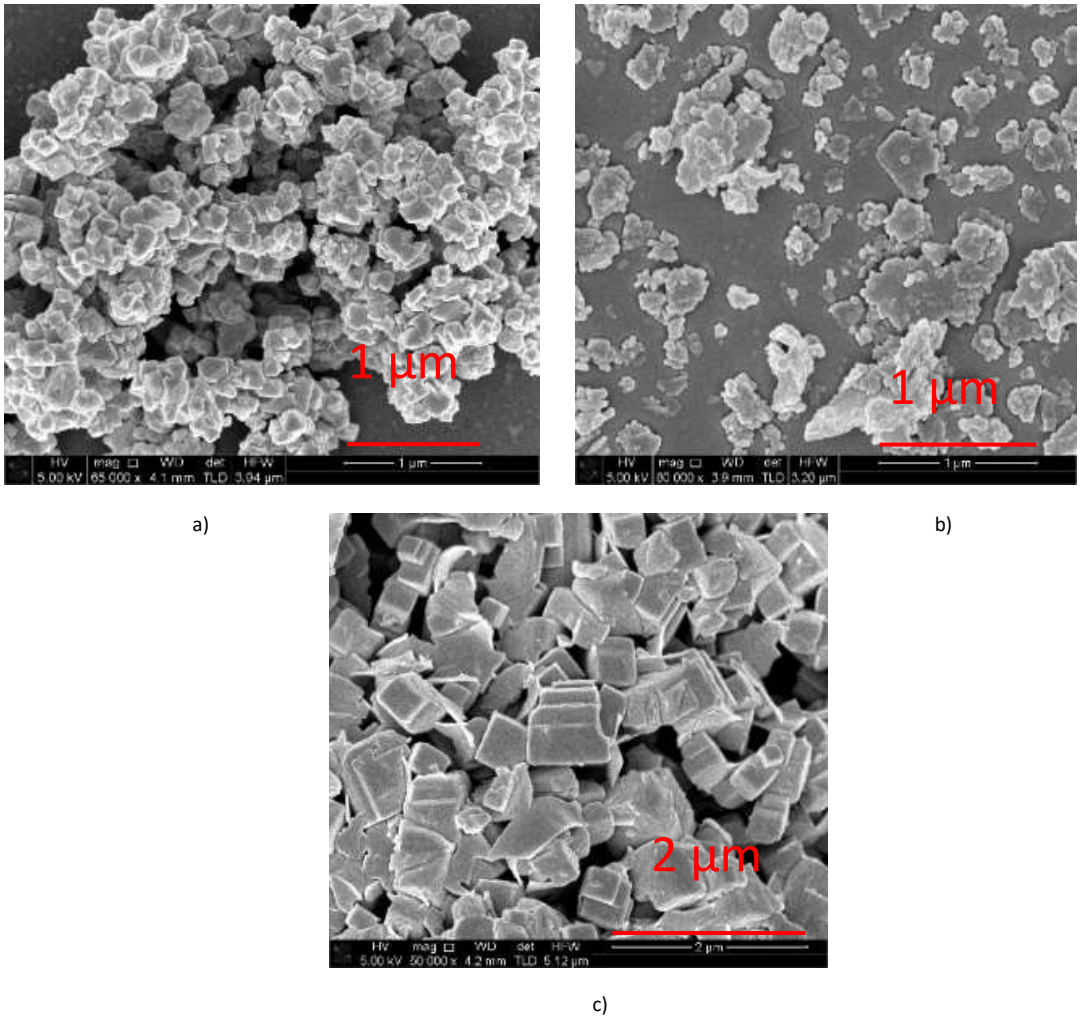

Figure 3-6. Scanning electron microscopy images of the different URMgO samples. More plate like aggregates can be observed for the nano sized materials (a) URMgO 50 nm and b) URMgO 100 nm) whereas the micro size (c) URMgO micro) MgO presented the cubic particle morphology.

Agglomeration of the particles can be observed for all the three samples, being the agglomeration more evident with the URMgO 50 nm and URMgO 100 nm, which also have clusters of spherical-like particles, whereas URMgO micro have a more cubic-like particle morphology.

3.3.2 Magnesium oxide as catalyst for the ketonic decarboxylation of dodecanoic acid

The ketonic decarboxylation of dodecanoic acid was performed using different catalyst loads (1% w/w, 3% w/w and 5% w/w relative to the reactant) of the as received MgO samples. The ketone yields produced by MgO 50 nm, MgO 100 nm and MgO micro are given in Figure 3-7(a), Figure 3-7(b) and Figure 3-7(c), respectively. The reaction time was set to be a one-hour reaction, as some experiments with higher reaction times (i.e., 12 hours and 6 hours show that the ketone yield did not vary significantly) trying to obtain the highest yield of ketone possible using the shortest reaction time possible. Moreover, different temperatures were tested for this study, setting the reaction at 250 °C, 280 °C and to 300 °C. All experiments were performed in triplicate. Figure 3-7 shows that increasing the temperature resulted in increased yield for all the MgO particle sizes. It is also evident that the difference in particle sizes from all MgO samples are not impacting greatly the yield of ketone at the optimal temperature of 300 °C. Interestingly, the ketone yield remains the same for all catalyst loadings at 300 °C. The three different particle sizes yield similar results, irrespective of the particle surface area (Table 3-2) or the crystallite domain size of the starting material (URMgO), as given in Table 3-1. It is important to notice that as no other product peak was observed during the post reaction analysis of the crude product mixture, selectivity towards the desired ketone product, 12-tricosanone, was assumed.

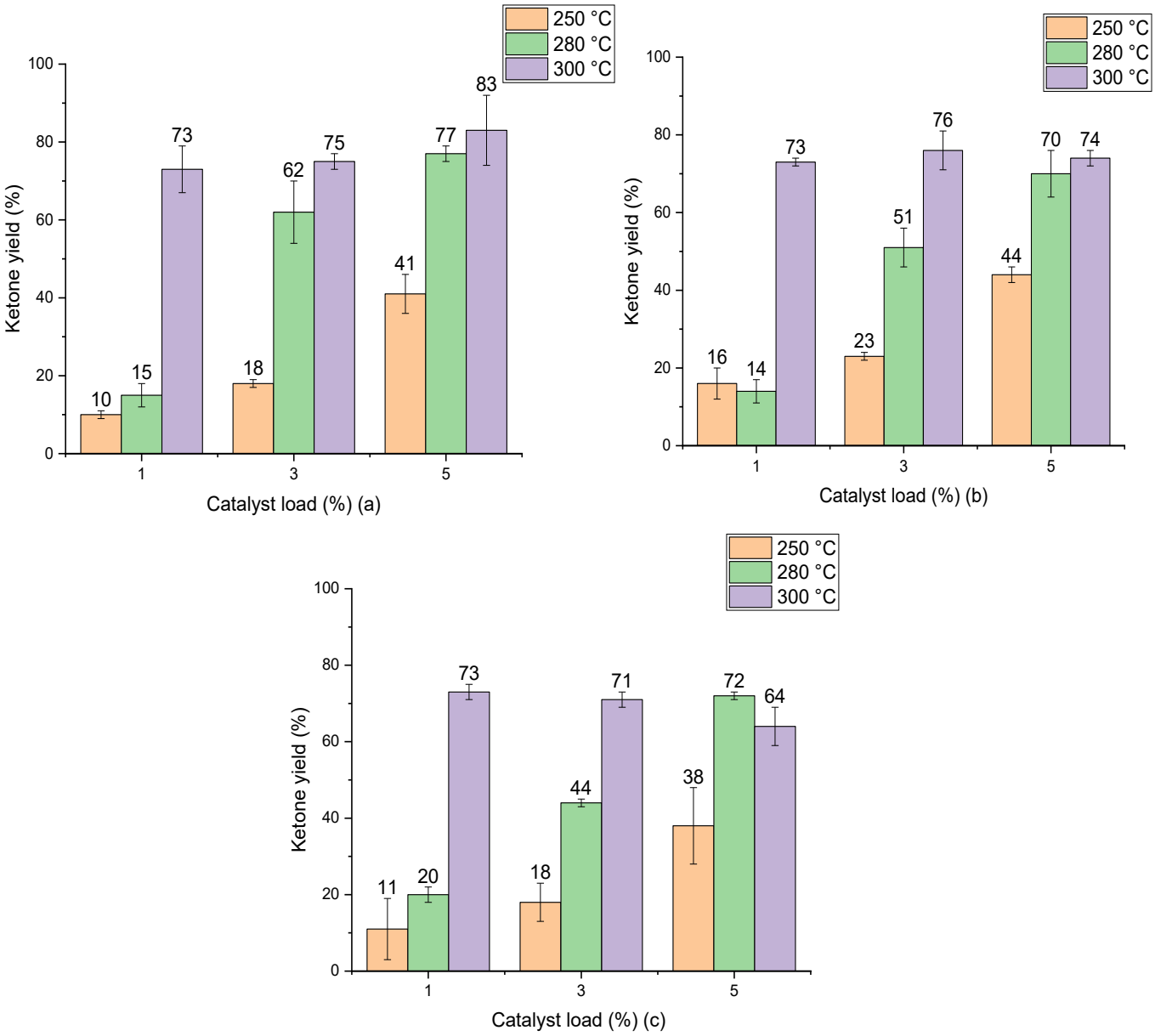

Figure 3-7. Ketone yield (12-tricosanone) product of ketonic decarboxylation of dodecanoic acid using the different catalyst samples. (a) shows the results from the URMgO 50 nm. (b) represents URMgO 100 nm and (c) represents URMgO micro. All samples shown a similar yield trend, and although the highest production was of 83 % in (c), the differences from one another at different particles sizes are not high enough to assume the particle size could be making a significant impact to the yield.

3.4 Discussion

In this section, analysis of the production of 12-tricosanone from dodecanoic acid through the reaction of ketonic decarboxylation using MgO of different particle sizes as the catalyst to promote the reaction was performed. First, the characterisation of the different catalyst samples (URMgO, RTMgO and SMgO) was discussed to further move towards the evaluation of different reaction parameters (e.g., temperature, catalyst load and particle size).

3.4.1 Characterisation of the MgO catalysts at different process stages

URMgO materials. XRD analysis of the URMgO show sharp and intense reflection corresponding to the MgO structure (Figure 3-1(a)). URMgO-100 also shows some secondary reflections at *ca* 38° and 59° two theta, which closely correspond with the more intense brucite ($Mg(OH)_2$) reflections [222]. The as received URMgO samples of different sizes, and particularly notable in the FTIR analysis (Figure 3-2(a)) for URMgO 100 nm and URMgO micro, showed the presence of some adsorbed CO_2, as carbonate, at *ca* 1410 cm^{-1} to 1480 cm^{-1}, related to the symmetric stretching of monodentate and bidentate species [213]. Though no strong water adsorption peak is observed at *ca* 3500 cm^{-1}, the brucite characteristic peak at *ca* 3700 cm^{-1} is also observed in Figure 3-2(a). This is clear indication of some rehydration to $Mg(OH)_2$. The latter was further investigated using the TGA analysis, given in Figure 3-3(a), which showed little surface bound water, with < 1% for URMgO micro and URMgO 50 nm, and slightly more (~2% mass) water on URMgO 100 nm. TGA analysis also evidenced the existence of some brucite phase in the starting material at the smaller particle sizes, with both URMgO 50 nm and URMgO 100 nm showing characteristic losses through dehydroxylation at an onset temperature of *ca* 280 °C. At above this temperature, all materials showed a small 1-2% mass loss, presumably through loss of the carbonate fraction evidenced in the FTIR (Figure 3-2(a)). It should be noted that the higher adsorption of carbonate by URMgO 100 nm and URMgO micro could be attributed to the samples being older batches than URMgO 50 nm, therefore, they have been more in contact with atmospheric carbon dioxide and water than the latter, forming $Mg(OH)_2$ and $MgCO_3$, which is in agreement with the TGA plot in 3-3(a). The URMgO samples were left to dry at 200 °C inside an oven for 24 hours and TGA was performed again, however, the behaviour of the

mass loss curves were the same as the ones presented in Figure 3-3(a). The SEM analysis in Figure 3-6 showed differences in morphology between the nanoparticles (i.e., URMgO 50 nm and URMgO 100 nm) and URMgO micro. Nanoparticles showed spherical agglomerates of plate-like particles whereas URMgO micro have cubic morphology. Specific surface area, given in Table 3-2, and crystallite domain size (from FWHM, Table 3-1), do not follow a trend according to particle size.

RTMgO materials. The XRD patterns for the RTMgO (Figure 3-1(b)) did not change significantly, when compared to the URMgO, though the presence of a minor phase, possibly owing to magnesium-dodecanoate complexes, was observed. The latter could be confirmed as magnesium dodecanoate was prepared as a reference compound and used for comparison, as observed in Figure 3-1(b). Nevertheless, and contrary to what is pointed out by Mekhemer *et al.,* [86] the bulk structure of the MgO was unchanged when in contact with a carboxylic acid at room temperature. FTIR results, presented in Figure 3-2(b), showed that after contact with dodecanoic acid the RTMgO samples all showed characteristic C-H stretching modes at *ca* 2900 cm^{-1}, showing the MgO adsorbs toluene/dodecanoic acid. C-H peaks associated to toluene were discarded as the samples were dried and put under vacuum, as described in Section 3.2.2. This was further confirmed by the characteristic symmetric/anti-symmetric stretching of the carboxylate group at 1450 cm^{-1} and 1567 cm^{-1}, respectively. The latter were also compared with the spectra obtained from the reference compound Mg Dodecanoate, which showed the same trend, as observed in Figure 3-2(b), which confirmed the presence of the carboxylate species. The TGA thermograms in Figure 3-3(b) showed a strong surface area effect for the adsorption of the organic molecules, with the low surface area (3.57 $m^2.g^{-1}$) RTMgO micron showing a ~5% mass loss above 300 °C, whereas the high surface area RTMgO 100 nm (60.47 $m^2.g^{-1}$) and RTMgO 50 nm (46.24 $m^2.g^{-1}$) show mass losses of ~19%, and 22% respectively, though including any small dehydroxylation contribution as noted above. The presence of a small shoulder at 450 °C for RTMgO 100 nm could be attributed to the formation of $MgCO_3$ as a result from the adsorption of environmental CO_2. The FTIR and TGA also indicate the presence of adsorbed water in the form of rehydrated $Mg(OH)_2$ at *ca* 3700 cm^{-1}. The FWHM (Table 3-1) for the RTMgO samples also closely follows those of the URMgO, indicating similar domain sizes within the particles.

SMgO materials. Following the reaction process, the recovered MgO materials (SMgO) were analysed again to allow comparison with the RTMgO. SMgO were evaluated from the other two temperatures (250 °C and 280 °C) to find if their bulk structure suffered any change as, for example, Snell & Shank found for ceria at a specific temperature at the onset of ketonic decarboxylation [83]. However, this was not the case. None of the samples showed significant changes to the XRD patterns reported in Figure 3-1, though the different particle size patterns now seem more uniform, suggesting a degree of recrystallization has occurred at the higher temperatures used. The latter argument is in agreement with the FWHM data obtained in Table 3-1 for all the MgO samples, with the SMgO showing very similar crystal domain sizes across the different particle sizes relative to the URMgO and RTMgO samples, where crystal domain sizes vary significantly according to particle size. This supports the hypothesis than the ketonic decarboxylation reaction happens to occur purely as a surface mechanism rather than affecting the bulk structure of the MgO, in contrast to the work of Pestman, *et al.,* [89] in which ketonic decarboxylation was postulated to only occur over the surface of the catalyst at nonstationary reaction conditions and a possibly bulk carboxylate restructuring of the latter occurring at stationary conditions. TGA analyses were also used to validate the information obtained through the PXRD (Figure 3-1(c)) and FTIR analysis (Figure 3-2(c)), in which decomposition curves from the different MgO samples were observed (Figure 3-3 (c)). SMgO samples show the presence of an FTIR adsorption at *ca* 1740 cm^{-1}, indicative of ketone C=O stretching, not present in the RTMgO samples. The relative intensity of the carboxylate symmetric and anti-symmetric bands, as compared to C-H stretching intensity, are also reduced in the SMgO samples, particularly in the high surface area nanoMgO, confirming the conversion of the dodecanoic acid starting material to the product. The FTIR of the SMgO samples shows no broad water adsorption band at *ca* 3500 cm^{-1}, as might be expected post heating in a non-polar solvent, though the TGA trace shows the SMgO 50 nm material to have picked up water during sample preparation. The % of material lost during pyrolysis in the TGA from 300 °C to 500 °C, indicating sorbed reactant/product, was close to 8%, 40% and 42% for the SMgO micro, SMgO 100nm and SMgO 50nm samples, respectively. This is approximately double that observed for the comparative samples treated at room temperature and, as for the RTMgO samples, a strong surface area effect is notice with the nanometer sized samples holding approximately five times the organic matter (% wt.) compared to the MgO micro.

In summary, the two roughly comparable URMgO 50 nm and URMgO 100 nm samples appear to show a strong surface area determined adsorption effect both pre- and post-reaction. If the active sites are of similar strength and the reaction is controlled by number of active sites available, we would expect to see a significant difference in yield for these two samples when compared to the URMgO micro. Through TPD-CO_2 desorption, a quantification of the active sites on the URMgO samples could be achieved, to further measure the basicity strength. Moreover, the plots, as observed in Figure 3-5, provides some insights regarding a possible crystallization of the material ca 310 °C (the exothermic peak observed in the DSC plots for all the URMgO samples) which seems to agree with the results reported in Table 3-1 regarding the FWHM of the SMgO. However, further in-depth analysis is required to disclose the latter crystallisation assumption. Thus, the behaviour of the URMgO adsorbing CO_2 through the TPD analysis, as observed in Figure 3-5, seems to be the same, probably to all the basic sites within the samples being of similar strength and quantity. In the next Sections we will explore the impact of various parameters on reaction yield for a fixed reaction time of 1 h.

3.4.2 Effect of temperature on ketonic decarboxylation over MgO

Test reactions were undertaken with dodecanoic acid dissolved in toluene, at the three different reaction conditions of 250 °C, 280 °C and 300 °C, and with no MgO catalyst present, to ascertain whether any thermal conversion occurred. No appreciable formation of the desired ketone product, 12-tricosanone, was observed in these tests. As observed in Figure 3-7, when the MgO catalyst was added to the dissolved dodecanoic acid, the desired ketone produce was obtained. From Figure 3-7 it is apparent that for the two lower temperatures used, the yield of 12-tricosanone was dependent on catalyst load. When temperature was increased from 250 °C to 280 °C, an increase on the yield of the ketone was observed in comparison with the results obtained for the lowest temperature reactions. This suggested that either (i) the reaction was controlled by the availability of certain active sites in the catalyst, which are temperature dependent, or (ii) the temperature was approaching the activation energy for the α-hydrogen abstraction from the carboxylate acid necessary for the ketonisation reaction [81-83], and the turnover frequency was limited at the catalyst base sites. It is notable that at *ca* 280 °C in the TGA analysis in Figure 3-3, the onset of dehydroxylation of any hydrated MgO is observed. When a reaction temperature of 300 °C

was used, the highest yield of ketone (> 70%) was observed in all but one case (mean of 64%) and, even allowing for the different catalyst loads and particle sizes used, the 12-tricosanone production was not significantly different from one another. If the reaction temperature was increased above 300 °C, a whole set of different aromatic products started to appear within the post-reaction analysis, probably by a pyrolytic degradation effect of the products [86]. PXRD analysis (Figure 3-1) of the post reaction catalyst (SMgO) shows the catalyst was largely unaltered. As Mekhemer, *et al.,* [86] noted, and verified by the post-reaction analysis of the spent catalyst (SMgO) by FTIR (shown in Figure 3-2(a)), some ketones remained adsorbed to the MgO surface, which due to coordination with Lewis acid sites [218,219], could be activated at high temperatures to undergo further reactions.

3.4.3 Effect of the catalyst loading for the ketonic decarboxylation of dodecanoic acid

It can be inferred from Figure 3-7 that there is a relationship between reaction temperature and catalyst loading, a directly proportional relationship of yield, temperature and catalyst load up until 300 °C. For all the MgO samples used during the ketonic decarboxylation experiments, when working at temperatures below 300 °C, it was required to increase the catalyst load with respect to the feed of dodecanoic acid to increase the production of the 12-tricosanone. At 250 °C, the temperature at which ketone production was started to be observed, 1% wt. of the catalyst seemed insufficient to generate a ketone yield above 10%, however, when increasing the loading up to 5% wt., a ketone yield of around 45 % was obtained. The same was true when working at 280 °C, increasing the catalyst load directly impacted the ketone production. However, once the temperature reached 300 °C, the catalyst loading did not affect the ketone yield, as with as low as 1 % wt. for all the MgO samples, the ketone yield was similar from one another (around 75 %). As discussed in Section 3.4.2, once the right temperature for the carboxylates to be activated was achieved, it could be assumed that these will react and so form 12-tricosanone, forming CO_2 and H_2O [220]. Raising the catalyst load increases the available surface area and number of catalytic sites, which may be a critical parameter for increased reactivity. If so, moving from large particle size to a small particle size for a given catalyst loading should give similar effects and this is considered in the next Section.

3.4.4 Effect of the particle size of different MgO powders for the ketonic decarboxylation of dodecanoic acid

When the catalytic activity of all the MgO powder samples were tested one against other, the three different particle sizes presented similar results, with no significant yield difference between one another, according to Figure 3-7. Nevertheless, it is worth noticing that there is indeed a minor positive particle size effect when evaluating the ketonic decarboxylation reaction at the highest temperature and catalyst load (300 °C and 5% wt., respectively). During the realisation of the experiments, it was expected that the smallest particle size MgO powder (URMgO 50 nm) would produce a significant amount of more ketone than the rest of the samples (URMgO 100 nm and URMgO micro) as the smaller the particle size the more surface area and therefore better results are expected for any heterogeneous catalyst. However, that was not the case. The yields stayed relatively similar between all the samples (~ 75 – 80 %, considering the standard deviation) when evaluated for all the ranges of catalyst loads (1 to 5% wt.) and temperatures (250 to 300 °C). It can be noted, due to the latter results that, if the reaction would be controlled by the number of active sites over the catalyst's surface area (see Table 3-2 for specific surface area measurements), a notable difference between the yields of 12-tricosanone would be observed when using the nano MgO samples compared when using the micro size one. This could be an indication that rather than controlling the reaction, the surface area effect is not directly related to the amount that could be produced when using an oxide for ketonic decarboxylation of fatty acids. However, when the FWHM of the reacted MgO catalysts (SMgO) are compared (in Table 3-1) it can be seen that all the different particle size MgO gave a similar crystallite domain size post reaction, possibly suggesting recrystallisation is happening at 300 °C. This now explains the similar reactivity, with the crystal domain size controlling conversion and this becomes similar across all the MgO, irrespective of the initial particle size, under reaction conditions [211,212]. Interestingly, Figure 3-2 shows a strong inverse correlation between particle size and the amount of mass loss in the RTMgO samples, relating to fatty acid sorption, and also in the SMgO samples, indicating surface area plays a role in the reaction process during sorption of the reactants.

3.4.5 MgO as an effective catalyst to promote ketonic decarboxylation

The studies from Corma, *et al.,* [95] and Mekhemer *et al.,* [86] provided good data regarding the effectivity of MgO powder to promote ketonic decarboxylation of carboxylic acids. Our recent studies [102,114] with a different type of material, the layered double hydroxides, also provided good ketone yields, with the catalytic activity being probably promoted by highly basic $Mg(OH)_2$ on the brucite-like layers [102,223,224]. Considering the latter, it could be plausible that besides low coordination O^{-2} promoting the deprotonation of the adsorbed carboxylic acids to convert them into carboxylate species that will further undergo ketonic decarboxylation through a β-ketoacid as recent studies suggest [82,225], the OH species could be adsorbed over the surface of the catalyst once water is generated, would hydroxylate the surface of the MgO, that could further deprotonate a carboxylic acid molecule leading to the formation of a likely reactive intermediate which then will react, followed by desorption of the desired ketone products. The latter assumption arise from the study of Bailly *et al.*, [119] in which it was probed that Brønsted basicity of MgO surfaces decreased when they were hydroxylated, but the latter was compensated by the highly reactive hydroxyl groups over the surface of the oxide.

3.4.6 Conclusion

Ketonic decarboxylation of fatty acids has been an extensively explored research topic with still inconclusive results regarding the best reaction conditions and mechanism. Here, the possible impacts of the particle size within the reaction conditions as well as small amounts of catalyst were tested for the ketonic decarboxylation of dodecanoic acid, with high ketone production at moderate temperatures using the inexpensive and accessible catalyst MgO.

It was observed that the reaction temperature is an important reaction parameter, as it was observed that for temperatures below 300 °C, more catalyst is needed to increase the yield of ketone. However, once 300 °C was reached, up to 1 % wt. of the catalyst delivered ketone yields above 70 %. Although it could be expected that the presence of more active sites over the surface of the smallest size catalyst would impact the ketone yield positively, both, the nano and the micro size MgO delivered similar results at 300 °C, even at different catalyst loads. The analysis performed using the spent catalyst (SMgO) suggest that recrystallisation occurs at 300 °C, with the crystallite size being a key parameter for the ketonic decarboxylation reaction. Overall, increased surface area and active site availability, whether through varying particle size or catalyst loading, were found to have less impact on reaction yield than the temperature.

4. Ketonic decarboxylation of different carboxylic acid mixtures using MgO as a heterogenous catalyst. The effect of a highly basic catalyst

4.1 Introduction

In Chapter 3, the ketonic decarboxylation of fatty acids using MgO of different particle sizes as the heterogeneous catalyst was evaluated, using dodecanoic acid as the only substrate for this reaction. From the results obtained in Chapter 3, it was clear that the homo ketonisation product (i.e., the symmetric ketone) 12-tricosanone was obtained with yields around 75%. Considering that the dodecanoic acid is the main fatty acid of coconut oil, it can be assumed that if available, dodecanoic acid can be obtained from some of the waste streams deriving from industrial processes, such as the industrial process to produce coconut milk [226]. For instance, during the latter mentioned process to produce coconut milk, coconut oil can potentially be recovered [226], nevertheless, the coconut oil does not only contain dodecanoic acid, it also contains other acids such as oleic acid, linoleic acid, palmitic acid, caprylic acid, among some others [227]. If coconut oil is put to react under the same reaction conditions explored in Chapter 3, chances are ketones will be formed. However, as the variety of acids within coconut oil is wide, the product distribution might vary, with one product being favoured over the others. It has also been suggested that during the sorption of the fatty acids over the surface of the catalyst, the charged surface might favour a specific alignment of the carboxylic acids, aligning the acids into a head to head configuration [102]. Therefore, the possible alignment of the fatty acids towards a preferred spatial configuration over the catalyst or the product distribution of the ketones products after performing the ketonic decarboxylation of carboxylic acid mixtures could be affected by the intrinsic characteristics of the latter carboxylic acids, such as the chain length, unsaturation in the acids, among others. When different carboxylic acids are reacted through the ketonic decarboxylation reaction, it is expected that the production of symmetric and asymmetric ketones will occur [228,229].

The studies of the cross-ketonisation reaction

The cross-ketonisation of two different carboxylic acids can produce an asymmetric ketone, according to the following reaction:

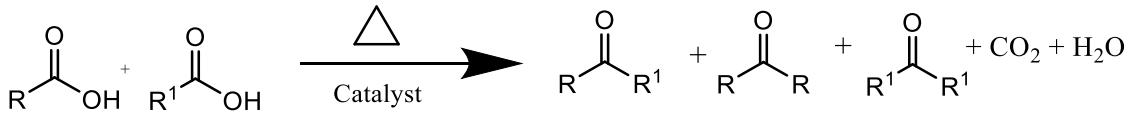

Figure 4-1. Ketonic decarboxylation of two different carboxylic acid to yield two different symmetrical ketones and one asymmetrical ketone, plus carbon dioxide and water.

As observed and as further tested in Chapter 3, the reaction needs the presence of a catalyst and heat. Important work has been done in recent years regarding the ketonic decarboxylation reaction. Ignatchenko *et al.,* [228] studied the effect of the a catalyst to make it selective towards a certain product. In their work, Ignatchenko *et al.*, [228] explored the ketonic decarboxylation reaction of acetic acid and isobutyric acid using catalysts based on the monoclinic form of zirconia as well as the anatase form of titania. Although no mention is done regarding why both catalysts were seleted, both of them are considered to be basic catalyst therefore, useful to study the ketonic decarboxylation reaction. Ignatchenko *et al.,* analysed the reaction (no solvent used, the acids fed straight into the reactor) to disclose the role of each reagent towards the production of the symmetric or the asymmetric ketone, with also involvement of other factors such as the ratio of the acids, the temperature and the type of catalyst used. They concluded that what dictated the product outcome and yields was determined not only by the concentration of the enolised carboxylates over the surface of the catalyst, but also by the post-enolisation step, in which a competition between the species that will undergo between what Ignatchenko *et al.,* named the enolic and carbonyl components. In a different study, Ignatchenko *et al.,* [225], through computational approaches, evaluated the cross-ketonisation of carboxylic acids using monocyclic zirconia as the catalyst. In their study, Ignatchenko *et al.*, [225] identified three potential steps which are enolisation, condensation and decarboxylation over the surface of the catalyst [225].

Moreover, Ignatchenko *et al.* suggested that many reaction steps during the ketonic decarboxylation of carboxylic acids over the surface of the catalysts should be treated as being reversible, however, and according to them, there was sufficient evidence to conclude that enolisation, condensation and decarboxylation were all reversible processes, as presented elsewhere [230].

Cross-ketonization of Complex Mixtures

Baylon *et al.,* [231] went one step further and transformed C_3 – C_6 mixtures of carboxylic acids into different olefins through cascade reactions (i.e., consecutive formation of one product that is further transformed into a different one). In other words, Baylon *et al.,* used acetic acid and propanoic acid to selectively transform the latter acids into C_3 and C_6 olefins, through the ketonisation, and subsequent aldolisation and self-deoxygenation reaction of the latter carboxylic acids. For instance, Baylon *et al.,* explored different ratios of acetic acid to propanoic acid and reported how varying the ratio of one another can affect the selectivity towards the yield of the cross-ketonisation product with respect to the homo-ketonisation product. In their study, Baylon *et al.,* increased the amount of the propanoic acid with respect the amount of acetic acid, that is, reduced the acetic acid to propanoic acid ratio, which according to them, favoured the formation of more cross-ketonisation product. Moreover, according to Baylon *et al.,* the acid sites on the catalyst surface are also important to drive the reaction towards the desired products, as they observed that over a catalyst as ZrO_2, the acetone that was formed when acetic acid was used as the only feedstock for the ketonic decarboxylation reacted further to decompose to form methane and CO_2, which Baylon *et al.,* attributed to the presence of the acid sites on the catalyst surface. In another study using a amphoteric catalyst (i.e., a catalyst with acid and basic sites) Lee *et al.,* [229] explored the ketonisation selectivity using a wide variety of fatty acids. The catalyst used by Lee *et al.,* was a commercial TiO_2 and the fatty acid employed were varied according to the degree of unsaturation and the carbon chain length. The fatty acids employed during the study were butanoic acid (C_4), pentanoic acid (C_5), hexanoic acid (C_6), octanoic acid (C_8), dodecanoic acid (C_{12}) and the C_{18} saturated and unsaturated carboxylic acids (i.e., stearic acid, oleic acid and linoleic acid). According to Lee *et al.,* the larger the carbon chain, the more prone the carboxylic acid is to undergo a McLafferty rearrangement (i.e., the molecules with a keto group suffer a β-clevage and gain a ϒ-hydrogen, which lead to an enol tautomerising

into a methyl-ketone and an alkene). Moreover, they also concluded that the presence of unsaturation favours the McLafferty rearrangements as well (i.e., the more unsaturation present, the more rearrangement occurs).

Sustainable And Circular Economy Based Feedstocks for Cross-Ketonization

In order to deliver truly sustainable ketones, the availability of fatty acids to be implemented in a possible circular economy framework (i.e., recycle, reuse or recover the substrates from waste streams or from a specific industrial process) needs to be considered. For instance, in Thailand, the 9th largest producer of coconut oil worldwide, *ca* 2000 to 3000 kg of coconut milk are lost as waste streams, where the coconut oil, which has as its main constituent dodecanoic acid, can be recovered through separation from the wastewater pond [226]. In another circular economy approach, through urea adduction, Guo *et al.,* [232] separated waste cooking oil into saturated (e.g., stearic and palmitic acid) and unsaturated fatty acids (e.g., oleic and linoleic), for the subsequent use of the latter and former acids as efficient collectors for reverse flotation desilication of iron ores. Chen *et al.,* [233] produced a comprehensive life cycle assessment of the production of caproic acid (i.e., hexanoic acid) from a biorefinery approach, in which mixed organic waste and ethanol are used to obtain the latter caproic acid through a process named chain elongation with the aid of microorganisms. Moreover, other set of volatile fatty acids can be obtained through waste recovery or waste treatment, as studied by Atasoi *et al.,* [234], in which different recovery strategies and methodologies were examined in order to find the best cost-effective approach, which would also varies according to the intended use of the latter fatty acids (i.e., acetic, propanoic, butyric, etc). According to Atasoi *et al.,* the recovered volatile fatty acids could be implemented in production processes such as biodiesel production, production of bioplastics and as a carbon source for denitrification processes. Such applications seem interesting, however, there is an economic challenge to recover the latter volatile fatty acids from waste streams, as the processes might not be economic feasible. Among some of the proposed recovery strategies are nanofiltration, solvent extraction, electrodialysis and bio-augmentation. From all the latter mentioned strategies to recover the volatile fatty acids from waste streams, Atasoi *et al.,* conclude the most economically feasible strategy would be implementing the bio-augmentation. The bio-augmentation strategy consists mainly in using microorganisms that can help to increase the yield of a desired product.

The results obtained in Chapter 3, in which a low-cost and environmentally friendly mineral, MgO, was evaluated in terms of its capabilities to favour the production of ketones derived from carboxylic acids through ketonic decarboxylation, were synergistic with exploring the use of biomass derived saturated and unsaturated carboxylic acids of short and long carbon chains to evaluate the behaviour of the latter acids to produce clean post-reaction mixtures of ketones. In this section of the study, we explore whether the difference in the carbon chain length, or the saturation of the different reactants have any significant effect in favouring one product or another (i.e., the symmetrical or the asymmetrical ketone) during the ketonic decarboxylation of carboxylic acids. The MgO remains as the selected catalyst to promote the ketonic decarboxylation of the carboxylic acids used in this section of the study, due to the intrinsic highly basic properties of the latter MgO, and also, because MgO is considered to be abundant and inexpensive (MgO oxide can be found in the nature as periclase, but also obtained from other minerals such as magnesite (i.e., $MgCO_3$), moreover, Mg is the eight most common element on earth) [235]. Dodecanoic acid was decided to be left as the constant reactant and mixed with different molecules such as pivalic acid (no α-hydrogen present), hexanoic acid (smaller unsaturated carbon chain), phenylacetic acid (phenyl group as substituent) and linoleic acid (larger double saturated carbon chain). All the corresponding structures of the fatty acids used in this section of the study were drew in Section 4.3. Taking into account that the carboxylic acids evaluated in this chapter can be potentially recovered from waste streams, as detailed a few paragrahps above, a sustainable production process that encompasses concepts such as circular economy can start to be envisioned, in which wastes and energy inputs are minimised, recovered and potentially reused, trying to achieve a "greener" production process. Nevertheless, sustainability and circular economy are concepts that will be further explored in detail in the coming chapters. The results obtained in this section of the study are expected to be further compliment with more experimental (Chapter 8, Section 8.1, Future-work) as due to the COVID restrictions and the cut of the funding, more laboratory work was impossible to be performed.

4.2 Experimental

For the evaluation of the different carboxylic acids as substrates for the ketonic decarboxylation, solely the 100 nm MgO sample (i.e., URMgO 100 nm) was used as the catalyst. Although during the experimental of Chapter 3, it was noted that the effect of temperature seemed to be more relevant than the surface area difference among the three MgO samples (i.e., URMgO 50 nm, URMgO 100nm and URMgO micro, referring to MgO samples of 50 nm, 100 nm and 44 microns, respectively) it was determined to keep working with the 100 nm MgO sample (i.e., URMgO 100 nm) as it was the sample that had the highest surface of the three, according to the nitrogen adsorption-desorption experiments. The methodologies and instrument employed for the characterisation of the URMgO 100 nm have been already explained in detail in the Chapter 2 and applied in the same exact manner as in Chapter 3. All the chemical reagents used were purchased from different chemical suppliers and used as received unless stated otherwise. Dodecanoic acid (Alfa Aesar, 98 %), phenylacetic acid (Sigma-Aldrich, 98.5 %), pivalic acid (Sigma-Aldrich, 99%), hexanoic acid (Alfa Aesar, 98%) and linoleic acid (Fluorochem, 98.5 %) were the carboxylic acid substrates. The symmetric and asymmetric ketones obtained from the reaction of the latter acids were also purchased from chemical suppliers when available. The purchased ketone standards were 12-tricosanone (Alfa Aesar, 98 %), 6-undecanone (Sigma-Aldrich, 99%) and 6-heptadecanone (Sigma-Aldrich, 98.5%). When the ketones were not available to be purchased, the post-reaction crude mixture was extracted as explained in Chapter 2, Section 2.4.3 and subsequently purified. Although full description of the characterisation and analytical techniques used in this chapter have been already explained in detail in Chapter 2, a brief description of all the techniques and analytical methods pertinent to Chapter 4 are included in the following sub-Sections.

4.2.1 Ketonic decarboxylation of the carboxylic acids

As explained in Chapter 2, Section 2.10, 1 mmol of each carboxylic acid (pair-wise, 2 mmol in total, as later observed in Table 4-2 and Table 4-3) as well as the catalyst (10% wt.) were put inside an autoclave (0.075 L Parr) using toluene (20 ml) as solvent (analytical grade, Fischer chemicals). Once sealed, the autoclave was purged with N_2 gas to remove any possible oxygen trace within the autoclave. Subsequently, the autoclave was heated up to the desired temperature (300 ˚C) and left to react for a one-hour period, as performed in

Chapter 3 (mostly due to evaluate the amount of ketone produced while keeping the reaction time the lowest possible). Once the reaction time was over, the vessel was left to cool down and, once at room temperature, the crude product mixture was extracted, as explained in Chapter 2, Section 2.4.3. The reaction carried out are further shown in Table 4-2 and Table 4-3.

4.2.2 Analysis of the extracted post-reaction crude product from the cross-ketonisation reaction

Once the crude post-reaction mixture was extracted, 2 ml of the sample was taken from the falcon tube and derivatised (using 100% excess of N,O-Bis(trimethylsilyl)trifluoroacetamide (BSTFA) and 100% excess of pyridine with respect the moles of acid used) as explained in Chapter 2, Section 2.4.2. Afterwards, 1 ml of the derivatised sample was put in a glass vial to be further analysed by GC-MS (detailed explanation of the procedure and instrumentation, see Chapter 2, Section 2.4.4) and another 1 ml of the derivatised sample was taken to be analysed by GC-FID (detailed explanation of the procedure and instrumentation, see Chapter 2, Section 2.4.3). Both results were compared, using the obtained data from GC-MS to perform a qualitative identification of the existing products within the crude post-reaction mixture. The obtained chromatograms from the GC-FID were used to quantify the obtained products using a calibration curve and the internal standard technique (see Chapter 2, Section 2.4.5). A typical chromatogram from the GC-FID obtained when analysing the crude post-reaction mixture, post-derivatisation, would look as the one in Figure 4-2.

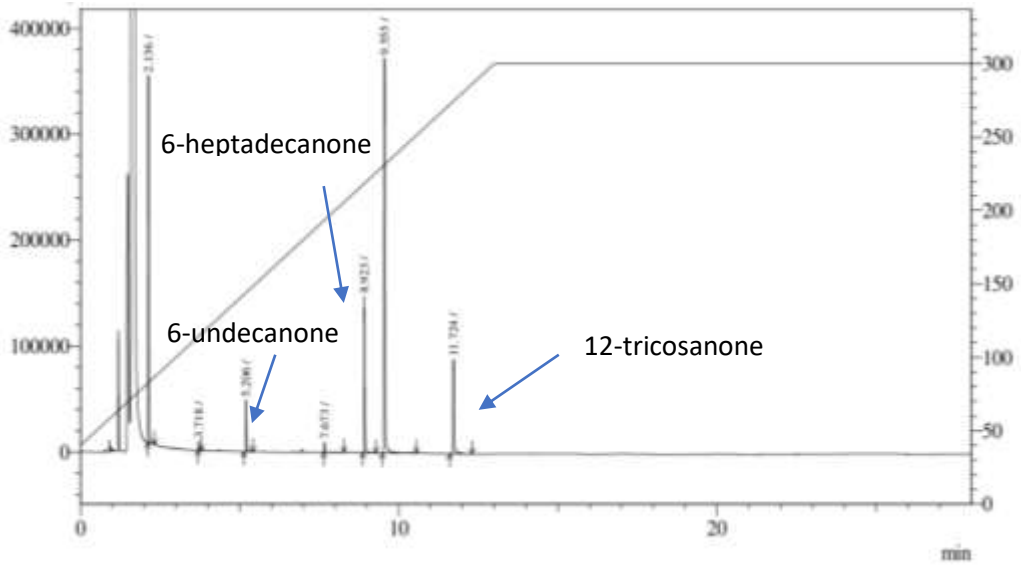

Figure 4-2. Chromatogram obtained from the analysis of the crude post-reaction mixture of dodecanoic acid and hexanoic acid. The x-axis corresponds to the retention time whereas the y-axis corresponds to the intensity. Based on the calibration curves made using the standards, the retention times of 5.20 min, 8.92 min and 11.72 min can be assigned to 6-undecanone, 6-heptadecanone and 12-tricosanone, respectively.

As observed in Figure 4-2, some defined and sharp peaks can be observed at different retention times, one after another, corresponding to the two symmetric and one asymmetric ketones (i.e., retention times of 5.20 minutes, 8.92 minutes and 11.72 minutes) products from the ketonic decarboxylation of the carboxylic acid mixtures. Through the derivatization of the sample, it is also possible to quantify, if any, the amount of the unreacted carboxylic acids. All the retention times were confirmed by using the purchased standards, when required (i.e., not knowing which peaks are related to which compounds). The GC-MS chromatograms as well as the m/z fractions for all the carboxylic acid mixtures are presented in Chapter 2, Section 2.4.3. Moreover, how the calibration curves for quantification of products were prepared are also described in Chapter 2, Section 2.4.3 and presented in Appendix A.

4.2.3 Purification of the extracted post-reaction crude product from the cross-ketonisation reaction

The remainder of the crude post-reaction mixture was separated and purified through column chromatography (for the specific procedure on the purification approach, see Chapter 2, Section 2.5). In this case, the only sample that was purified through a column, was the 1-phenyl-2-tridecanone, the asymmetric ketone product from the ketonic decarboxylation of dodecanoic acid with phenylacetic acid, as it was the only ketone that was not available through a supplier. In a typical ketonic decarboxylation experiment, 0.40 g (2 mmol) of dodecanoic acid were dissolved in 10 ml of toluene with 0.32 g (2 mmol) of phenyl acetic acid in the presence of the URMgO 100 nm inside a Parr Autoclave and put to react at 300 ˚ C (see Chapter 2, Section 2.10 for detailed explanation). After the crude post-reaction product was recovered and evaporated (Chapter 2, Section 2.4.3 and Chapter 2, Section 2.5.1, respectively), a few drops of toluene were used to fully dissolve the mixture of ketones inside the round bottom flask, to subsequently find a suitable eluent, based on a solvent polarity table, to obtain the best separation possible between spots, using a trial-and-error approach, resulting in a ratio of hexane to petroleum ether of 98:2 for the TLC analysis, as defined before (Chapter 2, Section 2.5). Once the eluent conditions were chosen, a column was chosen to proceed to the purification of the sample was performed as explained in Section 2.5. Once separated in different test tubes, each specific ketone was concentrated in a different round bottom flask, and the solvent evaporated. The solid products were then dissolved in toluene and further used to prepare a calibration curve for each ketone, as explained in Chapter 2, Section 2.4.5. As the autoclave to perform the ketonic decarboxylation reactions was small in volume, several reaction batches were repeated using the same reaction conditions to obtain more grams of the asymmetrical ketone and to be able to make a calibration curve of the latter asymmetrical ketone with up to12 data points, from 0.05 M to 0.01 M.

4.2.4 Catalyst characterisation

The characterisation of the MgO used in this chapter (URMgO 100 nm) corresponds to the one employed in Section 3.2.1, Chapter 3, which was also explained in detail in Chapter 2.

4.3 Results

The characterisation of the catalyst is shown in Figure 4-3. The data corresponds to the same characterisation data presented in Chapter 3, Section 3.2.1

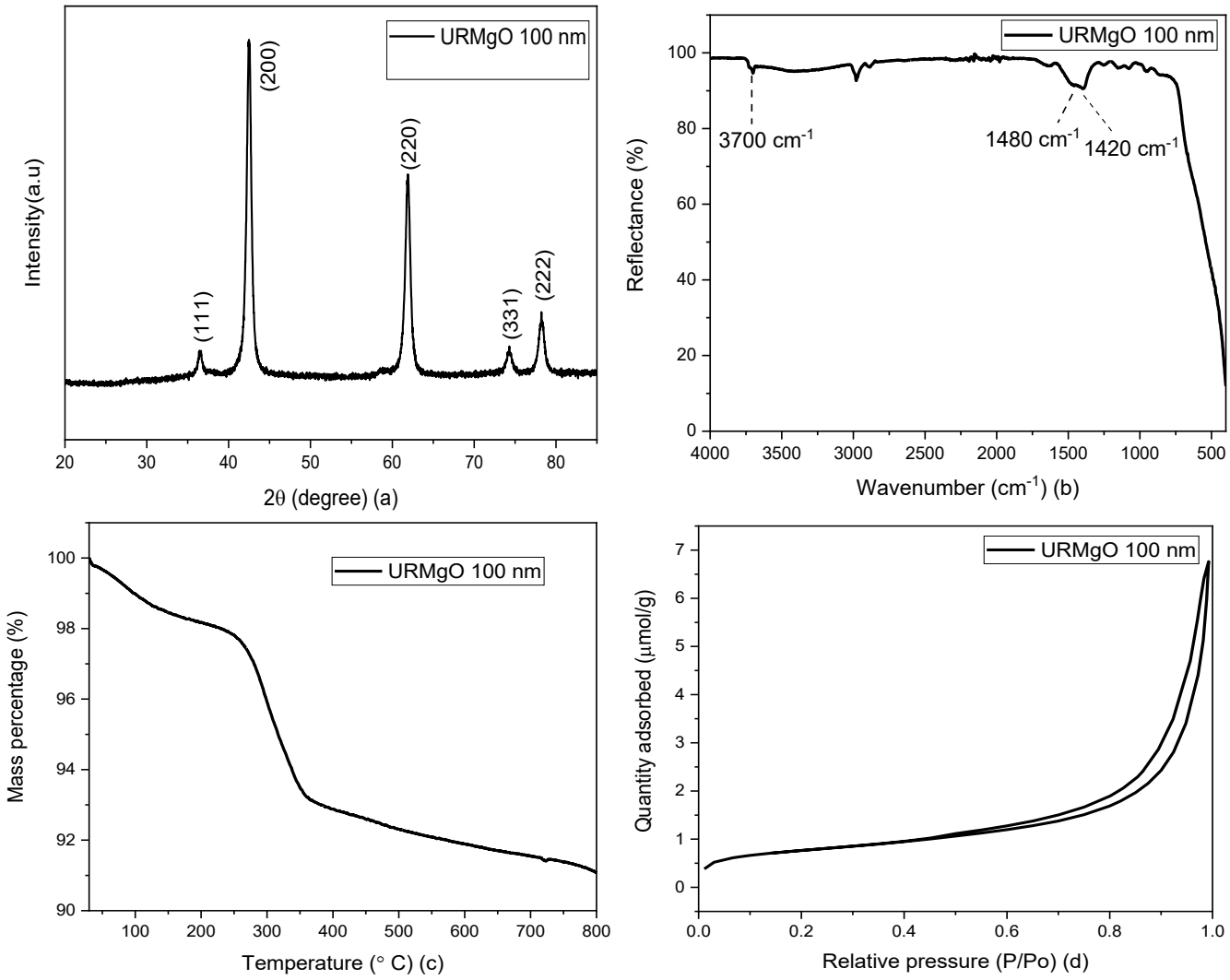

Figure 4-3. Characterisation of the URMgO 100 nm. a) Powder X-ray diffraction pattern. b) Fourier Transformed Infra-red analysis with characteristic peaks related to the adsorbed CO_2 (ca 1420 cm^{-1} and 1480 cm^{-1}). $Mg(OH)_2$ ca 3700 cm^{-1}c) Three decomposition steps are observed in the thermogravimetric analysis, mostly to the dehydration and decarboxylation of the sample. d) Nitrogen adsorption-desorption isotherms of the URMgO, with a clear hysteresis loop.

The typical diffraction peaks of the cubic phase of MgO obtained from Powder x-ray diffraction analysis (PXRD) can be observed in Figure 4-3(a). Those correspond to the sharp peaks *ca* 43 ˚, 62 ˚ and 74 ˚ which are assigned to the (200), (220) and (331) reflections, respectively [209,210]. MgO is highly hygroscopic and adsorbs atmospheric water and CO2 with relative ease, which is reflected in the FTIR plot in Figure 4-3(b). The symmetric stretching of bicarbonate species, usually observed in the range of 1410 to 1480 cm-1 and the symmetric stretching of monodentate carbonate species, usually present ca 1418 – 1420 cm-1, both are observed in Figure 4-3(b). Moreover, due to the highly hygroscopic capacity of MgO, from Figure 4-3(b) it can also be observed a small peak *ca* 3700 cm-1 related to the stretching vibration of the O-H bond, which can be assigned to the presence of the Mg(OH)2 (i.e, brucite) [132,215]. The TGA analysis of the URMgO 100 nm (Figure 4-3(c)) shows a dehydroxylation step ca 265 ˚ C followed by a decarbonylation step which corresponds well with the information obtained from the FTIR plot [114,220]. Finally, the adsorption-desorption isotherms of URMgO 100 nm (Figure 4-3(d)) corresponds with the expected plot to be observed for a mesoporous material (Type IV isotherm) with hysteresis [164].The pKa corresponding to each of the acids used is presented in Table 4-1. The information from each carboxylic acid was obtained from Pubchem webpage, in the National Library of Medicine [236].

Table 4-1. pKa table for the different acids employed as substrates for the ketonic decarboxylation reaction. The pKa is related to the O-H. The "a" labelling refers at the order the acids are presented in the subsequent tables, to be easily identified.

Molecule	**pKa**
Dodecanoic acid (2a)	5.3
Phenylacetic acid (3a)	4.3
Pivalic acid (1a)	4.9
Hexanoic acid (5a)	4.8
Linoleic acid (6a)	4.7

The differences in pKa among the samples in Table 4-1 seemed to be fairly similar from one another. Therefore, the acidity of all the species in Table 4-1 is expected to be fairly

similar, meaning that the acidity of the α-hydrogen of such species could also be considered similar between one another (except for the pivalic acid which lacks α-hydrogens), being all of the latter α-hydrogens susceptible of abstraction under the same reaction conditions. The latter assumption is based on the fact that there is no change in the number α-hydrogens or any stearic effect involved, therefore, the molecules in Table 4-1 in terms of acidity can be compared one another [237]. The results from the ketonic decarboxylation of the different carboxylic acid mixtures are presented in Table 4-2.

Table 4-2. Evaluation of the ketonic decarboxylation reaction to produce ketones mixing dodecanoic acid and phenyl acetic acid with pivalic acid. Entry 1, entry 2 and entry 3 correspond to different carboxylic acid mixtures.

Entry	Starting material (s)	Conversion of starting materials (%)	Product	Yield (%)	Standard deviation (%)
1	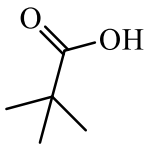 **1a**	0	No ketone	0	-
2	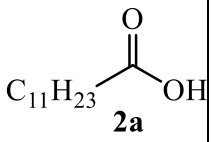 **2a** 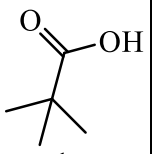 **1a**	98[a]	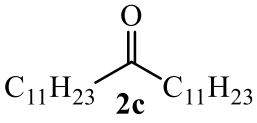 **2c**	22	7
3	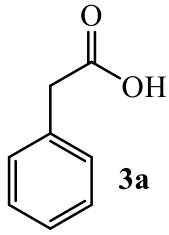 **3a** 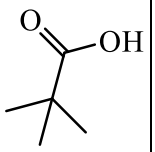 **1a**	99[b]	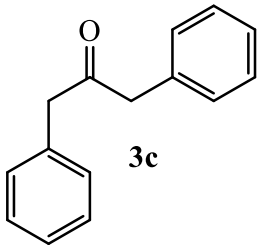 **3c**	18	5

Table 4-3. Different carboxylic acid mixtures and the respective obtained products through the ketonic decarboxylation reaction.

Entry	Starting material (s)	Conversion of starting materials (%)	Product	Yield (%)	Standard deviation (%)
4	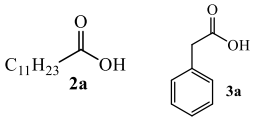	100*	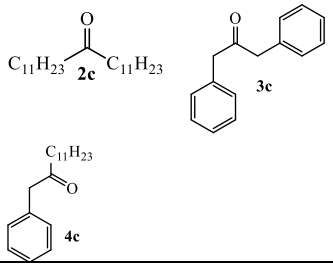	2c = 24, 4c = 40 and 3c = 18	2c = 1, 4c = 5 and 3c = 5
5	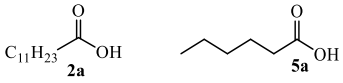	100*	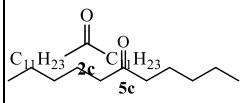	2c = 23, 5b = 45 and 5c = 21	2c = 1, 5b = 5 and 5c = 5
6	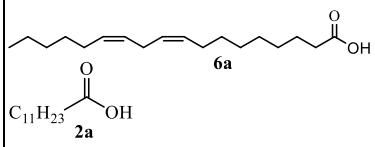	98[a]	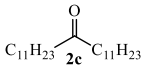	2c = 24	2c = 2
7	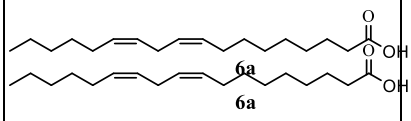	100	No ketone	N/A	N/A

*Conversion was considered to be 100 %, as no peaks related to the starting materials were observed in the chromatogram, when analysing the crude post-reaction mixture. [a] Refers to the conversion of the dodecanoic acid in this reaction mixture. [b] Refers to the conversion of the phenylacetic acid in this reaction mixture. The latter applies to Table 4-2 and Table 4-3.

Table 4-2 and Table 4-3 present the obtained ketone yields from the ketonic decarboxylation of different carboxylic acids mixtures. It is evident, from Table 4-2, that when pivalic acid was used as the only substrate for the ketonic decarboxylation, no ketone was formed (Entry 1, Table 4-2) as expected since it lack enolisable hydrogens. Moreover, when the dodecanoic acid was mixed with pivalic acid, no reaction occurred to form an asymmetric ketone (Entry 2, Table 4-2), again as expected. Rather, only the symmetric ketone (12-tricosanone) was formed since it is derived from a starting material that does contain enolisable hydrogens. The same situation was observed in Entry 3, Table 4-2, when pivalic acid was mixed with the phenylacetic acid. The symmetric product (1,3-diphenyl-2-propanone) was formed. Table 4-3 presents the mixing of dodecanoic acid with other substrates. In Entry 4, Table 4-3, dodecanoic acid was mixed with phenylacetic acid, whereas in Entry 2, Table 4-3 and Entry 3, Table 4-3, it was mixed with hexanoic acid and linoleic acid, respectively. The possible effects of chain length and carbon chain saturation would have on the ketonic decarboxylation was able to be evaluated, therefore, the aforementioned acids were selected, as mentioned in Section 4.1. Both, Entry 3, Table 4-3 and Entry 4, Table 4-3, showed similar overall yields for all produced ketones, however, the only quantified product in Entry 4, Table 4-3 was the 12-tricosanone product. Interestingly, the cross-ketonisation product between the dodecanoic acid and the linoleic acid produced two peaks of similar intensity in the chromatogram obtained through the use of the GC-FID, as observed in Appendix A, at a retention time of 14.12 minutes and 14.16 minutes, with several others small peaks of reduced intensity from 14.34 minutes up to 20 minutes. The sample was further analysed through GC-MS to identify the latter mentioned peaks (Appendix A), which according to the m/z ratio (m/z = 480) obtained from the mass analysis, could correspond to different isomers of the asymmetrical ketone, the ((20*Z*,23*Z*)-nonacosa-20,23-dien-12-one, with the chemical formula $C_{29}H_{54}O$. Moreover, several small unidentified peaks were formed, which did not happen to appear when performing the ketonic decarboxylation of the dodecanoic acid with the phenylacetic acid and the hexanoic acid. Moreover, a pKa table with the pKa values from each of the molecules used as substrates for the ketonic decarboxylation is presented in Table 4-1.

4.4 Discussion

4.4.1 The ketonic decarboxylation reaction using MgO

The ketonic decarboxylation reaction has been extensively explored in the literature, however, consensus still remains to be reached regarding the reaction mechanism, the reversibility of the latter mentioned mechanism, among others [89,225,228,230]. The efficiency of the URMgO 100 nm in promoting the homo ketonisation and the cross ketonisation of different carboxylic acids was reported in Table 4-2 and in Table 4-3. Contrary to what has been suggested by Pham *et al.,* [81] and Mekhemer *et al.,* [86] and as observed in Chapter 3, Section 3.3, when analyzing the RTMgO 100 nm through FTIR and PXRD (i.e., the URMgO 100 nm put in contact with dodecanoic acid/toluene and stirred at room temperature) no appreciable changes in the bulk structure of the MgO were observed, suggesting the reaction could be happening over the surface of the catalyst rather than through the bulk of the MgO. The temperature of the reaction was left at 300 ˚C, as based on the reaction behaviour in Chapter 3, Section 3.3.2, the best ketone yields were obtained at 300 ˚C, with a notable increase in the ketone production when raising the temperature from 250 ˚C to 300 ˚C. Thus, if the reaction temperature was increased over 300 ˚C, further pyrolysis of the products might occur, which is unfavourable when trying to quantify the maximum ketone yield attainable during the ketonic decarboxylation.

4.4.2 The use of equimolar carboxylic acid mixtures with similar pKa for the ketonic decarboxylation reaction

As the ketonic decarboxylation of different fatty acids mixtures was explored, the pKa of the selected acids did not vary a lot, as observed in Table 4-1. Although no quantitative data regarding the acidity of the α-hydrogens for each specific acid was found elsewhere, it is fair to say that as observed in Table 4-1, the acidity of the α-hydrogens should also be similar one another. From Table 4-2 it is evident that the presence of the latter mentioned α-hydrogens is needed in order to promote the ketonic decarboxylation reaction as it is observed in Entry 1, Table 4-2, that when the pivalic acid was left to react (the pivalic acid lacks α-hydrogens within the molecule's structure) no ketone was formed. However, and as observed in Table 4-2, in both, Entry 2 and Entry 3, the dodecanoic acid and the phenylacetic acid formed their respective symmetrical ketones, 12-tricosanone and 1,3-diphenyl acetone,

respectively. According to the literature, the presence of α-hydrogens is needed to start the mechanism of the ketonic decarboxylation, probably through the abstraction of the latter mentioned α-hydrogen over the surface of the catalyst [81,82,89]. The latter abstraction of the α-hydrogen is likely to occur after the sorption of the acid onto the surface of the catalyst. After trying to perform the ketonic decarboxylation using the dodecanoic acid with the pivalic acid and only obtaining the symmetrical ketone 12-tricosanone, which derives from the homo-ketonisation reaction of dodecanoic acid, the dodecanoic acid was mixed with other three substrates (i.e., phenylacetic acid, hexanoic acid and linoleic acid). The results are presented in Table 4-3. According to the study performed by Ignatchenko *et al.,* [228] using acetic acid and isobutyric acid acid,if both acids were put in equimolar amounts to react through the ketonic decarboxylation, both carboxylic acids can produce the maximum amount of the asymmetrical ketone. The latter seem to follow a binomial distribution of products, where the probability of forming the asymmetrical ketone is twice the probability of forming any of the symmetrical ketones. Therefore, in this study, equimolar amounts (1 mmol) of each acid were used. In a similar behaviour with what Ignatchenko *et al.,* [228] observed and as reported in Table 4-3, the overall yield of the asymmetric ketone in Entry 4 and in Entry 5 was superior when compared to the yield obtained for the symmetric ketones, almost by twice, which again follows the trend of a binomial distribution. The overall yield was calculated as follows:

$$\boldsymbol{Yield} = \frac{\boldsymbol{Fx}}{\boldsymbol{Fy0 - Fy}} \qquad 4.1$$

Where *Fx* refers to the moles of a product formed divided by the moles of the key reactant that has been consumed [238]. In both cases, for Entry 4, Table 4-3 and Entry 5, Table 4-3, the carbon chain length did not cause a significative difference in terms of the obtained yields, neither for the symmetric ketones nor the asymmetric ketones. In both entries, the yields seem to be of relative similarity. From Table 4-1 it can be observed that the pKa of all the molecules are fairly similar, which could be extrapolated to the acidity of the corresponding α-hydrogen, meaning all of the α-hydrogens might have similar acidity, which could vary from one molecule to another due to, for instance, the inductive effects

(e.g., phenyl group in the phenylacetic acid), etc. Nevertheless, there is no strong evidence to suggest the acidity of the molecules employed for the ketonic decarboxylation might differ hugely from one another and therefore have an impact on the reaction development [237]. As explored in Chapter 3, it seems that once the reaction temperature reaches *ca*. 300 ˚C, the activation energy for the chemical reaction to proceed is reached, which in conjunction with the presence of the α-hydrogen, completely favour the formation of the ketones. However, and as observed in Table 4-3, Entry 6, and Table 4-3, Entry 7, the long and unsaturated chain of the linoleic acid (6a), although sharing similar acidity in terms of pKa with the rest of the molecules (Table 4-1), with the α-hydrogen in an α-carbon as branched as the rest of the molecules as well (Table 4-1), when reacted at 300 ˚C, no symmetric ketone was formed.

4.4.3 The effect of using unsaturated carboxylic acids to produce ketones through the ketonic decarboxylation reaction.

Interestingly, in the Entry 6, Table 4-3, when put together to react, dodecanoic acid and linoleic acid did not favour a clean reaction as the other two entries. As observed in Figure A-7, Appendix A, the symmetrical ketone 12-tricosanone (retention time of 11.72 minutes) was obtained in a similar yield percentage (24%) with respect Entry 4 and Entry 5 in Table 4-3, however, the other expected symmetric ketone, the possible outcome of condensing two linoleic acids over the surface of the catalyst (i.e., (6*Z*, 9*Z*, 25*Z*, 28*Z*)-tetratriaconta-6,9,25,28-tetraen-17-one, $C_{34}H_{60}O$) was not observed in the chromatograms (Figure A-7, Appendix A) nor through m/z analysis. As observed in Figure A-8, Appendix A, the fragmentation analysis shows the presence of the asymmetric ketone (i.e., $C_{29}H_{52}O$, m/z = 418), in a broad peak that splits into 4 defined smaller peaks, (the retention time of the broad peak goes from 7.26 up to 7.73 minutes, which could correspond to the $C_{29}H_{52}O$, in different isomeric forms. There was also a small peak at a retention time of 5.05 minutes, which could be assigned to the 5-hexadecanone or the 6-pentadecanone. In any case, the symmetric product ketone from the possible condensation of the linoleic acid was not observed. It can be noted from the literature that most ketonic decarboxylation experiments has been focused in trying to understand the reaction mechanism, which according to some authors, the preferred route for the formation of the ketones proceeds through the formation of the β-keto acid intermediate for a subsequent decarboxylation[82,225,228,239].

In an interesting study, Smith *et al.,* [102] used stearic acid (i.e., $C_{18}H_{36}O_2$) as substrate, and through the ketonic decarboxylation reaction, they produced stearone (i.e., $C_{35}H_{70}O$) , the corresponding symmetric ketone. As catalysts, Smith *et al.,* employed layered double hydroxides, which are materials with high basicity and that are active towards the ketonic decarboxylation. The reactions produced in the work of Smith *et al.,* were clean and no undesired sub-products were obtained, rather the stearic acid fully converted into stearone. Although the stearic acid and the linoleic acid have the same carbon chain length (C18), in this study and as observed in Table 4-3 (Entry 6 and Entry 7) when used alone or in a mixture, the linoleic acid did not lead to produce the respective symmetric ketone. Although more experimental is needed using a less unsaturated specie such as oleic acid $C_{18}H_{34}O_2$, it seems evident than more than the carbon chain length having an effect in the production of the ketones, it is the unsaturation of the linoleic acid which is affecting the product distribution. The latter assumption could be supported with the fact that the hexanoic acid (5a), the dodecanoic acid (2a) and the stearic acid (previous work [102]), all the three different carboxylic acids fully consumed to form the corresponding symmetric ketones. Even the phenyl substituent in the phenylacetic acid (3a) which can be considered exert inductively withdrawing effects within the molecule did not affect the formation of the asymmetric and symmetric ketones (Table 4-2 and Table 4-3) in what can be considered a clean reaction with no undesired subproducts. However, at the high reaction temperatures of 300 ˚C, when unsaturated carboxylic acids such as linoleic acid (Table 4-3, Entries 6 and 7) were used, a competitive polymerisation reaction seemed to be happening which hindered a clean ketone production reaction. Rather, through the polymerisation of the unsaturated acids, different dimers or even trimers (i.e., dimer acids and trimer acids) could be forming, through the effect of the heat and the Diels-Alder reaction [240,241]. In a really extensive study, Lee *et al.,* [229] investigated the effect of the unsaturation of the fatty acids when the latter acids were used to produce ketones, through the ketonic decarboxylation. In the study, Lee *et al.,* used stearic acid, oleic acid and linoleic acid as substrates and TiO_2 as the catalyst. The reaction was carried out at 380 ˚C for a period of time of 12 hours. Interestingly, they concluded that the more unsaturated a carboxylic acid is, the less fatty derived ketones are produced through the ketonic decarboxylation reaction. Rather, the unsaturation would lead to the formation of conjugated polyunsaturated olefins such as dienes. The latter dienes, according to Lee *et al.,* are the product of the McLafferty rearrangement and cracking reactions. It remains unclear whether the amphoteric nature of the TiO_2 was causing more

cracking reactions when the unsaturation degree was increased from stearic, to oleic and finally to linoleic, however, Lee *et al.,* conclude the latter cracking behaviour is expected due to acidic sites in the TiO_2 favouring the acidification of the unsaturated C=C bonds. Nevertheless, the temperature used by Lee *et al.,* was *ca* 380 ˚C, which in Chapter 3 it was observed that when working with the dodecanoic acid, once the temperature was raised over 300 ˚C, cracking and pyrolytic products were observed. Therefore, it remains unclear whether using an amphoteric catalyst such as TiO_2 with lower temperatures would favour less cracking-derived products and more fatty-derived ketones would be produced. In an old patent Velde [242], proposed a methodology to produce ketones out of C_{18} unsaturated carboxylic acids (i.e., linoleic acid), using MgO as the catalyst and a ratio acid to catalyst from 100:30 at a temperature from 300 ˚C to 325 ˚C. In the patent, Velde claims the production of the ketones derived from linoleic acid was achieved. The results from Velde [242] seem to be in disagreement with the obtained data from Lee *et al.,* [229] however, the differences might arise due to the different temperatures used for each of the studies and the nature of the catalyst used. The conditions stated in the patent by Velde seems to be comparable with the conditions used in this part of the study, however, Velde did not used any solvent, whilst in this study, toluene was used to keep the formed ketone soluble and for the latter ketone to be quantified through gas chromatography. Therefore, it can be possible that the toluene, at the reaction temperatures of 300 ˚C is somehow favouring the polymerisation of the linoleic acid among other reactions such as cracking, preventing the desired symmetric ketone derived from linoleic acid to be formed. Interestingly, when the linoleic acid and the dodecanoic acid were put to react together (Table 4-3, Entry 6) the symmetric ketone indeed formed, however, according to the Figure A-7 and Figure A-8 in Appendix A, isomeric forms of the asymmetric ketones might exist in solution rather than an specific product. The latter results suggests that the ketonic decarboxylation reaction would proceed and compete against some sort of polymerisation of the unsaturated carboxylic acids, as when only the linoleic acid was left to react alone, even with the presence of the α-hydrogen and a basic catalyst as MgO, no symmetric ketone was obtained (Entry 7, Table 4-3). As observed in Figure A-7, Appendix A, no trace of the symmetric ketone was observed, rather a wide variety of sub-products, most of them unidentified, which might include other ketone species, which might support the assumption of the McLafferty rearrangement proposed by Lee *et al.,* [229]

Due to the covid restrictions and lack of funding to keep doing experimental work, the latter products obtained from the reaction of linoleic acid alone were not further identified and characterised. Moreover, more experimental is needed to understand why the symmetrical ketone was not formed

4.5 Conclusions

The ketonic decarboxylation is a reaction that has been intensively investigated over the years. The most accepted mechanism for the reaction to proceed is through the formation of a β-ketoacid mechanism over the surface of the catalyst and recent studies suggest the reaction could be reversible as well. The carboxylic acids containing the α-hydrogen are prone to favour the ketonic decarboxylation, nevertheless, in this study, as the acidity of tested carboxylic acids is fairly similar to one another, when put to react, the reaction should favour the homo and cross ketonisation of all the samples, with the exception of pivalic acid which lacks α-hydrogens, as mentioned earlier. As expected, pivalic acid was unreactive towards the ketonisation reaction. Interestingly, the presence of linoleic acid, which is a polyunsaturated carboxylic acid, did not favour the homo-ketonisation reaction, even though linoleic acid has a no branched α-carbon and the acidity of the molecule is fairly similar with the rest of the carboxylic acids used in this section of the study. Although more work is needed to understand how the polyunsaturated carboxylic acids interact (probably differently than a saturated carboxylic acid) over the surface of the highly basic MgO, it was observed that the symmetric ketone derived from the linoleic acid did not from properly. The latter behaviour might be attributed to different reaction conditions, such as possible rearrangement during the ketonisation (e.g., McLafferty rearrangement), or even to other reactions (e.g., polymersation) possible outperforming the latter ketonisation reaction. However, as the catalytic conditions in this study differ from the ones claiming the latter rearrangements or side-reactions, more work using MgO and other unsaturated carboxylic acids is needed, to understand whether or not the rearrangements or side-reactions correspond only occur when working with amphoteric catalyst. Moreover, when mixed with dodecanoic acid, the cross-ketonisation product was indeed formed. Nevertheless, the reaction was not clean, and a variety of by-products formed, probably isomerised forms of the latter asymmetric ketone.

It can be observed, from the conclusions of this work, that rather than a fully conclusive chapter, Chapter 4 is a preliminary chapter to be fully addressed in future work, as due to the pandemic restrictions and cut of funding, the laboratory work was stopped before gathering more data. Nevertheless, it was decided to be included within this thesis as it set the foundation of what can be done by future colleagues.

5. Adding value to waste minerals in a circular economy framework: Ochre derived layered double hydroxide catalysts in fatty acid ketonisation

5.1 Introduction

Treatment and reuse of waste is an important component of the emerging circular economy, where waste reduction and valorization is needed to address increasing population and associated increasing consumer demand, which directly drives an increase in the consumption of goods, energy and depletion of natural resources with associated increased waste to dispose of [243]. In particular, addressing climate change owing to emissions of greenhouse gases coming from industrial processes and fuel combustion is a major concern that requires immediate attention [3,13,243]. In recent years, significant research has been undertaken working towards routes to produce bio-derived synthons that otherwise would be produced by traditional petroleum derived routes [68,70,244]. As an example, the base catalyzed production of ketones from plant oil derived fatty (and other carboxylic) acids has become an important reaction for the production of bio-based lubricants, fuel blends, and detergents as well as a mechanism to reduce the oxygen content within pyrolysis oil from biomass [3,16,83,95], as already investigated in Chapter 3 and Chapter 4. In a recent study [102], we explored and tested the heterogeneous base catalytic activity of layered double hydroxides (LDH) to promote the formation of ketones from carboxylic acids through the ketonic decarboxylation reaction. Ketones are normally produced through oxidation of petroleum hydrocarbons, whereas ketonic decarboxylation is a deoxygenation reaction in which two carboxylic acids (for example, from tri-acylglycerides in plant oils) couple to form a ketone while releasing water and carbon dioxide [81,82]. A simple chemical equation to show ketonic decarboxylation is as follows:

$$R_1COOH + R_2COOH \longrightarrow R_1COR_2 + CO_2 + H_2O \qquad 5.1$$

Owing to their basic properties and structure [102,245,246] (LDHs are materials composed by metal hydroxide brucite-like layers with interlayers that contains anions and water exercising weakly bond interactions, balancing the compound), Al/Mg synthetic LDHs proved to be excellent mediators of the ketonic decarboxylation reaction at moderate temperatures (250 °C) and offer a possible route for upgrading biomass derived oils. LDHs consist of hexa-platy, 2-dimensional sheets of edge-sharing octahedra of metal cations

(commonly Mg^{2+} and Al^{+3}), with sheets stacked upon one another and with significant variation in cation composition possible during synthesis, allowing many actual and potential applications [245]. LDHs are generally prepared at scale using a co-precipitation method [126] from soluble metal salts, and due to this, and attending the need for a circular economy, the use of an acid soluble waste product sludge precipitated from acid mine drainage (AMD) treatment named ochre, which would typically be landfilled at a cost, could be an attractive cost-effective alternative source of cations to prepare LDHs. Ochre covers a group of ferric hydroxides, FeO(OH) or $Fe(OH)_3$. According to Dobbie *et al.*, ochre production in the UK is estimated to be 30,000 tonnes per year at a disposal cost up to £3 million per year [247]. Although only being used as pigments in fine art on small-scale, the use of ochre as a potential phosphorus removal method has also been explored in recent years, with promising results though no commercial application as yet [150,247-249]. However, to the best of our knowledge, ochre has not been used as yet as a cation source to synthesize Mg/Fe LDHs. In this paper, the use of the acid mine drainage precipitate ochre is investigated as a cation source material from which to synthesize LDHs and the resulting material's activity as a heterogeneous base catalyst to promote the ketonic decarboxylation reaction between carboxylic acids is assessed. Hence, the overall aim being the transformation of an unwanted, waste material (ochre) into an added-value, useful, chemical material (Mg/Fe LDH), with a range of potential sustainable chemical reaction applications, and herein exemplified by catalytic ketonic decarboxylation.

5.2 Experimental

All the characterisation techniques employed to characterise the ochre and the as-synthesised LDH materials used in this section of the study, have been explained in further details in Chapter 2 (i.e., PXRD, FTIR, TGA, ICP-OES, and Nitrogen adsorption/desorption isotherms) therefore they will not be described further as the same methodology to prepare all the samples was applied during the development of Chapter 3 to Chapter 7.

5.2.1 Ochre composition

Ochre was obtained from the Coal Authority, UK, from the primary drying lagoon at Saltburn Gill Water Treatment Scheme, Saltburn, Cleveland, UK; a treatment system for an ironstone mine. Transmission electron microscopy showed that the majority of the material was nano-crystalline [250]. Dewatering analysis and inductively coupled plasma – optical emission spectroscopy (ICP-OES) of the Saltburn ochre were performed to determine the composition. Dewatering was undertaken by placing an amount of ochre (approximately 5 g) in an oven at 70 °C until constant mass was attained. Mineralogy was determined by powder X-ray diffraction, as detailed below.

5.2.2 Catalyst preparation

The constant pH co-precipitation method (low saturation) was chosen to prepare the Mg-Fe-CO_3 LDH (LDH-CO_3) with a target Mg/Fe ratio of ~3.8 to 4. This Mg/Fe ratio was selected on the basis or prior work, where co-precipitated Mg/Al LDHs showed highest conversion for ketonic decarboxylation reactions [10]. Moreover, in a first approach to synthesize the LDH material using the ochre as one of the precursors, the Mg/Fe ratio of 4 was chosen due to the lack of access to ICP-OES analysis at the time starting to develop this chapter, considering the ochre being solely FeO(OH) with no other metals or impurities within the sample. Based on the results obtained through the latter synthesis and after performing several ICP-OES analysis of the ochre sample, another synthesis using the Mg/Fe ratio of 4 was performed, trying to do the stoichiometric calculations as perfect as possible based on the ICP-OES information obtained. Constant pH co-precipitation gives good control over nucleation rates and crystal morphology and composition homogeneity and allows for meaningful comparison with our previous study using Mg/Al LDH [10]. First, 5 g of Saltburn ochre (through ICP-OES analysis, in Table 5-1, the amount of iron in the 5 g Saltburn ochre is equivalent to 6.3 mmol) was dissolved in 50 ml of 3 M HCl (Fisher, laboratory reagent grade) and mixed with 50 ml (24 mmol Mg) of a 0.48 M solution of $Mg(NO_3)_2.6H_2O$ (Aldrich, 99%). The mixed solution was added dropwise into a three-neck round bottom flask with 100 ml of Na_2CO_3 (Fisher, laboratory reagent grade) solution (0.58 M), while stirred. To maintain the pH of the reaction at 10, 100 ml of NaOH 1M was added dropwise, simultaneously. The temperature was controlled using a hot plate and an oil bath, keeping both the temperature and the stirring of the reactions always at 65 °C and 300 rpm,

respectively. Once the dissolved ochre solution addition was finished within the dropping funnel, the three-neck round bottom flask was sealed and put into an oven at 70 °C to age the product for 24 hours. Immediately after the aging process, the crude mixture was filtered using a Büchner funnel and filter paper to recover the precipitate. The solid product was washed with 1 liter of de-ionized water and subsequently left in the oven at 70 °C for 24 hours to dry. After drying, the solid material was ground and sieved using a 250-micron sieve, leading to a fine brown powder. For a structural and catalytic comparison with the ochre derived LDH, another LDH using high purity metal salts was synthesized. A 0.04 M solution (40 mmol) of $MgCl_2.6H_2O$ was mixed with a 0.02 M solution (20 mmol) of $FeCl_3$., which was added dropwise into 100 ml of 0.58 M solution of Na_2CO_3 inside a three-neck round bottom flask using NaOH to regulate the pH at 10. The rest of the methodology follows exactly as before.

5.2.3 Ketonic decarboxylation reaction procedure

0.4004 g (2 mmol) of dodecanoic acid ($C_{12}H_{24}O_2$, TCI, 98%) was reacted at temperature ranging from 250 to 350 ℃ with different catalyst loadings (5% wt., 3% wt. and 1% wt. with respect to the feed of dodecanoic acid, in grams) inside an autoclave (0.075 L Parr) using toluene as solvent (analytical grade, Fisher) to convert the dodecanoic acid into the homo-ketonisation product, 12-tricosanone. Once sealed, the autoclave was purged with nitrogen four times to remove any trace of oxygen within the vessel. Afterwards, the autoclave was heated up to the desired temperature and left to react for one hour. Once the reaction time was over, the vessel was left to cool down and, once at room temperature, the crude product was taken out of the reactor using a 20 ml pipette. Further details about the autoclave use, see Chapter 2, Section 2.10.

5.2.4 Analysis of crude reaction product

The crude product was put into a 50 ml falcon tube and centrifuged using a Beckman Coulter Avanti J-20XP centrifuge (3000 RPM, 15 min) to separate the solid catalyst. The crude product was analyzed using a Shimadzu GC- 2010 instrument with a flame ionization detector (FID) with a HP-5 30 m length, 0.25 mm internal diameter and 0.25-micron film

thickness coating column (stationary phase: *5*% diphenyl / 95% dimethylpolysiloxane) using hydrogen (H_2) as the carrier gas. Before injection, a calibration curve using the internal standard method for the amount of the expected ketone was performed in order to perform the quantitative analysis (see Figure A-1, Appendix A).

5.3 Results

5.3.1 Saltburn ochre and as synthesized LDH-CO_3 (ochre derived and synthetic) characterization

The results from the ICP-OES analysis of the Saltburn ochre and the as synthesized LDH-CO_3 (ochre derived and synthetic) are shown in Table 5-1. To avoid confusion, the ochre derived LDH was named LDH-CO_3 whereas the synthetic LDH was termed SLDH-CO_3. The presence of different metals in the Saltburn ochre can be observed, with Fe being the most abundant by an order of magnitude, followed by Ca. The average amount of water in Saltburn ochre corresponds to 78.2% (See Table B-1, Appendix B). For the LDH-CO_3, the analysis suggests that the synthesized material contains an Mg/Fe ratio of 3 rather than the expected ratio of ~3.8. This reflects variability of composition of the Saltburn ochre, and assumption in the ochre being composed mainly of FeO(OH) in the calculated composition. The low-saturation method for co-precipitation was used for the synthesis of the LDH materials as it produces more crystalline precipitates when compared with the high saturation method, as well as being more commonly used for the synthesis of LDH materials [103]. Based on the obtained Mg/Fe ratio of 3 and following the literature [245,246], the estimated formula, $\left[Mg^{2+}_{0.75}Fe^{3+}_{0.25}(OH_2)\right]^{0.25+}(CO_3^{2-})_{0.125}\,.mH_2O$ for the LDH-CO_3 was calculated. In the same manner, and according to Table 5-1, the Mg/Fe ratio of SLDH-CO_3 was calculated and a value of 2.11 was obtained. The chemical formula of SLDH-CO_3 was calculated as $[Mg^{2+}_{0.68}Fe^{3+}_{0.32}(OH_2)]^{0.32+}(CO_3^{2-})_{0.16}.mH_2O$.

Table 5-1. Concentration of metals present in the Saltburn ochre and LDH-CO_3 samples dissolved in HCl (ppm), from ICP-OES analysis.

Element	Concentration (ppm) in 5 g of Saltburn Ochre	SD*	Concentration (ppm) in 15 mg of LDH-CO_3	SD*	Concentration (ppm) in 15 mg of SLDH-CO_3	SD*
Mg	32.4	1.4	270	37.8	190	30.5
Fe	6091	17.6	210	15.2	210	20.8
Ca	499.1	1.5	15	2.1	0.52	0.01
Si	12	0.12	8	2.8	6.6	2.8
Ba	0.4	0.1	0.94	0.5	0.94	0.5
Tb	1	0.012	0.77	2.3	0.31	2.3
K	0.09	0.1	0.72	0.6	0.56	0.6
Mn	6.3	0.1	0.62	0.1	1.1	0.1
Na	2	0.1	0.57	0.1	4.1	0.1
Sr	10.8	0.1	0.55	0.04	-	-

*The rest of the minor metal constituents are shown in the Appendix B, Table B-2. SD means standard deviation, of concentration measured in triplicate.

TGA analysis of the Saltburn ochre was performed to observe if any organic matter was present within the sample. The plot is shown in Figure 5-1, together with the one belonging to the LDH-CO_3 and it can be observed that the materials have very different mass loss profiles. The ochre sample loses mass in two main steps, one in the region of the 200 °C and the next one in between 200 °C and 650 °C. The first mass loss is due to the removal of physisorbed water on the sample, whereas the second one relates to the dehydroxylation of the sample as all the α-FeO(OH)(goethite) was completely transformed to α-Fe_2O_3 (hematite) [251-253], with the latter confirmed by XRD data of a calcined Saltburn ochre sample at 800 °C (Figure B-1, Appendix B). TGA analysis of the LDH-CO_3 exhibits a typical three stage decomposition, [254] with a total mass loss of 39.5% as the temperature reached 650 °C. These mass losses are due to the water adsorbed (up to *ca* 120 °C) and in the interlayer (up to 250 °C) being removed, followed by dehydroxylation and loss of the interlayer carbonate species, resulting in spinel formation at above 750 °C [103,254-256]. SLDH-CO_3 exhibited the same behavior as LDH-CO_3, as observed in Figure 5-1. Thus, the

two larger mass losses can be attributed to dehydroxylation and decomposition of the carbonate species existing in the interlayer.

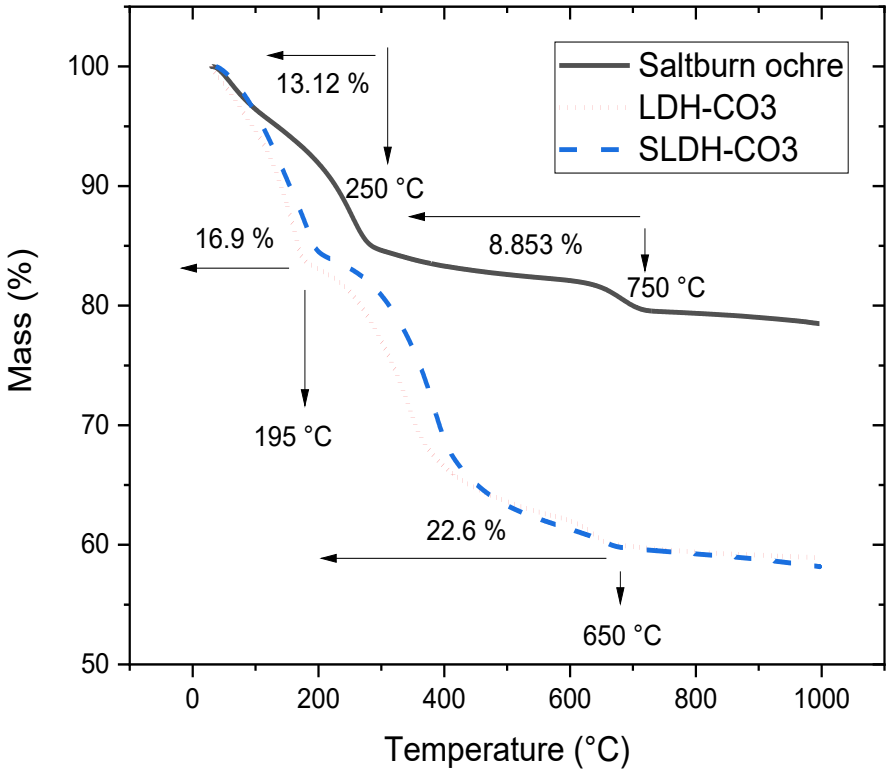

Figure 5-1. Thermogravimetric analysis of the Saltburn ochre and the as synthesized LDH-CO_3 and SLDH-CO_3 samples under a N_2 atmosphere.

The mineralogy of the Saltburn ochre was analyzed using powder XRD, as shown in Figure 5-2(a). The main reflections present in the sample are from goethite (α-FeO(OH)), which is generally the main iron phase observed in ochre [150]. The broad background feature arises owing to fluorescence effects associated with Fe phases. When compared to the powder XRD pattern of the ochre, it is clear a new phase has been formed in the LDH synthesis.

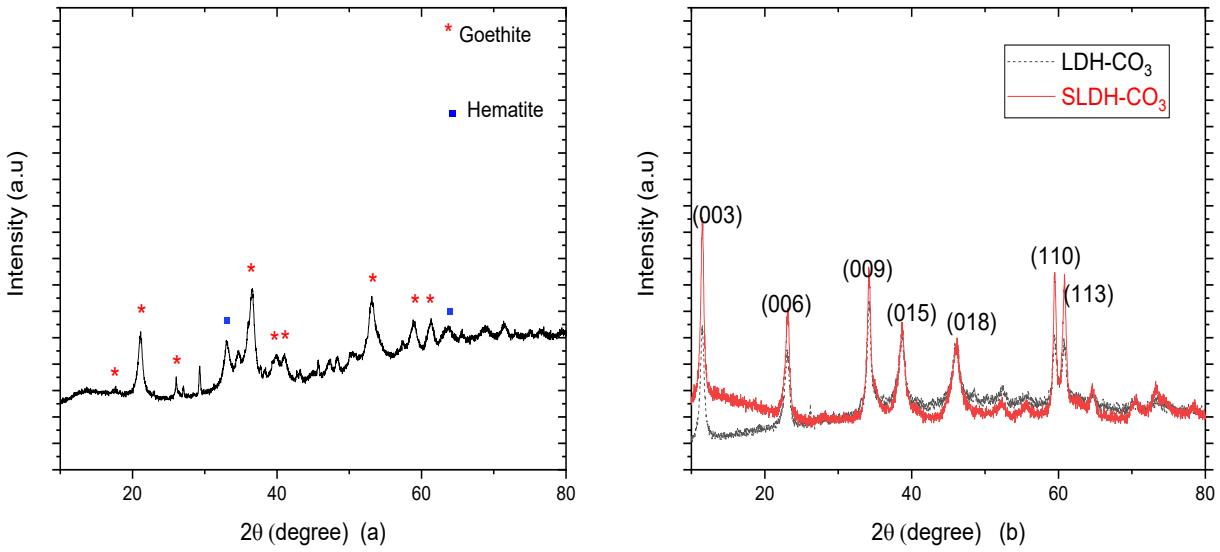

Figure 5-2. (a) Powder X-ray diffraction pattern of the Saltburn ochre. Characteristic reflection peaks from goethite can be observed as denoted by *; (b) Powder X-ray diffraction pattern of the synthesized LDH-CO3 and SLDH-CO_3 with characteristic diffraction peaks for LDH structures

The sharp reflections from the XRD pattern observed in Figure 5-2(b) correspond to those characteristic of LDHs, showing that the as synthesized material by the co-precipitation method is a well crystallized LDH [102,257-259]. The basal *d*-spacing and interlayer repeat distance from the sample LDH-CO_3 is 7.68 Å, typical for carbonate containing LDHs [103]. The crystal cell *a* parameter was calculated as 3.103 Å (using $a = 2d_{(110)}$), and the crystal cell *c* parameter (calculated as $c=3d_{(003)}$) was 23.1 Å in accord with the literature [123,254,260,261] and as explained in Chapter 2, Section 2.1. The broad background feature may be due to fluorescence, or possibly the presence of an amorphous Fe oxide phase. Using the same methodology, crystal cell parameters were calculated for SLDH-CO_3. The values of the *d*-spacing and interlayer repeat distance, as well as the values of *a* and *c* were 7.73 Å, 31.01 Å and 23.19 Å, respectively.

The FTIR spectra from the Saltburn ochre and the LDH-CO_3 and SLDH-CO_3 samples are presented in Figure 5-3. Principle adsorptions corresponding to the LDH are a broad adsorption band from 3000 to 3500 cm^{-1}, with an observable peak at 3410 cm^{-1}, corresponding to hydrogen bonded –OH and interlayer water [103,260], and a distinctive intense absorption at 1356 cm^{-1} corresponding to carbonate anti-symmetric stretching as well as an observable shoulder close to 2900 cm^{-1} related to stretching bonding of H-bonded

molecules (O-H bonded to the CO_3^{-2} in the interlayer) [256,259,262,263]. Regarding the Saltburn ochre sample, the peaks observed at 797 and 885 cm^{-1} can be attributed to those characteristic of goethite, due to the deformation of the O-H bonds [264-266], supporting the data obtained from the XRD. Taken together, XRD, TGA and FTIR analysis all confirm that the original ochre is comprised mainly of goethite and the material has been substantially, if not completely, re-precipitated as an LDH material.

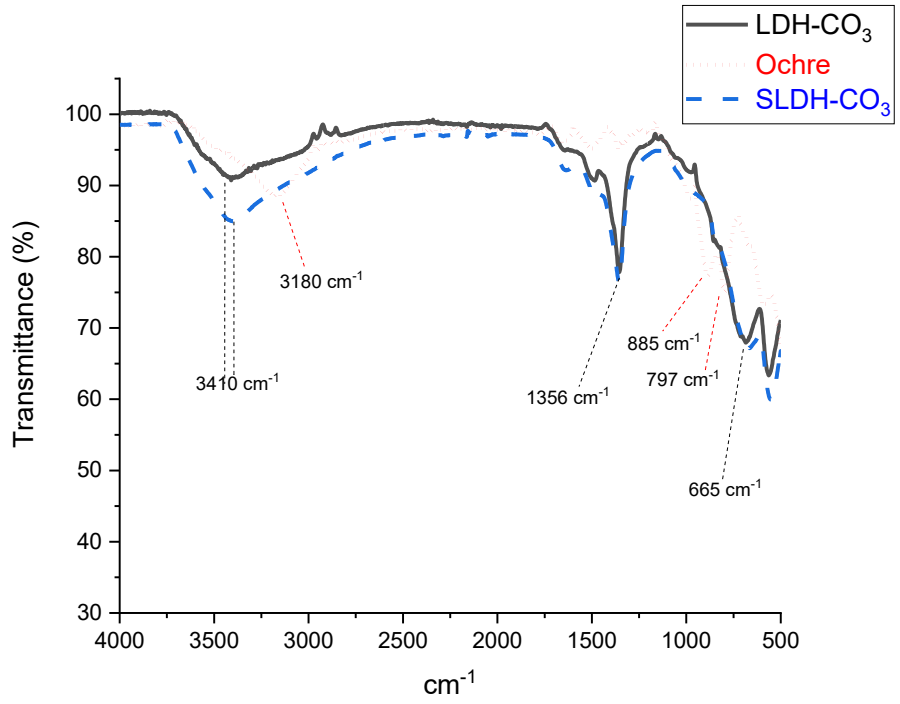

Figure 5-3. Fourier transform infrared spectra of both LDH samples and Saltburn ochre. OH stretching from 3000 to 3500 cm^{-1}. Stretching of the C=O bonds at 1356 cm^{-1}.

The plots from the nitrogen adsorption and desorption isotherms for calculation of the specific surface area as well as the pore size distribution curve are presented in Figure 5-4, for the BET (a) and the Barrett-Joyner-Halenda (BHJ) (b and c) methods, for both catalysts.

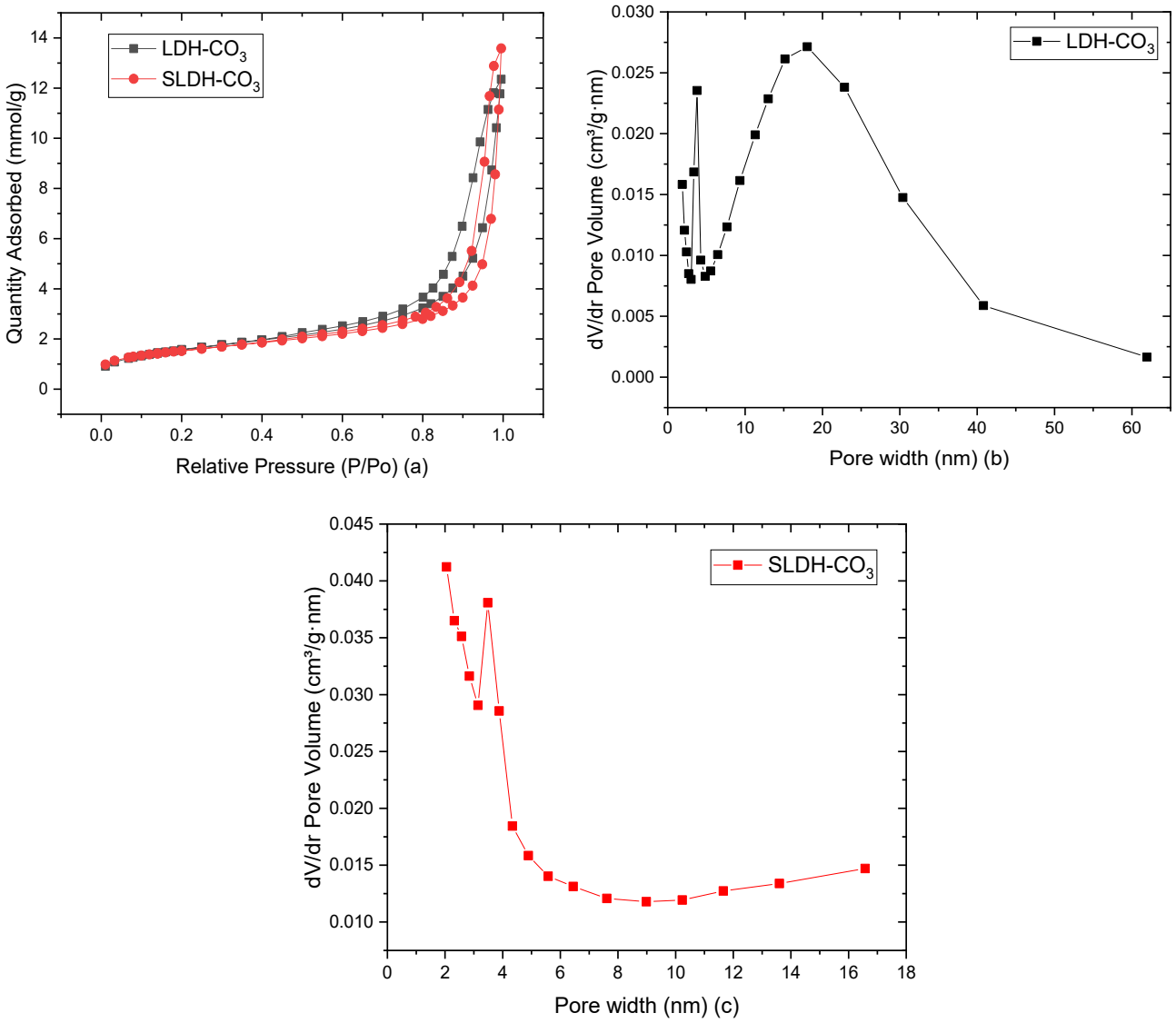

Figure 5-4. Nitrogen adsorption/desorption isotherms of the LDH-CO_3 and SLDH-CO_3 (a). Pore size distribution curves of the LDH-CO_3 (b) and SLDH-CO_3 (c). Regarding the BJH method, both samples were separated in two different plots.

The materials exhibited a classical Type IV isotherm related with mesoporous materials [159,164] with a narrow hysteresis loop, which means that the pores are uniformly distributed in a narrow arrangement [159,164]. This distribution was confirmed by Figure 5-4(b) for the LDH-CO_3 in which it can be observed that the majority of the pores are distributed between a width of 9 nm and 40 nm. On the other hand, the majority of the

mesopores for the SLDH-CO_3 were up 20 nm of width. A summary of the specific surface, pore volume as well as pore size for both samples can be observed in Table 5-2.

Table 5-2. Obtained results from specific surface area and pore parameters from the BET and the BHJ for the ochre based LDH (LDH-CO_3) as well as the synthetic one (SLDH-CO_3).

Parameter of the material	**LDH-CO_3**	**SLDH-CO_3**
Specific surface area (m^2 g^{-1})	125.91	20.92
Pore volume (cm^3/g)	0.39	0.13
Pore width (nm)	14.90	2.90

According to the reported data in Table 5-2, the BET surface area as well as the pore size parameters seem to be in agreement with the literature [102,267] for LDH materials, although they can vary between samples.

5.3.2 LDH-CO_3 as a catalyst for the ketonic decarboxylation of dodecanoic acid

Ketonic decarboxylation reactions were carried out using the ochre derived Mg/Fe LDH-CO_3 as a heterogeneous base catalyst, with dodecanoic acid (dodecanoic acid) as the substrate at two different temperatures (250 ℃ and 300 ℃) and with different catalyst loads ranging from 1% wt. to 5% wt. with respect to the feed in grams, as shown in Section 5.2. The results are presented in Figure 5-5. Conversion was considered to be 100% as well as selectivity towards the ketone, as no other significant peaks were observed in the chromatograms of the crude product mixture (Figure A-2, Appendix A) and as performed in our previous study [102]. To screen the potential use of Saltburn ochre as a heterogeneous catalyst and the capability of the waste material to promote the formation of ketones compared with the synthetic LDH-CO_3, 5% wt. of the Saltburn ochre was tested under the same conditions as those detailed in Section 5.2.4 for a reaction temperature of 300 ℃. The ketone yield was 16%, much lower (relatively) than that obtained with the as synthetic LDH-CO_3. Moreover, the SLDH-CO_3 catalyst was also screened in order to compare the activity of this material, made with high purity reagents, with the activity showed by the LDH-CO_3,

which was synthesized with the waste material ochre. The screening of the catalyst was performed once under the same conditions presented in Section 5.2.4 at a reaction temperature of 300 ℃ (Table B-3, Appendix B), as observed in Figure 5-5. Some literature reports state that for ketonic decarboxylation to occur, temperatures of above 320 ℃ are required [83,95]. In addition to this, in a previous study using LDH to favour the ketonisation, ketonic decarboxylation was achieved at 250 ℃ [102]. In addition, a control was performed where dodecanoic acid was screened without solvent and catalyst to temperatures at 300 ℃ and above, which resulted in decomposition of the reactant into volatiles and with no trace of ketone in the remaining crude product in the reaction vessel. Thus, taking into account the results when screening temperatures over 300 ℃ for these experiments and the results from our previous study, the temperature was set to two values, i.e., 250 ℃ and 300 ℃, for evaluation of the ketonisation reaction. For the evaluation of the LDH-CO_3, each reaction was carried out in triplicate, and, as observed in Figure 5-5, error bars show the standard deviation existing for each catalyst load percentage at both temperatures. However, regarding the 250 ℃ points, the deviation was so small that they can barely be discerned relative to the size of the data point markers.

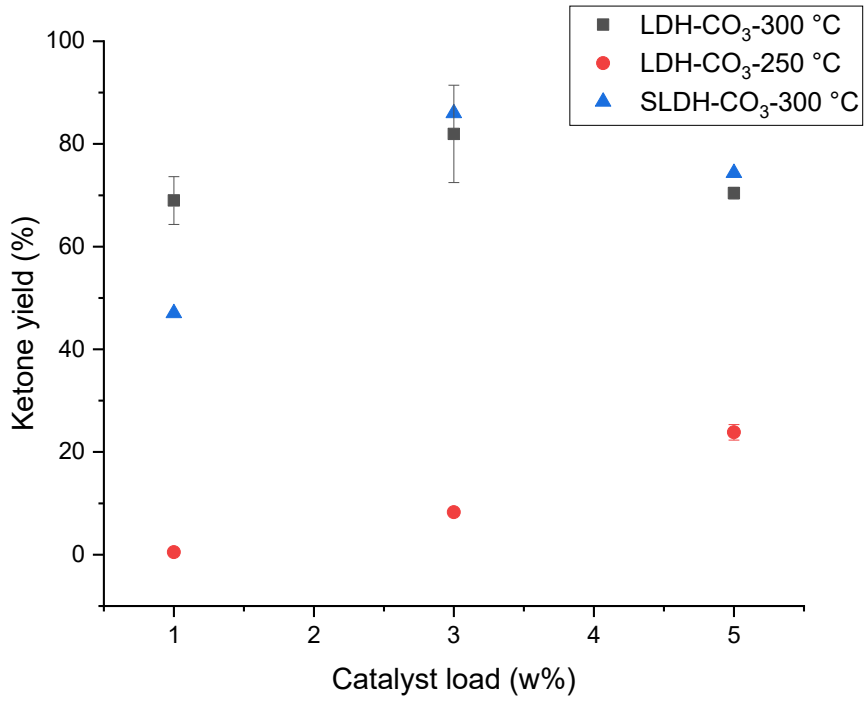

Figure 5-5. Yield of 12-tricosanone derived from the ketonic decarboxylation of dodecanoic acid with the LDH-CO_3 and SLDH-CO_3

It can be observed from the data above (Figure 5-5), that the ketonic decarboxylation of dodecanoic acid using the SLDH-CO_3 exhibited a higher conversion of the latter into the desired ketone, however, the difference in ketone yield between the two catalysts is slight. Nevertheless, an appreciable difference was observed at 1% wt. catalyst loading, where the LDH-CO_3 (i.e., the one made using the Saltburn ochre) delivered a better result than the synthetic one.

5.4 Discussion

Here, we valorise a waste product, ochre, from the Saltburn Gill treatment scheme, that would have otherwise been landfilled, through converting it to a Mg/Fe LDH-CO_3 solid base catalyst material. Though we use here a purchased Mg salt, waste streams containing dissolved Mg may be identified in order to accrue further environmental and sustainability benefits.

5.4.1 Characterisation of Ochre to LDH Conversion

Analysis of the ochre showed the sample was mainly goethite (ICP and XRD) with some Si, Ca compounds and water, with no observable presence of any organic matter, agreeing with the literature [150]. Despite other metals being found within the ochre sample, as identified by ICP-OES in Table 5-1, the high level of Fe made it a suitable donor waste material for the synthesis of the Mg/Fe LDH. The formed LDH structures have a very different XRD pattern to the ochre (Figure 5-2(a) and Figure 5-2(b)), and are low order, polycrystalline materials and have characteristic sharp, intense basal reflections with preferred orientation low 2θ angles and with almost equally intense, symmetric reflections at high 2θ angles, as seen in Figure 5-2(b) [102,257,258]. The obtained lattice parameters *a* and *c*, which represents the cation-cation distance in the layer and three times the distance in adjacent brucite-like layers, respectively, fits very well with the reported data for synthetic layered double hydroxides and natural hydrotalcites in the literature, with *a* and *c* values of 3.06 and 23 Å, respectively reported by Brito *et al.,* [255]. Cavani *et al.,* [103] reported values from 3.05 to 3.11 Å for *a* whereas for *c* values from 22.81 to 23.41 Å were reported. Other similar values of *a* and *c*, 3.04 and 23.64 Å, respectively were also reported by Cocheti *et al.* [268]. The symmetrical nature of the (011) reflections is interesting, indicating low turbostratic disorder within the prepared Mg/Fe LDH. The FTIR data provided further information about the LDHs materials, with hydrogen-bonded OH groups stretching evident in the region 3000 to 3500 cm^{-1} [256,262], related to the existence of water in the interlayer, with no similar high wavenumber vibrations in the ochre spectra, where interlayer regions are not present. The presence of a peak at 1356 cm^{-1} related to the carbonate anion is due to the anti-symmetric stretching of the C-O bond [103,259]. The data is characteristic of LDHs [269,270], supporting the XRD data above regarding a successful synthesis of the desired LDH material. The latter can also be supported with the FTIR plot of the Saltburn ochre observed in Figure 5-3, with

the characteristic goethite peaks at 797 and 885 cm^{-1} [264-266] and their total disappearance in the LDH spectra. No sharp absorbance was observed *ca* 3700 cm^{-1}, which would also indicate the presence of a brucite ($Mg(OH)_2$) phase. The nitrogen adsorption and desorption isotherms proved the mesoporous nature of the as synthesized LDH material (LDH-CO_3), with a narrow distribution of pore size and a relatively high surface area, both desirable characteristics for heterogeneous catalysts, with good adsorption properties favouring the diffusion of products and reactants [271]. When compared with the latter, the BET surface area calculated for the SLDH-CO_3 is smaller (see Table 5-1) however, when evaluated for carrying out the ketonic decarboxylation reaction at 300 °C, the yield of ketone produced was similar to the material with higher surface area (Table B-3, Appendix B), showing that the existing difference between both samples in terms of area might not be significant enough to effect product yield. The target ratio (R-value) of Mg^{2+}/Fe^{3+} for this study was ~3.8 to 4, however, and according to the ICP-OES analysis of the LDH-CO_3 sample, a ratio of Mg^{2+}/Fe^{3+} of 3 was obtained. The amount of Mg present in the LDH-CO_3 was less than expected according to the stoichiometry of the reactants used for the synthesis of the material. We speculate that this was due to the presence of amorphous Mg/Fe oxides in the sample as no other appreciable phases related to Mg, (for example $Mg(OH)_2$ or MgO) or Fe (for example FeO(OH) are observed either in the PXRD pattern or the FTIR spectra [272]. On the other hand, a Mg/Fe ratio of 2.1 was obtained for the SLDH-CO_3, as expected when synthesized, with the desired synthesis R-value set at 2. The use of ochre, therefore, may present a challenge in terms of obtaining well defined Mg/Fe ratios.

It should be noted that the stoichiometry for the Mg^{2+}/Fe^{3+} ratio for the LDH-CO_3 was based in the amount of iron present in the Saltburn ochre, which was first measured using ICP-OES on the latter and allowing for the dewatering analysis described in Table B-1, Appendix B. The element composition given in Table 5-1 is an average of the concentration of metals in the Saltburn ochre for several samples, with distribution being slightly heterogeneous owing to the nature of the waste material. The amount of M^{3+} substitution present in the layer, in this case, the Fe^{3+} cation, can vary depending on the methodology used for the synthesis as well as the conditions of the latter. A ratio of M^{2+}/M^{3+} varying from 2 to 6 has been observed in synthetic LDHs in the literature, with natural minerals mainly presenting a ratio of 2 or 3 [123]. The TGA plot in Figure 5-1 delivers a clear comparison between the as synthesized LDH-CO_3, SLDH-CO_3 and the Saltburn ochre. It can be observed

that, as expected and in agreement with the XRD and FTIR data, the ochre was transformed completely into the LDH material and the decomposition curve changed considerably as a result. Ochre is mainly composed of goethite, as observed in Figure 5-2(a), and all the mass loss observed in Figure 5-1 is due to the loss of adsorbed water and the dehydroxylation of the sample, with the goethite completely transformed into hematite when temperatures reached 700 °C and above [150,251,253]. When observing the TGA curve for both the LDH-CO_3 and SLDH-CO_3, literature reports a classical two stages decomposition in hydrotalcite-like materials, with the first mass loss due to the physisorbed and interlayer water, which ends at around 200 °C, and a second mass loss from 200 °C to approximately 600 °C due to the dehydroxylation and decomposition of the carbonate anion in the interlayer [103,254-256]. Both processes can be considered endothermic and dependent on different factors such as the cation ratio, pre-treatment of the samples and type of anions in the interlayer [103].

5.4.2 Ketonic decarboxylation of dodecanoic acid

The catalyst load and the temperature at which each reaction was performed have a direct impact on the formation of ketone. Thus, when no catalyst was used, ketone production did not occur. However, in the presence of catalytic amounts of the LDH materials, the ketone started to be generated, in lower yields at lower temperatures (250 °C) and in much higher yields when the temperature increased (300 °C), as shown in Figure 5-5. It should be noted that the raw Saltburn ochre did promote the ketonic decarboxylation of dodecanoic acid, however, the ketone yield was low (16% at 300 °C) when compared with those obtained with the Mg/Fe LDH-CO_3. Even though the ketone yield was low, the Saltburn ochre, which is mainly composed of goethite (see Figure 5-2(a)) did show some activity as a basic heterogeneous catalyst. The catalytic behavior of FeO(OH) has previously been observed for reforming or cracking of heavy oils [273,274], however, no reaction mechanism was described. According to recent literature, this catalytic behavior could be attributed to the presence of the existing O-H groups and the adsorbed carboxylic acids reacting through formation of a β-keto acid intermediate [82,102,239]. The need for a mineral surface to drive catalysis fits with the experimental data from other authors, indicating the surface plays a major role to promote the ketonic decarboxylation reaction, based on the organization of the reactants over the surface of the catalyst and the involvement of specific active sites

[102,206,275]. When no basic catalyst is present, the abstraction of the α-hydrogen does not occur which prevents the ketone forming [81]. In our previous study [102], up to 90% ketone yield was observed when Mg/Al LDHs were used at 250 °C for conversion of stearic acid, whereas in this study using the ochre derived LDH (LDH-CO_3) with dodecanoic acid, the highest ketone yield obtained at that temperature was 19% (see Figure 5-5). Higher conversion (of up to 80%) is attained with the LDH-CO_3 catalysts here at 300 °C. The effect of reaction time, substrate differences (dodecanoic *vs* stearic acid) and catalyst composition (Mg/Al vs Mg/Fe) is presently being investigated to understand these differences. The effectiveness of SLDH-CO_3 as a heterogeneous base catalyst to promote ketonic decarboxylation can be observed in Table B-3, Appendix B. Higher ketone yields were obtained when compared with the ochre derived LDH-CO_3 and it might be assumed that this is due to the purity of the reactants. However, the ketone yield obtained from the Saltburn ochre derived material with a catalyst loading of 3% wt. was close to the yield obtained with the high purity reactants, proving that ochre can be an efficient iron donor to produce highly active LDH materials, with impurities having negligible effect. Despite the different Mg/Fe ratio for both materials, the SLDH-CO_3 and LDH-CO_3, being different (2.11 and 3, respectively), our last study found that for different Mg/Al ratio LDH materials (from 2 to 6) similar behaviour for promoting ketonic decarboxylation was observed, suggesting the Mg/Fe ratio would have little effect and both samples can be compared for ketone production [102]. Several authors have pointed out that when reaching temperatures of around 300 to 450 °C, ketone formation from carboxylic acids can be enhanced [16,81,94,95], with a 100 % yield reached at 300 °C [95]. However, when temperatures of 450 °C or above were used, others have stated that the pyrolytic decomposition of the carboxylic acid takes over from the ketonic decarboxylation reaction [82,276]. In this manner, the increase in ketone yield observed in Figure 5-5 at 300 °C was not surprising, evidencing that neither long reaction times nor more than catalytic amounts of catalyst are needed to promote a ketone yield up to 80% [82,83,102].

5.3 Conclusions

Ochre, an Fe rich waste material produced from acid mine drainage treatment at Saltburn Gill, North East England, destined for landfill at cost to the taxpayer, was converted to a Mg/Fe layered double hydroxide (LDH) material, which was prepared with a M^{2+}/M^{3+} ratio of 3, of potential use as an industrial catalyst. The catalytic activity of raw Saltburn ochre was examined for its ability to carry out ketonic decarboxylation, however the performance of the latter was lower than the synthetic Mg/Fe LDH (LDH-CO_3 (i.e., which had used ochre as one of the main materials during its synthesis). Impurities in the ochre as received could have affected the synthesis process, but a number of analyses confirmed successful formation of the desired LDH, though with some loss of control of Mg/Fe ratio. This evidences the potential to convert materials with costly disposal routes into industrially relevant commodities, necessary to develop the circular economy. In an additive sustainable chemical process, this catalyst was tested for heterogeneous base catalyst activity for the ketonic decarboxylation of dodecanoic acid, a readily obtained component of plant oils. Short periods of contact time at temperatures of 300 °C and low catalyst loadings proved to be sufficient to promote up to 80% of ketone formation. The presence of trace impurities in the waste material appeared to have little effect on the reactivity, relative to materials tested in prior studies prepared from high purity chemical feedstocks [102]. This study delivers a proof of concept that moves beyond using green chemistry principles for the chemical reaction process, [277,278] to show how an efficient and green mixed metal catalyst can be obtained using ochre, a waste product from mine water treatment, to then undertake sustainable conversion of biomass derived fatty acids to provide a valuable feedstock, ketones. This exemplifies a circular economy approach with reagents sourced from waste materials and combined with sustainable processes based on biomass conversion.

6. Hydrogen production from a circular economy inspired catalysis: Photocatalysis activity of ochre-derived layered double hydroxide.

6.1 Introduction

The circular economy concept, where waste is revalorised and put to new use, has emerged in response to resource scarcity and energy demand required for mineral extraction and technology production, with consequent environmental impacts, as well as societal pressures [279]. As already explored in Chapter 5, in the UK, the waste mineral ochre (FeO(OH)) is producedLDHs have previously been prepared using waste materials with, for example, waste foundry sand derived Mg-Al LDHs used to successfully adsorb model pollutants, such as Congo red dye [280]. On a recent study, a dense porous LDH made of struvite, which is an undesirable product in wastewater treatment plants was produced by Kwok *et al.,* [141]. LDHs have also been prepared from boron mud and red mud industrial wastes, and used as phosphate sorbents, with the materials formed found to contain a wide variety of metals, such as magnesium, aluminium, calcium and iron [281]. LDH materials produced from ochre have previously been tested to promote ketonic decarboxylation of vegetable oil derived carboxylic acids, with good results, illustrating how circular economy and green economy principles can be integrated [114]. In this Chapter, and to further explore the capabilities of a LDH derived from the waste material ochre as a catalyst, not only for ketonic decarboxylation [114] (i.e., Chapter 5), but also to promote other clean energy reactions, the latter LDH material is studied here as a photocatalyst for the hydrogen evolution reaction. Hydrogen production from water has been exhaustively studied since 1972 as a process with no negative impacts on the environment [282,283]. The most widely studied material for photocatalysis over the past 20 years has been TiO_2 [284,285]. This is mainly due to the non-toxic and affordable character of TiO_2, however TiO_2 does suffer from some limitations, including not being able to absorb under visible light conditions and the existence of a broad band-gap (3.2 eV) [285-287]. Therefore, using TiO_2 to produce hydrogen yields a variety of results, with no agreement among the literature, as constant improvements develop to increase the ability of the material to harvest more energy from sunlight [286-288]. For example, Wang *et al.,* [289] obtained a hydrogen yield under UV irradiation conditions of 96.5 $\mu mol.g^{-1}h^{-1}$ using commercial TiO_2, which was later compared with the as synthesized, flower-like morphology, anatase nanospheres of TiO_2 yielding hydrogen production of 364.2 $\mu mol.g^{-1}h^{-1}$. In recent years, LDH materials have been used as

economical and effective photocatalytic alternatives to TiO_2 [290-292]. A wide diversity in yields of hydrogen production have been reported in the literature. Mg/Al/Fe – CO_3 LDHs yielded a production of 301 $\mu mol.g^{-1}h^{-1}$ under visible light conditions, using methanol as sacrificial agent [151], whereas Zn/Cr - NO_3 LDHs with CdS incorporated yielded 374 $\mu mol.g^{-1}h^{-1}$,also under visible light conditions[293]. For both studies, both LDH samples were poorly active towards visible light conditions. Once they were modified, the Mg/Al – CO_3 doped with Fe^{3+} and the Zn/Cr nanohybridized with CdS, production of hydrogen under visible light irradiation was possible. In terms of higher yields of hydrogen in the literature with LDHs, Zn/Cr LDHs have reportedly delivered a hydrogen production of 1732 $\mu mol.g^{-1}h^{-1}$ [294], again, under visible light conditions and using methanol as sacrificial agent. The latter study attributed the hydrogen production to the CO_3 in the interlayer playing a key role reducing the recombination effect, hence improving activity with visible light irradiation. Though a variety of LDHs have been tested for photocatalytic applications, to the best of our knowledge this is the first time an LDH material made of mining waste has been used to promote hydrogen production. In this chapter, an Mg/Fe based LDH $[Mg^{2+}_{0.8}\ Fe^{3+}_{0.2}(OH)_2]^{0.2+}.(CO_3^{2-})_{0.1}.yH_2O$ was synthesised by the co-precipitation method using the mining waste material ochre (mainly composed of goethite, FeO(OH)) as the Fe source (denoted LDH_{ochre}). Here, the ochre was obtained from the Saltburn Gill metal mine treatment scheme, Cleveland, UK and was characterised in Chapter 5. The produced LDH_{ochre} was evaluated for activity in hydrogen evolution catalysis. Results were compared with another Mg/Fe LDH of similar composition, made from high purity synthetic salts (denoted LDH_{syn}).

6.2 Experimental

As in Chapter 5, an LDH using ochre as one of the precursors was prepared. The desired M^{2+}/M^{3+} ratio was set again to 4, as concerns existed regarding the variability of the ochre in terms of the composition of the latter could prevent the formation of the desired LDH, or in case of the LDH forming, the targeted ratio could vary. Based on the latter concerns, a different approach in terms of stoichiometry was applied in this chapter, were the ochre's Fe^{3+} composition was based on data obtained by one of our group's master students, in which Fe^{3+} was considered to be 32 %wt. of the dry ochre waste. Following the same exact characterisation techniques, plus some other characterisation and measurement techniques regarding the hydrogen evolution reaction, an ochre derived LDH material was

synthesized and successfully evaluated as a hydrogen evolution catalyst. A brief description of the experimental, which was explained further in detail in Chapter 2, is presented below.

The ochre was provided by the Coal Authority, UK. The material was recollected from a primary drying lagoon at Saltburn Gill Water Treatment Scheme, located at Saltburn, Cleveland, UK. The latter drying lagoon corresponds to a treatment system for an ironstone mine. Powder X-ray Diffraction (PXRD) and Fourier Infra-red spectroscopy characterisation was taken from the obtained data used in Chapter 5, for the ochre sample.

6.2.1 Preparation of LDH_{ochre} and LDH_{syn}

To prepare LDH_{ochre}, 0.5 g of dried ochre (2.8 mmol of Fe^{3+}) was dissolved in 50 ml of 1 M HCl (Fisher, laboratory reagent grade) and mixed with 50 ml of a solution containing the Mg cation (2.35 g of $MgCl_2$.6H2O, 11 mmol of Mg^{2+}, Aldrich 99%). In a different approach to Chapter 5, Section 5.2.2, an excess of 3:1 of Na_2CO_3 (0.92 g Fisher, 8.6 mmol, laboratory reagent grade) with respect the amount of Fe used (32 %wt of ochre was considered to be Fe, with a standard deviation of 9 %) was dissolved in 100 ml of deionized water and poured into a three-neck round bottom flask and gently stirred until the temperature of the solution was 65 °C. The 3:1 CO_3^{-2} to Fe^{3+} excess was based on an unpublished work from our group, in which it was observed such excess ratio would be sufficient to favour the LDH formation. A pH meter was used to make sure the reaction pH was maintained around 10 to 11. The temperature was controlled through a hot plate and the flask heated using an oil bath. Once the temperature was stable, both Mg and Fe solutions were mixed and added dropwise through a dropping funnel. To keep the pH at 11, a solution of 1 M NaOH was also added dropwise (Aldrich, 99%). The stirring was kept at 700 rpm during the whole reaction. Once the reaction finished, the mixture was kept at 65 °C inside an oven and left age for 24 hours. The crude mixture was filtered using a Büchner funnel to recover the precipitate. The solid product was washed with 1 liter of de-ionized water and subsequently left in the oven at 70 °C for 24 hours to dry. To prepare $LDHs_{yn}$, the same methodology and respective stoichiometric calculations were applied, however, the Fe cation was obtained from iron chloride (FeCl3, Aldrich 99%).

6.2.3 Catalyst characterisation

All the characterisation techniques employed to characterise the ochre and the as-synthesised LDH materials used in this section of the study, have been explained in further details in Chapter 2 (i.e., PXRD, FTIR, TGA, ICP-OES, SEM, TEM and Nitrogen adsorption/desorption isotherms) therefore they will not be described further as the same methodology to prepare all the samples was applied during the development of Chapter 3 to Chapter 7.

6.2.4 Optical characterisation of LDH_{ochre} and $LDH_{syn.}$

Ultraviolet-visible Spectroscopy (UV-vis)

The optical characterisation of the as-synthesized LDHs was performed using a UV-vis NIR spectrophotometer (Cary 5000), setting the waveleght range from 200 nm to 800 nm. The instrument was coupled with an integration sphere for diffuse reflectance measurements. 0.5 g of the sample were used for such experiments.

Photoluminescence analysis

For the photoluminescence analysis, a fluorescence spectrophotometer (Agilent Cary Eclipse) was used. The excitation wavelength was set to the corresponding absorption band of the materials, with a scanning speed of 1000 nm/min. The experiments were performed at room temperature.

Photocatalytic activity of the LDH_{ochre} and LDH_{syn}

The photocatalytic hydrogen evolution test was performed by placing the sample (0.1 g) in a 250 mL glass reactor, using 200 mL of an aqueous solution (deonized water, and with 10% of MeOH for the sacrificial agent test). At the beginning of the test, N_2 was bubbled through the reaction media for 10 min to remove oxygen and other gases, prior to the reaction being initiated. Following the latter, the reactor was illuminated with a solar simulator integrated with a Xe lamp of 450 W. The H_2 produced was analised in a Thermo Scientific gas chromatograph coupled with a thermal conductivity detector, for every 30 min

during the 3 h experiment. No filter for UV was used for the experiment but, nevertheless, conditions similar to sunlight were approximated. The contribution to the spectrum caused by the UV is less tan 4 %.

6.3 Results

6.3.1 LDH_{ochre} and LDH_{syn} characterisation

In this study the Mg-Fe reactant ratio was set at 4, and it has been observed in previous studies that a M^{2+}/M^{3+} ratio of 2 produces a well-crystallized LDH with proven photocatalytic properties [294,295]. It is unclear whether the Mg/Fe ratio plays a key role in photocatalysis, and here we assess a lower Fe content. The target ratio was confirmed by energy dispersive spectroscopy (EDS) microanalysis using scanning electron microscopy (SEM), with a standard deviation calculation for both samples. The obtained EDS Mg/Fe for the LDH_{ochre} was 3.92 ± 0.7 and for LDH_{syn} was 4.14 ± 0.36 (Table B-4, Appendix B). The ICP-OES analysis gave bulk Mg/Fe for LDH_{ochre} and LDH_{syn} as 3.59 and 5.1, respectively.

Powder X-Ray diffraction (PXRD) confirmed the formation of an LDH in both samples [258,259], shown in Figure 6-1(a). Thus, a PXRD from the Saltburn ochre is also exhibited in Figure 6-1 (b). The low intensity reflections in Figure 6-1(a), although characteristic of LDH materials, indicate that neither sample was well-crystallized. Moreover, other phases were detected during the analysis, with some reflections corresponding to the ones of lansfordite ($MgCO_3$. 5 H_2O) as well as goethite (α-FeO(OH)). Figure 6-1(b) shows the reflections of the ochre sample with a broad background due to fluorescence, which is usually encountered

in samples with Fe phases. Characteristic peaks from goethite as well as hematite (Fe_2O_3) arise from the spectra, which are the main phases present in ochre.

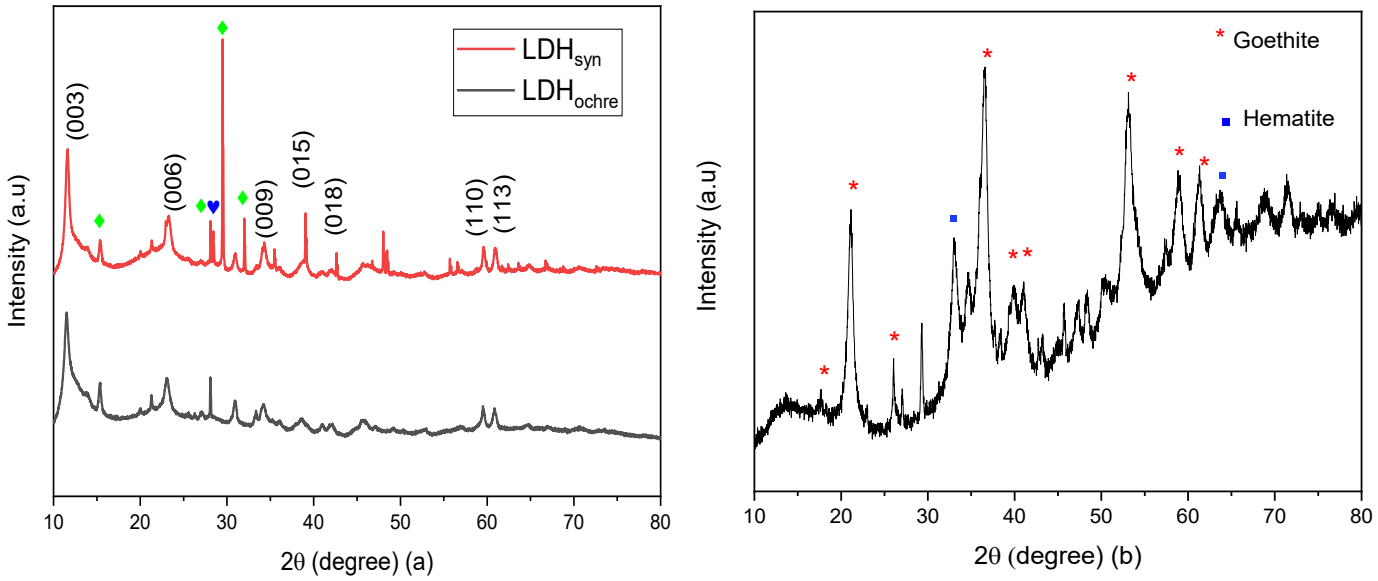

Figure 6-1. (a) Powder X-ray diffraction of LDH_{ochre} and LDH_{syn}. Typical LDH reflections could be observed, as well as the patterns related to lansfordite or hydromagnesite (green symbol) and goethite (blue symbol). (b) Diffraction peaks of the Saltburn ochre. Characteristic goethite and hematite peaks are observed.

A characteristic basal d-spacing, which corresponds to the LDH carbonate structure, was observed, of 7.76 Å and 7.60 Å for the LDH_{ochre} and LDH_{syn}, respectively [102,114]. The cell parameters a and c were also calculated, being 3.10 Å and 23.01 Å for LDH_{ochre}, and 3.09 Å and 22.8 Å for LDH_{syn} [254,260] (See Chapter 2, Section 2.1, for explanation on how to calculate the latter lattice parameters). Fourier transform infra-red (FTIR) spectroscopy data is displayed in Figure 6-2(a) for both, LDH_{ochre} and LDH_{syn}. Absorption peaks at 1359 cm^{-1} relate to the carbonate anti-symmetric stretching, and broad adsorption bands from 3000 to 3500 cm^{-1} associated with hydrogen bonded O-H which are characteristic of LDH are displayed [256,259]. The peaks at 680 cm^{-1} and 860 cm^{-1} could be assigned to the antisymmetric and symmetric deformation of the carbonate anion, v4 and v2, respectively [132,296]. Figure 6-2(b) shows the FTIR data from the ochre sample. Two characteristic goethite peaks are observed (797 and 885 cm^{-1}) due to the deformation of the O-H bonds [114]. There is a difference between both samples, LDH_{ochre} and $LDH_{syn,}$ regarding the intensity

of the peaks. As observed in Figure 6-1(a), both samples are not phase pure LDH, specifically LDH_{ochre}, as diffraction peaks corresponding to the presence of a lansfordite ($MgCO_3.5H_2O$) phase or a hydromagnesite ($Mg_5(CO_3)_4(OH)_2.4H_2O$) phase are observed. The latter presence of the lansfordite/hydromagnesite phase is also expected to be observed in the FTIR spectra at *ca* 1420 cm^{-1} and 1480 cm^{-1} [297,298], corresponding to the anti-symmetric stretching of the carbonate ion in these impurity phases, as showed in Figure 6-2(a). Moreover, the FTIR peak *ca* 580 cm^{-1} is also related to the presence of goethite within the sample [151], which agree with the observed PXRD plots for both samples. It can be noted then, that the peak assigned to the antisymmetric stretching of the carbonate anion in the interlayer of LDH_{ochre} (1359 cm^{-1}) is less intense when compared to the same peak for LDH_{syn}, whereas the peak at 1417 cm^{-1} in LDH_{ochre} related to the anti-symmetric stretching of the carbonate existing in the lansfordite/hydromagnesite phase is larger when compared to the same peak in LDH_{syn}.

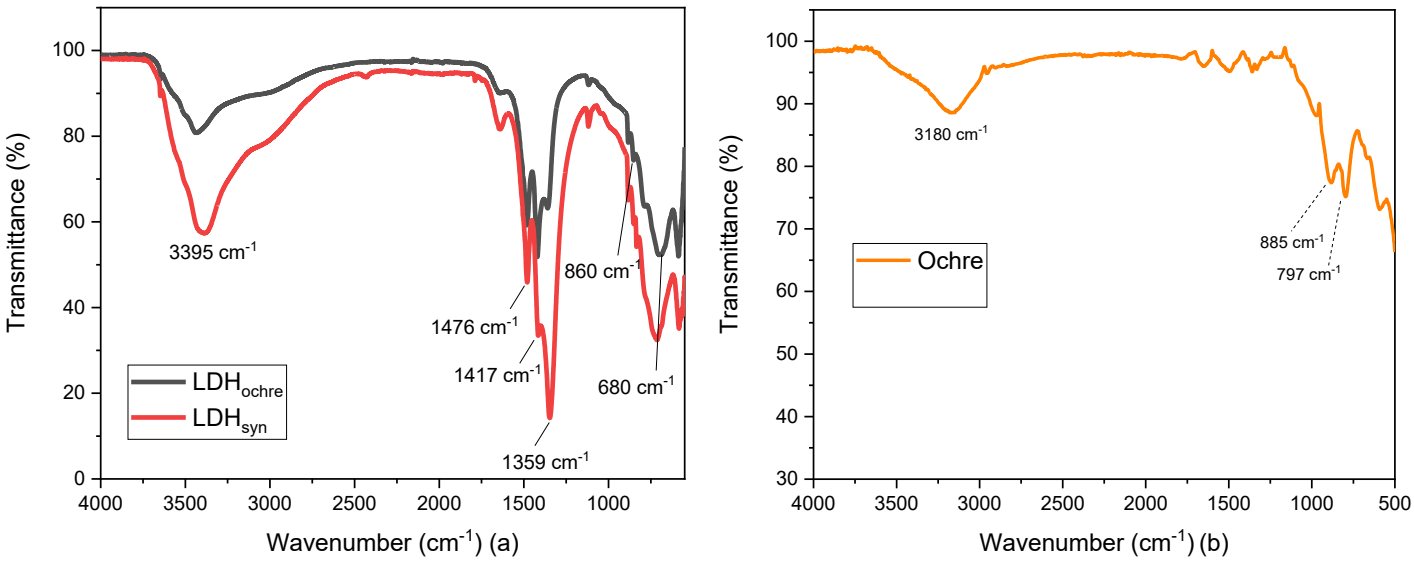

Figure 6-2. (a) Fourier transform infrared spectra of LDH_{ochre} and LDH_{syn}. Typical LDH C=O stretching at 1359 cm^{-1} are observed as well as the broad peak related to O-H at 3300 cm^{-1}. (b) Saltburn ochre Fourier transform infrared spectra with typical goethite related peaks at 797 and 885 cm^{-1} associated to the deformation of the O-H bonds.

Thermogravimetric analysis (TGA) profiles were obtained, as observed in Figure 6-3(a). For LDH samples, decomposition occurs in three different stages, typical for LDH materials [254], where adsorbed water (*ca* 120 ˚C) is lost followed by dehydroxylation and further decarboxylation of the LDH layers in following mass loss steps .

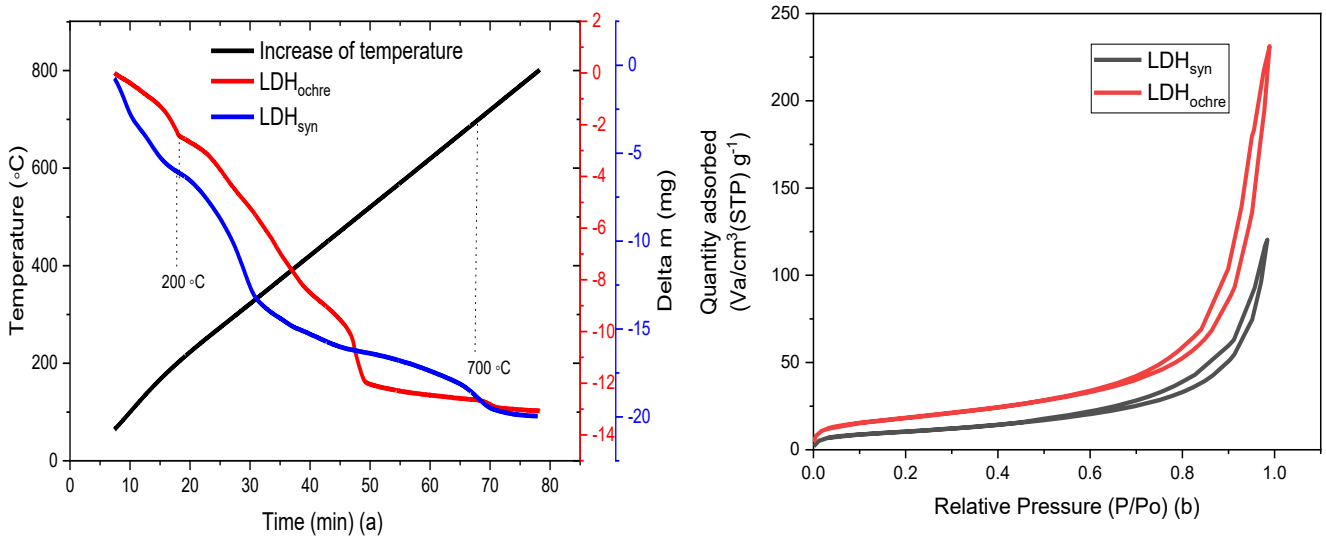

Figure 6-3. (a) Thermogravimetric analysis of LDH_{ochre} and LDH_{syn} under N_2 atmosphere with typical LDH decomposition stages. Adsorbed and interlayer water losses are observed ca 200 ˚C, followed by dehydroxylation and decarboxylation up to the spinel formation ca 700 ˚C (b). Nitrogen adsorption-desorption isotherms of LDH_{ochre} and LDH_{syn}.

Porosity of the material was evaluated by Brunauer-Emmet-Teller (BET) analysis, using N_2 adsorption and desorption measurements. The isotherms are shown in Figure 6-3(b). The LDH materials behave as mesoporous structures, with the a narrow hysteresis loop present in a type IV isotherm [160,164]. Surface area, as well as pore diameter and pore volume for the LDH_{ochre} were 66.5 $m^2.g^{-1}$, 21.51 nm and 0.35 $cm^3.g^{-1}$, respectively. For LDH_{syn}, the surface area, pore diameter and pore volume were 38.1 $m^2.g^{-1}$, 19.54 nm and 0.18 $cm^3.g^{-1}$, respectively.. SEM analysis gained insight into the morphology and structure of the LDH materials (Figure 6-4). Both samples, LDH_{ochre} and LDH_{syn}, Figure 6-4(a) and Figure 6-4(b), respectively showed a plate-like primary particle morphology, with agglomeration of the <

1 µm particles, frequently observed for LDH samples [299,300]. A TEM analysis trying to obtain further insight into the LDH sheets of LDH_{ochre} was performed, with the results presented in Figure 6-5(a) and Figure 6-5(b) for 500 nm and 200 nm magnification, respectively. From the TEM scan in Figure 6-5, typical pseudo hexagonal LDH crystals are observed[301].

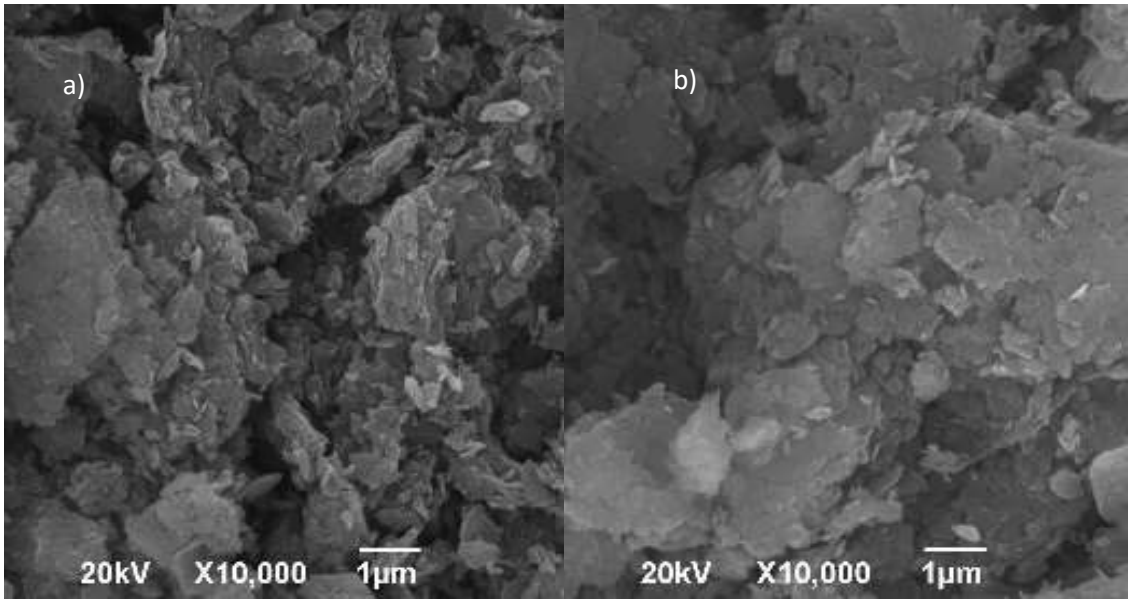

Figure 6-4. Scanning Electron Microscopy (SEM) of LDH_{ochre} (a) and LDH_{syn} (b). Plate-like structures are observed for both samples.

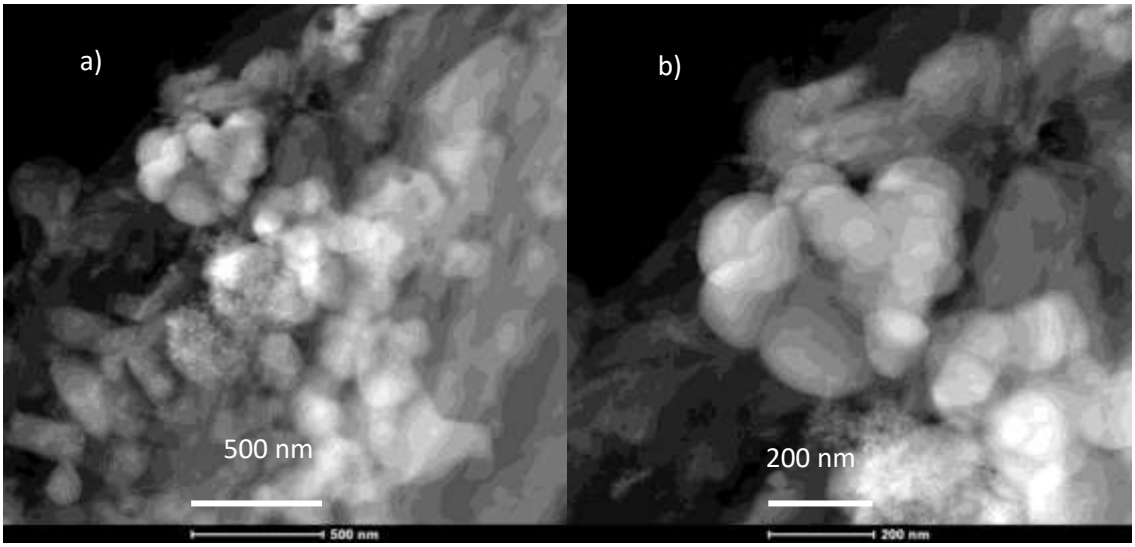

Figure 6-5. Transmission Electron Microscopy (TEM) of $LDH_{ochre.}$ (a) For a magnification of 500 nm and (b) for a magnification of 200 nm. Pseudohexagonal shapes are observed, typical of LDH materials.

6.3.2 Optical characterisation of LDH_{ochre} and LDH_{syn}

Optical characterisation of the material using UV-Vis (Figure 6-6), showed absorbance within the range 200 to 600 nm, which includes visible light. Both samples showed a similar maximum absorption at 265 nm, within the UV region.

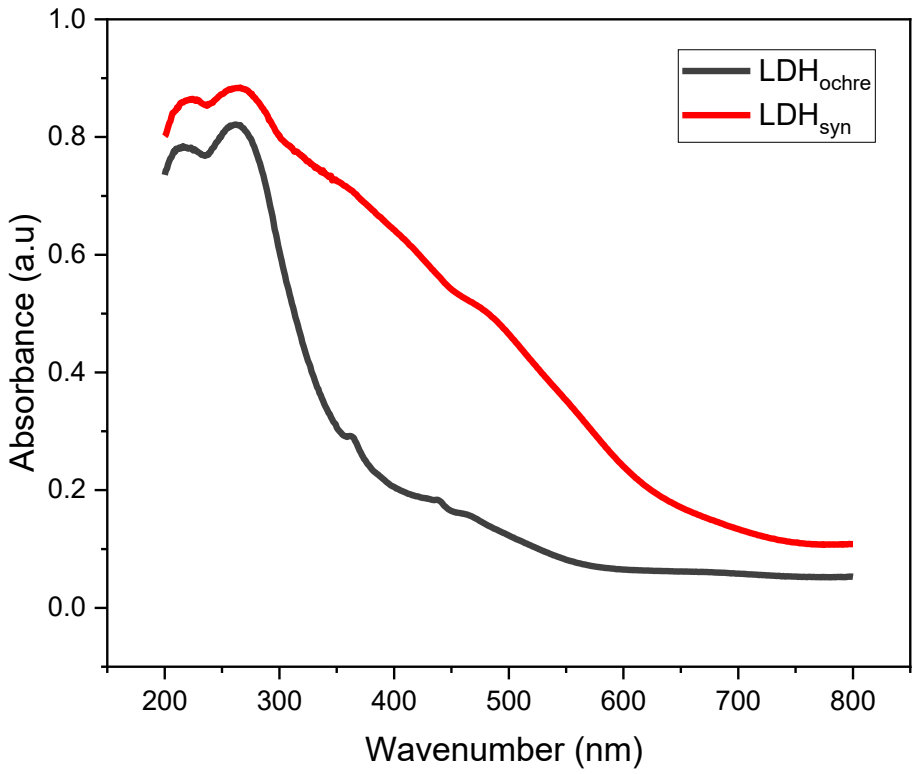

Figure 6-6. UV-vis characterisation of LDH_{ochre} and LDH_{syn} with maximum absorbance at 265 nm for both samples.

Figure 6-7 shows the data from the photoluminescence analysis, used to probe the recombination effect presented in both LDH samples. As observed in Figure 6-7, LDH_{ochre} presented a lower photoluminescence intensity compared with LDH_{syn}.

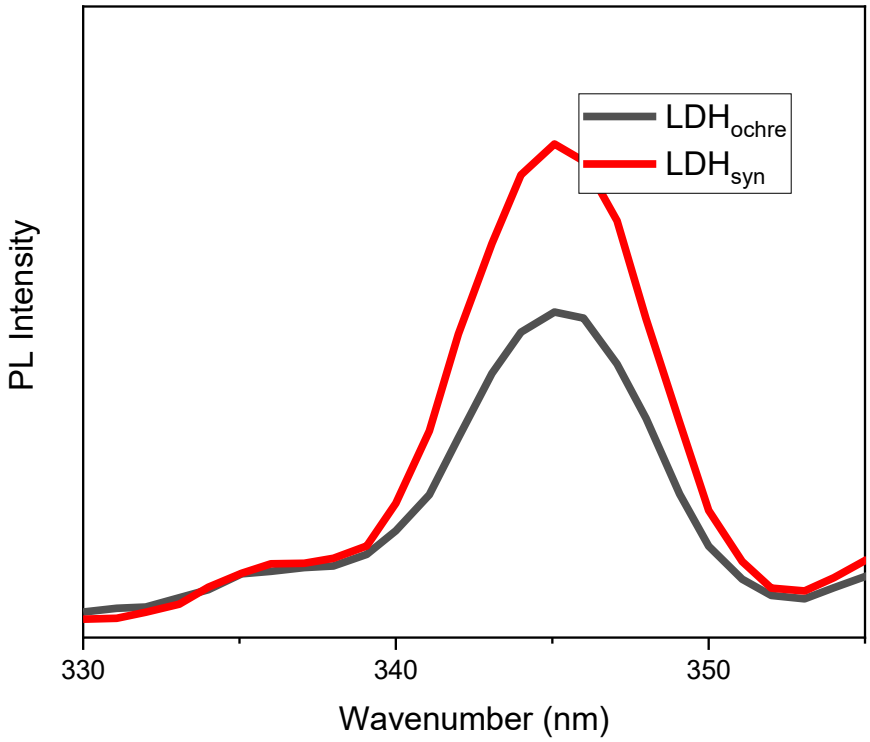

Figure 6-7. Photoluminescence spectrum of both LDH_{ochre} and LDH_{syn}.

6.3.3 Photocatalytic evaluation of LDH ochre and LDH syn for hydrogen evolution (H_2 evolution)

Following characterisation of both materials, photocatalytic testing used 200 ml of distilled water with a Xe lamp used as a solar simulator (450 W), with irradiation purely in the spectrum of solar light (i.e., visible light). Interestingly, when compared, the LDH_{ochre} showed a higher photocatalytic activity than the LDH_{syn}, as evidenced in Figure 6-8 for both, the aid of sacrificial agent (10% methanol) (a) and solely water (b).

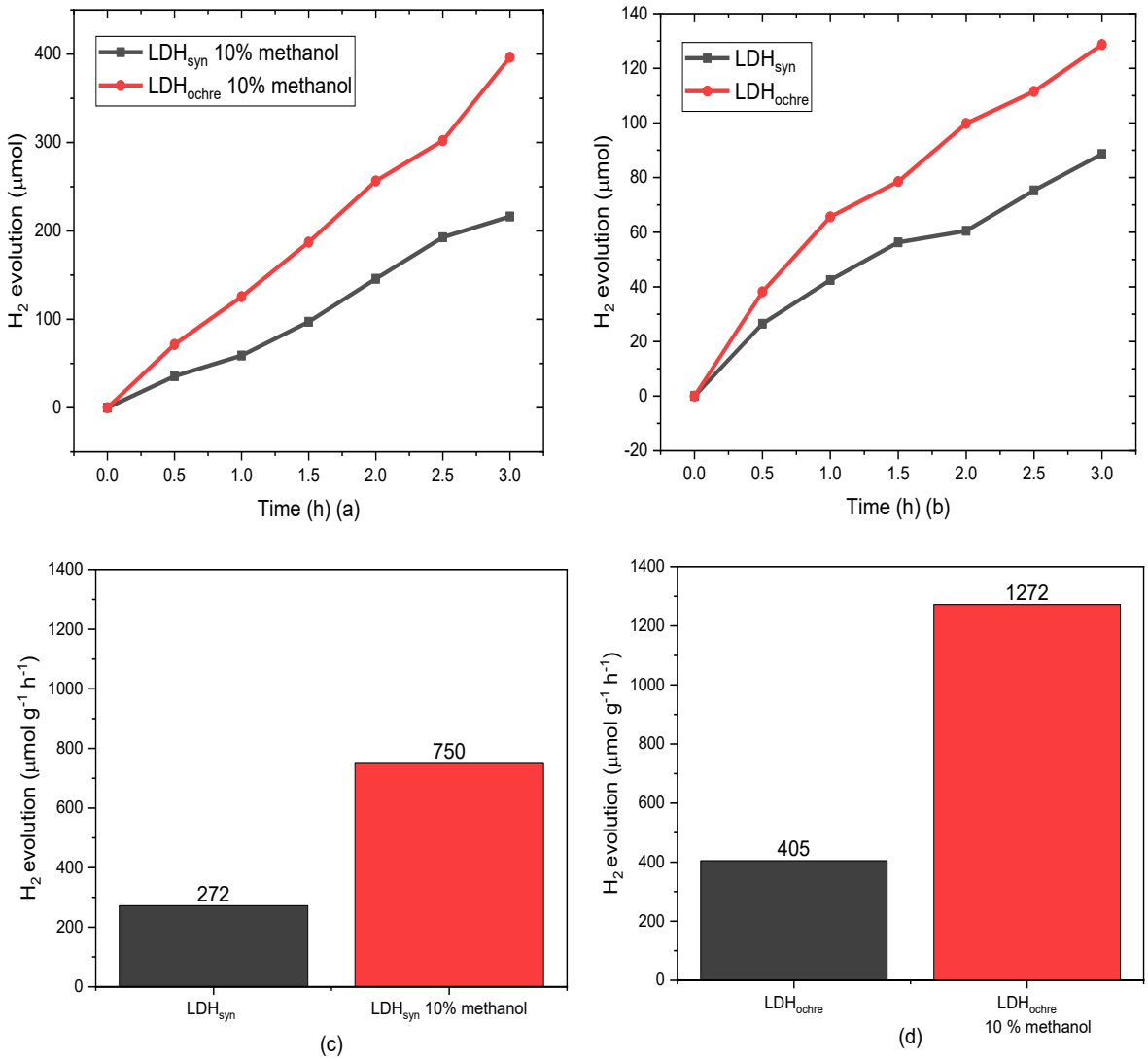

Figure 6-8. Evaluation of the H_2 evolution for both samples in Figure (a) and Figure (b) with an increased production regarding the material made of the waste ochre when compared to the one made of synthetic salts. Figure (c) and (d) show the production of hydrogen for both samples in $\mu mol.h^{-1}.g^{-1}$ using just water and with the aid of methanol as sacrificial agent.

Comparing Figure 6-8(a) and Figure 6-8(b), it can be observed that solely with water or with methanol acting as scavenger, production of hydrogen using the ochre made LDH was superior. The hydrogen production in $\mu mol.h^{-1}.g^{-1}$ is presented in Figure 6-8(c) and Figure 6-8(d) for both samples. From the latter it can be seen that LDH_{ochre} yielded a production of 1272 $\mu mol.h^{-1}.g^{-1}$, whereas LDH_{syn} produced 750 $\mu mol.h^{-1}.g^{-1}$.

6.4 Discussion

6.4.1 Characterisation of the LDH_{ochre} and LDH_{syn}

Due to the nature of the ochre and as observed in Chapter 5, not only Fe, are present within the LDH_{ochre} sample, however, as ochre is mainly composed by Fe (as observed through the PXRD and the FTIR), it was suitable to act as a M^{3+} donor during the synthesis of the LDH through co-precipitation method. The PXRD patterns observed in Figure 6-1(a) denotated a poor crystallinity for both samples with broad reflections and the presence of impurity phases, particularly in the ochre derived LDH materials (i.e., LDH_{syn}). Though synthetic LDHs tend to be polycrystalline, increased crystallinity is typically observed in those samples with M^{2+}/M^{3+} = 2, owing to this ratio allowing a perfectly ordered arrangement of the M^{3+} species. Here, the lower Fe content in the Mg^{2+}/Fe^{3+} = 4 samples may give a reduction in crystallinity [102,295] and unfavoured the formation of phase pure LDH material. The basal *d*-spacing parameter as well as the cell parameters *a* and *c* for both, LDH_{ochre} and LDH_{syn} are in agreement with the ones corresponding to typical LDH synthesis [102,114,260]. Some of the goethite phase observed in Figure 6-1(b) is still present in Figure 6-1(a), as a phase pure LDH material was not obtained. Moreover, from Figure 6-1(a) it also can be seen that there is a lansfordite/hydromagnesite phase in the samples. The latter is further supported by the asymmetric stretching carbonate peaks *ca* 1420 cm^{-1} and 1480 cm^{-1} in Figure 6-2(a). The lack of phase pure LDH material could be attributed to synthesis difficulties, such as a more precise control of pH and stirring system. Nevertheless, the FTIR plots in Figure 6-2(a) supported the PXRD data with a sharp peak at 1359 cm^{-1} which is characteristic of LDH materials and refer to the anti-symmetric stretching of the C-O bonds [102,114]. The presence of the interlayer water is also characteristic of LDH materials and it

was observed as a broad peak from 3000 to 3500 cm^{-1} [102,114]. In Figure 6-2(b) it can be observed the typical peaks related to the goethite (757 and 885 cm^{-1}). It can be observed in Figure 6-2(a) that the goethite peaks, although minimum, are still present for LDH_{ochre} which fits very well with the goethite phases detected through PXRD. The TGA data (Figure 6-3(a)) provided further insights into the formation of the LDH materials. In a typical LDH decomposition curve, usually three decomposition stages are observed. The first stage was up to 210 ˚C, caused by loss of bound water and interlayer water [114]. The other two major mass losses are due to the decarboxylation and dehydroxylation of the LDH, resulting in mixed metal oxide and subsequent spinel formation, at about 700 ˚C [114,254,255]. In Figure 6-3(b), the nitrogen adsorption-desorption isotherms showed a classical type IV isotherm shape with narrow hysteresis loop, both characteristic of mesoporous materials. Moreover, the LDH_{ochre} presented a higher surface area (66.5 $m^2.g^{-1}$) than LDH_{syn} (38.1 $m^2.g^{-1}$), which impacted directly when the samples were evaluated for their photocatalytic activity (H_2 evolution) as observed in Figure 6-8. The effect of the higher surface area could be one of the factors which produced a better performance of the LDH_{ochre} when compared to LDH_{syn}. When the data in Figure 6-8 (b) was normalized, it was observed that the production of H_2 by LDH_{syn} was superior per m^2 (total production of 76 μmol/m^2) than the production of LDH_{ochre} (69 μmol/m^2). However, the specific surface area of LDH_{ochre} is in fact bigger than the one for LDH_{syn}, therefore the former behaving better as a photocatalytic material (Figure B-2, Appendix B). The SEM analysis, observed in Figure 6-4, showed a plate-like morphology, which is one of the expected morphologies when producing LDH materials [191,299]. The plate-like morphology, although observable, is not well crystallised, agreeing with the broad reflection and low order indicated by the PXRD data. From the TEM images of the LDH_{ochre} in Figure 6-5, taken at different magnifications, the formation of pseudo-hexagonal plate-like crystals, which are characteristic of LDH materials, support the information obtained from the other characterisation techniques (i.e PXRD, FTIR, TGA and SEM). Another factor that could be impacting the photocatalytic activity behaviour of LDH_{ochre}, making the latter LDH_{ochre} more active is the presence of other metals in the sample. As observed in Table B-5, Appendix B, traces of Al, Na, V, Cr, Mn, Zn and Sr are in major amounts in LDH_{ochre} than in LDH_{syn}. Although in trace amounts, the catalytic activity of the LDH_{ochre} for the H_2 evolution reaction could have been boosted by such metals, as according to the literature, M^{III} cations can be seen as "dopants" when added into the synthesis of LDH, improving their capabilities for visible light absorption [290,302].

6.4.2 Optical characterisation of the LDH_{ochre} and LDH_{syn}

When characterized through UV-Vis (Figure 6-6) the maximum absorption obtained can be explained through ligand to metal charge transfer (LMCT) in the $Fe(OH)_6$ octahedral layer, as the absorption is expected to occur in the UV-Vis region [151,303,304]. The further absorption into the visible region of the spectra could be attributed to the presence of Fe^{3+} and the presence of the carbonate anion in the interlayer, as the literature suggests [291,302,305]. Silva *et al.,* [291] concluded that LDHs can be treated as doped semiconductors, whereas Parida *et al.,* [151] and Liu *et al.,* [305] attributed the better efficiency of their respective photocatalysts to the Fe^{3+} doping, increasing the capabilities of the materials to absorb more visible light. In this study, as Fe is the trivalent cation used to produce the LDHs, it is expected to observe the material harvesting light from the visible light wavelength, as shown in Figure 6-6 [151,306-308]. Nevertheless, further comparison with other LDHs of different trivalent cations needs to be performed to fully validate the latter. Thus, as observed in Figure 6-7, the recombination effect could also be playing a key role on the photocatalytic experiments. The intensity of the peaks is directly proportional to the recombination between the excited electrons and holes. It can be noted then, that the lower intensity presented by LDH_{ochre} is a clear indicator that recombination occurred less frequently than in the LDH_{syn}. A further consideration is that with the higher surface area of LDH_{ochre}, there exists more opportunity for water molecules to be adsorbed, increasing the photocatalytic properties of the material, ensuring more active sites for the reaction with the sorbed water to occur [295].

6.4.3 Evaluation of the photocatalytic activity of LDH_{ochre} and LDH_{syn}

6.4.3.1 Hydrogen evolution reaction

The photocatalytic testing used 200 ml of distilled water with a Xe lamp used as a solar simulator (450 W), with irradiation purely in the spectrum of solar light (i.e., visible light). When compared, the LDH_{ochre} showed a higher photocatalytic activity than the LDH_{syn}, as evidenced in Figure 6-8 for both, the aid of sacrificial agent (10% methanol) (a) and water (b). Comparing Figure 6-8(a) and Figure 6-8(b), it can be observed that solely with water or with methanol acting as scavenger, production of hydrogen using the ochre made LDH was superior. The hydrogen production in $\mu mol.h^{-1}.g^{-1}$ is presented in Figure 6-8(c) and Figure 6-8 (d) for both samples. From the latter it can be seen that LDH_{ochre} yielded a production of 1272 $\mu mol.h^{-1}.g^{-1}$, whereas LDH_{syn} produced 750 $\mu mol.h^{-1}.g^{-1}$. The difference in yield between both samples could be attributed to the higher surface area of the LDH_{ochre}, as discussed in Section 6.3.1. The efficiency of the LDH_{ochre} with production of 1272 $\mu mol.h^{-1}.g^{-1}$ can be compared with some literature values. Parida and Mohapatra [294] obtained a maximum hydrogen production of 1732 $\mu mol.h^{-1}g^{-1}$ under visible light conditions, using a Zn/Cr-CO_3 LDH material, with methanol as sacrificial agent. Though crystallite size and surface area were not measured by Parida and Mohapatra [294], the XRD plots presented seem sharper and clearer than the ones obtained in this present study. As mentioned before, [309,310] crystallinity as well the surface area could be intimately related. A higher crystallinity in the Zn/Cr-CO_3 could be causing the higher hydrogen production, however lack of data makes correlation difficult. According to Parida and Mohapatra, the presence of the CO_3^{-2} anion enhanced the hydrogen production of the Zn/Cr LDH (1732 $\mu mol.h^{-1}g^{-1}$) when compared with other, non-carbonate, Zn/Cr LDH (1092 $\mu mol.h^{-1}g^{-1}$). The phenomena could be explained due to the oxidation of carbonate anions in the holes of the semiconductor, reducing the recombination effect, thus being beneficial for the electron/hole disunion [294]. In a more comparable study, also performed by Parida *et al.,* [151] Mg/Al-CO_3 LDH doped with Fe^{3+} yielded a production of hydrogen of 301 $\mu mol.g^{-1}h^{-1}$ under visible light irradiation, using methanol as sacrificial agent. The amount of hydrogen produced from LDH_{ochre} in this present study shows a significant advance for using low value metal ions, obtained which could be potentially obtained from waste materials.

6.4.3.2 Possible reaction mechanism for the hydrogen evolution reaction

The LDH_{ochre} sheets are composed of MO_6 octahedral units which, in conjunction with the effect of the surface area and crystallinity of the material, the metal-total charge transfer (MMCT) through the oxo-brindge of the Mg-O-Fe and the presence of the carbonate anion in the interlayer, involve several variables that could be impacting the behaviour of the photocatalyst, suggesting that more than one single factor could be responsible for the activity of the material [151,294,302,311]. As a preliminary suggestion from this study and based on the results obtained from the optical characterisation of the materials (Section 2.1.1) and the prior literature, the presence of iron in the sample favours the behaviour through increasing the capabilities of the LDH to harvest more energy from the visible light. When exposed to the photons, the electrons are excited and move from the valence band (VB) of the O 2p orbital to the conduction band of the Fe-3d orbital, producing the electron-hole pairs needed to carry on the water splitting, with the presence of Fe^{3+} critical for the hydrogen evolution reaction to be improved by harvesting more energy from the visible light wavelenght [151,294,302]. Moreover, according to Parida *et al.,* [294] the carbonate anion plays a crucial role enhancing the properties of the material, though further studies needs to be performed with other anions in the interlayer to conform this. According to Parida *et al.,* peroxicarbonates forms from the coupling of two carbonate radicals which are produced by the oxidation of the carbonate anion. The peroxi-carbonates would further react with the generated holes to decompose into CO_2 which then will further react with the adsorbed hydroxyl groups to form HCO_3^- and CO_3^{-2}, decreasing the recombination rate of electron and holes, increasing the photocatalytic activity of the material. In future work, post-reaction characterisation would be performed in order to better understand the reaction pathway. Finally, it is suggested that recombination is also reduced due to the effect of the MMCT through the oxo-bridging of the Mg-O-Fe sites, transferring electrons from one metal to another as a result of visible light excitation, preventing recombination of the charge carriers [302,305].

6.5 Conclusions

Following circular economy principles, an LDH material (LDH_{ochre}) with photocatalytic activity was synthesized using the mining waste ochre from Saltburn, England. The capabilities of the latter were tested against another LDH (LDH_{syn}), following the same synthesis steps but made of synthetic salts. The performance of the LDH_{ochre} was superior when compared with the analagous LDH_{syn} for production of hydrogen through the hydrogen evolution reaction. It is though that this is mainly due to the difference in surface area, though further work is underway to confirm this, as normalized hydrogen production for LDH_{ochre} and LDH_{syn} (69 μmol/m^2 and 76 μmol/m^2 , respectively) were close one another. Compared with LDHs in the literature used for hydrogen production under visible light irradiation, LDH_{ochre} demonstrated promising behaviour as the yield of hydrogen produced was comparable, competing against other LDHs of different compositions, such as doped ones or nanocomposite LDH materials. Production of high value materials from waste streams such as ochre, feeding into clean energy production, exemplify the principles of the modern circular economy approach**.**

7. Synthesis and characterisation of Struvite-Ochre LDHs

7.1 Introduction

In a recent study, Geissdoerfer *et al.*, [2] compiled over 100 definitions of the circular economy concept in the literature, to formulate the following statement: "The circular economy is an economic system in which resource input and waste, emission and energy leakages are minimised by cycling, extending, intensifying, and dematerialising material and energy loops. This can be achieved through digitalisation, sharing solutions, long-lasting product design, maintenance, repair, reuse, remanufacturing, refurbishing, and recycling". Moreover, the circular economy concept gains in importance year by year, as it seems the world is trying to work towards reducing the harmful impact that societal development since the industrial revolution has caused to the planet [312,313]. Nevertheless, the circular economy has encountered several barriers when developing, such as lack of economic viability or lack of commitment from the private and the governmental sectors towards the development of circular economy projects [26]. In the spirit of the latter statement, Chapter 5 studied using a material obtained from waste as a donor for M^{III} cations, in this specific case the Fe^{3+} cation, in order to develop a catalyst material. The M^{III} cation was obtained from the mining pollution waste ochre, an and LDH was prepared using a synthetic salt for the M^{2+} species and the ochre for the M^{3+} species, via a co-precipitation method. The latter LDH was further evaluated as a heterogeneous catalyst for the ketonic decarboxylation of dodecanoic acid (Chapter 5) and as a photocatalyst to promote the production of hydrogen (Chapter 6). Nevertheless, using LDH materials for sustainability purposes is not novel. Sayed *et al.,* [314] prepared a Mg-Al LDH through the co-precipitation method. The latter LDH in conjunction with the mineral metakaolin was denoted as a new geopolymer used for the transesterification of biodiesel. The yields obtained by Sayed *et al.,* were above *ca* 92%. On a similar approach in terms of biomass conversion, Smith *et al.,* [102] evaluated the efficiency of the Mg-Al LDHs of different R-values as promoters of the ketonic decarboxylation of stearic acid at moderate temperatures (*ca* 250 ˚C) with excellent yield (~90%). Mahgoub *et al.*, [315] used Zn-Al LDHs, synthesised through the co-precipitation, to adsorb levofloxacin from water effluents. The new formed composite Zn-Al LDH with levofloxacin was then evaluated in terms of toxicity and as anti-inflammatory agent in rats. Parida *et al.,* [151] synthesized Mg-Al LDHs through co-precipitation as well, and based on the semiconductor

theory, "doped" the material with iron, to increase the capabilities of the latter formed Mg-Al LDH to absorb more visible light in order to increase the production of hydrogen through photocatalytic mechanism. Moreover, LDHs have also been used in conjunction with other waste materials such as chicken bones or even made from recycling waste materials. Belviso, *et al.,* [316] used red-mud, which is mainly composed of iron oxy-hydroxides (e.g., goethite or hematite) and aluminium hydroxides, which after being in contact with NaOH and a ultrasonic water bath, produced crystalline LDH materials. The latter LDH was then mixed with zeolite to form a composite that was further used to remove methylene blue with superior capabilities than the regular LTA commercial zeolite. Ping *et al.,* [142] used the serpentine tailings in China , from which MgO was extracted and subsequently used to prepare a Mg-Al LDH. Moreover, Ping *et al.,* also used the Mg-Al LDH as a Pb and P adsorbent, with an adsorption of Pb and P of 99% and 85%, respectively. In an interesting approach, Alquzweeni and Alkizwini [317] mixed chicken bones using the co-precipitation method to coat the latter chicken bones with Mg-Al LDH material. The coated chicken bones with LDHs were successfully used as an adsorbent of cadmium from water, with an efficiency of *ca* 95 %. In a recent and novel approach, Kwok *et al.,* [152] successfully achieved the synthesis of a dense porous LDH material using struvite ($Mg^{2+} + NH_4^+ + H_nPO_4^{(3-n)-} + 6H_2O \rightarrow MgNH_4PO_4.6H_2O + nH^+$) as the M^{II} cation donor during the co-precipitation synthesis. The M^{II} cation was obtained from Mg present in the struvite. According to Kwok *et al.,* the obtained material was particularly high in density, which is key to catalytic and sorbent applications using fluidised beds. Moreover, the LDH also has a higher surface area when compared with other LDH materials prepared through co-precipitation. The PXRD pattern obtained from the as-synthesized material is shown in Figure 7-1.

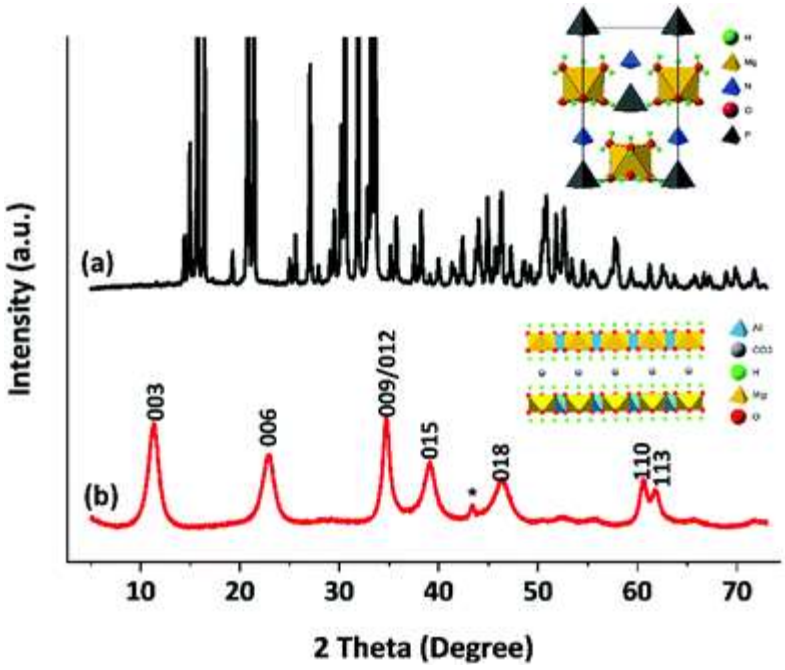

Figure 7-1. (a) Struvite powder x-ray diffraction pattern and (b) Mg-Al CO_3 powder $_x$-ray diffraction pattern. Taken with permission from Kwok et al., [152].

Struvite is an interesting material from a circular economy perspective, as it is found as a waste product within pipelines and tanks in wastewater treatment plants (WWTP). If certain process conditions are met in terms of temperature, pH, ammonia content and phosphorous (P) concentration, struvite precipitates [152,318]. According to Kleeman *et al.,* [319], in the UK, most of the P used comes from fertilisers (up to 56%) but also from detergents, processed foods, industrial applications, animal foods, etc. It is expected that P consumption by society will increase during the next century, and as exploitation of phosphate bearing rocks is a non-renewable approach to obtain P, strategies towards a diverse range of sustainable and possible new activities for obtaining P need to be adopted and further developed over the next decades [319,320]. Moreover, as P is always present in significant amounts in wastewater streams and there are strict regulations to fulfil in terms of P discharge from WWTP under the European Union Water Framework Directive, recovery of P is critical. In many places with large populations, WWTPs anaerobic digestor (AD) plants are implemented to reduce the amount of solids and co-generate biogas. However, owing to the alkalinity and reducing conditions generated by AD systems, a high concentration of ammonia (NH_4^+) is generated, and struvite may be formed, impacting the operation of the WWTP. Struvite forms as

concretions, reducing the diameter of the pipes, augmenting the energy needed to pump the sludge and the maintenance cost of such pipelines [318,319] as well as forming a granular material that causes wear on pump impellors. Ochre is also a waste stream, arising from legacy water pollution from the coal and metal mining industry, as already discussed in Chapter 5 and Chapter 6In this thesis, ochre from mining waste streams has been extensively studied and used as a mineral precursor to form LDH materials, for further use as catalysts for biomass conversion reactions or photocatalytic applications. Giving use to what, otherwise, would be considered a waste stream (i.e., struvite and ochre), purposely removed to favour a more cost-effective process in a WWTP, and using the struvite to produce a value-added catalyst that can be potentially used in a diverse range of applications is of much interest in the search for sustainable and green products and processes, as the recovery of struvite will not only be beneficial for the WWTP processes in terms of cost savings, but also, as the struvite is a direct product obtained from a waste stream, the latter struvite can be potentially processed not only to produce LDH, but also to provide phosphorus and nitrogen in the form of a fertilizer[321,322]. Such approach reuse and recycle a waste material (i.e., struvite), extending the use of such struvite, deriving in waste and energy reduction while increasing the added-value products obtained from water waste streams. Due to the positive results obtained when synthesizing an LDH using ochre as one of the mineral precursors (Chapter 5), and considering the results from Kwok *et al.,* [152] in preparing a struvite derived LDH, it seems now feasible to synthesize an LDH wholly from waste. As such, synthesis of a LDH material with a R-value = 2 and R-value = 4 is explored here using the waste struvite, collected from the pipelines in a local WWTP, and ochre sludge from local mining remediation activities, through co-precipitation.

7.2 Experimental

The struvite sample was provided by Northumbrian Water Ltd and was obtained at the Bran Sands WWTP, Middlesbrough, UK. The received struvite was in a form of a solid block of concretion that needed to be further ground in order to be used. The ochre sample was taken from the primary drying lagoon at Saltburn Gill Water Treatment Scheme in Saltburn, Cleveland, UK and provided by the Coal Authority, UK. The following chemicals were purchased and used as received: Na_2CO_3 (99%, Alfa Aesar), NaOH (98%, Alfa Aesar), HCl concentration of 37%, 98%, Aldrich). Synthetic struvite hexahydrate was purchased as a comparison (98.5%, Alfa Aesar). The co-precipitation methodology was used to synthesize two struvite-ochre LDH materials (given the nomenclature SO-LDH) with an R-value = 2 (SO-LDH-R2) and a R-value = 4 (SO-LDH-R4). A full description on how the co-precipitation methodology was performed has already been detailed in Chapter 1, Section 1.6 and Chapter 2, Section 2.10. The characterization of the raw materials (i.e., struvite and ochre) and the synthesized struvite-ochre LDHs (SO-LDH-R2 and SO-LDH-R4) by powder X-ray diffraction (PXRD), Fourier transform infrared (FTIR) spectroscopy, thermogravimetric analysis (TGA), inductively coupled plasma – optical emission spectroscopy (ICP-OES) and ICP mass spectrometry (ICP-MS) were performed and utilized in the same manner as described in Chapter 5 and in Chapter 6. However, a brief description of the synthetic procedure to prepare the LDHs, and the analysis methods employed, are presented below for completeness. As a point of comparison, and to tune the synthesis parameters before the preparation of the SO-LDHs, two other LDHs were also synthesized through the co-precipitation method, however, these LDHs were synthesized using the ochre as the Fe^{3+} donor and synthetic struvite (98.5%, Alfa Aesar) as the Mg^{2+} donor. These latter LDHs were named SSO-LDH-R2 and SSO-LDH-R4.

7.2.1 Synthesis of the SOLDHs SSOLDHs through co-precipitation

In a typical co-precipitation procedure at low-supersaturation conditions, to make the SO-LDH-R2 (R-value 2), 0.5 g of ochre (4.51 mmol Fe^{3+}) and 2.21 g of waste struvite (9.02 mmol Mg^{2+}) were dissolved in 100 ml of 1 M HCl (keeping the R-value = 2). Each solution was then added into a dropping funnel and left to drop inside a three-necked round bottom flask, which contained a 3:1 mol excess of Na_2CO_3 with respect to the Fe^{3+}. The pH of the solution was maintained at ~ pH 11.3 with the aid of 1 M NaOH solution. The temperature was set at 65 ˚C and the stirring at 1000 rpm. Once the dropping funnel containing the acidic mixture of metals was empty, the stirring was stopped, and the three-necked round bottom flask was left to age at 70 ˚C overnight. Subsequently, the product was recovered through vacuum filtration and washed abundantly with distilled water. The solid was left inside an oven at 70 ˚C to dry and then re-equilibrated with the atmosphere prior to analysis. To prepare the SO-LDH-R4 (R-value 4), the same preparation procedure was followed, only making the pertinent stoichiometric adjustments, that is 0.5 g of ochre (4.51 mmol Fe^{3+}) to 4.43 g of struvite (18.05 mmol Mg^{2+}). For the synthesis of the SSO-LDH-R2 and SSO-LDH-R4, the same procedure was employed, however, as the ICP analysis were unavailable due to a broken instrument by the time of the experiments needed to be performed, when calculated the amount of Fe^{3+} present within the ochre sample, the assumption of 32 %wt. was used, as in Chapter 6, which was based on previous ICP-OES experimental data from the Greenwell group. The pertinent corrections were done (i.e., proper measurements of the Fe^{3+} and Mg^{2+} within the samples of ochre and struvite, respectively), and the proper stoichiometric calculations were applied for the ochre and the synthetic struvite hexahydrate to maintain the desired R-value= 2 and R-value = 4. Nevertheless, before preparing the SO-LDHs in this section, triplicate ICP-OES analysis to calculate the amount of Fe^{3+} and Mg^{2+} within the ochre and the waste struvite samples, respectively, were performed, by dissolving 10 mg of dried ochre into 10 ml of 1 M HCl. The same method was applied to calculate the amount of Mg^{2+} within the waste struvite samples.

7.2.2 Characterisation of the Layered-Double Hydroxide materials

All the characterisation techniques employed to characterise the ochre, the struvite and the as-synthesised LDH materials used in this section of the study, have been explained in further details in Chapter 2 (i.e., PXRD, FTIR, TGA, ICP-OES, SEM, and Nitrogen adsorption/desorption isotherms) therefore they will not be described further as the same methodology to prepare all the samples was applied during the development of Chapter 3 to Chapter 7.

7.3 Results

7.3.1 Struvite and ochre characterisation (waste mineral precursors)

The characterisation results of the ochre and the struvite are shown in Figure 7-2.

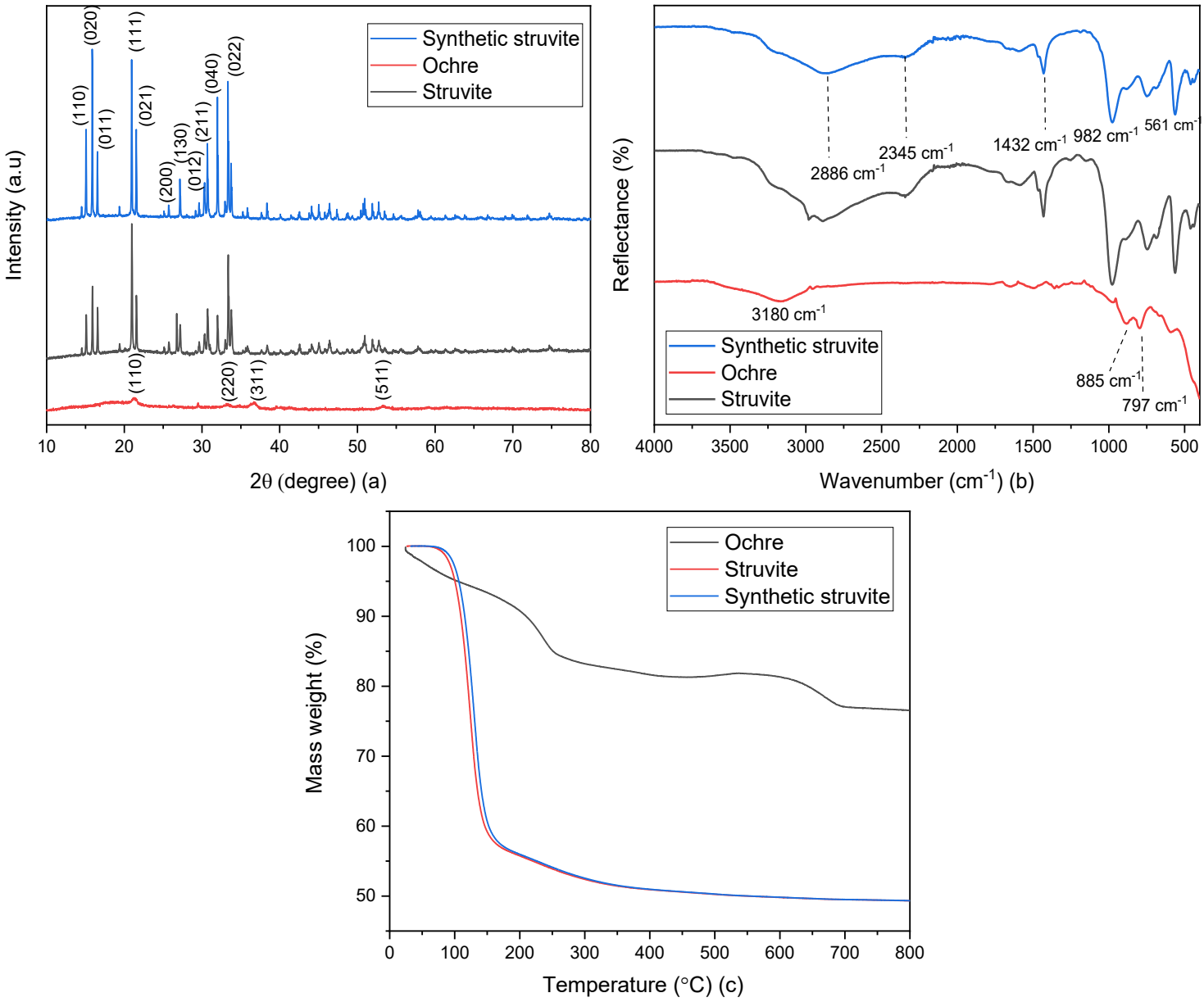

Figure 7-2. Characterisation of the ochre and struvite used to make the SO-LDHs. (a) Shows the diffraction peaks obtained from the Powder X-Ray Diffraction. (b) Fourier Transformed Infra-Red of both samples. (c) Thermogravimetric analysis of both samples.

Figure 7-2 shows the characterisation of the mineral precursors, ochre and the struvite (both synthetic and waste), used for the synthesis of the SSO-LDHs and the SO-LDHs. Figure 7-2(a) presents the PXRD analysis of all the samples. It can be observed that the main reflections present in the ochre sample can be assigned to the characteristic reflections encountered in goethite (α-FeO(OH)), as this represents the main iron mineral phase existing in the ochre sample [114,150]. Both struvite samples diffraction peaks were compared with the literature [152,323]. All the peaks were indexed as struvite, with sharper peaks for the synthetic struvite sample when compared with the waste struvite one. The FTIR of ochre in Figure 7-2(b) have two defined peaks at 797 cm^{-1} and 885 cm^{-1}, which were assigned to the deformation of the O-H bonds in the goethite [114,265]. The struvite (both samples) FTIR has two peaks at 561 cm^{-1} and 982 cm^{-1}, which were attributed to the v_4 bending vibration of PO_4^{3-} and the symmetric and anti-symmetric vibrations of PO_4^{-3}, respectively. The sharp peak at 1432 cm^{-1} was assigned to the H-N-H v_4 asymmetric bending vibration of the NH_4^+ [152,321]. The broad peak which develops from *ca* 3300 cm^{-1} to *ca* 2200 cm^{-1} refers to the O-H stretching from the water in the sample and the v_1 asymmetric stretching assigned to the N-H [152]. Decomposition analysis through TGA of both struvite samples and the ochre are shown in Figure 7-2(c). Struvite lost approximately 50 % of its original weight, which corresponds with the dehydration of the sample and the loss of ammonia as NH_3 [324,325]. For both struvite samples the decomposition behaviour was practically identical. Considering the molecular formula of the struvite ($MgNH_4PO_4.6H_2O$), if the water and ammonia were lost, the expected mass reduction would be up to 51%, which correlated well with the obtained TGA data for the struvite samples. The ochre mass loss was attributed mainly to the loss of adsorbed water and dehydroxylation of the sample to finally be converted into hematite *ca* 700 ˚C [114]. The SEM analysis of both struvite samples are shown in

Figure 7-3. The characteristic trapezium morphology of struvite can be observed [326], although in the case of Figure 7-3(a), not completely clear and highlighted in red to aid the reader. For the ochre (e.g., Figure 7-3(b)), a series of hexagonal-like plates agglomerated, which seems to be in agreement with the literature [327].

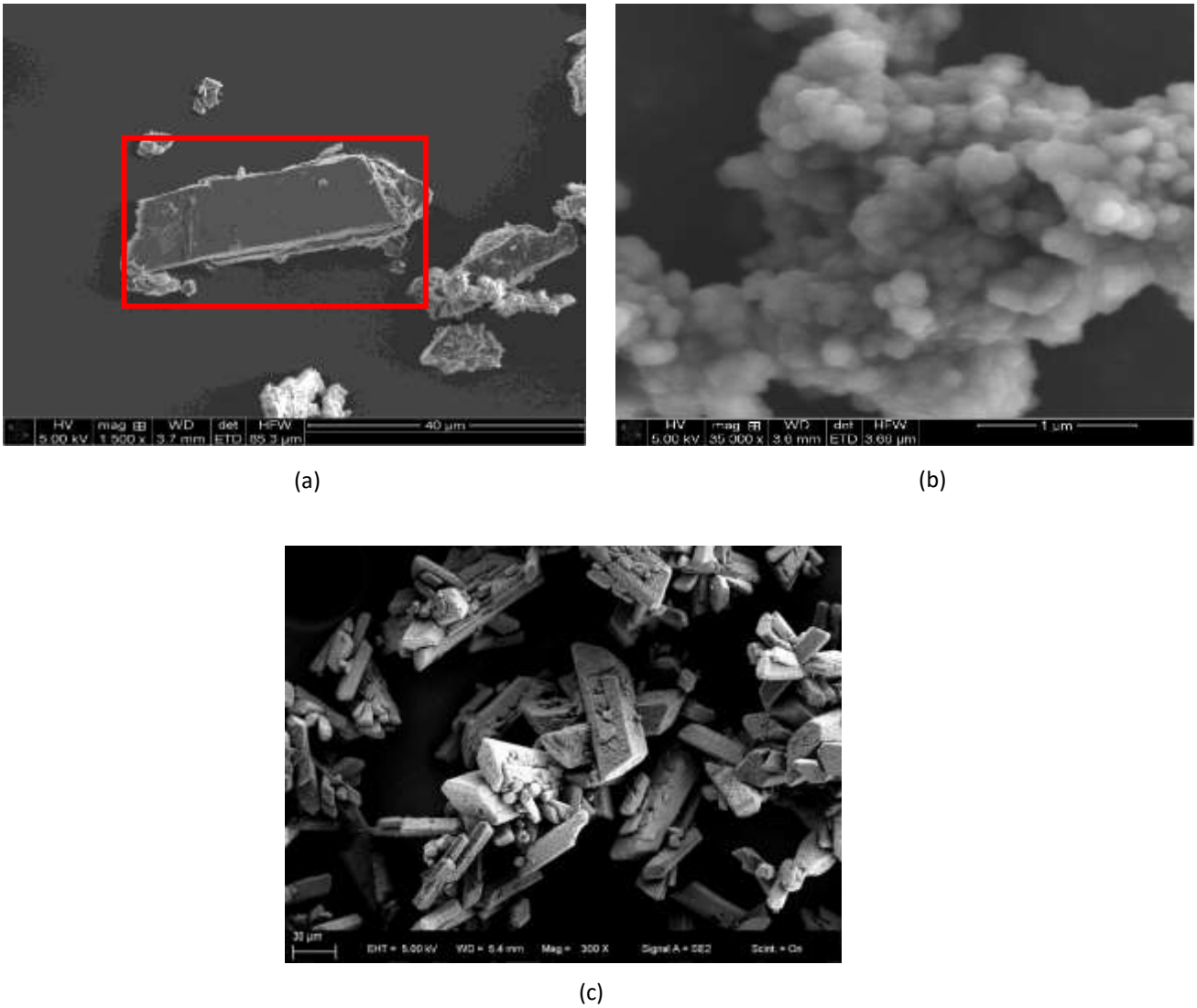

(a) (b)

(c)

Figure 7-3 Scanning electron microscopy images of (a) struvite (from waste). Although the image is lacking some clarity, in the red box can be observed a trapezium-like morphology. b) ochre from Saltburn, England. c) Synthetic struvite sample from chemical supplier.

The ICP-OES analysis of the struvite and the ochre, in terms of Mg^{2+} and Fe^{3+} respectively, was 50.5 %wt. of Fe^{3+} for the ochre and 9.52 % wt. of Mg^{2+} for the struvite, with a standard deviation (i.e., SD) of 0.02 and 0.09, respectively. Taking into consideration the latter % wt. composition, the samples were weighed and used as described in Section 7.2.1. to prepare the respective SO-LDH materials.

7.3.2 Synthetic struvite-ochre LDH (SSOLDH)characterisation

The results from the characterisation of the SSO-LDH-R2 and SSO-LDH-R4 are shown in Figure 7-4.

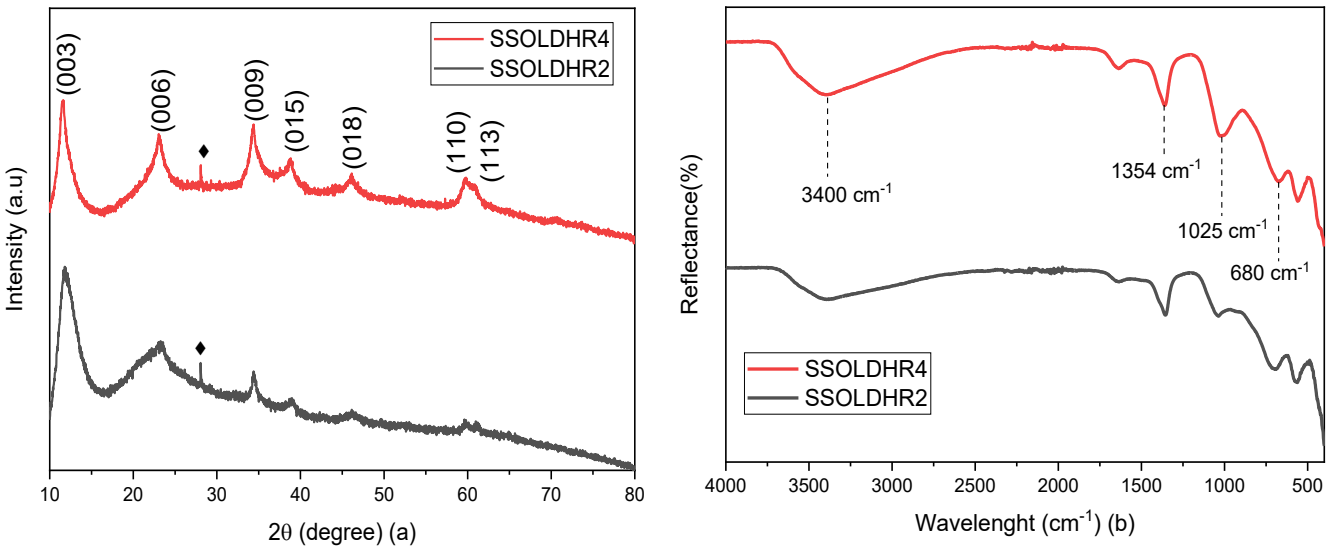

Figure 7-4 (a) Powder X-ray Diffraction analysis of SSO-LDH-R2 and SSO-LDH-R4. Typical LDH diffraction patterns can be observed for both samples. The black ◊ corresponds to an impurity related to the possible presence of a goethite phase. (b) Fourier Transformed Infra-Red analysis of the SSOLDHR2 and SSOLDHR4.

Both SSO-LDH-R2 and SSO-LDH-R4 were characterised through PXRD, FTIR and SEM. The lack of TGA data for the SSO-LDHs was due to staff absence in the CoVid 19 pandemic,

so no TGA of the SSO-LDHs were performed. According to Figure 7-4(a), LDHs were successfully formed using the ochre and the synthetic struvite hexahydrate, leading to the formation of the characteristic diffraction pattern expected to be observed in LDH materials [102,114]. The PXRD diffraction pattern seemed to be slightly sharper and with more defined peaks for the SSO-LDH-R4 sample. It seems apparent that both SSO-LDHs did not form a phase pure LDH material, with a broad feature possibly indicating some amorphous material observed at *ca* 25˚. Moreover, a small peak *ca* 28˚ is observed, which could be attributed to the presence of a goethite phase for both samples [114]. Impurity phases were also indicated within the FTIR analysis of both samples. The FTIR analysis (Figure 7-4b)) of both SSO-LDH-R2 and SSO-LDH-R4 samples presented characteristic peaks related to anti-symmetric stretching (v4) of the carbonate in the interlayer of the LDH [114,132,152] at 1354 cm^{-1}, with a further clear peak at *ca* 1020 cm^{-1} which was assigned to the anti-symmetric and symmetric (v3) stretching of the phosphate anion [152,328]. This suggests the product was a mixed interlayer LDH containing carbonate and phosphate anions. Although both samples contain all the characteristic peaks related to LDHs, the small peak observed *ca* 570 cm^{-1} could be either assigned to the presence of either hematite (i.e., α-Fe_2O_3) or goethite (i.e., FeO(OH)), on the basis of the literature [151]. Finally, a broadband at *ca* 3400 cm^{-1} was assigned to the OH vibrations. In Figure 7-5, the SEM images of both, SSO-LDH-R2 and SSO-LDH-R4 are shown. It was observed that both samples had a *rose des sables* morphology, characteristic of LDH materials [102], although it is evident that the samples are lacking crystallinity.

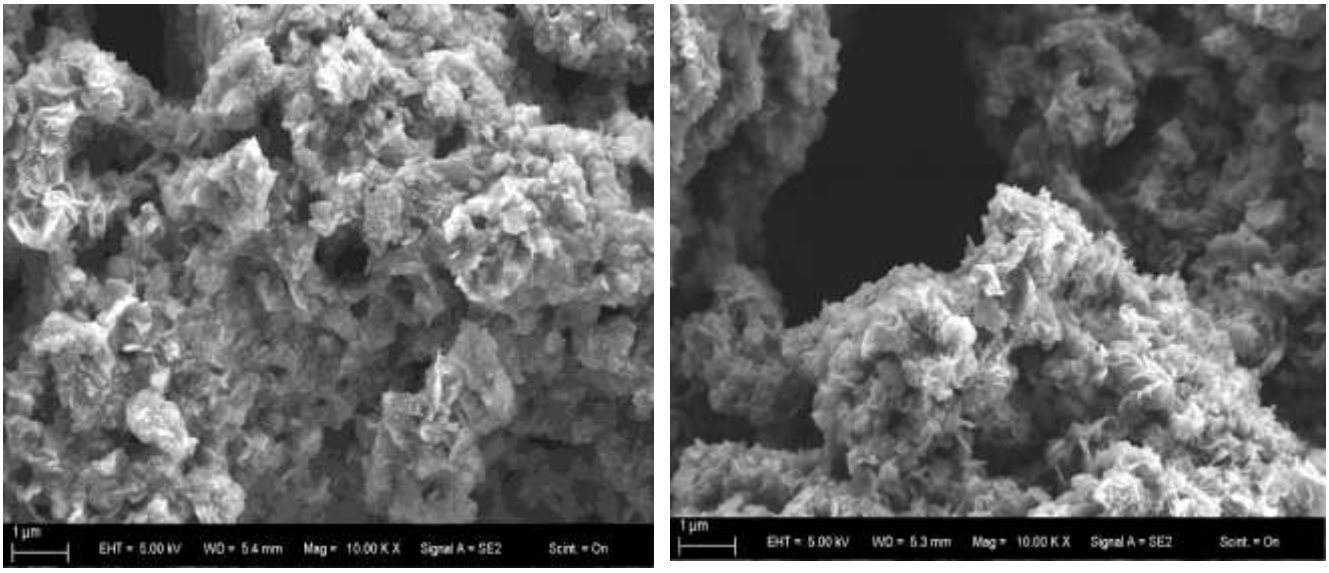

(a) (b)

Figure 7-5 Scanning electron microscopy images of (a) SSO-LDH-R2 and (b) SSO-LDH-R4.

Moreover, the *d*-spacing and the corresponding unit cell parameters *a* and *c* from SSO-LDH-R2 and SSO-LDH-R4 were calculated according to the literature and as previously explained in Chapter 2, Section 2.1 [254,261]. Thus, the FWHM as well as the crystallite size were also calculated, for both samples. The results are presented in Table 7-1.

Table 7-1. Unit cell parameters and d-spacing of SSOLDHR2 and SSOLDHR4.

Sample	***d*-spacing (Å)**	**Unit cell parameter *a* ($a=2d_{(110)}$) (Å)**	**Unit cell parameter *c* ($c=3d_{(003)}$) (Å)**	**FWHM***	**Crystallite size (nm)**
SSO-LDH-R2	7.64	3.08	22.92	2.050	3.9
SSO-LDH-R4	7.49	3.09	22.48	1.600	4.9

*The FWHM was calculated using the diffraction peak with the highest intensity. For SSO-LDH-R2 and for SSO-LDH-R4, the peak used was the (003) in Figure 7-4(a).

Finally, the ICP-OES analysis of both SSO-LDH-R2 and SSO-LDH-R4 was performed. The results are presented in Table 7-2. Although the desired R-values for SSO-LDH-R2 and SSO-LDH-R4 were 2 and 4, respectively, the targeted R-values for each of the two samples was not fully achieved.

Table 7-2. R-values and Mg and Fe composition of SSO-LDH-R2 and SSO-LDH-R4 obtained through ICP-OES.

Sample	Amount of sample obtained (g)	Initial Fe^{3+} (g)* in the ochre	Initial Mg^{2+} (g) in the struvite	Mg (%wt) ICP-OES	Fe (%wt) ICP-OES	Final Fe^{3+} (g) in the SSO-LDH	Final Mg^{2+} (g) in the SSO-LDH	[Mg]/[Fe] (ICP-OES)
SSO-LDH-R2	0.72	0.16	0.13	13.01	21.50	0.15	0.09	1.41
SSO-LDH-R4	1.35	0.16	0.27	13.39	11.13	0.15	0.18	2.80

*The amount of iron within the ochre sample was considered 32% wt.

From Table 7-2, a mass balance from the synthesis process regarding the Fe^{3+} cation and the Mg^{2+} cation can be performed, taking into account the initial amount of Fe^{3+} from the ochre and the Mg^{2+} from the synthetic struvite and the final amounts of Fe^{3+} and Mg^{2+} within the SSO-LDHs. As observed in Table 7-2 almost all the Fe^{3+} was retained in the final product (~93%) in both, the SSO-LDH-R2 and SSO-LDH-R4, however, that was not the case for the Mg^{2+}. In the case of the magnesium, only the 69% and 66% of the initial magnesium was in the SSO-LDH-R2 and the SSO-LDH-R4, respectively.

7.3.3 Struvite-Ochre LDH (SOLDH)characterisation

The results from the characterisation of the SO-LDH-R2 and SO-LDH-R4 are shown in Figure 7-6.

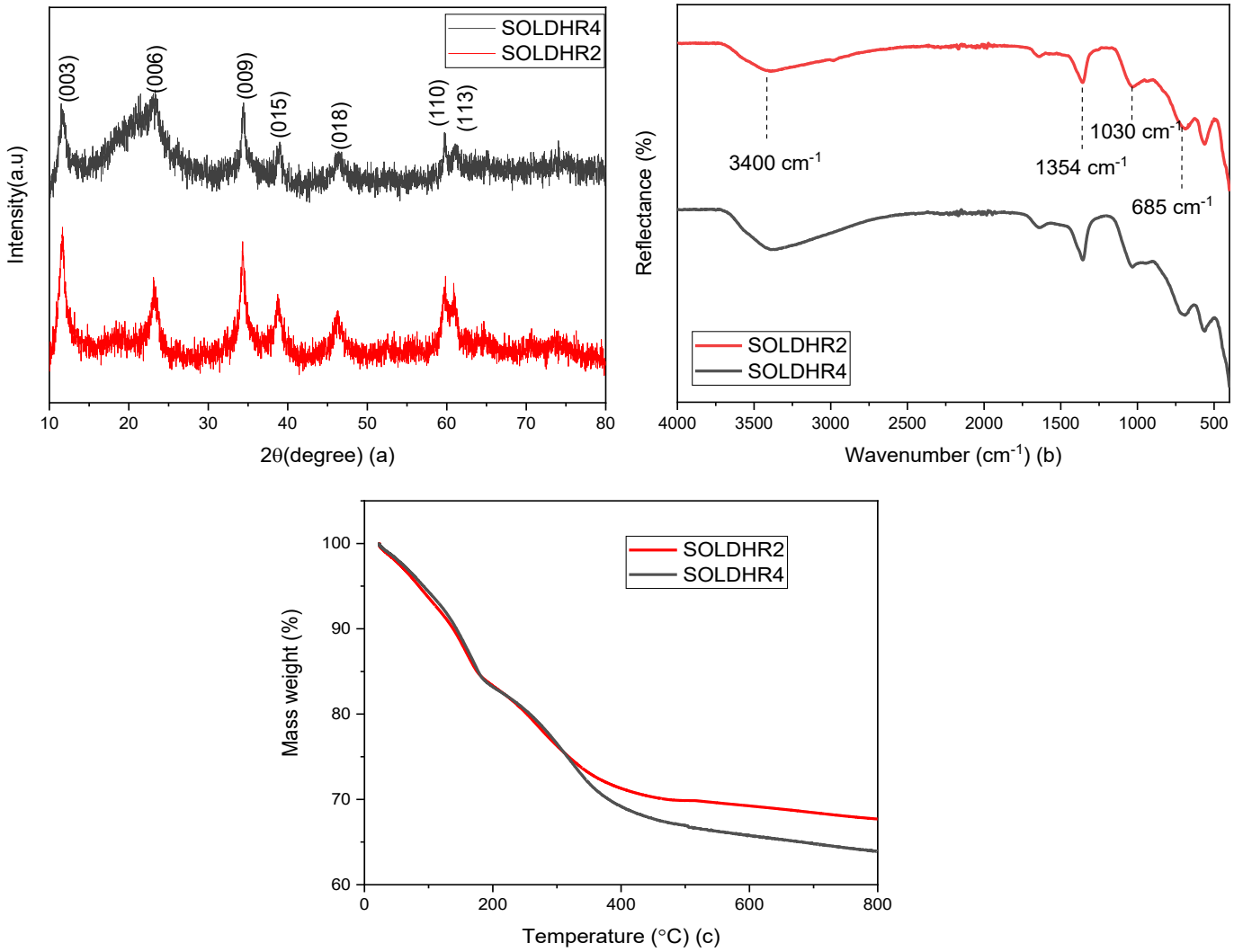

Figure 7-6 Characterisation of SO-LDH-R2 and SO-LDH-R4, showing (a) the diffraction peaks obtained from the powder X-Ray diffraction, (b) FTIR of both samples, (c) thermogravimetric analysis.

Considering the nature of the struvite and the ochre, with both being waste materials, without any pre-treatment prior to acid dissolution before being used during the co-precipitation to produce the SO-LDHs, well defined peaks for both SO-LDH-R2 and SO-LDH-R4 can be observed from the PXRD patterns in

Figure 7-6(a). The diffraction patterns for both samples correspond very well with the ones expected for LDH materials in the literature [102,114]. However, a broad peak before the peak at *ca* 20 ˚might be attributed to the presence of an amorphous Fe phase, which again seemed to be in agreement with the observed FTIR peak *ca* 570 cm^{-1}, as was also noted with the SSO-LDH samples. As both the struvite and the ochre were two waste materials, the Fe concentration may vary, as well as other elements, from batch to batch when used as precursors (as evidenced by the ICP-OES analysis of the ochre and struvite samples (Section 7.3.1)), making it difficult to make an exact stoichiometric calculation in terms of the Fe^{3+} existing within the samples. Moreover, from Figure 7-6(a), the basal *d*-spacing and the unit cell parameters for both, SO-LDH-R2 and SO-LDH-R4 were calculated. The unit cell parameters were also calculated and the FWHM and crystallite size were also obtained. The results are presented in Table 7-3.

Table 7-3. Unit cell parameters and d-spacing of SO-LDH-R2 and SO-LDH-R4.

Sample	***d*-spacing (Å)**	**Unit cell parameter *a* ($a=2d_{(110)}$) (Å)**	**Unit cell parameter *c* ($c=3d_{(003)}$) (Å)**	**FWHM***	**Crystallite size (nm)**
SO-LDH-R2	7.58	3.08	22.75	1.100	7.2
SO-LDH-R4	7.69	3.09	23.08	6.990	1.1

*The FWHM was calculated using the diffraction peak with the highest intensity. For SSO-LDH-R2 and for SSO-LDH-R4, the peak used was the (003) in Figure 7-6(a).

The FTIR plots in Figure 7-6(b) for SO-LDH-R2 and SO-LDH-R4 show the characteristic peak at 1354 cm^{-1} for both samples, which was assigned to the anti-symmetric stretching (v3) of the carbonate anions in the interlayer, whereas the small peak *ca* 685 cm^{-1} was assigned to the anti-symmetric deformation (v4) of the carbonate anion [114,132]. The broad peak *ca* 3400 cm^{-1} was attributed to the stretching vibrations of the OH molecules bonded to the metals (i.e., Mg and Fe) in the layers [114,132]. The small peak *ca.* 1000 cm^{-1} was related to the anti-symmetric (v3) and the symmetric vibrations of the PO_4^{-3} anion (as expected, as the PO_4^{-3} is part of the struvite, which was used as a raw material) [152]. The TGA analysis of both samples, SO-LDH-R2 and SO-LDH-R4 (Figure 7-6(c)) shows a well-

defined three-step decomposition, with a clear mass loss of 15 % from room temperature up to 200 ˚C. The latter mass loss was mainly attributed to the loss of adsorbed and interlayer water [114,152]. The next mass loss step was due to the dehydroxylation of the LDH layers and the removal of the interlayer carbonate anion, which goes from 200 ˚C up to *ca* 450 ˚C [114,152]. Finally, the sample's weight stabilized when forming the spinel at *ca* 700 ˚C. Figure 7-7 shows the SEM analysis of SO-LDH-R2 and SO-LDH-R4. As observed in Figure 7-7(a), SO-LDH-R2 had a higher crystallinity than SO-LDH-R4, which was further observed when comparing both SEM images. Figure 7-7(a) had a clear *rose des sables* structure, which was one type of morphology expected to be observed in the LDHs [102,152]. Contrary to the SEM image of SO-LDH-R2, the SEM image of SO-LDH-R4 (i.e., Figure 7-7(b)) is less resolved, though, nevertheless, *rose des sables* forms can also be observed.

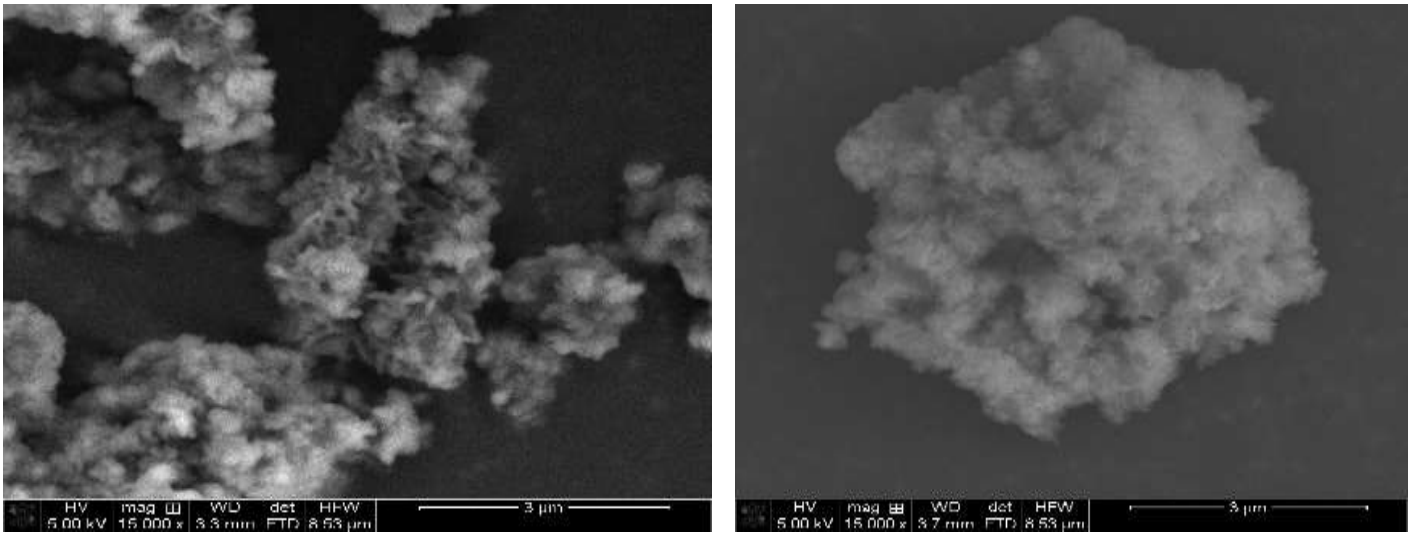

(a) (b)

Figure 7-7 Scanning electron microscopy images of (a) SO-LDH-R2 and (b) SO-LDH-R4 showing the *rose de sables* morphology typical of layered double hydroxide minerals.

SO-LDH-R2 and SO-LDH-R4 were also characterized through ICP-OES to confirm the targeted R-value = 2 and R-value = 4 from the co-precipitation experiments. The results are presented in Table 7-4. The amount of iron within the ochre sample and the amount of

magnesium in the waste struvite were calculated by triplicate through ICP-OES, as reported in the Section 7.3.1.

Table 7-4. Molar metal ratio, Mg and Fe composition of SO-LDH-R2 and SO-LDH-R4 obtained through inductively coupled plasma atomic emission spectroscopy.

Sample	**Amount of sample obtained (g)**	**Initial Fe^{3+} (g) in the ochre**	**Initial Mg^{2+} (g) in the waste struvite**	**Mg (%wt) ICP-OES**	**Fe (%wt) ICP-OES**	**Final Fe^{3+} (g) in the SO-LDH**	**Final Mg^{2+} (g) in the SO-LDH**	**[Mg]/[Fe] (ICP-OES)**
SO-LDH-R2	0.9	0.25	0.21	14.8	26.2	0.23	0.12	1.31
SO-LDH-R4	1.3	0.25	0.43	18.3	16.8	0.21	0.23	2.51

In a similar manner as occurred with the reported data in Table 7-2, if a mass balance of the Fe^{3+} and the Mg^{2+} is stablish between the precursors and the SO-LDHs, it can be observed that the initial Fe^{3+} is in a 92% and a 84% in the SO-LDH-R2 and SO-LDH-R4, however the a considerable amount of Mg^{2+} was lost during the synthesis procedure, as the SO-LDH-R2 and the SO-LDH-R4 only had a 57% and a 53% of the initial magnesium amount, respectively.

7.4 Discussion

7.4.1 Characterisation of the precursors for the synthesis of the Layered-Double Hydroxides

As observed in Figure 7-2, the precursors used for the preparation of the LDHs (i.e., synthetic struvite, ochre and waste struvite) were characterised. The synthetic struvite and the waste struvite, as observed in Figure 7-2(a) shared practically the same PXRD diffraction pattern, with no significant presence of an amorphous phase within the sample. Moreover, the FTIR and TGA plots, both also presented in Figure 7-2 were extremely similar, for both, the synthetic struvite and waste struvite. Although there was a chance that the waste struvite would contain more impurities than the synthetic struvite, due to the nature of the former material, the characterisation data led to think that both struvite samples share fairly similar composition and therefore could be expected for them to behave similarly when used as LDH precursors. As observed in Figure 7-3(a), the waste struvite was analysed through SEM, showing some coffin-like morphology was observed for the sample, which in conjunction with the PXRD data (Figure 7-2(a)), seems to agree with the literature [152,320,329] regarding the waste struvite crystals belonging to an orthorhombic system. Moreover, the coffin-like morphology from the waste struvite seems similar to the observed morphology from the synthetic struvite Figure 7-3(c). The presence of the phosphate anions observed in the FTIR (Figure 7-2(b)) for both struvite samples, indicates that it is a possibility that the phosphate (ca at 561 cm^{-1} and 982 cm^{-1}) can be also incorporated as the interlayer anion, in conjunction with the carbonate anion. In the Table C-1, Appendix C, it can be observed that, in comparison with the synthetic struvite, some metals such as aluminium, sodium and manganese are present within the sample of waste struvite in higher amounts. The presence of such metals could be negatively impacting the crystallinity of the sample, reducing the latter crystallinity of struvite due to competition to form other phosphates [322]. The ochre characterisation in Figure 7-2(a) presented a PXRD patter characteristic of the goethite, being the latter the most abundant iron phase within the sample [114,327], with the characteristic agglomeration of particles observed in Figure 7-3(b). According to Table C-1, in Appendix C, aluminium, sodium and manganese are some of the main impurities within the ochre sample. Being aluminium and sodium, some of the main impurities in both, the ochre and the waste struvite samples, there is a chance those impurities could be retained by the LDHs once formed, which can derive in further undesirable formation of other phases

within the LDHs. The TGA plots in Figure 7-2(c) for all samples seems to agree with the expected mass loss when the latter samples were heated, with both struvite samples losing ca 50 % of weight, which correlates well with the amount of expected mass to decompose when performing TGA, according to the struvite chemical formula $MgNH_4PO_4.6H_2O$.

7.4.2 Synthesis and characterisation of the layered double hydroxides using ochre and synthetic struvite

Before attempting to form an LDH material solely made out of waste materials, using both precursors (i.e., ochre and struvite), a preliminary approach forming LDHs made using only ochre as the waste precursor and synthetic struvite hexahydrate (i.e., SSO-LDH-R2 and SSO-LDH-R4) was undertaken. The synthesis needed to be first approximated using a synthetic source of struvite, rather than using the waste struvite from the beginning. As observed by the results obtained in Figure 7-4, conversion of the ochre and synthetic struvite precursors into LDHs was achieved. As observed in Figure 7-4(a), the characteristic diffraction peaks expected to be observed for LDH materials [102,152] with the lattice parameters *a* and c of 3.08 Å and 22.92 Å, for SSO-LDH-R2 and the lattice parameters *a* and c of 3.09 Å and 22.48 Å for SSO-LDH-R4, all of them in good agreement with the literature, as the sample can be considered to be a hydrotalcite-like compound, crystallised in a rhombohedral 3R symmetry[103]. For both, SSO-LDH-R2 and SSO-LDH-R4, the *d*-spacing obtained was 7.64 and 7.49 Å, respectively, which also corresponds well with the expected *d*-spacing to be observed when using carbonate as the interlayer anion[103,152]. The FTIR in Figure 7-4(b) confirmed the data obtained from the PXRD, proving the presence of the anti-symmetric stretching (v4) of the carbonate anion in the interlayer at 1354 cm^{-1}, which means LDH material was formed. However, as evidenced by the small peak at *ca* 1020 cm^{-1}, the phosphate anion is also present within the material, which probably co-exists in the interlayer in conjunction with the carbonate anion[152,328]. Thus, in Figure 7-4(b) a small peaks *ca* 570 cm^{-1} and 680 cm^{-1} can be assigned to the stretching vibrations of the M-O (i.e., the vibration of the metal oxides bonds). As observed in the PXRD plot in Figure 7-4(a) for both LDH samples, a small peak *ca* 28° was assigned to the possible presence of a goethite phase within the samples, which is further supported by the small FTIR peak *ca* 570 cm^{-1} usually associated to the stretching vibration of the Fe-O[151]. The SEM analysis, of both SSO-LDH-R2 and SSO-LDH-R4 is presented in Figure 7-5. For both samples, typical *rose de*

sables morphology are observed [102,152]. Although crystallinity is present in both samples, it remains unknown whether changing some of the reaction parameters such as decreasing the reaction temperature, or ageing the product at lower temperatures would keep favouring dissolution of the struvite, as the recent literature suggests the less dissolved the struvite is, the larger the crystals obtained [152]. The presence of the impurities observed in Table C-1, in the Appendix C, for the ochre, were also encountered within the SSO-LDH-R2 and SSO-LDH-R4 in considerable %wt. Among the metals encountered being part of the LDHs composition were aluminium, sodium, zinc and manganese. The presence of such impurities could be also hindering the formed LDHs from obtained a more crystalline structure, which would be reflected in a more reduced FWHM (Table 7-1) as although not showing specific diffraction peaks related to specific impurities, some of the oxides or hydroxides formed with the latter impurities, can be in the form of amorphous material [330,331], which seems to be present in the SSO-LDH samples. According to Table 7-2, the R-values of 2 and 4, for the SSO-LDH-R2 and SSO-LDH-R4 respectively, were not obtained, rather, a $[Mg^{2+}]/[Fe^{3+}]$ of 1.40 and 2.80 for SSO-LDH-R2 and SSO-LDH-R4, respectively, were achieved. It remains unknown at this point of the study why some cations were not fully incorporated into the layers, whether some reactions conditions could be varied to improve the $[Mg^{2+}]/[Fe^{3+}]$ of the final product towards a closer R-value. Based on the positive results obtained from the synthesis of the SSO-LDHs using ochre and synthetic struvite, the synthesis of the struvite-ochre LDHs completely made out of waste materials as precursors was further explored.

7.4.3 Synthesis and characterisation of the layered double hydroxides using ochre and waste struvite

According to Kwok *et al.,* [152], if a pre-treatment of NaOH is given to the struvite (i.e., suspend the struvite in a 1M NaOH solution for 1 hour), the efficiency of the process to make a phase pure struvite LDH can be improved. As the struvite did not dissolve, Kwok *et al.,* suggested the reaction might proceed through a solid-solid topotactic transformation. Nevertheless, this was not the case when trying to use the struvite and the ochre to make the SO-LDHs. No LDH was obtained when trying the Kwok *et al.,* synthetic approach, (see Figure 1-C, Appendix C for the PXRD diffraction pattern of the synthesis product) therefore other alternative methods of synthesis were attempted. As observed in Figure 1-C, no phase

pure LDH was formed. Some LDH as well as some struvite phases can be observed, nevertheless the sample was far from being phase pure LDH. Increasing temperature or leaving the sample age for longer period of times could favour struvite dissolution, which could then favour the obtention of a more crystalline LDH with no presence of starting material, nevertheless the latter approach was not further explored. Due to the struvite being more soluble in acidic environments [332], and already using 1 M HCl to dissolve the ochre in previous experiments, 1 M HCl was also used to digest the struvite. However, posterior experimental showed that when using waste struvite amounts over 1.2 g and leave them to digested in acid, the latter waste struvite sample presented difficulties to be fully dissolved in 1 M HCl, leaving a small amount of a black undissolved residue. As described in section 7.2, the amount of struvite was fixed based on the initial fixed amount of dry ochre used, therefore, more than 1 g of waste struvite was used during the making of SO-LDH-R2 and SO-LDH-R4. The black residue was also found to be present within the dropping funnel used during the co-precipitation procedure. The latter residue was not present when using synthetic struvite to perform the synthesis of the SSO-LDHs. As the black residue was not further analysed post-reaction (with the leftovers within the dropping funnel) the characteristics of the latter residue remain unknown. Nevertheless, it was assumed that the residue after digestion of the waste struvite could derive from an undissolved impurity or be a small amount of undissolved $MgHPO_4$ [320]. The latter assumption was considered as an elemental mass balance for Mg^{2+} and Fe^{3+} was carried out with the information obtained from the ICP-OES for the waste struvite, the ochre, and both the SO-LDHs (Table C-2 in the Appendix C) where it is observed than in both cases half the amount of Mg was not incorporated within the final product, as the only source of Mg was from the parent waste struvite and half of it was not quantified within the final SO-LDH. As mentioned by Shih *et al.,* [332], increasing the concentration of the HCl solution would improve the solubility of the struvite. Shin *et al.,* observed that when the HCl concentration was increased to 5 M, the struvite fully dissolved, however, a 5 M HCl decreased the pH of the co-precipitation reaction very rapidly, as well as introducing significant Cl^- counter anion concentrations. This would make the process difficult to regulate with the addition of the NaOH solution to keep the pH above 10. Therefore, for subsequent synthesis of LDHs using waste struvite, small amounts of the precursors should be used, where no more than 1.5 g of struvite are used, to favour full dissolution of the parent struvite. The elemental analysis of the ochre and struvite prior to their use as the mineral precursors to produce the SO-LDHs was the most

important characterisation step prior to the synthesis. As already discussed in Section 7.1 and as observed in Table C-1, Appendix C, the ochre and struvite contain a wide variety of metals as both are waste materials with a lot of impurities and that did not have a pre-treatment before being used to produce the SO-LDHs. If the amount of Fe and Mg for ochre and struvite are known, respectively, stoichiometry calculations can be performed to approximate the desired R-values of 2 and 4. However, as further addressed by the ICP-OES (Table 7-4), the obtained $[Mg^{2+}]/[Fe^{3+}]$ ratios for the SO-LDH-R2 and SO-LDH-R4 were 1.31 and 2.51, respectively. Moreover, the data obtained from the ICP-OES of the SSO-LDHs (i.e., Table 7-2) shows similar Fe^{3+} and Mg^{2+} %wt. composition when compared with the SO-LDHs, which could then mean that either some of the Mg^{2+} or the Fe^{3+} are not being properly incorporated into the hydroxide lattice. In a study performed by Gregoire *et al.,* [333] regarding the mechanistic aspect of the LDH formation, the synthesis of a Mg-Fe LDH was analysed and according to Gregoire *et al.,* during the formation of the LDH, a first stage occurs where a ferric oxohydroxide is formed (i.e., FeO(OH) specie). The latter ferric oxohydroxide is expected to have the M^{2+} species condensing over the surface for nucleation to start. Is in this point where Gregoire *et al.,* suggests that the Mg^{2+} cations are lacking affinity to condense over the ferric oxohydroxide surface as only some of the Mg^{2+} would incorporate and the latter will crystallise as $Mg(OH)_2$. Nevertheless, further experiments trying different R-values are needed and also further analysis of the obtained LDHs are also needed in order to understand why the R-values of 2 and 4 for SO-LDH-R2 and SO-LDH-R4, respectively were not fully achieved and whether or not the mechanism proposed by Gregoire *et al.,* a few lines above is happening when forming the respective SO-LDHs. The excess of the sodium carbonate solution (CO_3^{-2} : Fe^{3+} = 3:1) was based on previous unpublished work from this group, which suggested the latter ratio would be favourable. The excess of carbonate anion as well as he high pH of the solution (above 10) would favour supersaturation conditions [203,334]. In a comprehensive study to identify key parameters to tune during the co-precipitation methodology for LDHs preparation, Sun *et al.,* [335], concluded that the mean particle size of the LDHs as well as the monodispersed particle size distribution of the latter can be controlled through careful manipulation of the molar amount of the divalent and trivalent cations, the molar relation of the anion with the trivalent cation, the stirring rate and the addition rate. If the latter parameters can be controlled when making SO-LDHs, crystallinity and particle size could be potentially improved which would derivate in a catalyst of superior characteristics than when not controlling the latter

parameters, which would be highly beneficial when the SO-LDHs are used for catalytic or adsorption applications. The PXRD data (Figure 7-1(a)) proved the highly crystalline structure of the waste struvite, which retained practically the same diffraction pattern as the synthetic struvite obtained from the supplier, even though the sample of the waste struvite was obtained from inside a pipeline within a WWTP.

After being used as the mineral precursor with the ochre and analysing the obtained products, from Figure 7-6(a) it can be observed that both, SO-LDH-R2 and SO-LDH-R4 resulted in an LDH formation with the possible presence of an amorphous phase. Further studies would be needed to confirm the latter presence of any amorphous materials within the LDHs. The *d*-spacing and the unit cell parameters from Table 7-1 and Table 7-3 are in agreement with the expected values reported in the literature (~7 to 7.5 Å) for LDH containing carbonate as the interlayer anion[103,203]. Thus, from Figure 7-6(b), the FTIR of both, SOLDHR2 and SOLDHR4 (Figure 7-6(b)) shows the presence of the PO_4^{-2} anion, with a peak at 1030 cm^{-1}, which can be attributed to the anti-symmetric (v3) and the symmetric vibrations of the latter phosphate anion[152,328], that could be lying within the interlayer in conjunction with the carbonate anion, which also has a well-defined anti-symmetric (v3) stretching peak at 1354 cm^{-1} [102,114]. However, as the *d*-spacing of the SO-LDH-R2 and SO-LDH-R4 are 7.49 and 7.58 Å, respectively, the latter *d*-spacing values correlates very well with the expected *d*-spacing values when only carbonate exists in the interlayer of the material. Taking into account that the FTIR indeed shows the presence of the phosphate anion, it can be assumed that the phosphate is also co-existing in the interlayer with the carbonate anion, however the carbonate/phosphate ratio in the interlayer was not quantified. The TGA analysis in Figure 7-6(c) supports the obtained data from the PXRD and the FTIR, with the mass lost expected to be observed when heating LDH materials up to 800 ˚C. The first mass lost is due to the loss of adsorbed and interlayer water *ca* 200 ˚C, subsequently followed by dehydroxylation, the loss of the phosphates anions and the loss of the interlayer carbonate, until the formation of the spinel *ca.* 700 ˚C [102,114,152]. Due to the nature of the struvite, if carbonate is not used during the production of the LDH, and if manipulated in an inert atmosphere, a Mg-Fe PO_4 LDH can be potentially produced. However, further experimentation would be performed to address the latter assumption. According to the literature elsewhere[320,336], the strong acidic conditions of HCl favour a steady liberation of the ammonium ion, which remains in solution. Ideally, after the reaction is completed and

the LDH separated, the amount of N and P within the supernatant should be quantified, to be further recovered through different approaches [320,336], following the circular economy approach of obtaining added-value products out of waste, as the recovered N and P out of the struvite can be potentially used as a source of nutrients for fertilisers. The SEM images from the struvite (Figure 7-3(a)) show a needle-like and coffin-like morphology, which according to the literature, can be some of the different morphologies the struvite can adopt [332]. The SO-LDH-R2 and SO-LDH-R4 were also analysed through SEM and as observed in Figure 7-7, *rose des sables* morphologies for both samples, the SO-LDH-R2 and the SO-LDH-R4 were obtained. Based on the obtained characterisation of the materials after the synthesis, the results are of interest, showing the possibility of synthesizing a useful material out of waste precursors, which can have multiple applications, such as being a heavy metals and anions adsorbent [337], an heterogeneous basic catalyst to favour reactions such as biodiesel production or ketonic decarboxylation [114], or as a photocatalyst [292], to favour the production of hydrogen through visible light irradiation. Though no time remained in this PhD study to ascertain this, samples have been sent to the group of Prof. Dermot O'Hare at Oxford University to test for carbon capture materials.

7.4.4 The circular economy framework

The circular economy concept, as defined by Geissdoerfer *et al.,* [2] in which it is expected that in a sustainable economy, the inputs and wastes are minimized and their use cycle extended, was applied withing this chapter of the study. In a first approach, two waste materials that otherwise would be disposed (i.e., ochre and struvite collected from WWTP pipelines) were used as mineral precursors to prepare LDH materials. Although the co-precipitation process is not considered feasible to be a green scalable process[102,103], mostly due to the highly basic nature of the formed supernatant, it is interesting nevertheless the co-precipitation of two waste materials to form an added-value product. However, the LDH material is not the only product that could be obtained from the preparation of the latter LDH. During the co-precipitation process in acidic conditions, NH_4^+ will be in solution, and depending on the conditions of pH, phosphates can also be dissolved or remain as insoluble material. The latter ammonia and phosphate can be potentially recovered with further treatment after the LDH obtention to use them as a potential fertilizer source. Thus, with the formed LDH, other processes within the circular economy approach

can be explored. Mg-Fe LDH has been widely used in the literature for different purposes related sustainability. In Chapter 5, a Mg-Fe LDH made partially of waste (i.e., a synthetic source of magnesium and the iron obtained from the ochre waste) was used to promote the production of ketones through the ketonic decarboxylation of dodecanoic acid, a feedstock that can be potentially obtained from waste coconut oil [114]. Das *et al.,* also produced a Mg-Fe LDH with carbonate as the interlayer anion to be further calcined and use to remove selenium from wastewater effluents [267]. Also employing a Mg-Fe LDH with carbonate anion in the interlayer, Yadav *et al.,* [338] explored the removal of arsenate from water. Moreover, in Chapter 6, the production of a Mg-Fe LDH also using ochre as one of the mineral precursors was developed and evaluated as a photocatalyst to promote the production of hydrogen. Therefore, if followed properly, a complete circular economy framework for the use of ochre and waste struvite will employ both materials to produce an added-value product such an LDH, with a potential use to tackle or offer a solution to an environmental problem, while giving a use to all the subproducts obtained from the preparation of the latter LDH through co-precipitation.

7.5 Conclusions

Though LDHs have previously been prepared from waste material sources of either the M^{2+} or M^{3+} species, for the first time here we prepare a Mg/Fe LDH from two complimentary waste streams. The struvite and the ochre, both waste streams from industrial processes (i.e., wastewater treatment and mining, respectively) proved to be efficient mineral precursors, the ochre providing the Fe^{3+} cation whereas the struvite provided the Mg^{2+} to form Mg-Fe CO_3 LDHs. Before preparing the SO-LDHs, a first approach using ochre and synthetic struvite was done, which resulted in two LDH materials, SSO-LDH-R2 and SSOL-LDH-R4. Through the PXRD, FTIR and SEM, both SSO-LDHs were characterised and the presence of other phases or even amorphous material within the sample was not discarded. Once it was possible to synthesize the SSO-LDHs, the LDHs wholly made of waste struvite and ochre (i.e., SO-LDHs) were attempted to be synthesised. Two different R-values for the latter SO-LDHs were aimed to be prepared, 2 and 4, however, the co-precipitation conditions and the intrinsic characteristics of the precursors could have affected products, as the obtained $[Mg^{2+}]/[Fe^{3+}]$ values were not exactly 2 nor 4. The formation of the SO-LDH materials from the struvite and ochre was further supported by the FTIR, TGA and SEM analysis of the samples. As a first approach, it seems highly relevant the successful synthesis of an LDH wholly made of waste, however, further experimentation is needed to find the optimal process conditions to tune the characteristics of the resultant LDHs into a crystalline phase pure material. Nevertheless, the obtained results prove added-value catalysts can be obtained from waste streams, giving value to what otherwise would be considered a useless waste material.

8. Conclusions of this thesis

This work was focused on exploring the transformation of biomass and exploring the reaction parameters involved in such biomass transformations. Moreover, the production of energy through catalytic processes and the revalorization of waste materials were also studied. Therefore, the foundation of this work lies in the research of processes and materials related to sustainable and green chemistry. Since the postulation of the green chemistry principles in the 90's, the concept of green chemistry has been pushed hard, gaining in importance year by year, as the climatic and pollution issues in today's world urge the transition of the mankind towards a more sustainable and circular economy [2,339]. When doing research within a green chemistry framework, heterogeneous catalysis and biomass are concepts that have been intimately related and extensively developed over the years [102,103,152,267,313]. In the search of greener alternatives, researchers have found in biomass a potential alternative to tackle the adverse environmental issues (e.g., air and water pollution, GHG emissions due to fossil fuels, depletion of non-renewable resources, etc) that modern societies suffer nowadays [3,4,12]. As mentioned before, heterogeneous catalysis and the obtention of biomass derived products are areas of research that are intimately related. When a heterogeneous catalyst is chosen for a specific reaction, all the variables involving the reaction process are studied, including the obtention of the latter catalyst (i.e., whether it was synthesised on-site, purchased, etc), the catalyst properties, the reaction conditions and parameters and the post-reaction procedure. In the literature, heterogeneous catalysts such as metal oxides, zeolites, minerals, among others have been used to produce a wide range of biomass derived products, such as bio-derived synthons (i.e., alkanes, bioethers, ketones, etc), biofuels or lubricants [3,4,16,83,136]. In the early 1991, Cavani *et al.,* [103] developed a comprehensive study of a hydrotalcite-like material, named Layered double hydroxides (LDHs). LDH can also be used for a wide variety of applications, including adsorption, photocatalysis, biomass conversion, among others and are a versatile material that can be included within the vast range of compounds what is considered heterogeneous catalyst [102,136,151,261]. Nevertheless, increased efforts have arisen in recent years to not only produce sustainable products, but also ensure that in the whole production process, inputs and wastes are minimised, both in materials and energy and that the obtained products can have an expanded life cycle and can potentially be recycled and reused, sticking to the principle of what has been called circular economy [2,152]. It is in the context of the latter circular economy that using low-cost and environmentally friendly

materials for chemical reactions or exploring greener reaction substrates and pathways become more and more important. For instance, Alquzweeni and Alkizwini [317] coated chicken bones with an LDH and tried the latter as an adsorbent for cadmium out of waste water. Belviso *et al.,* [316] produced an LDH material through an ultrasonic bath of red-mud and the latter LDH was further mixed with zeolite to form an LDH-zeolite composite as an adsorbent of RO16 dye. Kwok *et al.,* [152] used waste struvite from a water treatment plant to prepare a highly crystalline LDH material that has high surface area, high density and porosity, with excellent capabilities to adsorb CO_2. Today's literature is not vast enough in terms of circular economy processes, however, in the recent years, more studies with a circular economy focus are being developed, as mentioned a few lines above.

On the basis of contextualising this work in the area of sustainability, biomass transformation processes and revalorisation of waste materials were studied. The ketonic decarboxylation of dodecanoic acid using MgO of different sizes proved to be efficient with the data suggesting the crystallite size of the MgO catalyst playing an important role for the latter ketonic decarboxylation reaction to yield similar results even when surface area of the samples differ greatly from one sample to another. Moreover, according to the data, the most important parameter affecting the ketonic decarboxylation, to obtain yields of ketones above 70 % is the temperature, with 300 ˚C being the optimal temperature, as going over 300 ˚C will favour pyrolysis decomposition of the reaction products and working under 300 ˚C will not favour full conversion of the starting materials.

Even when a highly basic oxide such as MgO was used to promote the ketonic decarboxylation of carboxylic acids, when trying to decarboxylate a polyunsaturated carboxylic acid such as linoleic acid, the homo ketonisation product of the latter unsaturated acids was not favoured, with some preliminary results indicating a polymerisation reaction outperforming the ketonisation or the possibility of a rearrangement during the ketonisation, as no clean ketone products were observed from the crude post-reaction mixture. Different carboxylic acids were tested, trying to vary the carbon chain lengths of the latter acids while trying to keep the acids within the scope of acids that could be obtained from biomass sources. No matter the length of the carbon chain, if the acid contained an α-hydrogen, the acids (i.e, phenylacetic acid, dodecanoic acid and hexanoic acid) underwent through cross-ketonisation and homo-ketonisation, yielding a clear post-reaction mixture of two symmetrical and one asymmetrical ketone in relatively similar yields. However,

linoleic acid did not favour a clean post-reaction product, as no homo-ketone from the linoleic acid was formed nor a unique cross-ketonisation product. Further experimental is needed trying a wider set of carboxylic acids, including acids containing other unsaturation as well as electron donor and withdrawing groups, go grasp more insights into the reaction mechanism. Nevertheless, magnesium oxide proved to be an efficient catalyst to transform fatty acids into ketones, favouring both, the formation of the symmetrical and the asymmetrical ketone products.

The synthesis of LDHs using waste materials capable of donating M^{III} and M^{II} cations, such as ochre and struvite, respectively, was proved to be feasible, at least through the co-precipitation approach. In a previous study from the Greenwell group [102], Mg-Al LDH materials were prepared and used as catalysts for the ketonic decarboxylation of stearic acid. Based on the latter results, and in the search of revalorising waste materials, the mining sludge ochre was used as a mineral precursor to prepare a Mg-Fe LDH and used the latter material as a catalyst for the ketonic decarboxylation of dodecanoic acid. Similarly to the work of Smith *et al.*, [102], the ochre-LDH material (i.e., partially made of waste) proved to be efficient in transforming the dodecanoic acid into the acid's respective homo-ketonisation product, with yields *ca* 75%. During the experiments, the ochre composition was heterogeneous, which varied the expected amount of Fe to be present within the sample and caused difficulties to reproduce the same exact R-value of the LDH. Moreover, another batch of an ochre-LDH material was attempted to be made, however, crystallinity was deficient and different oxide phases were formed. Nevertheless, and as a first approach, the ochre-LDH was used as a photocatalyst and proved to be efficient to harvest light from the visible light wavelength to produce hydrogen.

The revalorisation of the ochre from a waste to a precursor to produce an LDH was an idea adopted from the perspective of sustainability and the needs from a society to transition into a circular economy. In such scenario, a production process would minimise energy and material inputs and wastes, while reusing, recycling and producing added-value products with an extended life spam[2,12]. Therefore, the production of an LDH wholly made of waste was further explored using waste struvite from a wastewater treatment plant pipelines in conjunction of the ochre as the mineral precursors for the co-precipitation reaction. LDHs were successfully synthesized, however, the desired R-values were not obtained and the activity of the material as an efficient adsorbent or catalyst was not tested,

which would further support the sustainability framework in which the production of LDHs wholly made of waste is sitting on. Characterisation of the latter LDH proved further experimental needs to be done in order to improve the crystallinity of the material and attain the desired R-values.

8.1 Future work

Interesting conclusions were obtained during this study, however, more experimental work is needed to further understand why the unsaturated carboxylic acids are not giving a clean reaction towards the formation of ketones and test whether the use of catalyst with higher lattice energy or a carboxylic acid with less unsaturated bonds would lead to different results. Moreover, the test of other carboxylic acids with the presence of electron withdrawing or electron donor groups could also be of interest, and how the presence of such groups will affect the acidity of the α-hydrogen and consequently the production of ketones. Further studies trying to understand the role of the crystallite size to promote the ketonic decarboxylation are also needed, expanding the range of the different particle sizes of MgO and the reusability of the MgO catalyst, to evaluate the number of cycles the catalyst can be used until its activity gets reduced.

Moreover, the effectiveness of producing LDHs through the use of waste materials such as the mining wastes (potential sources of Fe and Mg)[142], red-mud (source of Al, Ca and Fe)[316], and eggshells (source of Ca) [340], just to name a few of the recent studies, needs to be further explored, as the capabilities of LDHs to be used in a wide variety of applications, such as to remove heavy metal ions from wastewater, promote the production of hydrogen, the formation of valuable chemical commodities and also using them as drug delivery agents into the human body are remarkable. It is also of interest keep exploring the possibility of generating such LDHs from waste but using an eco-friendlier synthesis approach such as the co-hydration procedure, which will not generate highly basic supernatants that need to receive treatment before disposal, making the production of LDHs a more sustainable process, which aligns very well with the current approach of the societies towards the development of sustainable and feasible infrastructures and materials.

Finally, all the work performed in this study converged with the context of my home country, Mexico where the contamination problem and the lack of future projects

focused on sustainability represent a potential risk for the future generations living in Mexico. Some of the materials developed in this thesis are already being tested as fluorine adsorbents in Mexico as as transesterification catalysts to produce biodiesel, however, these experiments are on early stage of development. Such projects are strongly related to some of the main pollution problems in Mexico, such as water bodies being contaminated with chemicals or with oils from the cooking industry.

Moreover, in this thesis, a better understanding of the properties of base solid heterogeneous catalysts such as MgO or LDHs laid the foundation for the development of future projects in Mexican universities once the author of this work returns home, which will hopefully contribute to the devopment of interesting projects to keep fighting against the pollution problems in Mexico.

A. Appendix

Preparation of calibration curves for product quantification

In the coming sections, the preparation of the mother solutions and the dilutions to make the calibration curves used to quantify the reaction products are explained.

Preparation of the 12-tricosanone calibration curve

A mother solution of 12-tricosanone (Alfa Aesar, 98%) of 0.04 M was prepared. Using the Equation 2.5 in Chapter 2, section 2.4.5, small vials of diluted 12-tricosanone solutions were prepared. The dilutions and the subsequent GC-FID analysis to obtain the peak area of both, the analyte (12-tricosanone), and the internal standard (Eicosane) are presented in Table A-1. The calibration curve is presented in Figure A-1.

Table A-1. Dilutions and concentrations of the analyte (12-tricosanone) and the internal standard (Eicosane) for the calibration curve preparation.

Concentration of the analyte	Concentration of the Internal Standard	Area of the analyte (Aa)	Area of the Internal Standard (AIS)	Ratio (Aa/AIS)	Ratio (Ca/CIS)
0.04	0.1	879937	732169	1.20	0.400
0.035	0.1	728923	734503	0.99	0.350
0.03	0.1	623854	736496	0.85	0.300
0.02	0.1	416893	758041	0.55	0.200
0.015	0.1	287871	770781	0.37	0.150
0.01	0.1	126282	810590	0.16	0.100
0.005	0.1	16255	837638	0.02	0.050
0	0.1	0	734608	0.00	0

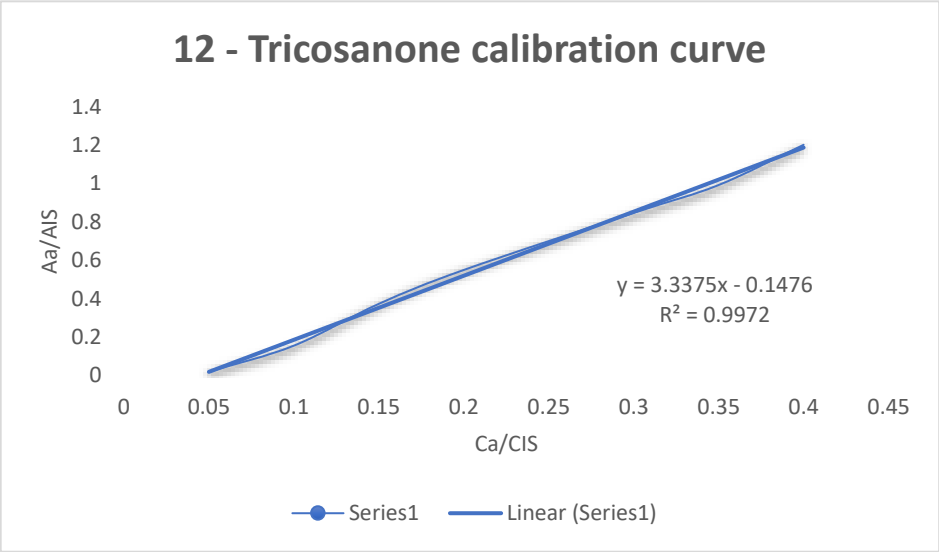

Figure A-1. 12-Tricosanone calibration curve

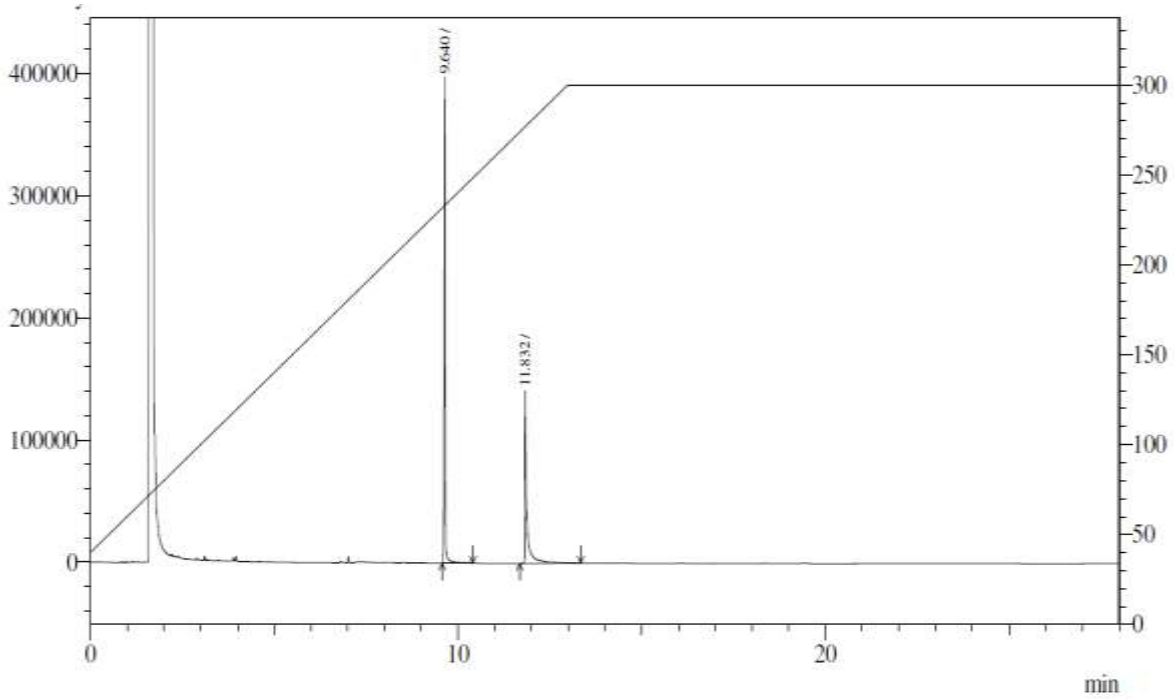

Figure A-2. Chromatogram of the crude reaction product, with the small peak at 11.83 related to the 12-tricosanone and the sharp, high peak at 9.60 representing the internal standard eicosane.

Preparation of the 1-phenyl-2-tridecanone calibration curve

A mother solution of 1-phenyl-2-tridecanone of 0.025 M was prepared. Using the Equation 2.5 in section 2.4.5, small vials of diluted 1,3-diphenyl-2-propanone solutions were prepared. The dilutions and the subsequent GC-FID analysis to obtain the peak area of both, the analyte (1-phenyl-2-tridecanone), and the internal standard (Eicosane) are presented in Table A-2. The calibration curve is presented in Figure A-3.

Table A-2. Dilutions and concentrations of the analyte (1-phenyl-2-tridecanone) and the internal standard (Eicosane) for the calibration curve preparation.

Concentration of the analyte	Concentration of the Internal Standard	Area of the analyte (Aa)	Area of the Internal Standard (AIS)	Ratio (Aa/AIS)	Ratio (Ca/CIS)
0.025	0.1	430545	776991	0.55	0.250
0.023	0.1	406052	792075	0.51	0.230
0.02	0.1	343248	765010	0.45	0.200
0.017	0.1	283905	778123	0.36	0.170
0.012	0.1	200855	783622	0.26	0.120
0.01	0.1	173639	813198	0.21	0.100
0.007	0.1	93448	815079	0.11	0.070
0.005	0.1	57838	864303	0.07	0.050
0.002	0.1	16908	841162	0.02	0.020

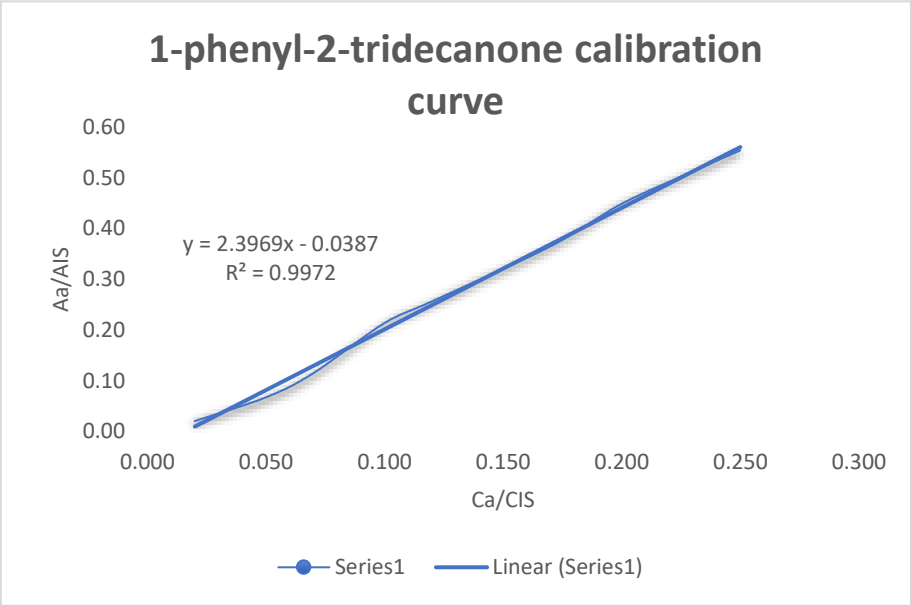

Figure A-3. 1-phenyl-2-tridecanone calibration curve

Preparation of the 1,3-diphenyl-2-propanone calibration curve

A mother solution of 1,3-diphenyl-2-propanone of 0.175 M was prepared. Using the Equation 2.5 in section 2.4.5, small vials of the diluted 1,3-diphenyl-2-propanone solutions were prepared. The dilutions and the subsequent GC-FID analysis to obtain the peak area of both, the analyte (1,3-diphenyl-2-propanone), and the internal standard (Eicosane) are presented in Table A-3. The calibration curve is presented in Figure A-4.

Table A-3. Dilutions and concentrations of the analyte (1,3-diphenyl-2-propanone) and the internal standard (Eicosane) for the calibration curve preparation.

Concentration of the analyte	Concentration of the Internal Standard	Area of the analyte (Aa)	Area of the Internal Standard (AIS)	Ratio (Aa/AIS)	Ratio (Ca/CIS)
0.175	0.1	2044398	731881	2.79	1.750
0.15	0.1	1780933	720901	2.47	1.500
0.125	0.1	1532563	747867	2.05	1.250
0.1	0.1	1250387	762447	1.64	1.000
0.05	0.1	767201	830226	0.92	0.500
0	0.1	0	721348	0.00	0.000

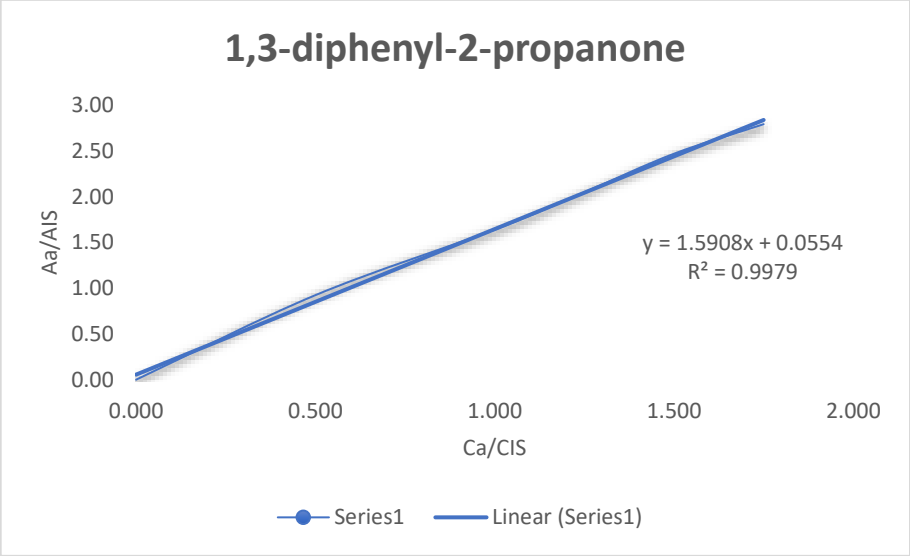

Figure A-4. Calibration curve of the 1,3-diphenyl-2-propanone

Preparation of the 6-heptadecanone calibration curve

A mother solution of 6-heptadecanone of 0.05 M was prepared. Using the Equation 2.5 in section 2.4.5, small vials of the diluted 6-heptadecanone solutions were prepared. The dilutions and the subsequent GC-FID analysis to obtain the peak area of both, the analyte (6-heptadecanone), and the internal standard (Eicosane) are presented in Table A-4. The calibration curve is presented in Figure A-5.

Table A-4. Dilutions and concentrations of the analyte (6-heptadecanone) and the internal standard (Eicosane) for the calibration curve preparation.

Concentration of the analyte	Concentration of the Internal Standard	Area of the analyte (Aa)	Area of the Internal Standard (AIS)	Ratio (Aa/AIS)	Ratio (Ca/CIS)
0.05	0.1	565143	698557	0.81	0.500
0.04	0.1	440835	751369	0.59	0.400
0.035	0.1	400239	744989	0.54	0.350
0.025	0.1	267840	717011	0.37	0.250
0.015	0.1	162151	753751	0.22	0.150
0.01	0.1	115193	692051	0.17	0.100
0.005	0.1	55331	717028	0.08	0.050

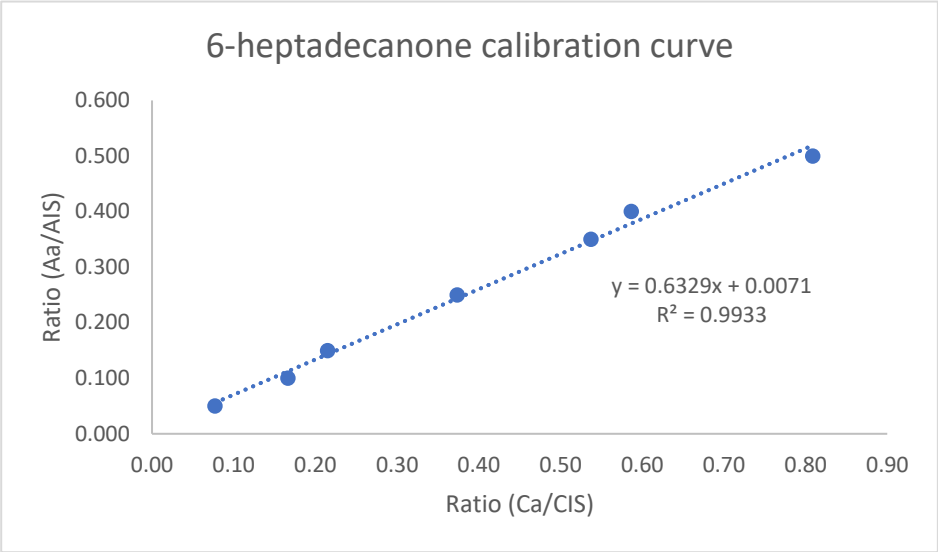

Figure A-5. Calibration curve of the 6-heptadecanone

Preparation of the 6-undecanone calibration curve

A mother solution of 6-undecanone 0.05 M was prepared. Using the Equation 2.5 in section 2.4.5, small vials of the diluted 6-undecanone solutions were prepared. The dilutions and the subsequent GC-FID analysis to obtain the peak area of both, the analyte (6-undecanone), and the internal standard (Eicosane) are presented in Table A-5. The calibration curve is presented in Figure A-6.

Table A-5. Dilutions and concentrations of the analyte (6-undecanone) and the internal standard (Eicosane) for the calibration curve preparation.

Concentration of the analyte	Concentration of the Internal Standard	Area of the analyte (Aa)	Area of the Internal Standard (AIS)	Ratio (Aa/AIS)	Ratio (Ca/CIS)
0.1	0.1	682849	712599	0.96	1.000
0.09	0.1	618003	722149	0.86	0.900
0.08	0.1	537180	729684	0.74	0.800
0.07	0.1	471600	711206	0.66	0.700
0.06	0.1	402567	719736	0.56	0.600
0.05	0.1	334605	708312	0.47	0.500
0.04	0.1	272140	710737	0.38	0.400
0.03	0.1	200305	711425	0.28	0.300
0.02	0.1	135083	706706	0.19	0.200
0.01	0.1	64242	707302	0.09	0.100

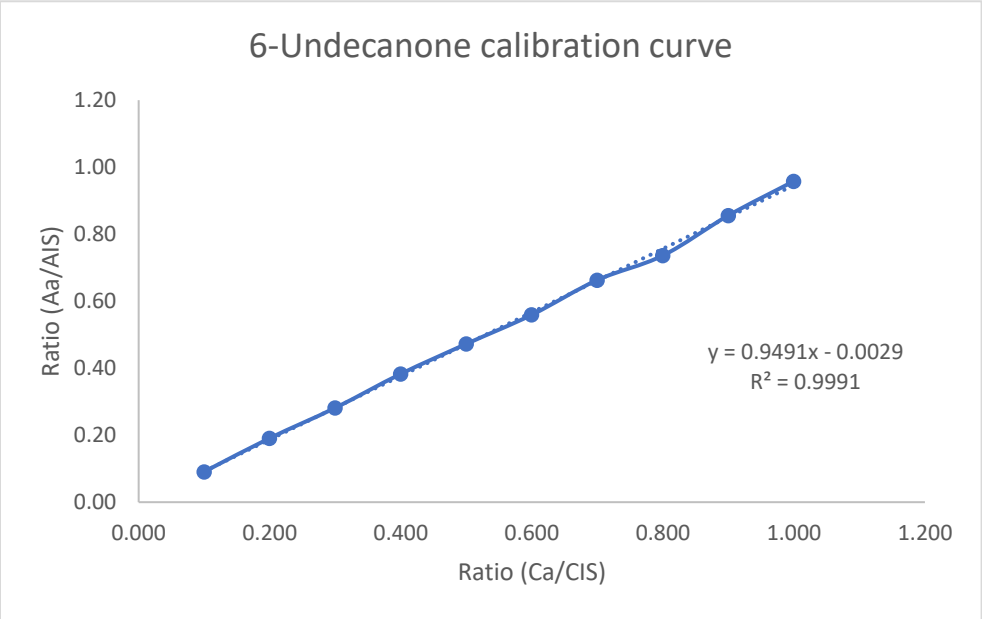

Figure A-6. Calibration curve of the 6-undecanone

GC-FID chromatograms

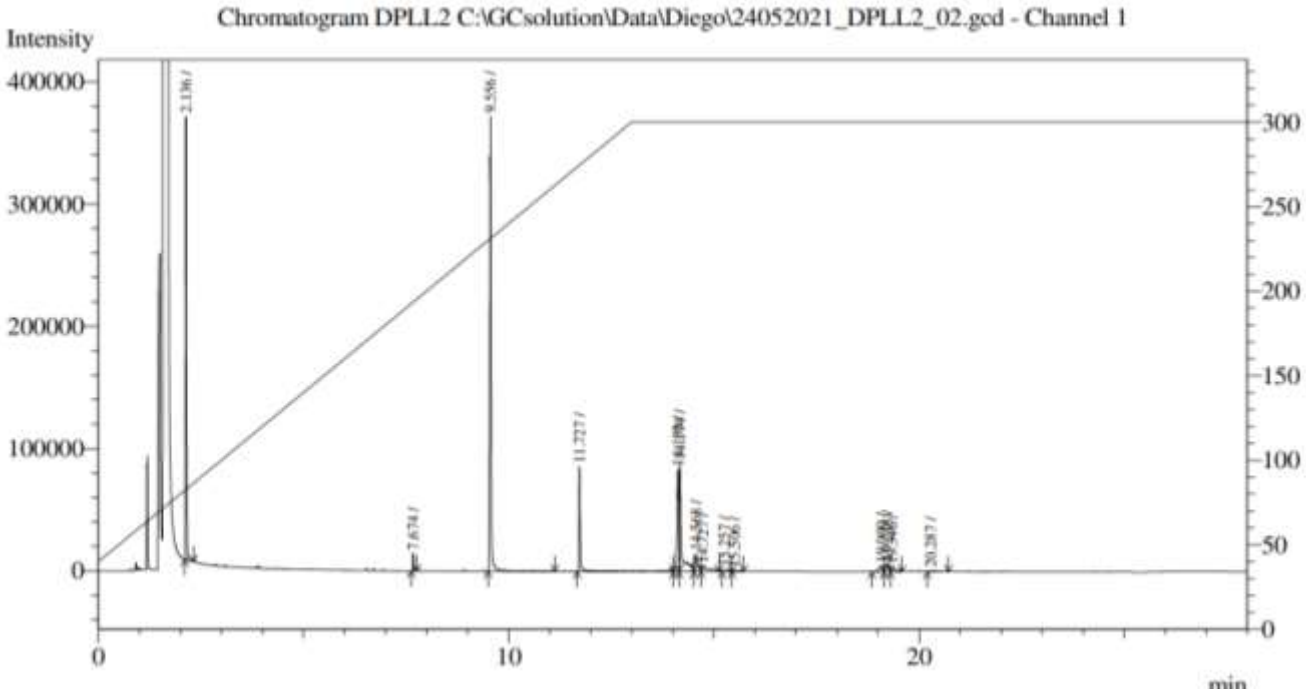

Figure A-7. Chromatogram corresponding to Entry 6 in Table 4-2 of the post reaction crude mixture of the ketonic decarboxylation of the linoleic acid and the dodecanoic acid.

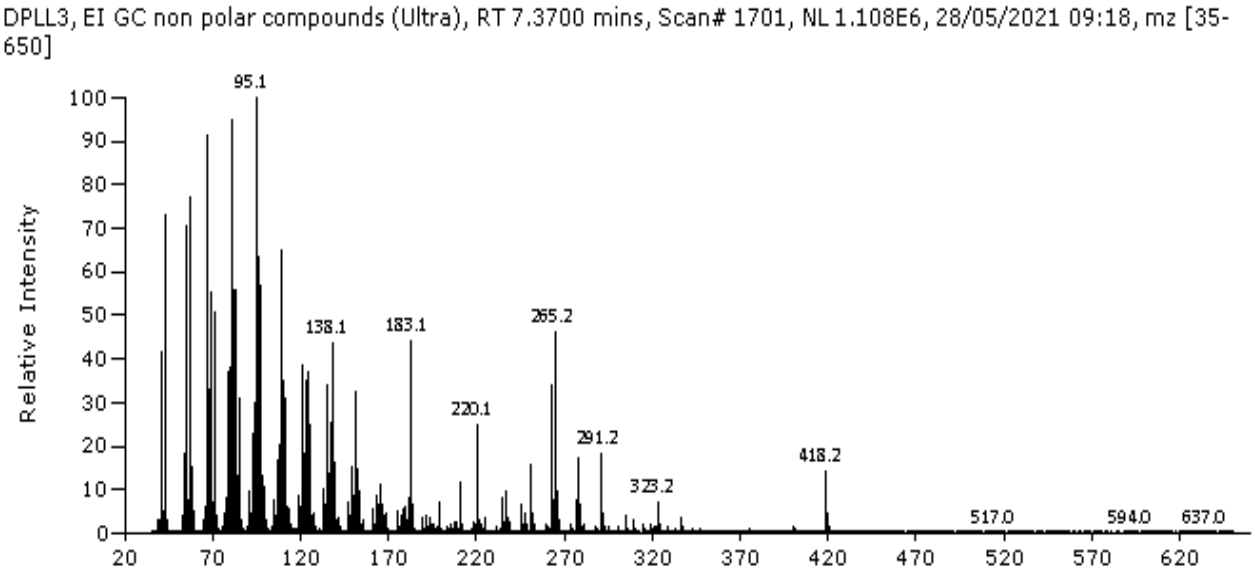

Figure A-8 m/z analysis of the unidentified product obtained at retention time of 7.37 min.

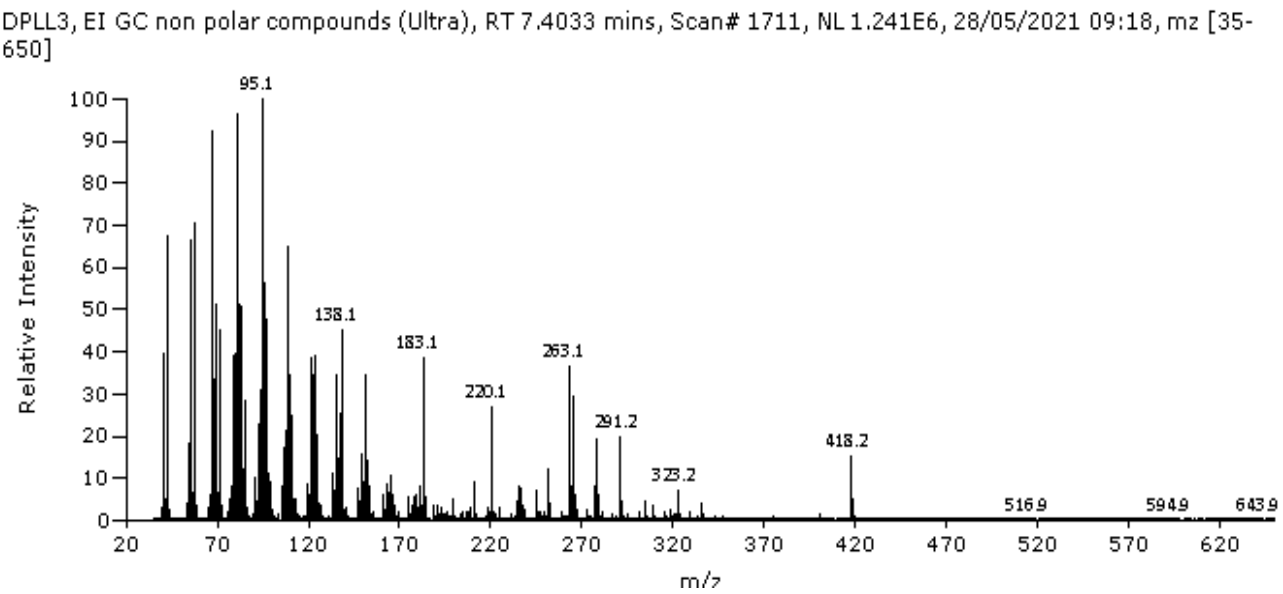

Figure A-9 m/z analysis of the unidentified product obtained at retention time of 7.40 min.

B. **Appendix**

Dewatering analysis of the waste material Saltburn ochre was performed as observed in Table B-1. The amount of water present in the sample was important to the stoichiometric calculations to find the appropriate concentration of iron in the sample and use the appropriate amount of Mg for the preparation of the catalyst.

Table B-1. Dewatering analysis of Saltburn ochre samples at constant temperature of 60 °C.

Mass of wet ochre (g)	Mass of dry ochre	Weight Loss (%)
5.6493	1.1591	79.5
6.0755	1.3878	77.2
6.4830	1.4390	77.8
	Average	78.2

ICP-OES analysis of LDH-CO_3

The ICP analysis of the LDH-CO_3 scanned for a whole range of metals, as showed in Table B-2. According to the technician in charge of the instrument, for semi-quantitative analysis of most elements the instrument scans across the electromagnetic spectrum from 190 to 800nm. The emission lines recorded are then processed with the 'Image' software, which compares them with those in its library to identify and quantify the elements present in the sample.

Table B-2. All metals present in 15 mg of LDH-CO_3 according to ICP-OES analysis.

LDH-CO_3	Element	Concentration (ppm)
	Ni	0.06
	Tm	0.06
	K	0.74
	Nb	0.08
	Dy	0.1
	Y	0.07
	Rh	0.15
	Er	0.06
	Cu	0.06
	Ga	0.21
	Rb	0.31
	Cd	0.14
	V	0.2
	As	0.07
	Gd	0.14
	Pr	0.24
	Zn	0.22
	Se	0.29
	La	0.53
	Nd	0.28
	Sr	0.55
	Na	0.57
	Mn	0.62
	Tc	0.53
	Tb	0.77
	Ba	0.94
	Mg	260
	Si	7.7
	Ca	15
	Fe	220
	Re	0.09
	W	0.45
	Os	0.15
	Ir	0.07
	Pt	0.08
	Pb	0.14
	Bi	0.06
	U	0.73

Ketone yield percentage was calculated using standards of 12-tricosanone and eicosane. As no other appreciable peaks were observed in the crude product mixture than those related to 12-tricosanone (Figure A-2, Appendix A) it was assumed no side reactions and full selectivity towards the ketone product was happening. The screening of the synthetic LDH (SLDH-CO_3) at 300 °C is presented in Table B-3.

Table B-3. Ketone yield using the (SLDH-CO_3) at 300 °C

300 ℃				250 ℃	
Catalyst load % (LDH-CO_3)	**Ketone yield (%)**	**Catalyst load % (SLDH-CO_3)**	**Ketone yield (%)**	**Catalyst load % (LDH-CO_3)**	**Ketone yield (%)**
1	68	1	47	1	0.5
3	81	3	86	3	8
5	70	5	74	5	24

The PXRD diffraction peaks from a calcined Saltburn ochre sample at 800 °C were used to prove right the data plotted in the TGA graphs, to help to interpret the loss of mass within the Saltburn ochre samples, which was related to the dehydroxilation of the latter, transforming all the FeO(OH) (goethite) into Fe_2O_3 while, at the same time, comparing the results with the existing literature.

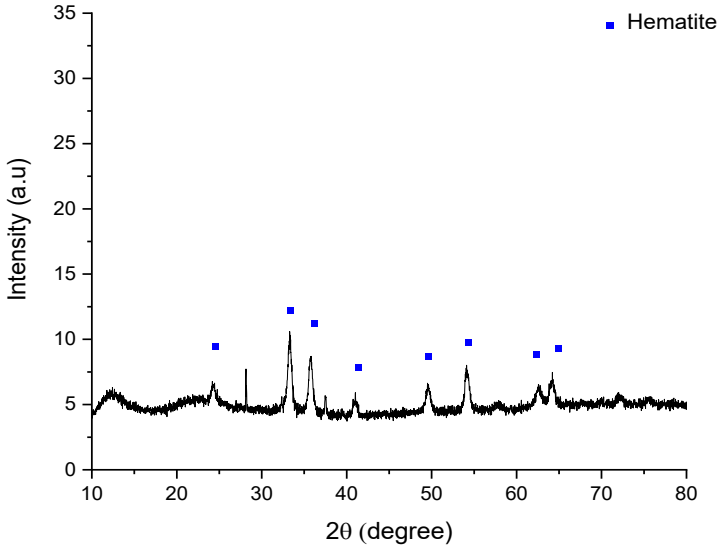

Figure B-1. Powder X-ray diffraction of the calcined ochre at 800 °C. The sample was calcined for 3 hours under in a muffle.

To determine the proper M^{II}/M^{III} ratio from the as-synthesized LDH_{ochre} and the LDH_{syn} analysis through EDS and ICP-OES were performed.

Table B-4. M^{II}/M^{III} ratio of LDH_{ochre} and LDH_{syn} through EDS

LDH_{ochre}	**Element**	**Atomic %**	**SD**
	Mg	26.2	0.8
	Fe	6.7	1.0
		3.9	0.7
LDH_{syn}	**Element**	**Atomic %**	**SD**
	Mg	23.4	1.9
	Fe	5.7	0.9
		4.1	0.4

An ICP-MS analysis of both, LDH_{ochre} and LDH_{syn} was performed to observe the presence of any other metal in the sample, as ochre comes from the waste mining sludge which might contain other M^{III} cations, which according to the literature would favour more visible light absorption.

Table B-5. ICP-MS scan for all possible metals present in LDH_{ochre} and LDH_{syn}

ppm mg/kg	LDH_{ochre}	LDH_{syn}	Possible interferences
7Li	nd	nd	
9Be	nd	nd	
11B	0.03	0.02	
23Na	3.70	49.48	
24Mg	na	na	C2
27Al	0.16	0.09	
31P	nd	nd	
39K	0.41	0.28	CO_2
44Ca	10.44	1.47	CO_2 N_2O SiO
45Sc	0.01	nd	SiO
47Ti	0.01	0.01	SiO
51V	2.80	2.14	
52Cr	0.44	0.35	
55Mn	0.19	0.01	
56Fe	na	na	ArO
59Co	nd	nd	
60Ni	0.12	0.04	
65Cu	0.26	0.05	
66Zn	0.44	0.19	
69Ga	nd	nd	
72Ge	0.08	0.09	
75As	0.44	0.38	
82Se	nd	nd	
85Rb	nd	nd	
88Sr	0.19	nd	
89Y	nd	nd	
90Zr	nd	nd	
93Nb	nd	nd	
95Mo	0.03	0.02	
101Ru	nd	nd	
103Rh	nd	nd	
105Pd	0.01	nd	

107Ag	nd	nd	
111Cd	nd	nd	
115In	nd	nd	
118Sn	0.01	nd	
121Sb	nd	nd	
125Te	nd	nd	
133Cs	nd	nd	
137Ba	0.02	nd	
139La	nd	nd	
140Ce	nd	nd	
141Pr	nd	nd	
146Nd	nd	nd	
147Sm	nd	nd	
153Eu	nd	nd	
157Gd	nd	nd	
159Tb	nd	nd	
163Dy	nd	nd	
165Ho	nd	nd	
166Er	nd	nd	
169Tm	nd	nd	
172Yb	nd	nd	
175Lu	nd	nd	
178Hf	nd	nd	
181Ta	nd	nd	
182W	nd	nd	
185Re	nd	nd	
189Os	nd	nd	
193Ir	nd	nd	
195Pt	nd	nd	
197Au	nd	nd	
202Hg	nd	nd	
205Tl	nd	nd	
208Pb	0.01	nd	
209Bi	nd	nd	
232Th	nd	nd	
238U	nd	nd	

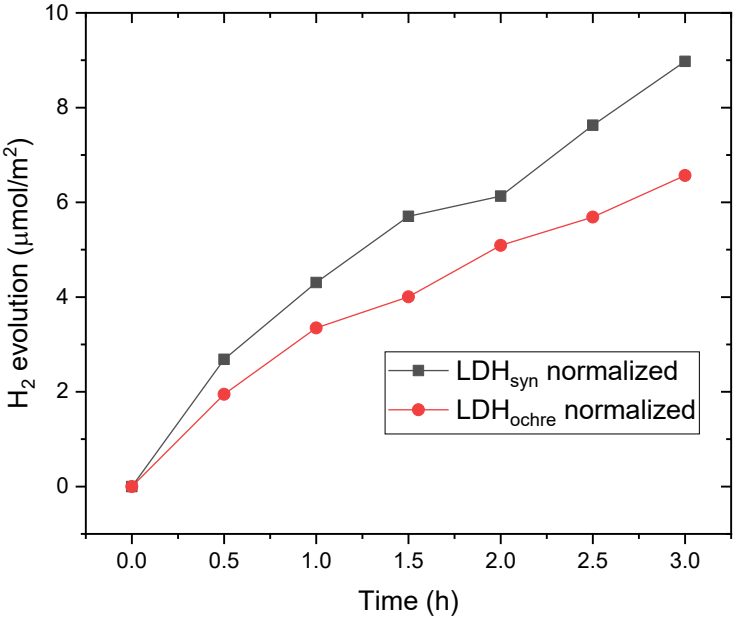

Figure B-2. Normalized production of hydrogen from LDH_{ochre} and LDH_{syn}

C. **Appendix**

Table C-1. ICP-MS analysis of all the different metals in the ochre, struvite, SO-LDH-R2 and SO-LDH-R4.

Metal in ppm (mg/kg)	Ochre	Waste struvite	SO-LDH-R2	SO-LDH-R4	Possible interferences
7Li	1.6	1.5	1.6	1.7	
9Be	nd	nd	nd	nd	
11B	23.0	1.6	4.6	3.7	
23Na	682.9	347.4	825.6	604.7	
24Mg	na	na	na	na	Concentration too high to quantify
27Al	204.7	686.6	736.3	877.4	
31P	91.1	11568.6	2661.1	2635.9	
39K	64.1	113.1	39.5	36.5	CO2
44Ca	na	na	na	na	CO2 N2O SiO Noisy background, unable to quantify
45Sc	8.3	nd	5.7	7.0	SiO
47Ti	12.6	970.9	167.1	176.6	SiO
51V	254.6	526.4	394.6	398.5	ClO
52Cr	29.3	394.5	58.2	53.9	ArC
55Mn	415.5	1210.8	1771.1	2116.3	
56Fe	na	na	na	na	Concentration too high to quantify
59Co	17.1	33.4	21.2	23.0	
60Ni	53.5	268.6	34.7	24.6	
65Cu	1.1	59.7	11.9	9.6	
66Zn	103.5	106.1	168.3	104.8	
69Ga	2.0	54.0	4.0	3.3	
72Ge	70.2	31.1	42.9	35.8	FeO
75As	156.5	26.4	nd	7.7	ArCl
82Se	nd	5.8	17.3	13.7	
85Rb	nd	1.1	nd	nd	
88Sr	511.8	31.7	502.9	332.2	
89Y	33.9	nd	15.6	10.0	
90Zr	nd	2.1	21.3	21.5	
93Nb	nd	4.4	nd	nd	
95Mo	nd	52.7	1.0	nd	
101Ru	nd	nd	nd	nd	
103Rh	nd	nd	nd	nd	
105Pd	2.0	nd	nd	nd	

107Ag	nd	20.3	2.3	1.6	
111Cd	nd	nd	nd	nd	
115In	nd	nd	nd	nd	
118Sn	12.3	158.8	20.1	11.1	
121Sb	97.3	99.9	74.4	57.4	
125Te	nd	nd	nd	nd	
133Cs	nd	nd	nd	nd	
137Ba	23.8	838.6	48.9	34.3	
139La	nd	19.3	nd	nd	
140Ce	nd	21.3	nd	nd	
141Pr	nd	1.6	nd	nd	
146Nd	2.1	4.6	1.1	nd	
147Sm	1.3	nd	nd	nd	
153Eu	nd	nd	nd	nd	
157Gd	3.8	nd	1.8	nd	
159Tb	nd	nd	nd	nd	
163Dy	3.5	nd	1.5	1.0	
165Ho	nd	nd	nd	nd	
166Er	1.8	nd	nd	nd	
169Tm	nd	nd	nd	nd	
172Yb	1.1	nd	nd	nd	
175Lu	nd	nd	nd	nd	
178Hf	nd	nd	nd	nd	
181Ta	nd	nd	nd	nd	
182W	nd	47.2	nd	nd	
185Re	nd	nd	nd	nd	
189Os	nd	nd	nd	nd	
193Ir	nd	nd	nd	nd	
195Pt	nd	nd	nd	nd	
197Au	2.3	nd	nd	nd	
202Hg	nd	122.8	11.8	6.5	
205Tl	nd	nd	nd	nd	
208Pb	1.9	269.7	58.9	67.2	
209Bi	nd	20.4	nd	nd	
232Th	nd	nd	nd	nd	
238U	nd	1.8	nd	nd	

nd = not detected
na = not available

Table C-2 ICP-MS analysis of all the different metals in the SSO-LDH-R2 and SSO-LDH-R4

Metal in ppm (mg/kg)	Synthetic struvite	SSO-LDH-R2	SSO-LDH-R4	Possible interferences
7Li	nd	16	22	
9Be	nd	nd	nd	
11B	32	77	80	
23Na	183	370	258	
24Mg	na	na	na	Concentration too high to quantify
27Al	23	115	100	
31P	767	5	nd	
39K	nd	nd	68	CO2
44Ca	245	3222	2058	CO2 N2O SiO
45Sc	nd	nd	nd	SiO
47Ti	29	11	9	SiO
51V	350	1068	1018	
52Cr	38	100	88	
55Mn	1	48	28	
56Fe	nd	na	na	Concentration too high to quantify
59Co	nd	1	nd	
60Ni	13	22	9	
65Cu	nd	5	3	
66Zn	10	60	26	
69Ga	1	5	6	
72Ge	22	26	19	
75As	40	85	48	
82Se	nd	3	5	
85Rb	nd	nd	nd	
88Sr	nd	45	28	
89Y	nd	3	2	
90Zr	2	7	6	
93Nb	nd	nd	nd	
95Mo	2	6	5	
101Ru	nd	nd	nd	
103Rh	nd	nd	nd	
105Pd	nd	nd	nd	
107Ag	1	2	2	
111Cd	nd	63	3	
115In	nd	nd	nd	
118Sn	4	6	6	
121Sb	31	51	44	

125Te	nd	nd	nd	
133Cs	nd	nd	nd	
137Ba	nd	4	5	
139La	nd	nd	nd	
140Ce	nd	nd	nd	
141Pr	nd	nd	nd	
146Nd	nd	nd	nd	
147Sm	nd	nd	nd	
153Eu	nd	nd	nd	
157Gd	nd	nd	nd	
159Tb	nd	nd	nd	
163Dy	nd	nd	nd	
165Ho	nd	nd	nd	
166Er	nd	nd	nd	
169Tm	nd	nd	nd	
172Yb	nd	nd	nd	
175Lu	nd	nd	nd	
178Hf	nd	nd	nd	
181Ta	nd	nd	nd	
182W	nd	1	nd	
185Re	nd	nd	nd	
189Os	nd	nd	nd	
193Ir	nd	nd	nd	
195Pt	nd	nd	nd	
197Au	nd	nd	nd	
202Hg	nd	1	nd	
205Tl	nd	nd	nd	
208Pb	nd	1	nd	
209Bi	nd	nd	nd	
232Th	nd	nd	nd	
238U	nd	nd	nd	

nd = not detected
na = not available

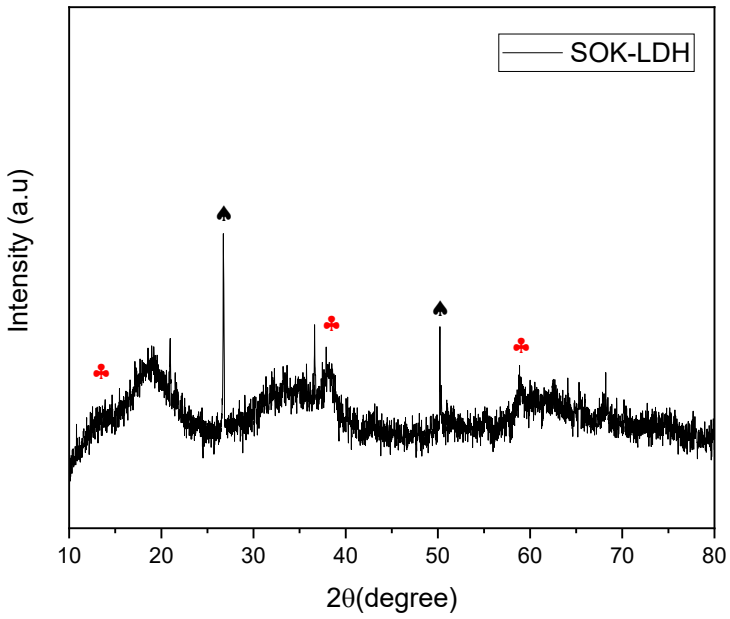

Figure C-1 Powder X-ray diffraction pattern of the synthesis of the waste struvite and ochre LDH synthesis dispersing the waste struvite in a solution with Na_2CO_3 and NaOH. The red symbol represents potential LDH phase whereas the black symbol represents diffraction peaks related to struvite.

References

1. Geissdoerfer, M.; Pieroni, M.P.P.; Pigosso, D.C.A.; Soufani, K. Circular business models: A review. *Journal of Cleaner Production* **2020**, *277*, 123741, doi:10.1016/j.jclepro.2020.123741.
2. Geissdoerfer, M.; Savaget, P.; Bocken, N.M.P.; Hultink, E.J. The Circular Economy – A new sustainability paradigm? *Journal of Cleaner Production* **2017**, *143*, 757-768, doi:10.1016/j.jclepro.2016.12.048.
3. Reprinted with permission from Shylesh, S.; Gokhale, A.A.; Ho, C.R.; Bell, A.T. Novel Strategies for the Production of Fuels, Lubricants, and Chemicals from Biomass. *Accounts of Chemical Research* **2017**, *50*, 2589-2597, doi:10.1021/acs.accounts.7b00354. Copyright 2021 American Chemical Society.
4. Smith, B.; Greenwell, H.C.; Whiting, A. Catalytic upgrading of tri-glycerides and fatty acids to transport biofuels. *Energy & Environmental Science* **2009**, *2*, 262-271, doi:10.1039/B814123A.
5. Horváth, I.T. Introduction: Sustainable Chemistry. *Chemical Reviews* **2018**, *118*, 369-371, doi:10.1021/acs.chemrev.7b00721.
6. Chamie, J. *World Population: 2020 Overview*; 18/01/21, 2020.
7. Nations, U. *World Population Prospects 2019: Highlights*; United Nations, Department of Economic and Social Affairs, Population Division: 2019, 2019.
8. Ahmad, T.; Zhang, D. A critical review of comparative global historical energy consumption and future demand: The story told so far. *Energy Reports* **2020**, *6*, 1973-1991, doi:10.1016/j.egyr.2020.07.020.
9. Badassa, B.; Sun, B.; Qiao, L. Sustainable Transport Infrastructure and Economic Returns: A Bibliometric and Visualization Analysis. *Sustainability* **2020**, *12*, 20-33, doi:10.3390/su12052033.
10. Manayil, J.C.; Osatiashtiani, A.; Mendoza, A.; Parlett, C.M.A.; Isaacs, M.A.; Durndell, L.J.; Michailof, C.; Heracleous, E.; Lappas, A.; Lee, A.F., et al. Impact of Macroporosity on Catalytic Upgrading of Fast Pyrolysis Bio-Oil by Esterification over Silica Sulfonic Acids. *Chemsuschem* **2017**, *10*, 3506-3511, doi:10.1002/cssc.201700959.
11. de_Richter, R.; Caillol, S. Fighting global warming: The potential of photocatalysis against CO2, CH4, N2O, CFCs, tropospheric O3, BC and other major contributors to climate change. *Journal of Photochemistry and Photobiology C: Photochemistry Reviews* **2011**, *12*, 1-19, doi:https://doi.org/10.1016/j.jphotochemrev.2011.05.002.
12. Chu, S.; Majumdar, A. Opportunities and challenges for a sustainable energy future. *Nature* **2012**, *488*, 294, doi:10.1038/nature11475.
13. Noraini, M.Y.; Ong, H.C.; Badrul, M.J.; Chong, W.T. A review on potential enzymatic reaction for biofuel production from algae. *Renewable and Sustainable Energy Reviews* **2014**, *39*, 24-34, doi:10.1016/j.rser.2014.07.089.
14. Hoang, N.H.; Fogarassy, C. Sustainability Evaluation of Municipal Solid Waste Management System for Hanoi (Vietnam)—Why to Choose the 'Waste-to-Energy' Concept. *Sustainability* **2020**, *12*, 1085, doi:10.3390/su12031085.
15. Taušová, M.; Mihaliková, E.; Čulková, K.; Stehlíková, B.; Tauš, P.; Kudelas, D.; Štrba, Ľ.; Domaracká, L. Analysis of Municipal Waste Development and Management in Self-Governing Regions of Slovakia. *Sustainability* **2020**, *12*, 5818, doi:10.3390/su12145818.

16. Simakova, I.L.; Murzin, D.Y. Transformation of bio-derived acids into fuel-like alkanes via ketonic decarboxylation and hydrodeoxygenation: Design of multifunctional catalyst, kinetic and mechanistic aspects. *Journal of Energy Chemistry* **2016**, *25*, 208-224, doi:10.1016/j.jechem.2016.01.004.
17. Chávez, C.S.; Caro, D.; Thomsen, M. Environmental Assessment of Alternatives for Biowaste Treatment in Mexico City. *Frontiers in Energy Research* **2019**, *7*, doi:10.3389/fenrg.2019.00030.
18. Rodriguez, A.; Castrejón-Godínez, M.; Ortiz-Hernandez, L.; Enrique, S.-S. *MANAGEMENT OF MUNICIPAL SOLID WASTE IN MEXICO*; 2015.
19. Chavarria-Hernandez, J.; Ordonez, L.; Barahona-Pérez, L.; Castro-Gomez, M.; Paredes-Cervantes, S. Perspectives on the utilization of waste fat from beef cattle and fowl for biodiesel production in Mexico: Potential production of biodiesel from animal fat in Mexico. *Journal of Chemical Technology & Biotechnology* **2016**, *92*, doi:10.1002/jctb.5057.
20. Sheinbaum-Pardo, C.; Calderón-Irazoque, A.; Ramírez-Suárez, M. Potential of biodiesel from waste cooking oil in Mexico. *Biomass and Bioenergy* **2013**, *56*, 230-238, doi:https://doi.org/10.1016/j.biombioe.2013.05.008.
21. Ranganathan, S.; Dutta, S.; Moses, J.A.; Anandharamakrishnan, C. Utilization of food waste streams for the production of biopolymers. *Heliyon* **2020**, *6*, e04891, doi:10.1016/j.heliyon.2020.e04891.
22. Sherwood, J. The significance of biomass in a circular economy. *Bioresource Technology* **2020**, *300*, 122755, doi:10.1016/j.biortech.2020.122755.
23. RedCorn, R.; Fatemi, S.; Engelberth, A.S. Comparing End-Use Potential for Industrial Food-Waste Sources. *Engineering* **2018**, *4*, 371-380, doi:10.1016/j.eng.2018.05.010.
24. Grycová, B.; Koutník, I.; Pryszcz, A. Pyrolysis process for the treatment of food waste. *Bioresource Technology* **2016**, *218*, 1203-1207, doi:10.1016/j.biortech.2016.07.064.
25. Galanakis, C.M. Recovery of high added-value components from food wastes: Conventional, emerging technologies and commercialized applications. *Trends in Food Science & Technology* **2012**, *26*, 68-87, doi:10.1016/j.tifs.2012.03.003.
26. Kirchherr, J.; Piscicelli, L.; Bour, R.; Kostense-Smit, E.; Muller, J.; Huibrechtse-Truijens, A.; Hekkert, M. Barriers to the Circular Economy: Evidence From the European Union (EU). *Ecological Economics* **2018**, *150*, 264-272, doi:https://doi.org/10.1016/j.ecolecon.2018.04.028.
27. Alonso, D.M.; Bond, J.Q.; Dumesic, J.A. Catalytic conversion of biomass to biofuels. *Green Chemistry* **2010**, *12*, 1493-1513, doi:10.1039/C004654J.
28. Gollakota, A.R.K.; Kishore, N.; Gu, S. A review on hydrothermal liquefaction of biomass. *Renewable and Sustainable Energy Reviews* **2018**, *81*, 1378-1392, doi:10.1016/j.rser.2017.05.178.
29. Li, H.; Riisager, A.; Saravanamurugan, S.; Pandey, A.; Sangwan, R.S.; Yang, S.; Luque, R. Carbon-Increasing Catalytic Strategies for Upgrading Biomass into Energy-Intensive Fuels and Chemicals. *ACS Catalysis* **2017**, 10.1021/acscatal.7b02577, 148-187, doi:10.1021/acscatal.7b02577.
30. Saxena, R.C.; Adhikari, D.K.; Goyal, H.B. Biomass-based energy fuel through biochemical routes: A review. *Renewable and Sustainable Energy Reviews* **2009**, *13*, 167-178, doi:10.1016/j.rser.2007.07.011.
31. Azizi, K.; Keshavarz Moraveji, M.; Abedini Najafabadi, H. A review on bio-fuel production from microalgal biomass by using pyrolysis method. *Renewable and Sustainable Energy Reviews* **2017**, 10.1016/j.rser.2017.10.033, doi:10.1016/j.rser.2017.10.033.

32. Srinophakun, P.; Thanapimmetha, A.; Rattanaphanyapan, K.; Sahaya, T.; Saisriyoot, M. Feedstock production for third generation biofuels through cultivation of Arthrobacter AK19 under stress conditions. *Journal of Cleaner Production* **2017**, *142*, 1259-1266, doi:10.1016/j.jclepro.2016.08.068.
33. Vassilev, S.V.; Vassileva, C.G. Composition, properties and challenges of algae biomass for biofuel application: An overview. *Fuel* **2016**, *181*, 1-33, doi:10.1016/j.fuel.2016.04.106.
34. Saladini, F.; Patrizi, N.; Pulselli, F.M.; Marchettini, N.; Bastianoni, S. Guidelines for emergy evaluation of first, second and third generation biofuels. *Renewable and Sustainable Energy Reviews* **2016**, *66*, 221-227, doi:10.1016/j.rser.2016.07.073.
35. Carneiro, M.L.N.M.; Pradelle, F.; Braga, S.L.; Gomes, M.S.P.; Martins, A.R.F.A.; Turkovics, F.; Pradelle, R.N.C. Potential of biofuels from algae: Comparison with fossil fuels, ethanol and biodiesel in Europe and Brazil through life cycle assessment (LCA). *Renewable and Sustainable Energy Reviews* **2017**, *73*, 632-653, doi:10.1016/j.rser.2017.01.152.
36. Mariscal, R.; Maireles-Torres, P.; Ojeda, M.; Sadaba, I.; Lopez Granados, M. Furfural: a renewable and versatile platform molecule for the synthesis of chemicals and fuels. *Energy & Environmental Science* **2016**, *9*, 1144-1189, doi:10.1039/C5EE02666K.
37. Hossain, M.Z.; Chowdhury, M.B.I.; Jhawar, A.K.; Xu, W.Z.; Charpentier, P.A. Continuous low pressure decarboxylation of fatty acids to fuel-range hydrocarbons with in situ hydrogen production. *Fuel* **2018**, *212*, 470-478, doi:10.1016/j.fuel.2017.09.092.
38. Capuano, D.; Costa, M.; Di Fraia, S.; Massarotti, N.; Vanoli, L. Direct use of waste vegetable oil in internal combustion engines. *Renewable and Sustainable Energy Reviews* **2017**, *69*, 759-770, doi:10.1016/j.rser.2016.11.016.
39. No, S.-Y. Inedible vegetable oils and their derivatives for alternative diesel fuels in CI engines: A review. *Renewable and Sustainable Energy Reviews* **2011**, *15*, 131-149, doi:10.1016/j.rser.2010.08.012.
40. Hellier, P.; Ladommatos, N.; Yusaf, T. The influence of straight vegetable oil fatty acid composition on compression ignition combustion and emissions. *Fuel* **2015**, *143*, 131-143, doi:10.1016/j.fuel.2014.11.021.
41. Sidibé, S.S.; Blin, J.; Vaitilingom, G.; Azoumah, Y. Use of crude filtered vegetable oil as a fuel in diesel engines state of the art: Literature review. *Renewable and Sustainable Energy Reviews* **2010**, *14*, 2748-2759, doi:10.1016/j.rser.2010.06.018.
42. Fermoso, J.; Pizarro, P.; Coronado, J.M.; Serrano, D.P. Advanced biofuels production by upgrading of pyrolysis bio-oil. *Wiley Interdisciplinary Reviews: Energy and Environment* **2017**, *6*, e245-n/a, doi:10.1002/wene.245.
43. Laesecke, J.; Ellis, N.; Kirchen, P. Production, analysis and combustion characterization of biomass fast pyrolysis oil – Biodiesel blends for use in diesel engines. *Fuel* **2017**, *199*, 346-357, doi:10.1016/j.fuel.2017.01.093.
44. Cai, W.; Liu, R.; He, Y.; Chai, M.; Cai, J. Bio-oil production from fast pyrolysis of rice husk in a commercial-scale plant with a downdraft circulating fluidized bed reactor. *Fuel Processing Technology* **2018**, *171*, 308-317, doi:10.1016/j.fuproc.2017.12.001.
45. Kay Lup, A.N.; Abnisa, F.; Wan Daud, W.M.A.; Aroua, M.K. A review on reactivity and stability of heterogeneous metal catalysts for deoxygenation of bio-oil model compounds. *Journal of Industrial and Engineering Chemistry* **2017**, *56*, 1-34, doi:10.1016/j.jiec.2017.06.049.
46. Khromova, S.A.; Smirnov, A.A.; Selishcheva, S.A.; Kukushkin, R.G.; Dundich, V.O.; Trusov, L.I.; Yakovlev, V.A. Magnesium-containing catalysts for the decarboxylation of bio-oil. *Catalysis in Industry* **2013**, *5*, 260-268, doi:10.1134/s2070050413030069.

47. Joshi, G.; Pandey, J.K.; Rana, S.; Rawat, D.S. Challenges and opportunities for the application of biofuel. *Renewable and Sustainable Energy Reviews* **2017**, *79*, 850-866, doi:10.1016/j.rser.2017.05.185.
48. Slade, R.; Bauen, A. Micro-algae cultivation for biofuels: Cost, energy balance, environmental impacts and future prospects. *Biomass and Bioenergy* **2013**, *53*, 29-38, doi:10.1016/j.biombioe.2012.12.019.
49. Filiciotto, L.; Balu, A.M.; Van der Waal, J.C.; Luque, R. Catalytic insights into the production of biomass-derived side products methyl levulinate, furfural and humins. *Catalysis Today* **2018**, *302*, 2-15, doi:10.1016/j.cattod.2017.03.008.
50. Hermida, L.; Abdullah, A.Z.; Mohamed, A.R. Deoxygenation of fatty acid to produce diesel-like hydrocarbons: A review of process conditions, reaction kinetics and mechanism. *Renewable and Sustainable Energy Reviews* **2015**, *42*, 1223-1233, doi:10.1016/j.rser.2014.10.099.
51. Romero, M.; Pizzi, A.; Toscano, G.; Casazza, A.A.; Busca, G.; Bosio, B.; Arato, E. Preliminary experimental study on biofuel production by deoxygenation of Jatropha oil. *Fuel Processing Technology* **2015**, *137*, 31-37, doi:10.1016/j.fuproc.2015.04.002.
52. Issariyakul, T.; Dalai, A.K. Biodiesel from vegetable oils. *Renewable and Sustainable Energy Reviews* **2014**, *31*, 446-471, doi:10.1016/j.rser.2013.11.001.
53. Kamal-Eldin, A.; Andersson, R. A multivariate study of the correlation between tocopherol content and fatty acid composition in vegetable oils. *Journal of the American Oil Chemists' Society* **1997**, *74*, 375-380, doi:10.1007/s11746-997-0093-1.
54. Banerji, R.; Chowdhury, A.R.; Misra, G.; Sudarsanan, G.; Verma, S.C.; Srivastava, G.S. Jatropha seed oils for energy. *Biomass* **1985**, *8*, 277-282, doi:10.1016/0144-4565(85)90060-5.
55. Klass, D.L. *Biomass for Renewable Energy, Fuels, and Chemicals*; Elsevier Science: 1998.
56. Danner, H.; Braun, R. Biotechnology for the production of commodity chemicals from biomass. *Chemical Society Reviews* **1999**, *28*, 395-405, doi:10.1039/A806968I.
57. Straathof, A.J.J.; Bampouli, A. Potential of commodity chemicals to become bio-based according to maximum yields and petrochemical prices. *Biofuels, Bioproducts and Biorefining* **2017**, *11*, 798-810, doi:10.1002/bbb.1786.
58. García-Martín, J.F.; Barrios, C.C.; Alés-Álvarez, F.-J.; Dominguez-Sáez, A.; Alvarez-Mateos, P. Biodiesel production from waste cooking oil in an oscillatory flow reactor. Performance as a fuel on a TDI diesel engine. *Renewable Energy* **2018**, 10.1016/j.renene.2018.03.002, doi:10.1016/j.renene.2018.03.002.
59. Thangavelu, S.K.; Ahmed, A.S.; Ani, F.N. Review on bioethanol as alternative fuel for spark ignition engines. *Renewable and Sustainable Energy Reviews* **2016**, *56*, 820-835, doi:10.1016/j.rser.2015.11.089.
60. Oh, Y.-K.; Hwang, K.-R.; Kim, C.; Kim, J.R.; Lee, J.-S. Recent developments and key barriers to advanced biofuels: A short review. *Bioresource Technology* **2018**, 10.1016/j.biortech.2018.02.089, doi:10.1016/j.biortech.2018.02.089.
61. Pattanaik, B.P.; Misra, R.D. Effect of reaction pathway and operating parameters on the deoxygenation of vegetable oils to produce diesel range hydrocarbon fuels: A review. *Renewable and Sustainable Energy Reviews* **2017**, *73*, 545-557, doi:10.1016/j.rser.2017.01.018.
62. Buffi, M.; Cappelletti, A.; Rizzo, A.M.; Martelli, F.; Chiaramonti, D. Combustion of fast pyrolysis bio-oil and blends in a micro gas turbine. *Biomass and Bioenergy* **2018**, *115*, 174-185, doi:10.1016/j.biombioe.2018.04.020.

63. Lu, Q.; Zhou, M.-x.; Li, W.-t.; Wang, X.; Cui, M.-s.; Yang, Y.-p. Catalytic fast pyrolysis of biomass with noble metal-like catalysts to produce high-grade bio-oil: Analytical Py-GC/MS study. *Catalysis Today* **2018**, *302*, 169-179, doi:10.1016/j.cattod.2017.08.029.
64. Kumar, R.; Enjamuri, N.; Shah, S.; Al-Fatesh, A.S.; Bravo-Suárez, J.J.; Chowdhury, B. Ketonization of oxygenated hydrocarbons on metal oxide based catalysts. *Catalysis Today* **2017**, 10.1016/j.cattod.2017.09.044, doi:10.1016/j.cattod.2017.09.044.
65. Oliver-Tomas, B.; Renz, M.; Corma, A. Direct conversion of carboxylic acids (Cn) to alkenes (C2n−1) over titanium oxide in absence of noble metals. *Journal of Molecular Catalysis A: Chemical* **2016**, *415*, 1-8, doi:10.1016/j.molcata.2016.01.019.
66. Energy, U.S.D.o. *BASIC RESEARCH NEEDS: CATALYSIS FOR ENERGY*; Office of Basic Energy Sciences Workshop, August 6-8, 2007, 2007; p 254.
67. Janampelli, S.; Darbha, S. Selective and reusable Pt-WOx/Al2O3 catalyst for deoxygenation of fatty acids and their esters to diesel-range hydrocarbons. *Catalysis Today* **2017**, 10.1016/j.cattod.2017.06.030, doi:10.1016/j.cattod.2017.06.030.
68. Na, J.-G.; Yi, B.E.; Kim, J.N.; Yi, K.B.; Park, S.-Y.; Park, J.-H.; Kim, J.-N.; Ko, C.H. Hydrocarbon production from decarboxylation of fatty acid without hydrogen. *Catalysis Today* **2010**, *156*, 44-48, doi:10.1016/j.cattod.2009.11.008.
69. Baldiraghi, F., Stanislao, M. D., Faraci, G. , Perego, C. , Marker, T. , Gosling, C. , Kokayeff, P. , Kalnes, T. and Marinangeli, R. . Ecofining: New Process for Green Diesel Production from Vegetable Oil. In *Sustainable Industrial Chemistry*, F. Cavani, G.C., S. Perathoner, and F. Trifiró, Ed. 2009; 10.1002/9783527629114.ch8.
70. Na, J.-G.; Han, J.K.; Oh, Y.-K.; Park, J.-H.; Jung, T.S.; Han, S.S.; Yoon, H.C.; Chung, S.H.; Kim, J.-N.; Ko, C.H. Decarboxylation of microalgal oil without hydrogen into hydrocarbon for the production of transportation fuel. *Catalysis Today* **2012**, *185*, 313-317, doi:10.1016/j.cattod.2011.08.009.
71. Elliott, W.W.; Hammick, D.L. 748. Mechanism of decarbonylation. The kinetics of the decarbonylation of benzoylformic acid in slightly aqueous sulphuric acid. *Journal of the Chemical Society (Resumed)* **1951**, 10.1039/JR9510003402, 3402-3407, doi:10.1039/JR9510003402.
72. Liu, Y.; Yang, X.; Liu, H.; Ye, Y.; Wei, Z. Nitrogen-doped mesoporous carbon supported Pt nanoparticles as a highly efficient catalyst for decarboxylation of saturated and unsaturated fatty acids to alkanes. *Applied Catalysis B: Environmental* **2017**, *218*, 679-689, doi:10.1016/j.apcatb.2017.06.065.
73. Simakova, I.; Simakova, O.; Mäki-Arvela, P.; Murzin, D.Y. Decarboxylation of fatty acids over Pd supported on mesoporous carbon. *Catalysis Today* **2010**, *150*, 28-31, doi:10.1016/j.cattod.2009.07.064.
74. Snåre, M.; Kubičková, I.; Mäki-Arvela, P.; Eränen, K.; Wärnå, J.; Murzin, D.Y. Production of diesel fuel from renewable feeds: Kinetics of ethyl stearate decarboxylation. *Chemical Engineering Journal* **2007**, *134*, 29-34, doi:10.1016/j.cej.2007.03.064.
75. Snåre, M.; Kubičková, I.; Mäki-Arvela, P.; Eränen, K.; Murzin, D.Y. Heterogeneous Catalytic Deoxygenation of Stearic Acid for Production of Biodiesel. *Industrial & Engineering Chemistry Research* **2006**, *45*, 5708-5715, doi:10.1021/ie060334i.
76. Romero, M.J.A.; Pizzi, A.; Toscano, G.; Busca, G.; Bosio, B.; Arato, E. Deoxygenation of waste cooking oil and non-edible oil for the production of liquid hydrocarbon biofuels. *Waste Management* **2016**, *47*, 62-68, doi:10.1016/j.wasman.2015.03.033.
77. Fu, J.; Shi, F.; Thompson, L.T.; Lu, X.; Savage, P.E. Activated Carbons for Hydrothermal Decarboxylation of Fatty Acids. *ACS Catalysis* **2011**, *1*, 227-231, doi:10.1021/cs1001306.

78. Hossain, M.Z.; Jhawar, A.K.; Chowdhury, M.B.I.; Xu, W.Z.; Wu, W.; Hiscott, D.V.; Charpentier, P.A. Using Subcritical Water for Decarboxylation of Oleic Acid into Fuel-Range Hydrocarbons. *Energy & Fuels* **2017**, *31*, 4013-4023, doi:10.1021/acs.energyfuels.6b03418.
79. Zhang, Z.; Yang, Q.; Chen, H.; Chen, K.; Lu, X.; Ouyang, P.; Fu, J.; Chen, J.G. In situ hydrogenation and decarboxylation of oleic acid into heptadecane over a Cu-Ni alloy catalyst using methanol as a hydrogen carrier. *Green Chemistry* **2018**, *20*, 197-205, doi:10.1039/C7GC02774E.
80. Domínguez-Barroso, M.V.; Herrera, C.; Larrubia, M.A.; Alemany, L.J. Diesel oil-like hydrocarbon production from vegetable oil in a single process over Pt–Ni/Al2O3 and Pd/C combined catalysts. *Fuel Processing Technology* **2016**, *148*, 110-116, doi:10.1016/j.fuproc.2016.02.032.
81. Pham, T.N.; Sooknoi, T.; Crossley, S.P.; Resasco, D.E. Ketonization of Carboxylic Acids: Mechanisms, Catalysts, and Implications for Biomass Conversion. *ACS Catalysis* **2013**, *3*, 2456-2473, doi:10.1021/cs400501h.
82. Pulido, A.; Oliver-Tomas, B.; Renz, M.; Boronat, M.; Corma, A. Ketonic Decarboxylation Reaction Mechanism: A Combined Experimental and DFT Study. *ChemSusChem* **2013**, *6*, 141-151, doi:10.1002/cssc.201200419.
83. Snell, R.W.; Shanks, B.H. Insights into the Ceria-Catalyzed Ketonization Reaction for Biofuels Applications. *ACS Catalysis* **2013**, *3*, 783-789, doi:10.1021/cs400003n.
84. Wu, K.; Yang, M.; Pu, W.; Wu, Y.; Shi, Y.; Hu, H.-s. Carbon Promoted ZrO2 Catalysts for Aqueous-Phase Ketonization of Acetic Acid. *ACS Sustainable Chemistry & Engineering* **2017**, *5*, 3509-3516, doi:10.1021/acssuschemeng.7b00226.
85. Jenkins, R.W.; Moore, C.M.; Semelsberger, T.A.; Chuck, C.J.; Gordon, J.C.; Sutton, A.D. The Effect of Functional Groups in Bio-Derived Fuel Candidates. *ChemSusChem* **2016**, *9*, 922-931, doi:10.1002/cssc.201600159.
86. Mekhemer, G.A.H.; Halawy, S.A.; Mohamed, M.A.; Zaki, M.I. Ketonization of acetic acid vapour over polycrystalline magnesia: in situ Fourier transform infrared spectroscopy and kinetic studies. *Journal of Catalysis* **2005**, *230*, 109-122, doi:10.1016/j.jcat.2004.09.030.
87. Yamada, Y.; Segawa, M.; Sato, F.; Kojima, T.; Sato, S. Catalytic performance of rare earth oxides in ketonization of acetic acid. *Journal of Molecular Catalysis A: Chemical* **2011**, *346*, 79-86, doi:10.1016/j.molcata.2011.06.011.
88. Pham, T.N.; Shi, D.; Sooknoi, T.; Resasco, D.E. Aqueous-phase ketonization of acetic acid over Ru/TiO2/carbon catalysts. *Journal of Catalysis* **2012**, *295*, 169-178, doi:10.1016/j.jcat.2012.08.012.
89. Pestman, R.; Koster, R.M.; van Duijne, A.; Pieterse, J.A.Z.; Ponec, V. Reactions of Carboxylic Acids on Oxides: 2. Bimolecular Reaction of Aliphatic Acids to Ketones. *Journal of Catalysis* **1997**, *168*, 265-272, doi:10.1006/jcat.1997.1624.
90. Corma, A.; Oliver-Tomas, B.; Renz, M.; Simakova, I.L. Conversion of levulinic acid derived valeric acid into a liquid transportation fuel of the kerosene type. *Journal of Molecular Catalysis A: Chemical* **2014**, *388-389*, 116-122, doi:10.1016/j.molcata.2013.11.015.
91. Pacchioni, G. Ketonization of Carboxylic Acids in Biomass Conversion over TiO2 and ZrO2 Surfaces: A DFT Perspective. *ACS Catalysis* **2014**, *4*, 2874-2888, doi:10.1021/cs500791w.
92. Neunhoeffer, O.; Paschke, P. Über den Mechanismus der Ketonbildung aus Carbonsäuren. *Berichte der deutschen chemischen Gesellschaft (A and B Series)* **1939**, *72*, 919-929, doi:10.1002/cber.19390720442.
93. Nagashima, O.; Sato, S.; Takahashi, R.; Sodesawa, T. Ketonization of carboxylic acids over CeO2-based composite oxides. *Journal of Molecular Catalysis A: Chemical* **2005**, *227*, 231-239, doi:10.1016/j.molcata.2004.10.042.

94. Deng, L.; Fu, Y.; Guo, Q.-X. Upgraded Acidic Components of Bio-oil through Catalytic Ketonic Condensation. *Energy & Fuels* **2009**, *23*, 564-568, doi:10.1021/ef800692a.
95. Corma, A.; Renz, M.; Schaverien, C. Coupling Fatty Acids by Ketonic Decarboxylation Using Solid Catalysts for the Direct Production of Diesel, Lubricants, and Chemicals. *ChemSusChem* **2008**, *1*, 739-741, doi:10.1002/cssc.200800103.
96. Wang, S.; Iglesia, E. Experimental and theoretical assessment of the mechanism and site requirements for ketonization of carboxylic acids on oxides. *Journal of Catalysis* **2017**, *345*, 183-206, doi:10.1016/j.jcat.2016.11.006.
97. Shutilov, A.A.; Simonov, M.N.; Zaytseva, Y.A.; Zenkovets, G.A.; Simakova, I.L. Phase composition and catalytic properties of ZrO2 and CeO2-ZrO2 in the ketonization of pentanoic acid to 5-nonanone. *Kinetics and Catalysis* **2013**, *54*, 184-192, doi:10.1134/s0023158413020134.
98. Gliński, M.; Kijeński, J.; Jakubowski, A. Ketones from monocarboxylic acids: Catalytic ketonization over oxide systems. *Applied Catalysis A: General* **1995**, *128*, 209-217, doi:10.1016/0926-860X(95)00082-8.
99. Tosoni, S.; Pacchioni, G. Acetic acid ketonization on tetragonal zirconia: Role of surface reduction. *Journal of Catalysis* **2016**, *344*, 465-473, doi:10.1016/j.jcat.2016.10.002.
100. Gumidyala, A.; Sooknoi, T.; Crossley, S. Selective ketonization of acetic acid over HZSM-5: The importance of acyl species and the influence of water. *Journal of Catalysis* **2016**, *340*, 76-84, doi:10.1016/j.jcat.2016.04.017.
101. Stefanidis, S.D.; Karakoulia, S.A.; Kalogiannis, K.G.; Iliopoulou, E.F.; Delimitis, A.; Yiannoulakis, H.; Zampetakis, T.; Lappas, A.A.; Triantafyllidis, K.S. Natural magnesium oxide (MgO) catalysts: A cost-effective sustainable alternative to acid zeolites for the in situ upgrading of biomass fast pyrolysis oil. *Applied Catalysis B: Environmental* **2016**, *196*, 155-173, doi:10.1016/j.apcatb.2016.05.031.
102. Smith, B.; Li, L.; Perera-Solis, D.; Gildea, L.; Zholobenko, V.; Dyer, P.; Greenwell, H. Ketone Formation via Decarboxylation Reactions of Fatty Acids Using Solid Hydroxide/Oxide Catalysts. *Inorganics* **2018**, *6*, 121, doi:10.3390/inorganics6040121.
103. Cavani, F.; Trifirò, F.; Vaccari, A. Hydrotalcite-type anionic clays: Preparation, properties and applications. *Catalysis Today* **1991**, *11*, 173-301, doi:10.1016/0920-5861(91)80068-K.
104. Greenwell, H.C.; Jones, W.; Stamires, D.N.; O'Connor, P.; Brady, M.F. A one-pot synthesis of hybrid organo-layered double hydroxide catalyst precursors. *Green Chemistry* **2006**, *8*, 1067-1072, doi:10.1039/B605851E.
105. Sherwood, T.K. Diffusion phenomena in heterogeneous catalysis. *Pure and Applied Chemistry* **1965**, *10*, 595-610, doi:10.1351/pac196510040595.
106. Fadhel, A.Z.; Pollet, P.; Liotta, C.L.; Eckert, C.A. Combining the benefits of homogeneous and heterogeneous catalysis with tunable solvents and nearcritical water. *Molecules (Basel, Switzerland)* **2010**, *15*, 8400-8424, doi:10.3390/molecules15118400.
107. Dumesic, J.A.; Huber, G.W.; Boudart, M. Principles of Heterogeneous Catalysis. In *Handbook of Heterogeneous Catalysis*, 2008; 10.1002/9783527610044.hetcat0001.
108. Wei, Z.; Xu, C.; Li, B. Application of waste eggshell as low-cost solid catalyst for biodiesel production. *Bioresource Technology* **2009**, *100*, 2883-2885, doi:10.1016/j.biortech.2008.12.039.
109. Mohamed, R.M.; Kadry, G.A.; Abdel-Samad, H.A.; Awad, M.E. High operative heterogeneous catalyst in biodiesel production from waste cooking oil. *Egyptian Journal of Petroleum* **2020**, *29*, 59-65, doi:10.1016/j.ejpe.2019.11.002.

110. Mukhopadhyay, P.; Chakraborty, R. Recycling of Solid Waste to Heterogeneous Catalyst for Production of Valuable Fuel Additives. In Proceedings of Waste Management and Resource Efficiency; pp. 947-959.
111. Maneerung, T.; Kawi, S.; Dai, Y.; Wang, C.-H. Sustainable biodiesel production via transesterification of waste cooking oil by using CaO catalysts prepared from chicken manure. *Energy Conversion and Management* **2016**, *123*, 487-497, doi:10.1016/j.enconman.2016.06.071.
112. Castro-León, G.; Baquero-Quinteros, E.; Loor, B.G.; Alvear, J.; Montesdeoca Espín, D.E.; De La Rosa, A.; Montero-Calderón, C. Waste to Catalyst: Synthesis of Catalysts from Sewage Sludge of the Mining, Steel, and Petroleum Industries. *Sustainability* **2020**, *12*, 9849, doi:10.3390/su12239849.
113. Zhao, R.; Tian, Z.; Zhao, Z. Effect of calcination temperature on rare earth tailing catalysts for catalytic methane combustion. *Green Processing and Synthesis* **2020**, *9*, 734-743, doi:10.1515/gps-2020-0053.
114. Perera-Solis, D.D.; Pimlott, M.; Fidment, E.; Whiting, A.; Greenwell, H.C. Adding Value to Waste Minerals in a Circular Economy Framework: Ochre-Derived Layered Double Hydroxide Catalysts in Fatty Acid Ketonisation. *Minerals* **2019**, *9*, 681, doi:10.3390/min9110681.
115. Wagh, A.S. Chapter 3 - Raw Materials. In *Chemically Bonded Phosphate Ceramics (Second Edition)*, Wagh, A.S., Ed. Elsevier: 2016; 10.1016/B978-0-08-100380-0.00003-8pp. 35-49.
116. Küünal, S.; Rauwel, P.; Rauwel, E. Chapter 14 - Plant extract mediated synthesis of nanoparticles. In *Emerging Applications of Nanoparticles and Architecture Nanostructures*, Barhoum, A., Makhlouf, A.S.H., Eds. Elsevier: 2018; 10.1016/B978-0-323-51254-1.00014-2pp. 411-446.
117. Liu, L.; Luo, X.-B.; Ding, L.; Luo, S.-L. 4 - Application of Nanotechnology in the Removal of Heavy Metal From Water. In *Nanomaterials for the Removal of Pollutants and Resource Reutilization*, Luo, X., Deng, F., Eds. Elsevier: 2019; 10.1016/B978-0-12-814837-2.00004-4pp. 83-147.
118. Tahir, M.B.; Rafique, M.; Rafique, M.S.; Fatima, N.; Israr, Z. Chapter 6 - Metal oxide- and metal sulfide-based nanomaterials as photocatalysts. In *Nanotechnology and Photocatalysis for Environmental Applications*, Tahir, M.B., Rafique, M., Rafique, M.S., Eds. Elsevier: 2020; 10.1016/B978-0-12-821192-2.00006-1pp. 77-96.
119. Bailly, M.-L.; Chizallet, C.; Costentin, G.; Krafft, J.-M.; Lauron-Pernot, H.; Che, M. A spectroscopy and catalysis study of the nature of active sites of MgO catalysts: Thermodynamic Brønsted basicity versus reactivity of basic sites. *Journal of Catalysis* **2005**, *235*, 413-422, doi:10.1016/j.jcat.2005.09.004.
120. Demirbas, A. Biodiesel from Vegetable Oils with MgO Catalytic Transesterification in Supercritical Methanol. *Energy Sources, Part A: Recovery, Utilization, and Environmental Effects* **2008**, *30*, 1645-1651, doi:10.1080/15567030701268401.
121. Ryu, H.W.; Lee, H.W.; Jae, J.; Park, Y.-K. Catalytic pyrolysis of lignin for the production of aromatic hydrocarbons: Effect of magnesium oxide catalyst. *Energy* **2019**, *179*, 669-675, doi:10.1016/j.energy.2019.05.015.
122. Zheng, Y.; Cao, L.; Xing, G.; Bai, Z.; Huang, J.; Zhang, Z. Microscale flower-like magnesium oxide for highly efficient photocatalytic degradation of organic dyes in aqueous solution. *RSC Advances* **2019**, *9*, 7338-7348, doi:10.1039/C8RA10385B.
123. He, J.; Wei, M.; Li, B.; Kang, Y.; Duan, X.; Evans, D.G. *Layered Double Hydroxides*; Springer: 2006.

124. L, C.; Pavan, P.; Valim, J. Comparative Study of the Coprecipitation Methods for the Preparation of Layered Double Hydroxides. *Journal of the Brazilian Chemical Society* **2000**, *11*, doi:10.1590/S0103-50532000000100012.
125. Manohara, G.V.; Whiting, A.; Greenwell, H.C. Reduced to Hierarchy: Carbon Filament-Supported Mixed Metal Oxide Nanoparticles. *ACS Omega* **2019**, *4*, 20230-20236, doi:10.1021/acsomega.9b02534.
126. Xu, M.; Wei, M. Layered Double Hydroxide-Based Catalysts: Recent Advances in Preparation, Structure, and Applications. *Advanced Functional Materials* **2018**, *28*, 1802943, doi:10.1002/adfm.201802943.
127. Bing, W.; Zheng, L.; He, S.; Rao, D.; Xu, M.; Zheng, L.; Wang, B.; Wang, Y.; Wei, M. Insights on Active Sites of CaAl-Hydrotalcite as a High-Performance Solid Base Catalyst toward Aldol Condensation. *ACS Catalysis* **2018**, *8*, 656-664, doi:10.1021/acscatal.7b03022.
128. Feng, J.; He, Y.; Liu, Y.; Du, Y.; Li, D. Supported catalysts based on layered double hydroxides for catalytic oxidation and hydrogenation: general functionality and promising application prospects. *Chemical Society Reviews* **2015**, *44*, 5291-5319, doi:10.1039/C5CS00268K.
129. Gupta, N.K.; Nishimura, S.; Takagaki, A.; Ebitani, K. Hydrotalcite-supported gold-nanoparticle-catalyzed highly efficient base-free aqueous oxidation of 5-hydroxymethylfurfural into 2,5-furandicarboxylic acid under atmospheric oxygen pressure. *Green Chemistry* **2011**, *13*, 824-827, doi:10.1039/C0GC00911C.
130. Fan, G.; Li, F.; Evans, D.G.; Duan, X. Catalytic applications of layered double hydroxides: recent advances and perspectives. *Chem Soc Rev* **2014**, *43*, 7040-7066, doi:10.1039/c4cs00160e.
131. Greenwell, H.C.; Marsden, C.C.; Jones, W. Synthesis of organo-layered double hydroxides by an environmentally friendly co-hydration route. *Green Chemistry* **2007**, *9*, 1299-1307, doi:10.1039/B706445D.
132. Madej, D.; Tyrała, K. In Situ Spinel Formation in a Smart Nano-Structured Matrix for No-Cement Refractory Castables. *Materials (Basel, Switzerland)* **2020**, *13*, doi:10.3390/ma13061403.
133. Bish, D.L.; Brindley, G.W. A reinvestigation of takovite, a nickel aluminum hydroxy-carbonate of the pyroaurite group. *American Mineralogist* **1977**, *62*, 458-464.
134. Bhojaraj; Arulraj, J.; Kolinjavadi, M.R.; Rajamathi, M. Solvent-Mediated and Mechanochemical Methods for Anion Exchange of Carbonate from Layered Double Hydroxides Using Ammonium Salts. *ACS Omega* **2019**, *4*, 20072-20079, doi:10.1021/acsomega.9b03261.
135. Intasa-ard, S.; Imwiset, K.; Bureekaew, S.; Ogawa, M. Mechanochemical methods for the preparation of intercalation compounds, from intercalation to the formation of layered double hydroxides. *Dalton Transactions* **2018**, *47*, 2896-2916, doi:10.1039/C7DT03736H.
136. Greenwell, H.C.; Jones, W.; Rugen-Hankey, S.L.; Holliman, P.J.; Thompson, R.L. Efficient synthesis of ordered organo-layered double hydroxides. *Green Chemistry* **2010**, *12*, 688-695, doi:10.1039/B916301H.
137. Xu, Z.P.; Lu, G.Q. Hydrothermal Synthesis of Layered Double Hydroxides (LDHs) from Mixed MgO and Al2O3: LDH Formation Mechanism. *Chemistry of Materials* **2005**, *17*, 1055-1062, doi:10.1021/cm048085g.
138. Klemkaite, K.; Prosycevas, I.; Taraskevicius, R.; Khinsky, A.; Kareiva, A. Synthesis and characterization of layered double hydroxides with different cations (Mg, Co, Ni, Al), decomposition and reformation of mixed metal oxides to layered structures. *Open Chemistry* **2011**, *9*, 275-282, doi:10.2478/s11532-011-0007-9.

139. Santos, R.M.M.; Tronto, J.; Briois, V.; Santilli, C.V. Thermal decomposition and recovery properties of ZnAl–CO3 layered double hydroxide for anionic dye adsorption: insight into the aggregative nucleation and growth mechanism of the LDH memory effect. *Journal of Materials Chemistry A* **2017**, *5*, 9998-10009, doi:10.1039/C7TA00834A.
140. Teixeira, A.C.; Morais, A.F.; Silva, I.G.N.; Breynaert, E.; Mustafa, D. Luminescent Layered Double Hydroxides Intercalated with an Anionic Photosensitizer via the Memory Effect. *Crystals* **2019**, *9*, 153, doi:10.3390/cryst9030153.
141. Kwok, W.L.J.; Suo, H.; Chen, C.; Leung, D.W.J.; Buffet, J.-C.; O'Hare, D. Synthesis of dense porous layered double hydroxides from struvite. *Green Chemistry* **2021**, 10.1039/D0GC04410E, doi:10.1039/D0GC04410E.
142. Ping, Z.; Bin, X.; Hehua, L.; Hui, L.; Guangren, Q. A Novel Approach to Recycle Waste Serpentine Tailing for Mg/Al Layered Double Hydroxide Used as Adsorption Material. *Environmental Engineering Science* **2021**, *38*, 99-106, doi:10.1089/ees.2020.0105.
143. Li, Q.; Wei, G.; Yang, Y.; Li, Z.; Zhang, L.; Huang, Q. Mechanochemical synthesis of Fe2O3/Zn-Al layered double hydroxide based on red mud. *Journal of Hazardous Materials* **2020**, *394*, 122566, doi:10.1016/j.jhazmat.2020.122566.
144. Yi, S.; Gao, B.; Sun, Y.; Wu, J.; Shi, X.; Wu, B.; Hu, X. Removal of levofloxacin from aqueous solution using rice-husk and wood-chip biochars. *Chemosphere* **2016**, *150*, 694-701, doi:10.1016/j.chemosphere.2015.12.112.
145. Stephen, J.L.; Periyasamy, B. Innovative developments in biofuels production from organic waste materials: A review. *Fuel* **2018**, *214*, 623-633, doi:10.1016/j.fuel.2017.11.042.
146. Eibner, S.; Margeriat, A.; Broust, F.; Laurenti, D.; Geantet, C.; Julbe, A.; Blin, J. Catalytic deoxygenation of model compounds from flash pyrolysis of lignocellulosic biomass over activated charcoal-based catalysts. *Applied Catalysis B: Environmental* **2017**, *219*, 517-525, doi:10.1016/j.apcatb.2017.07.071.
147. Serrano-Ruiz, J.C.; Luque, R.; Sepúlveda-Escribano, A. Transformations of biomass-derived platform molecules: from high added-value chemicals to fuelsvia aqueous-phase processing. *Chemical Society Reviews* **2011**, *40*, 5266-5281, doi:10.1039/C1CS15131B.
148. Pham, T.N.; Shi, D.; Resasco, D.E. Kinetics and Mechanism of Ketonization of Acetic Acid on Ru/TiO2 Catalyst. *Topics in Catalysis* **2014**, *57*, 706-714, doi:10.1007/s11244-013-0227-7.
149. V., A.; Warrier, A.R. Production of biodiesel from waste cooking oil using MgO nanocatalyst. *AIP Conference Proceedings* **2019**, *2115*, 030609, doi:10.1063/1.5113448.
150. Sapsford, D.; Santonastaso, M.; Thorn, P.; Kershaw, S. Conversion of coal mine drainage ochre to water treatment reagent: Production, characterisation and application for P and Zn removal. *Journal of Environmental Management* **2015**, *160*, 7-15, doi:10.1016/j.jenvman.2015.06.004.
151. Parida, K.; Satpathy, M.; Mohapatra, L. Incorporation of Fe3+ into Mg/Al layered double hydroxide framework: effects on textural properties and photocatalytic activity for H2 generation. *Journal of Materials Chemistry* **2012**, *22*, 7350-7357, doi:10.1039/C2JM15658J.
152. Kwok, W.L.J.; Suo, H.; Chen, C.; Leung, D.W.J.; Buffet, J.-C.; O'Hare, D. Synthesis of dense porous layered double hydroxides from struvite. *Green Chemistry* **2021**, *23*, 1616-1620, doi:10.1039/D0GC04410E.
153. Guinier, A. *X-Ray Diffraction: In Crystals, Imperfect Crystals, and Amorphous Bodies*; Dover Publications: 2013.
154. Waseda, Y.; Matsubara, E.; Shinoda, K. *X-Ray Diffraction Crystallography: Introduction, Examples and Solved Problems*; Springer Berlin Heidelberg: 2011.
155. Pecharsky, V.; Zavalij, P. *Fundamentals of Powder Diffraction and Structural Characterization of Materials*; Springer US: 2005.

156. Smith, B.C. *Fundamentals of Fourier Transform Infrared Spectroscopy, Second Edition*; Taylor & Francis: 2011.
157. Cristy, A.A.; Ozaki, Y.; Gregoriou, V.G. *Modern Fourier: Transform Infrared Spectroscopy*; Elsevier Science: 2001.
158. Society, R.C. Introdution to Infrared Spectroscopy (IR). Availabe online: http://www.rsc.org/learn-chemistry/resource/res00000283/spectroscopy-in-a-suitcase-ir-student-resources?cmpid=CMP00001302 (accessed on 17/07/2018).
159. Rouquerol, F.; Rouquerol, J.; Sing, K.S.W. *Adsorption by Powders and Porous Solids: Principles, Methodology and Applications*; Elsevier Science: 1999.
160. Sing, K. The use of nitrogen adsorption for the characterisation of porous materials. *Colloids and Surfaces A: Physicochemical and Engineering Aspects* **2001**, *187-188*, 3-9, doi:10.1016/S0927-7757(01)00612-4.
161. Che, M.; Vedrine, J.C. *Characterization of Solid Materials and Heterogeneous Catalysts: From Structure to Surface Reactivity*; Wiley: 2012.
162. Sing, K.S.W. Reporting physisorption data for gas/solid systems with special reference to the determination of surface area and porosity (Recommendations 1984). *Pure and Applied Chemistry* **1985**, *57*, 603-619, doi:10.1351/pac198557040603.
163. Leofanti, G.; Padovan, M.; Tozzola, G.; Venturelli, B. Surface area and pore texture of catalysts. *Catalysis Today* **1998**, *41*, 207-219, doi:10.1016/S0920-5861(98)00050-9.
164. Richards, R. *Surface and Nanomolecular Catalysis*; CRC Press: 2006.
165. Dollimore, D.; Spooner, P.; Turner, A. The bet method of analysis of gas adsorption data and its relevance to the calculation of surface areas. *Surface Technology* **1976**, *4*, 121-160, doi:https://doi.org/10.1016/0376-4583(76)90024-8.
166. Gregg, S.J.; Sing, K.S.W. *Adsorption, Surface Area and Porosity*; Academic Press Inc: New York, 1982.
167. Jennings, W. *Analytical Gas Chromatography*; Elsevier Science: 2012.
168. McNair, H.M.; Miller, J.M. *Basic Gas Chromatography*; Wiley: 2011.
169. Dettmer-Wilde, K.; Engewald, W. *Practical Gas Chromatography: A Comprehensive Reference*; Springer Berlin Heidelberg: 2014.
170. Barry, E.F.; Grob, R.L. *Columns for Gas Chromatography: Performance and Selection*; Wiley: 2007.
171. Rahman, M.M.; Abd El-Aty, A.; Choi, J.; Shin, H.; Shin, S.C.; Shim, J. *Basic Overview on Gas Chromatography Columns*; 2015; 10.1002/9783527678129.assep024.
172. Gohlke, R.S.; McLafferty, F.W. Early gas chromatography/mass spectrometry. *Journal of the American Society for Mass Spectrometry* **1993**, *4*, 367-371, doi:10.1016/1044-0305(93)85001-E.
173. Scientific, T.F. What is GC-MS? Availabe online: https://www.thermofisher.com/uk/en/home/industrial/mass-spectrometry/mass-spectrometry-learning-center/gas-chromatography-mass-spectrometry-gc-ms-information.html (accessed on 2021).
174. Moldoveanu, S.C.; David, V. Gas Chromatography - Derivatization, Sample Preparation, Application. 2018; 10.5772/intechopen.81954.
175. van den Berg, J.J.; Winterbourn, C.C.; Kuypers, F.A. Hypochlorous acid-mediated modification of cholesterol and phospholipid: analysis of reaction products by gas chromatography-mass spectrometry. *Journal of Lipid Research* **1993**, *34*, 2005-2012.
176. Skoog, D.A.; Holler, F.J.; Crouch, S.R. *Principles of Instrumental Analysis*; Cengage Learning: 2017.
177. Dayton, C. *Column Chromatography*; NY Research Press: 2015.

178. Chakravarti, B.; Mallik, B.; Chakravarti, D.N. Column Chromatography. *Current Protocols Essential Laboratory Techniques* **2016**, *13*, 6.2.1-6.2.15, doi:10.1002/cpet.6.
179. Coskun, O. Separation techniques: Chromatography. *North Clin Istanb* **2016**, *3*, 156-160, doi:10.14744/nci.2016.32757.
180. Brown, M.E. *Introduction to Thermal Analysis: Techniques and Applications*; Springer Netherlands: 2006.
181. Haines, P.J. *Thermal Methods of Analysis: Principles, Applications and Problems*; Springer Netherlands: 2012.
182. Gabbott, P. *Principles and Applications of Thermal Analysis*; Wiley: 2008.
183. Hatakeyama, T.; Zhenhai, L. *Handbook of Thermal Analysis*; Wiley: 1998.
184. Valente, J.S.; Rodriguez-Gattorno, G.; Valle-Orta, M.; Torres-Garcia, E. Thermal decomposition kinetics of MgAl layered double hydroxides. *Materials Chemistry and Physics* **2012**, *133*, 621-629, doi:10.1016/j.matchemphys.2012.01.026.
185. Höhne, G.; Hemminger, W.F.; Flammersheim, H.J. *Differential Scanning Calorimetry*; Springer Berlin Heidelberg: 2013.
186. Rafiquzzaman, S.M.; Rahman, M.A.; Kong, I.-S. Chapter 5 - Ultrasonic-Assisted Extraction of Carrageenan. In *Seaweed Polysaccharides*, Venkatesan, J., Anil, S., Kim, S.-K., Eds. Elsevier: 2017; 10.1016/B978-0-12-809816-5.00005-0pp. 75-81.
187. Ishii, T.; Kyotani, T. Chapter 14 - Temperature Programmed Desorption. In *Materials Science and Engineering of Carbon*, Inagaki, M., Kang, F., Eds. Butterworth-Heinemann: 2016; 10.1016/B978-0-12-805256-3.00014-3pp. 287-305.
188. Boss, C.B.; Fredeen, K.J. *Concepts, Instrumentation and Techniques in Inductively Coupled Plasma Optical Emission Spectrometry*, 3rd ed.; Perkin Elmer: 2004.
189. Ul-Hamid, A. *A Beginners' Guide to Scanning Electron Microscopy*; Springer International Publishing: 2018.
190. Zhou, W.; Wang, Z.L. *Scanning Microscopy for Nanotechnology: Techniques and Applications*; Springer New York: 2007.
191. Nagendra, B.; Rosely, C.V.; Leuteritz, A.; Reuter, U.; Gowd, B. Polypropylene/Layered Double Hydroxide Nanocomposites: Influence of LDH Intralayer Metal Constituents on the Properties of Polypropylene. *ACS Omega* **2017**, *2*, 20-31, doi:10.1021/acsomega.6b00485.
192. Imani, M.M.; Safaei, M. Optimized Synthesis of Magnesium Oxide Nanoparticles as Bactericidal Agents. *Journal of Nanotechnology* **2019**, *2019*, 6063832, doi:10.1155/2019/6063832.
193. Rather, S.U. Synthesis, characterization, and hydrogen uptake studies of magnesium nanoparticles by solution reduction method. *Materials Research Bulletin* **2014**, *60*, 556–561, doi:10.1016/j.materresbull.2014.09.027.
194. Ayache, J.; Beaunier, L.; Boumendil, J.; Ehret, G.; Laub, D. *Sample Preparation Handbook for Transmission Electron Microscopy: Methodology*; Springer New York: 2014.
195. Kerdcharoen, T.; Wongchoosuk, C. 11 - Carbon nanotube and metal oxide hybrid materials for gas sensing. In *Semiconductor Gas Sensors*, Jaaniso, R., Tan, O.K., Eds. Woodhead Publishing: 2013; 10.1533/9780857098665.3.386pp. 386-407.
196. De Caro, C.; Claudia, H. *UV/VIS Spectrophotometry - Fundamentals and Applications*; Mettler-Toledo: 2015.
197. Gauglitz, G. Ultraviolet and Visible Spectroscopy. In *Handbook of Analytical Techniques*, 2001; 10.1002/9783527618323.ch16pp. 419-463.
198. Perkampus, H.H.; Grinter, H.C.; Threlfall, T.L. *UV-VIS Spectroscopy and Its Applications*; Springer Berlin Heidelberg: 2013.

199. Owen, T.; Technologies, A. *Fundamentals of UV-visible Spectroscopy: A Primer*; Agilent Technologies: 2000.
200. Wang, F.; Liu, X.-K.; Gao, F. Chapter 1 - Fundamentals of Solar Cells and Light-Emitting Diodes. In *Advanced Nanomaterials for Solar Cells and Light Emitting Diodes*, Gao, F., Ed. Elsevier: 2019; 10.1016/B978-0-12-813647-8.00001-1pp. 1-35.
201. Perkowitz, S. *Optical Characterization of Semiconductors: Infrared, Raman, and Photoluminescence Spectroscopy*; Academic Press: 1993.
202. Razeghi, M. *Fundamentals of Solid State Engineering*; Springer US: 2006.
203. He, J.; Wei, M.; Li, B.; Kang, Y.; Evans, D.G.; Duan, X. Preparation of Layered Double Hydroxides. In *Layered Double Hydroxides*, Duan, X., Evans, D.G., Eds. Springer Berlin Heidelberg: Berlin, Heidelberg, 2006; 10.1007/430_006pp. 89-119.
204. Zhang, L.; Xu, C.; Champagne, P. Overview of recent advances in thermo-chemical conversion of biomass. *Energy Conversion and Management* **2010**, *51*, 969-982, doi:10.1016/j.enconman.2009.11.038.
205. Li, D.; Xin, H.; Du, X.; Hao, X.; Liu, Q.; Hu, C. Recent advances for the production of hydrocarbon biofuel via deoxygenation progress. *Science Bulletin* **2015**, *60*, 2096-2106, doi:10.1007/s11434-015-0971-0.
206. Ignatchenko, A.V. Density Functional Theory Study of Carboxylic Acids Adsorption and Enolization on Monoclinic Zirconia Surfaces. *The Journal of Physical Chemistry C* **2011**, *115*, 16012-16018, doi:10.1021/jp203381h.
207. Renz, M. Ketonization of Carboxylic Acids by Decarboxylation: Mechanism and Scope. *European Journal of Organic Chemistry* **2005**, *2005*, 979-988, doi:10.1002/ejoc.200400546.
208. Dang, L.; Nai, X.; Zhu, D.; Jing, Y.; Liu, X.; Dong, Y.; Li, W. Study on the mechanism of surface modification of magnesium oxysulfate whisker. *Applied Surface Science* **2014**, *317*, 325-331, doi:10.1016/j.apsusc.2014.07.205.
209. Li, S. Combustion synthesis of porous MgO and its adsorption properties. *International Journal of Industrial Chemistry* **2019**, *10*, 89-96, doi:10.1007/s40090-019-0174-7.
210. Ma, Q.; Liu, Y.; Liu, C.; He, H. Heterogeneous reaction of acetic acid on MgO, α-Al2O3, and CaCO3 and the effect on the hygroscopic behaviour of these particles. *Physical Chemistry Chemical Physics* **2012**, *14*, 8403-8409, doi:10.1039/C2CP40510E.
211. Holder, C.F.; Schaak, R.E. Tutorial on Powder X-ray Diffraction for Characterizing Nanoscale Materials. *ACS Nano* **2019**, *13*, 7359-7365, doi:10.1021/acsnano.9b05157.
212. Mukherjee, S.S.; Bai, F.; MacMahon, D.; Lee, C.-L.; Gupta, S.K.; Kurinec, S.K. Crystallization and grain growth behavior of CoFeB and MgO layers in multilayer magnetic tunnel junctions. *Journal of Applied Physics* **2009**, *106*, 033906, doi:10.1063/1.3176501.
213. Hanif, A.; Dasgupta, S.; Nanoti, A. Facile Synthesis of High-Surface-Area Mesoporous MgO with Excellent High-Temperature CO2 Adsorption Potential. *Industrial & Engineering Chemistry Research* **2016**, *55*, 8070-8078, doi:10.1021/acs.iecr.6b00647.
214. Mara, R.T.; Sutherland, G.B.B.M. The Infrared Spectrum of Brucite [Mg(OH)2]*. *J. Opt. Soc. Am.* **1953**, *43*, 1100-1102, doi:10.1364/JOSA.43.001100.
215. Philipp, R.; Fujimoto, K. FTIR spectroscopic study of carbon dioxide adsorption/desorption on magnesia/calcium oxide catalysts. *The Journal of Physical Chemistry* **1992**, *96*, 9035-9038, doi:10.1021/j100201a063.
216. Oldham, C. Complexes of Simple Carboxylic Acids. In *Progress in Inorganic Chemistry*, 1968; 10.1002/9780470166116.ch3pp. 223-258.
217. Shifu, W.; Jinguang, W.; Guangxian, X. *FT-IR Spectra Of The C=O And C-H Stretching Vibration Of Lauric Acid*; SPIE: 1989; Vol. 1145.

218. Sanz, J.F.; Oviedo, J.; Márquez, A.; Odriozola, J.A.; Montes, M. Adsorption of Acetone onto MgO: Experimental and Theoretical Evidence for the Presence of a Surface Enolate. *Angewandte Chemie International Edition* **1999**, *38*, 506-509, doi:10.1002/(sici)1521-3773(19990215)38:4<506::aid-anie506>3.0.co;2-f.
219. Zaki, M.I.; Hasan, M.A.; Pasupulety, L. Surface Reactions of Acetone on Al2O3, TiO2, ZrO2, and CeO2: IR Spectroscopic Assessment of Impacts of the Surface Acid−Base Properties. *Langmuir* **2001**, *17*, 768-774, doi:10.1021/la000976p.
220. Sugiyama, S.; Sato, K.; Yamasaki, S.; Kawashiro, K.; Hayashi, H. Ketones from carboxylic acids over supported magnesium oxide and related catalysts. *Catalysis Letters* **1992**, *14*, 127-133, doi:10.1007/BF00764227.
221. Landoll, M.; Holtzapple, M. Thermal decomposition of mixed calcium carboxylate salts: Effects of lime on ketone yield. *Biomass and Bioenergy* **2011**, *35*, 3592-3603, doi:10.1016/j.biombioe.2011.05.012.
222. Matos, C.R.S.; Xavier, M.J.; Barreto, L.S.; Costa, N.B.; Gimenez, I.F. Principal Component Analysis of X-ray Diffraction Patterns To Yield Morphological Classification of Brucite Particles. *Analytical Chemistry* **2007**, *79*, 2091-2095, doi:10.1021/ac061991n.
223. Constantino, V.R.L.; Pinnavaia, T.J. Structure-reactivity relationships for basic catalysts derived from a Mg2+/A13+ /CO3−layered double hydroxide. *Catalysis Letters* **1994**, *23*, 361-367, doi:10.1007/BF00811370.
224. Pinnavaia, T.J.; Chibwe, M.; Constantino, V.R.L.; Yun, S.K. Organic chemical conversions catalyzed by intercalated layered double hydroxides (LDHs). *Applied Clay Science* **1995**, *10*, 117-129, doi:10.1016/0169-1317(95)00010-2.
225. Ignatchenko, A.V.; McSally, J.P.; Bishop, M.D.; Zweigle, J. Ab initio study of the mechanism of carboxylic acids cross-ketonization on monoclinic zirconia via condensation to beta-keto acids followed by decarboxylation. *Molecular Catalysis* **2017**, *441*, 35-62, doi:10.1016/j.mcat.2017.07.019.
226. Buathong, P.; Boonvitthya, N.; Truan, G.; Chulalaksananukul, W. Whole-Cell Biotransformation of 1,12-Dodecanedioic Acid from Coconut Milk Factory Wastewater by Recombinant CYP52A17SS Expressing Saccharomyces cerevisiae. *Processes* **2020**, *8*, 969, doi:10.3390/pr8080969.
227. Boateng, L.; Ansong, R.; Owusu, W.B.; Steiner-Asiedu, M. Coconut oil and palm oil's role in nutrition, health and national development: A review. *Ghana Med J* **2016**, *50*, 189-196.
228. Ignatchenko, A.V.; DeRaddo, J.S.; Marino, V.J.; Mercado, A. Cross-selectivity in the catalytic ketonization of carboxylic acids. *Applied Catalysis A: General* **2015**, *498*, 10-24, doi:10.1016/j.apcata.2015.03.017.
229. Lee, K.; Kim, M.; Choi, M. Effects of Fatty Acid Structures on Ketonization Selectivity and Catalyst Deactivation. *ACS Sustainable Chemistry & Engineering* **2018**, *6*, doi:10.1021/acssuschemeng.8b02576.
230. Ignatchenko, A.V.; Cohen, A.J. Reversibility of the catalytic ketonization of carboxylic acids and of beta-keto acids decarboxylation. *Catalysis Communications* **2018**, *111*, 104-107, doi:10.1016/j.catcom.2018.04.002.
231. Baylon, R.A.L.; Sun, J.; Martin, K.J.; Venkitasubramanian, P.; Wang, Y. Beyond ketonization: selective conversion of carboxylic acids to olefins over balanced Lewis acid–base pairs. *Chemical Communications* **2016**, *52*, 4975-4978, doi:10.1039/C5CC10528E.
232. Guo, W.; Zhu, Y.; Han, Y.; Luo, B.; Wei, Y. Separation Mechanism of Fatty Acids from Waste Cooking Oil and Its Flotation Performance in Iron Ore Desiliconization. *Minerals* **2017**, *7*, 244, doi:10.3390/min7120244.

233. Chen, W.-S.; Strik, D.P.B.T.B.; Buisman, C.J.N.; Kroeze, C. Production of Caproic Acid from Mixed Organic Waste: An Environmental Life Cycle Perspective. *Environmental Science & Technology* **2017**, *51*, 7159-7168, doi:10.1021/acs.est.6b06220.
234. Atasoy, M.; Owusu-Agyeman, I.; Plaza, E.; Cetecioglu, Z. Bio-based volatile fatty acid production and recovery from waste streams: Current status and future challenges. *Bioresour Technol* **2018**, *268*, 773-786, doi:10.1016/j.biortech.2018.07.042.
235. Jahnen-Dechent, W.; Ketteler, M. Magnesium basics. *Clin Kidney J* **2012**, *5*, i3-i14, doi:10.1093/ndtplus/sfr163.
236. Pubchem. Availabe online: https://pubchem.ncbi.nlm.nih.gov/ (accessed on 08/08/21).
237. Smith, M.B. *Organic Synthesis*; Elsevier Science: 2016.
238. Fogler, H.S. *Elements of Chemical Reaction Engineering*; Prentice Hall PTR: 2006.
239. Oliver-Tomas, B.; Gonell, F.; Pulido, A.; Renz, M.; Boronat, M. Effect of the Cα substitution on the ketonic decarboxylation of carboxylic acids over m-ZrO2: the role of entropy. *Catalysis Science & Technology* **2016**, *6*, 5561-5566, doi:10.1039/C6CY00395H.
240. Conroy, N. Polymerization of unsaturated fatty acids. 1972.
241. Cowan, J.C. Dimer Acids. *Journal of the American Oil Chemists' Society* **1962**, *39*, 534-545, doi:10.1007/BF02672546.
242. Velde, H. Liquid phase decarboxylation of fatty acids to ketones. 1968.
243. De Bhowmick, G.; Sarmah, A.K.; Sen, R. Lignocellulosic biorefinery as a model for sustainable development of biofuels and value added products. *Bioresource Technology* **2018**, *247*, 1144-1154, doi:10.1016/j.biortech.2017.09.163.
244. Janampelli, S.; Darbha, S. Selective and reusable Pt-WOx/Al2O3 catalyst for deoxygenation of fatty acids and their esters to diesel-range hydrocarbons. *Catalysis Today* **2017**, *309*, 219-226, doi:10.1016/j.cattod.2017.06.030.
245. Goh, K.-H.; Lim, T.-T.; Dong, Z. Application of layered double hydroxides for removal of oxyanions: A review. *Water Research* **2008**, *42*, 1343-1368, doi:10.1016/j.watres.2007.10.043.
246. Evans, D.G.; Slade, R.C.T. Structural Aspects of Layered Double Hydroxides. In *Layered Double Hydroxides*, Duan, X., Evans, D.G., Eds. Springer Berlin Heidelberg: Berlin, Heidelberg, Germany, 2006; 10.1007/430_005pp. 1-87.
247. Dobbie, K.E.; Heal, K.V.; Aumônier, J.; Smith, K.A.; Johnston, A.; Younger, P.L. Evaluation of iron ochre from mine drainage treatment for removal of phosphorus from wastewater. *Chemosphere* **2009**, *75*, 795-800, doi:10.1016/j.chemosphere.2008.12.049.
248. Heal, K.V.; Smith, K.; Younger, P.; McHaffie, H.; Batty, L. Removing phosphorus from sewage effluent and agricultural runoff using recovered ochre. In *Phosphorus in Environmental Technology: Principles and Applications*, Valsami-Jones, E., Ed. IWA Publishing: 2004; pp. 321-335.
249. Littler, J.; Geroni, J.N.; Sapsford, D.J.; Coulton, R.; Griffiths, A.J. Mechanisms of phosphorus removal by cement-bound ochre pellets. *Chemosphere* **2013**, *90*, 1533-1538, doi:10.1016/j.chemosphere.2012.08.054.
250. Satterley, C. Personal correspondance with Jon Aumonier. 2019.
251. Bumajdad, A.; Ali, S.; Mathew, A. Characterization of iron hydroxide/oxide nanoparticles prepared in microemulsions stabilized with cationic/non-ionic surfactant mixtures. *Journal of Colloid and Interface Science* **2011**, *355*, 282-292, doi:10.1016/j.jcis.2010.12.022.
252. Song, S.; Jia, F.; Peng, C. Study on decomposition of goethite/siderite in thermal modification through XRD, SEM and TGA measurements. *Surface Review and Letters (SRL)* **2014**, *21*, 1-6, doi:10.1142/S0218625X1450019X.

253. Zhang, C.; Zhu, J.; Rui, X.; Chen, J.; Sim, D.; Shi, W.; Hng, H.H.; Lim, T.M.; Yan, Q. Synthesis of hexagonal-symmetry α-iron oxyhydroxide crystals using reduced graphene oxide as a surfactant and their Li storage properties. *CrystEngComm* **2012**, *14*, 147-153, doi:10.1039/C1CE05965C.
254. Shekoohi, K.; Hosseini, F.S.; Haghighi, A.H.; Sahrayian, A. Synthesis of some Mg/Co-Al type nano hydrotalcites and characterization. *MethodsX* **2017**, *4*, 86-94, doi:10.1016/j.mex.2017.01.003.
255. Brito, A.; Borges, M.E.; Garín, M.; Hernández, A. Biodiesel Production from Waste Oil Using Mg−Al Layered Double Hydroxide Catalysts. *Energy & Fuels* **2009**, *23*, 2952-2958, doi:10.1021/ef801086p.
256. del Arco, M.; Malet, P.; Trujillano, R.; Rives, V. Synthesis and Characterization of Hydrotalcites Containing Ni(II) and Fe(III) and Their Calcination Products. *Chemistry of Materials* **1999**, *11*, 624-633, doi:10.1021/cm9804923.
257. Novillo, C.; Guaya, D.; Allen-Perkins Avendaño, A.; Armijos, C.; Cortina, J.L.; Cota, I. Evaluation of phosphate removal capacity of Mg/Al layered double hydroxides from aqueous solutions. *Fuel* **2014**, *138*, 72-79, doi:10.1016/j.fuel.2014.07.010.
258. Das, J.; Patra, B.S.; Baliarsingh, N.; Parida, K.M. Adsorption of phosphate by layered double hydroxides in aqueous solutions. *Applied Clay Science* **2006**, *32*, 252-260, doi:10.1016/j.clay.2006.02.005.
259. Brian, G.; Erwan, A.; Christian, R.; Cedric, C. Tuning and Investigating the Structure of MII-FeIII Layered Double Hydroxides (MII = NiII, CoII and MgII) in Relation to their Composition: From Synthesis to Anionic Exchange Properties. *Current Inorganic Chemistry (Discontinued)* **2015**, *5*, 169-183, doi:10.2174/1877944105666150420235630.
260. Xie, Y.; Yuan, X.; Wu, Z.; Zeng, G.; Jiang, L.; Peng, X.; Li, H. Adsorption behavior and mechanism of Mg/Fe layered double hydroxide with Fe3O4-carbon spheres on the removal of Pb(II) and Cu(II). *Journal of Colloid and Interface Science* **2019**, *536*, 440-455, doi:10.1016/j.jcis.2018.10.066.
261. Ding, Y.; Liu, L.; Fang, Y.; Zhang, X.; Lyu, M.; Wang, S. The Adsorption of Dextranase onto Mg/Fe-Layered Double Hydroxide: Insight into the Immobilization. *Nanomaterials* **2018**, *8*, 173, doi:10.3390/nano8030173.
262. Ahmed, I.M.; Gasser, M.S. Adsorption study of anionic reactive dye from aqueous solution to Mg–Fe–CO3 layered double hydroxide (LDH). *Applied Surface Science* **2012**, *259*, 650-656, doi:10.1016/j.apsusc.2012.07.092.
263. Jia, X.; Li, D.; Evans, D.G.; Lin, Y. Optimization of the wash process and wash water recycling in the preparation of MgZnAl–CO3 layered double hydroxides. *Particuology* **2010**, *8*, 231-233, doi:10.1016/j.partic.2010.03.005.
264. Morterra, C.; Chiorlno, A.; Borello, E. An IR spectroscopic characterization of α-FeOOH (goethite). *Materials Chemistry and Physics* **1984**, *10*, 119-138, doi:10.1016/0254-0584(84)90042-7.
265. Prasad, P.S.R.; Shiva Prasad, K.; Krishna Chaitanya, V.; Babu, E.V.S.S.K.; Sreedhar, B.; Ramana Murthy, S. In situ FTIR study on the dehydration of natural goethite. *Journal of Asian Earth Sciences* **2006**, *27*, 503-511, doi:10.1016/j.jseaes.2005.05.005.
266. Xiao, W.; Jones, A.M.; Collins, R.N.; Bligh, M.W.; Waite, T.D. Use of fourier transform infrared spectroscopy to examine the Fe(II)-Catalyzed transformation of ferrihydrite. *Talanta* **2017**, *175*, 30-37, doi:10.1016/j.talanta.2017.07.018.
267. Das, J.; Sairam Patra, B.; Baliarsingh, N.; Parida, K.M. Calcined Mg–Fe–CO3 LDH as an adsorbent for the removal of selenite. *Journal of Colloid and Interface Science* **2007**, *316*, 216-223, doi:10.1016/j.jcis.2007.07.082.

268. Cocheci, L.; Barvinschi, P.; Pode, R.; Popovici, E.; Seftel, E. Structural characterization of some Mg/Zn-Al type hydrotalcites prepared for chromate sorption from wastewater. *Chem. Bull. Politehnica Univ* **2010**, *55*, 17.
269. Yang, K.; Yan, L.-g.; Yang, Y.-m.; Yu, S.-j.; Shan, R.-r.; Yu, H.-q.; Zhu, B.-c.; Du, B. Adsorptive removal of phosphate by Mg–Al and Zn–Al layered double hydroxides: Kinetics, isotherms and mechanisms. *Separation and Purification Technology* **2014**, *124*, 36-42, doi:10.1016/j.seppur.2013.12.042.
270. Zhou, J.; Yang, S.; Yu, J.; Shu, Z. Novel hollow microspheres of hierarchical zinc–aluminum layered double hydroxides and their enhanced adsorption capacity for phosphate in water. *Journal of Hazardous Materials* **2011**, *192*, 1114-1121, doi:10.1016/j.jhazmat.2011.06.013.
271. Pal, N.; Bhaumik, A. Mesoporous materials: versatile supports in heterogeneous catalysis for liquid phase catalytic transformations. *RSC Advances* **2015**, *5*, 24363-24391, doi:10.1039/C4RA13077D.
272. Grégoire, B.; Ruby, C.; Carteret, C. Hydrolysis of mixed Ni2+–Fe3+ and Mg2+–Fe3+ solutions and mechanism of formation of layered double hydroxides *Dalton Transactions* **2013**, *42*, 15687-15698, doi:10.1039/C3DT51521D.
273. Masuda, T.; Kondo, Y.; Miwa, M.; Shimotori, T.; Mukai, S.R.; Hashimoto, K.; Takano, M.; Kawasaki, S.; Yoshida, S. Recovery of useful hydrocarbons from oil palm waste using ZrO2 supporting FeOOH catalyst. *Chemical Engineering Science* **2001**, *56*, 897-904, doi:10.1016/S0009-2509(00)00303-1.
274. Masuda, T.; Miwa, Y.; Hashimoto, K.; Ikeda, Y. Recovery of oil from waste poly(ethylene terephthalate) without producing any sublimate materials. *Polymer Degradation and Stability* **1998**, *61*, 217-224, doi:10.1016/S0141-3910(97)00133-X.
275. Takagi, K.; Shichi, T.; Usami, H.; Sawaki, Y. Controlled photocycloaddition of unsaturated carboxylates intercalated in hydrotalcite clay interlayers. *Journal of the American Chemical Society* **1993**, *115*, 4339-4344, doi:10.1021/ja00063a060.
276. Maher, K.D.; Kirkwood, K.M.; Gray, M.R.; Bressler, D.C. Pyrolytic Decarboxylation and Cracking of Stearic Acid. *Industrial & Engineering Chemistry Research* **2008**, *47*, 5328-5336, doi:10.1021/ie0714551.
277. Torok, B.; Dransfield, T. *Green Chemistry: An Inclusive Approach*; Elsevier Science: 2017.
278. Anastas, P.; Eghbali, N. Green Chemistry: Principles and Practice. *Chemical Society Reviews* **2010**, *39*, 301-312, doi:10.1039/B918763B.
279. Kalmykova, Y.; Sadagopan, M.; Rosado, L. Circular economy – From review of theories and practices to development of implementation tools. *Resources, Conservation and Recycling* **2018**, *135*, 190-201, doi:10.1016/j.resconrec.2017.10.034.
280. Ahmed, D.N.; Naji, L.A.; Faisal, A.A.H.; Al-Ansari, N.; Naushad, M. Waste foundry sand/MgFe-layered double hydroxides composite material for efficient removal of Congo red dye from aqueous solution. *Scientific Reports* **2020**, *10*, 2042, doi:10.1038/s41598-020-58866-y.
281. Hu, P.; Zhang, Y.; Lv, F.; Tong, W.; Xin, H.; Meng, Z.; Wang, X.; Chu, P.K. Preparation of layered double hydroxides using boron mud and red mud industrial wastes and adsorption mechanism to phosphate. *Water and Environment Journal* **2017**, *31*, 145-157, doi:10.1111/wej.12212.
282. Fujishima, A.; Honda, K. Electrochemical Photolysis of Water at a Semiconductor Electrode. *Nature* **1972**, *238*, 37-38, doi:10.1038/238037a0.

283. Kumaravel, V.; Imam, M.D.; Badreldin, A.; Chava, R.K.; Do, J.Y.; Kang, M.; Abdel-Wahab, A. Photocatalytic Hydrogen Production: Role of Sacrificial Reagents on the Activity of Oxide, Carbon, and Sulfide Catalysts. *Catalysts* **2019**, *9*, 276.
284. Alfonso-Herrera, L.A.; Huerta-Flores, A.M.; Torres Martínez, L.M.; Ramírez-Herrera, D.J.; Rivera-Villanueva, J.M. M-008: A stable and reusable metalorganic framework with high crystallinity applied in the photocatalytic hydrogen evolution and the degradation of methyl orange. *Journal of Photochemistry and Photobiology A: Chemistry* **2020**, *389*, 112240, doi:10.1016/j.jphotochem.2019.112240.
285. Hernández-Alonso, M.D.; Fresno, F.; Suárez, S.; Coronado, J.M. Development of alternative photocatalysts to TiO2: Challenges and opportunities. *Energy & Environmental Science* **2009**, *2*, 1231-1257, doi:10.1039/B907933E.
286. Zhang, G.; Teng, F.; Zhao, C.; Chen, L.; Zhang, P.; Wang, Y.; Gong, C.; Zhang, Z.; Xie, E. Enhanced photocatalytic activity of TiO2/carbon@TiO2 core–shell nanocomposite prepared by two-step hydrothermal method. *Applied Surface Science* **2014**, *311*, 384-390, doi:10.1016/j.apsusc.2014.05.072.
287. Fresno, F.; Portela, R.; Suárez, S.; Coronado, J.M. Photocatalytic materials: recent achievements and near future trends. *Journal of Materials Chemistry A* **2014**, *2*, 2863-2884, doi:10.1039/C3TA13793G.
288. Gao, Q.; Si, F.; Zhang, S.; Fang, Y.; Chen, X.; Yang, S. Hydrogenated F-doped TiO2 for photocatalytic hydrogen evolution and pollutant degradation. *International Journal of Hydrogen Energy* **2019**, *44*, 8011-8019, doi:10.1016/j.ijhydene.2019.01.233.
289. Wang, D.; Kanhere, P.; Li, M.; Tay, Q.; Tang, Y.; Huang, Y.; Sum, T.C.; Mathews, N.; Sritharan, T.; Chen, Z. Improving Photocatalytic H2 Evolution of TiO2 via Formation of {001}–{010} Quasi-Heterojunctions. *The Journal of Physical Chemistry C* **2013**, *117*, 22894-22902, doi:10.1021/jp407508n.
290. Mohapatra, L.; Parida, K. A review on the recent progress, challenges and perspective of layered double hydroxides as promising photocatalysts. *Journal of Materials Chemistry A* **2016**, *4*, 10744-10766, doi:10.1039/C6TA01668E.
291. Silva, C.G.; Bouizi, Y.; Fornés, V.; García, H. Layered Double Hydroxides as Highly Efficient Photocatalysts for Visible Light Oxygen Generation from Water. *Journal of the American Chemical Society* **2009**, *131*, 13833-13839, doi:10.1021/ja905467v.
292. Megala, S.; Sathish, M.; Harish, S.; Navaneethan, M.; Sohila, S.; Liang, B.; Ramesh, R. Enhancement of photocatalytic H2 evolution from water splitting by construction of two dimensional gC3N4/NiAl layered double hydroxides. *Applied Surface Science* **2020**, *509*, 144656, doi:10.1016/j.apsusc.2019.144656.
293. Zhang, G.; Lin, B.; Yang, W.; Jiang, S.; Yao, Q.; Chen, Y.; Gao, B. Highly efficient photocatalytic hydrogen generation by incorporating CdS into ZnCr-layered double hydroxide interlayer. *RSC Advances* **2015**, *5*, 5823-5829, doi:10.1039/C4RA11757C.
294. Parida, K.; Mohapatra, L. Recent progress in the development of carbonate-intercalated Zn/Cr LDH as a novel photocatalyst for hydrogen evolution aimed at the utilization of solar light. *Dalton transactions (Cambridge, England : 2003)* **2011**, *41*, 1173-1178, doi:10.1039/c1dt10957j.
295. Baliarsingh, N.; Mohapatra, L.; Parida, K. Design and development of a visible light harvesting Ni–Zn/Cr–CO32− LDH system for hydrogen evolution. *Journal of Materials Chemistry A* **2013**, *1*, 4236-4243, doi:10.1039/C2TA00933A.
296. Zeng, R.; Li, X.-T.; Liu, Z.-G.; Zhang, F.; Li, S.-Q.; Cui, H.-Z. Corrosion resistance of Zn-Al layered double hydroxide/poly(lactic acid) composite coating on magnesium alloy AZ31. *Frontiers of Materials Science* **2015**, *9*, doi:10.1007/s11706-015-0307-7.

297. Selvamani, T.; Sinhamahapatra, A.; Bhattacharjya, D.; Mukhopadhyay, I. Rectangular MgO microsheets with strong catalytic activity. *Materials Chemistry and Physics* **2011**, *129*, 853-861, doi:10.1016/j.matchemphys.2011.05.055.
298. Li, S.; Wang, Z.; Chang, T.-T. Temperature Oscillation Modulated Self-Assembly of Periodic Concentric Layered Magnesium Carbonate Microparticles. *PloS one* **2014**, *9*, e88648, doi:10.1371/journal.pone.0088648.
299. Cao, Y.; Zheng, D.; Dong, S.; Zhang, F.; Lin, J.; Wang, C.; Lin, C. A Composite Corrosion Inhibitor of MgAl Layered Double Hydroxides Co-Intercalated with Hydroxide and Organic Anions for Carbon Steel in Simulated Carbonated Concrete Pore Solutions. *Journal of The Electrochemical Society* **2019**, *166*, C3106-C3113, doi:10.1149/2.0141911jes.
300. Halajnia, A.; Oustan, S.; Najafi, N.; Khataee, A.R.; Lakzian, A. The adsorption characteristics of nitrate on Mg–Fe and Mg–Al layered double hydroxides in a simulated soil solution. *Applied Clay Science* **2012**, *70*, 28-36, doi:10.1016/j.clay.2012.09.007.
301. Hur, T.-B.; Phuoc, T.; Chyu, M. New approach to the synthesis of layered double hydroxides and associated ultrathin nanosheets in de-ionized water by laser ablation. *Journal of Applied Physics - J APPL PHYS* **2010**, *108*, doi:10.1063/1.3518510.
302. Mohapatra, L.; Patra, D.; Parida, K.; Zaidi, S.J. Enhanced Photocatalytic Activity of a Molybdate-Intercalated Iron-Based Layered Double Hydroxide. *European Journal of Inorganic Chemistry* **2017**, *2017*, 723-733, doi:10.1002/ejic.201601191.
303. Radha, S.; Vishnu Kamath, P. Electronic spectra of anions intercalated in layered double hydroxides. *Bulletin of Materials Science* **2013**, *36*, 923-929, doi:10.1007/s12034-013-0538-0.
304. Skoog, D.A.; West, D.M.; Holler, F.J.; Crouch, S.R. *Fundamentals of Analytical Chemistry*; Cengage Learning: 2013.
305. Liu, M.; Qiu, X.; Miyauchi, M.; Hashimoto, K. Energy-Level Matching of Fe(III) Ions Grafted at Surface and Doped in Bulk for Efficient Visible-Light Photocatalysts. *Journal of the American Chemical Society* **2013**, *135*, 10064-10072, doi:10.1021/ja401541k.
306. Jin, Q.; Fujishima, M.; Tada, H. Visible-Light-Active Iron Oxide-Modified Anatase Titanium(IV) Dioxide. *The Journal of Physical Chemistry C* **2011**, *115*, 6478-6483, doi:10.1021/jp201131t.
307. Othman, S.H.; Abdul Rashid, S.; Mohd Ghazi, T.I.; Abdullah, N. Fe-Doped TiO2 Nanoparticles Produced via MOCVD: Synthesis, Characterization, and Photocatalytic Activity. *Journal of Nanomaterials* **2011**, *2011*, 571601, doi:10.1155/2011/571601.
308. Lee, H.; Reddy, D.A.; Kim, Y.; Chun, S.Y.; Ma, R.; Kumar, D.P.; Song, J.K.; Kim, T.K. Drastic Improvement of 1D-CdS Solar-Driven Photocatalytic Hydrogen Evolution Rate by Integrating with NiFe Layered Double Hydroxide Nanosheets Synthesized by Liquid-Phase Pulsed-Laser Ablation. *ACS Sustainable Chemistry & Engineering* **2018**, *6*, 16734-16743, doi:10.1021/acssuschemeng.8b04000.
309. Kim, D.S.; Kwak, S.-Y. The hydrothermal synthesis of mesoporous TiO2 with high crystallinity, thermal stability, large surface area, and enhanced photocatalytic activity. *Applied Catalysis A: General* **2007**, *323*, 110-118, doi:10.1016/j.apcata.2007.02.010.
310. Peng, T.; Zhao, D.; Dai, K.; Shi, W.; Hirao, K. Synthesis of Titanium Dioxide Nanoparticles with Mesoporous Anatase Wall and High Photocatalytic Activity. *The Journal of Physical Chemistry B* **2005**, *109*, 4947-4952, doi:10.1021/jp044771r.
311. Kim, S.J.; Lee, Y.; Lee, D.K.; Lee, J.W.; Kang, J.K. Efficient Co–Fe layered double hydroxide photocatalysts for water oxidation under visible light. *Journal of Materials Chemistry A* **2014**, *2*, 4136-4139, doi:10.1039/C3TA14933A.

312. Ekwurzel, B.; Boneham, J.; Dalton, M.W.; Heede, R.; Mera, R.J.; Allen, M.R.; Frumhoff, P.C. The rise in global atmospheric CO2, surface temperature, and sea level from emissions traced to major carbon producers. *Climatic Change* **2017**, *144*, 579-590, doi:10.1007/s10584-017-1978-0.
313. Grossman, G.M.; Krueger, A.B. Economic Growth and the Environment*. *The Quarterly Journal of Economics* **1995**, *110*, 353-377, doi:10.2307/2118443.
314. Sayed, M.R.; Abukhadra, M.R.; Abdelkader Ahmed, S.; Shaban, M.; Javed, U.; Betiha, M.A.; Shim, J.-J.; Rabie, A.M. Synthesis of advanced MgAl-LDH based geopolymer as a potential catalyst in the conversion of waste sunflower oil into biodiesel: Response surface studies. *Fuel* **2020**, *282*, 118865, doi:10.1016/j.fuel.2020.118865.
315. Mahgoub, S.M.; Shehata, M.R.; Abo El-Ela, F.L.; Farghali, A.; Zaher, A.; Mahmoud, R.K. Sustainable waste management and recycling of Zn–Al layered double hydroxide after adsorption of levofloxacin as a safe anti-inflammatory nanomaterial. *RSC Advances* **2020**, *10*, 27633-27651, doi:10.1039/D0RA04898D.
316. Belviso, C.; Piancastelli, A.; Sturini, M.; Belviso, S. Synthesis of composite zeolite-layered double hydroxides using ultrasonic neutralized red mud. *Microporous and Mesoporous Materials* **2020**, *299*, 110108, doi:10.1016/j.micromeso.2020.110108.
317. Alquzweeni, S.S.; Alkizwini, R.S. Removal of Cadmium from Contaminated Water Using Coated Chicken Bones with Double-Layer Hydroxide (Mg/Fe-LDH). *Water* **2020**, *12*, 2303.
318. Stratful, I.; Scrimshaw, M.D.; Lester, J.N. Removal of Struvite to Prevent Problems Associated with its Accumulation in Wastewater Treatment Works. *Water Environment Research* **2004**, *76*, 437-443, doi:10.2175/106143004X151491.
319. Kleemann, R.; Clift, R.; Morse, S.; Pearce, P.; Chenoweth, J.; Saroj, D. Evaluation of Local and National Effects of Recovering Phosphorus at Wastewater Treatment Plants. *Resources Conservation and Recycling* **2015**, *105*, doi:10.1016/j.resconrec.2015.09.007.
320. Siciliano, A.; Limonti, C.; Curcio, G.M.; Molinari, R. Advances in Struvite Precipitation Technologies for Nutrients Removal and Recovery from Aqueous Waste and Wastewater. *Sustainability* **2020**, *12*, 7538.
321. Huang, H.; Xiao, D.; Liu, J.; Hou, L.; Ding, L. Recovery and removal of nutrients from swine wastewater by using a novel integrated reactor for struvite decomposition and recycling. *Scientific reports* **2015**, *5*, 10183, doi:10.1038/srep10183.
322. Kataki, S.; West, H.; Clarke, M.; Baruah, D.C. Phosphorus recovery as struvite from farm, municipal and industrial waste: Feedstock suitability, methods and pre-treatments. *Waste management (New York, N.Y.)* **2016**, *49*, 437-454, doi:10.1016/j.wasman.2016.01.003.
323. Prywer, J.; Torzewska, A.; Płociński, T. Unique Surface and Internal Structure of Struvite Crystals Formed by Proteus mirabilis. *Urological research* **2012**, *40*, doi:10.1007/s00240-012-0501-3.
324. A.P, M.; Rahiman, M.; Duwal, S.; Pd, R. Investigation on growth and morphology of in vitro generated struvite crystals. *Biocatalysis and Agricultural Biotechnology* **2019**, *17*, doi:10.1016/j.bcab.2019.01.023.
325. Frost, R.; Weier, M.; Erickson, K. Thermal decomposition of struvite. *Journal of Thermal Analysis and Calorimetry* **2004**, *76*, doi:10.1023/B:JTAN.0000032287.08535.b3.
326. Chauhan, C.K.; Joshi, M.J. In vitro crystallization, characterization and growth-inhibition study of urinary type struvite crystals. *Journal of Crystal Growth* **2013**, *362*, 330-337, doi:10.1016/j.jcrysgro.2011.11.008.
327. Máša, B.; Pulišová, P.; Bezdicka, P.; Michalková, E.; Subrt, J. Ochre precipitates and acid mine drainage in a mine environment. *Ceramics - Silikaty* **2012**, *56*.

328. Khitous, M.; Salem, Z.; Halliche, D. Removal of phosphate from industrial wastewater using uncalcined MgAl-NO 3 layered double hydroxide: batch study and modeling. *Desalination and Water Treatment* **2015**, *57*, 1-12, doi:10.1080/19443994.2015.1077745.
329. Sidorczuk, D.; Kozanecki, M.; Civalleri, B.; Pernal, K.; Prywer, J. Structural and Optical Properties of Struvite. Elucidating Structure of Infrared Spectrum in High Frequency Range. *The Journal of Physical Chemistry A* **2020**, *124*, 8668-8678, doi:10.1021/acs.jpca.0c04707.
330. Cheah, L.A.; Manohara, G.V.; Maroto-Valer, M.M.; Garcia, S. Layered Double Hydroxide (LDH)-Derived Mixed Metal Oxides (MMOs): A Systematic Crystal-Chemical Approach to Investigating the Chemical Composition and its Effect on High Temperature CO2 capture. *ChemistrySelect* **2020**, *5*, 5587-5594, doi:10.1002/slct.201904447.
331. Murayama, N.; Maekawa, I.; Ushiro, H.; Miyoshi, T.; Shibata, J.; Valix, M. Synthesis of various layered double hydroxides using aluminum dross generated in aluminum recycling process. *International Journal of Mineral Processing* **2012**, *110-111*, 46-52, doi:10.1016/j.minpro.2012.03.011.
332. Shih, K.; Yan, H. Chapter 26 - The Crystallization of Struvite and Its Analog (K-Struvite) From Waste Streams for Nutrient Recycling. In *Environmental Materials and Waste*, Prasad, M.N.V., Shih, K., Eds. Academic Press: 2016; 10.1016/B978-0-12-803837-6.00026-3pp. 665-686.
333. Grégoire, B.; Ruby, C.; Carteret, C. Hydrolysis of mixed Ni(2+)-Fe3+ and Mg(2+)-Fe3+ solutions and mechanism of formation of layered double hydroxides. *Dalton Trans* **2013**, *42*, 15687-15698, doi:10.1039/c3dt51521d.
334. Sadjadi, S. Chapter 13 - Catalysts Intercalated in Layered Double Hydroxides. In *Encapsulated Catalysts*, Sadjadi, S., Ed. Academic Press: 2017; 10.1016/B978-0-12-803836-9.00013-4pp. 443-476.
335. Sun, X.; Neuperger, E.; Dey, S.K. Insights into the synthesis of layered double hydroxide (LDH) nanoparticles: Part 1. Optimization and controlled synthesis of chloride-intercalated LDH. *Journal of colloid and interface science* **2015**, *459*, 264-272, doi:10.1016/j.jcis.2015.07.073.
336. Siciliano, A.; Stillitano, M.A.; Limonti, C.; Marchio, F. Ammonium Removal from Landfill Leachate by Means of Multiple Recycling of Struvite Residues Obtained through Acid Decomposition. *Applied Sciences* **2016**, *6*, 375.
337. Hibino, T. Evaluation of anion adsorption properties of nanocomposite polymer hydrogels containing layered double hydroxides. *Applied Clay Science* **2014**, *87*, 150-156, doi:10.1016/j.clay.2013.10.024.
338. Yadav, M.K.; Gupta, A.K.; Ghosal, P.S.; Mukherjee, A. Effect of coexisting ions on adsorptive removal of arsenate by Mg-Fe-(CO3) LDH: multi-component adsorption and ANN-based multivariate modeling. *Journal of Environmental Science and Health, Part A* **2021**, *56*, 572-584, doi:10.1080/10934529.2021.1898870.
339. de Marco, B.A.; Rechelo, B.S.; Tótoli, E.G.; Kogawa, A.C.; Salgado, H.R.N. Evolution of green chemistry and its multidimensional impacts: A review. *Saudi Pharmaceutical Journal* **2019**, *27*, 1-8, doi:10.1016/j.jsps.2018.07.011.
340. Jafari Foruzin, L.; Rezvani, Z.; Habibi, B. New ternary-component layered double hydroxide as a low-cost and efficient electrocatalyst for water oxidation: NiCaFe-LDH from eggshell bio-waste. *Applied Clay Science* **2020**, *188*, 105511, doi:10.1016/j.clay.2020.105511.